OXYGEN TRANSPORT AND CELL DISTRIBUTION OF SMOOTH MUSCLE CONSTRUCT CULTURED UNDER FLOW

CHAN WING YUE

School of Mechanical and Aerospace Engineering

A thesis submitted to the Nanyang Technological University
in fulfillment of the requirement for the degree of
Doctor of Philosophy

2010

Abstract

Internal oxygen transport is important in the development of tissue construct *in vitro*. A new bioreactor culture system and a mathematical model were established to investigate oxygen transport in relation to cell distribution of esophageal smooth muscle tissue construct cultured under medium flow. The bioreactor system was designed to enable *in-situ* oxygen profiling in the flow bioreactors to capture real-time spatial oxygen data in the growing construct; the mathematical model assuming oxygen-dependent growth kinetics was formulated using Volume Averaging Method (VAM) for the transport phenomena in the multiphasic tissue construct. The experimental results showed that increasing external medium flow across the construct surface improved not only the external oxygen transport by convection, but also the internal oxygenation that consequently increased the cellularity and improved the uniformity of cell distribution. Exposing only top surface with medium flow (single flow configuration) resulted in both decreasing oxygen level and cell density across the construct thickness. Exposing both top and bottom surface with flows (double flow configuration) led to symmetrical oxygen profiles with minimum point occurring near the core of the construct, and the cell distribution was greatly improved compared with those of single flow configuration and static culture. The simulation results demonstrated a good agreement with the experimental data in most of the cases, suggesting a strong correlation between oxygen transport and cell distribution in the construct cultured in the bioreactor.

Acknowledgements

My studies cannot be reached to this point without my brother's financial support at those hard times. His story inspires me at times to pursue what you believe is right for you.

First, I would like to acknowledge our lab technician, Mdm. Heng Chee Hoon who gives me limitless support. Without her, I would have given up and left the graduate program. Her patience and kindness really help me go through countless hard times. She will be so missed especially when we exchange ideas on Buddhism and life, and also those small talks we had.

Along the path of my Ph.D., I am really lucky to get to know three important friends for the last 2 years in NTU: Shigeaki Kinoshita, Wade Kiyohide and Norzana who validate my values in integrity and sincerity. Shig(-eaki), a friend who I hung out almost every evening in the lab for a year always has insights about the world and integrity. Kiyo(-hide), another great friend who finished his Ph.D. in NTU showed me how persistency can conquer and (Norz-)Ana, a pint-sized Malaysian Ph.D. student who attached in our lab for 6 months is a superwoman of her kind and demonstrates me how "gets the most out of it" is done.

I spent 90 % of my time in the lab and I really need to thank the Lab director, Prof. Sandy Chian Kerm Sin for granting me so much freedom in his lab and later, hired me to help make ends meet and entrusted me with a lot of responsibilities.

Next, I deeply appreciated Prof. Vladimir Kulish's last minute reach-out to be my supervisor when he has 5 to 6 Ph.D. students in hand and his continued patience and

tolerance over my thesis submission. At the same time, I also have to thank Head of Division, Prof Lua Aik Chong and Chair, Prof. Lin Shih Fu for making arrangement on the supervisor issue and supporting my endless candidature extensions and title change. Furthermore, meeting with Associate chair, Prof. Sam Zhang really helped me understand my problems.

I also would like to thank all the FYP, Msc., Ph.D., Eureka, polytechnic students and professors I had served or guided for the last 5 years to help me polish my technical, communication and organization skills. Furthermore, the foreign students who I helped prepare for their entry exam in Brighton School lightened up my life with the youth color of their countries.

The establishment of the mathematical model between 2003 and 2004 could not be possible without the help from Prof. Stephen Whitakers' serial papers on the subject and one personal email communication.

Finally, it is hard but my pleasure to be in NTU which grants me an invaluable opportunity to learn and grow.

Table of Content

List of Figures

Nomenclature

Abbreviation

AAS	Antibiotics-antimycotic solution
ASTM	American Society of Testing and Materials
BSA	Bovine serum albumin
DAB	3,3'-diaminobenzidine
DAPI	4',6-diamidino-2-phenylindole
DNA	Deoxyribonucleic acid
DNase	Deoxyribonuclease
DPBS	Dulbecco's phosphate buffered saline
EDTA	Ethylenediaminetetraacetic acid
HEPES	4-(2-hydroxyethyl)-1-piperazineethanesulfonic acid
HRP	Horseradish peroxidase
HK	Hexokinase
IgG	Immunoglobulin
IU	Incubation unit
NAD+	Nicotinamide adenine dinucleotide
NADH	Reduced form of NAD+
OCT	Optimal Cutting Temperature
PBS	Phosphate buffered saline
PESMCs	Porcine esophageal smooth muscle cells
SEM	Scanning electron microscopy
SEM	Standard error of mean
VAM	Volume averaging method
pO_2	Partial pressure of oxygen
pCO_2	Partial pressure of carbon dioxide
RWV	Rotating wall vessel
CFD	Computational Fluid Dynamics
DHT	Dehydrothermal method
DMEM	Dulbecco's Modified Eagle Medium
ECM	Extracellular matrix
PDMS	Polydimethylsiloxane
PGA	Polyglycolic acid
PLA	Polylactic acid
SIS	Small intestinal submucosa
UV	Ultraviolet
HARV	High aspect ratio vessel

STLV	Slow-turning lateral vessel
RCCS	Rotary cell culture system
HFB	Hydrofocusing bioreactor
GAG	Glycosaminoglycan
PHA	Polyhydeoxyalkanoate
L/G	Lactic-to-glucose ratio
ATP	Adenosine triphosphate
PFC	Perflurocarbon
MTS	3-(4,5-dimethylthiazol-2-yl)-5-(3-carboxymethoxyphenyl)-2-(4-sulfophenyl)-2H-tetrazolium, inner salt
UDF	User defined functions
REV	Representative elementary volume
H&E	Hematoxylin and eosin (stain)
wt	Weight
vol	Volume

Letters

A	Surface area of interface between 2 phases, m^2
A_w	Well area of a 24-well plate, m^2
$A_{\beta\sigma}$ (or $A_{\sigma\beta}$)	Surface area of $\beta\sigma$-interface or $\sigma\beta$-interface, m^2
$A_{\sigma\gamma}$ (or $A_{\gamma\sigma}$)	Surface area of $\beta\sigma$-interface or $\sigma\gamma$-interface, m^2
$A_{\beta\gamma}$ (or $A_{\gamma\beta}$)	Surface area of $\beta\sigma$-interface or $\beta\gamma$-interface, m^2
Ab	Absorbance measured by microplate reader, [-]
C_i	Concentration of species i, kg/m^3
$C_{i,\beta}$	Concentration of species i in medium phase, kg/m^3
$C_{i,\sigma}$	Concentration of species i in cell phase, kg/m^3
$C_{i,o}$	Inlet concentration of solute i, kg/m^3
C_o	Dissolved oxygen concentration at the bioreactor inlet or at time = 0, kg/m^3
C_0	Dissolved oxygen concentration at medium height δ shown in Fig 5.1, kg/m^3
$C_{O,\beta}$	Dissolved oxygen concentration in medium phase, kg/m^3
$C_{O,\sigma}$	Dissolved oxygen concentration in cell phase, kg/m^3
$\hat{C}_{i,\beta}$	Spatial deviation concentration of species i in medium phase defined in A.30, kg/m^3

$\hat{C}_{i,\sigma}$	Spatial deviation concentration of species i in cell phase defined in A.31, kg/m^3
$\hat{C}_{p,pc}$	Specific heat capacity of polycarbonate, J/K.kg
CL%	Crosslink index of scaffold based on Ninhydrin test defined in equation 5.1.1, %
$D_{i,\beta}$ or $\mathbf{D}_{i,\beta}$	Binary diffusivity (or its tensor) of solute i in water, m^2/s
$D_{i,\sigma}$ or $\mathbf{D}_{i,\sigma}$	Diffusivity (or its tensor) of species i in cell phase, m^2/s
$D_{eff,G}$	Effective diffusivity of glucose within the biofilm defined in equation 2.4.20, m^2/s
$D_{eff,i}$	Effective diffusivity of species i within the construct defined by equation 4.1.25, A37 and A.53, m^2/s
$D''_{eff,G}$	Effective diffusivity of glucose within the biofilm defined in equation 2.4.17
$D''_{eff,i}$	Effective diffusivity of solute i within the construct defined by equation A.36, m^2/s
$\mathcal{D}$	Dimensionless diffusivity of oxygen defined in equation 4.1.55, [-]
Da_1	Damökhler number for oxygen transport defined in equation 4.1.52 and 4.1.53, [-]
Da_2	Damökhler number for cell growth defined in equation 4.1.57 and 4.1.58, [-]
DD%	Degree of scaffold degradation defined in equation 5.1.2, %
$d_{\sigma\beta}$	Diameter from center to σβ-interface in 3-phase Chang's cell shown in Figure 4.1, m
E_o	Surface concentration of transported proteins of simple carrier model, kg/m^2
$\vec{f}$	Closure vector of medium phase in equation A.38
$G_{1,i}$	Parameter for species i defined in equation A.54a
$G_{2,i}$	Parameter for species i defined in equation A.54b
$G_{3,i}$	Parameter for species i defined in equation A.54c
$\vec{g}$	Closure vector of cell phase in equation A.39
H	Height of bulk medium in culture well or bioreactor, m
h	Thickness of scaffold or tissue construct, m
I	Unit tensor
K	Dimensionless permeability, [-]
$\mathbf{K}_\beta$	Permeability tensor defined in equation 4.1.22 and A.21, m^2
K_C	Contois constant, [-]
K'_C	Contois constant estimated in monolayer cell culture, kg/m cell
K''_C	Dimensionless Contois constant defined equation 4.1.59, [-]
K_I	Inhibitory constant, kg/m^3

K''_M	Dimensionless modified half saturation constant defined in equation 4.1.54, [-]
$K_{M,i}$	Half saturation constant of species i in Michaelis-Menton kinetics, kg/m^3
$K_{M,G}$	Half saturation constant of glucose in Michaelis-Menton kinetics, kg/m^3
$K''_{M,G}$	Modified half saturation constant of glucose in Michaelis-Menton kinetics defined in equation 2.4.19, kg/m^3
$K_{M,O}$	Half saturation constant of oxygen in Michaelis-Menton kinetics, kg/m^3
K_S	Half saturation constant in Monod Kinetics, kg/m^3
K_X	Constant in Logistic model, kg/m^3
$K_{eq,i}$	Equilibrium constant of species i between β- and σ- phase, [-]
k_m	Mass transfer coefficient, m/s
k_{pc}	Thermal conductivity of polycarbonate, W/K.m
L	Length of the bioreactor domain studied, m
L_E	Entrance length, m
l	Length of the scaffold or tissue construct, m
ℓ	Length of representative elementary volume or unit cell or length scale, m
ℓ_{bf}	Thickness of biofilm, m
ℓ_β	Length scale of medium or extracellular or void phase, m
ℓ_σ	Length scale of cell phase, m
ℓ_γ	Length scale of scaffold phase, m
m_c	mass of a single cell, kg
N_o	Initial cell-seeding density, number of cells/m^3 scaffold
N_σ	Cells per area, cells/m^2
$\vec{n}$	Unit normal vector of interface or boundary surface, [-]
$\vec{n}_{\omega\eta}(\text{or}-\vec{n}_{\eta\omega})$	Outward unit vector normal to ωη-interface, [-]
$\vec{n}_{\beta\sigma}(\text{or}-\vec{n}_{\sigma\beta})$	Outward unit vector normal to σβ-interface, [-]
$\vec{n}_{\sigma\gamma}(\text{or}-\vec{n}_{\sigma\gamma})$	Outward unit vector normal to σγ-interface, [-]
$\vec{n}_{\beta\gamma}(\text{or}-\vec{n}_{\gamma\beta})$	Outward unit vector normal to βγ-interface, [-]
P_σ	Concentration of metabolite product produced by cells, kg/m^3
p_β	Hydrostatic pressure of medium, Pa
$\bar{p}$	Scaled pressure, Pa
R	Radius of representative elementary volume (REV) or Chang's unit cell, m
R_i	Source or sink rate of species i, kg/m^3.s

R'_O	Oxygen consumption flux, $kg/m^2.s$
R_p	Radius of inlet port of bioreactor, m
R_σ	Growth rate or cell mass deposition rate, kg/m^3s
R'_σ	Cell growth flux, $cells/m^2.s$
Re	Reynolds number
r	Radial coordinate
r_G	Metabolic rate constant of glucose of first order kinetics, s^{-1}
r''_G	Modified metabolic rate constant of glucose of first order kinetics defined in equation 2.4.25 , s^{-1}
$r_{i,\sigma}$	Maximum consumption rate of species i by cell phase, kg/m^3s
$r_{\sigma\beta}$	Radius from center to $\sigma\beta$-interface in Chang's cell defined in equation A.54d, m
$r_{\sigma\gamma}$	Radius from center to $\sigma\gamma$-interface in Chang's cell, m
r_σ	Specific growth rate of cell phase (biomass), s^{-1}
$r''_{G,max}$	Modified maximum consumption rate of substrate A defined in equation 2.4.18, kg/m^3s
$r_{i,max}$	Maximum consumption or production rate of species i defined in equation 4.1.11, kg/m^3s
$r_{O,max}$	Maximum consumption rate of oxygen, kg/m^3s
$r_{G,max}$	Maximum consumption rate of glucose, kg/m^3s
$r_{\sigma,max}$	Maximum specific growth rate of cell phase, s^{-1}
Sc	Schmidt number defined in equation 4.1.46 and 4.1.47, [-]
T	Temperature, ^oC
T_{os}	Overshoot temperature, ^oC
t	Time, s
$\bar{t}$	Time scale, s
$\vec{u}$	Displacement vector of the interface, m/s
V	Volume of representative elementary volume (REV), m^3
V_β	Volume of medium phase in representative elementary volume (REV),m^3
V_γ	Volume of scaffold phase in representative elementary volume (REV), m^3
V_σ	Volume of cell phase in representative elementary volume (REV), m^3
$V'_{\sigma,max}$	Maximum allowable volume occupied by cells in monolayer culture, m^3
V_c	Cell volume, m^3/ 1 cell
$\vec{v}_\beta$	Medium velocity, m/s
v_{av}	Inlet average velocity, m/s

v_{max}	Maximum velocity, m/s
$\bar{v}$	Scaled velocity, m/s
W	Width of bioreactor, m
W(t)	Dry weight of scaffold after incubation in the culture medium for time t, mg
W_o	Dry weight of scaffold before incubation, mg
w	Width of the scaffold or tissue construct, m
X	Dimensionless oxygen concentration, [-]
x	x-coordinate
y	y-coordinate
z	z-coordinate

Greek letters

α	Dimensionless parameter defined in equation 2.4.28
α_{pc}	Thermal diffusivity of polycarbonate, m^2/s
δ	Boundary thickness in static culture well shown in Figure 5.1, m
ε_i	Volume fraction parameter of species i defined in equation 4.1.24
ε_j	Volume fraction of phase j defined in equation 4.1.18, m^3/m^3
ε_o	Initial porosity of scaffold, m^3/m^3
ε_β	Volume fraction of medium or extracellular or void phase, m^3/m^3
ε_γ	Volume fraction of the scaffold phase, m^3/m^3
ε_σ	Volume fraction of cell phase, m^3/m^3
ϕ	Dimensionless height ratio (=H/2h) defined in equation 4.1.64, [-]
Γ	Membrane resistance of simple carrier model, $kg.s/m^3$
γ	Dimensionless parameter defined in equation 2.4.22, [-]
Φ	Parameter defined in equation A.20, 1/m.s
κ	Dimensionless parameter defined in equation 2.4.21 and 2.4.27, [-]
κ_i	Dimensionless parameter of species i defined in equation A.46a, [-]
μ_β	Dynamic viscosity of medium, Pa.s
ν_β	Kinematic viscosity of medium, $kg/m.s^2$
ξ_i	Dimensionless parameter of species i defined in equation A.46b, [-]

Π_β	Dimensionless pressure defined in equation 4.1.45, [-]
ρ_{pc}	Density of polycarbonate, kg/m^3
ρ_σ	Cell mass concentration, kg/m^3
$<\rho_\sigma>^\sigma$	Density of a single cell, kg/m^3
Ψ_j	Physical quantity of phase j within REV
τ	Dimensionless time, [-]
$\widetilde{\chi}_{i,\sigma}$	$K_{eq,i}C_{i,\sigma}$ defined in equation A.44
$\vec{\varpi}_\beta$	Dimensionless medium velocity, [-]
ϖ_{max}	Dimesnionless maximum medium velocity, [-]
ψ	Dimesnionless y-coordinate

Symbols

Δ	Discrepancy between simulation and experimental results defined in equation 5.4.1

Subscripts

av	Average
C	Carbon dioxide
CL	Crosslinked
c	Single cell
eff	Effective (parameter)
exp	Experiment
G	Glucose
i	Index of species
j	Index of phase
L	Lactate
max	Maximum
n	normal direction to the specified plane
O	Oxygen
o	Inlet or initial
os	Overshoot
sim	Simulation
UNCL	Uncrosslinked
x	x-direction in Cartesian coordinate
y	y-direction in Cartesian coordinate

z	z-direction in Cartesian coordinate
β	Medium or extracellular or void phase
γ	Scaffold phase
η	Bulk medium region
σ	Cell phase
ω	Cell-seeded Scaffold or tissue-construct region
0	At level of z = 0

Operators

erf	Error function, defined as, $\mathrm{erf}(x) = \frac{2}{\sqrt{\pi}} \int_0^{x_1} e^{-x^2} dx$
$\nabla(..)$	Gradient operator
$\nabla\cdot(..)$	Divergence operator
∇^2 (or $\nabla\cdot\nabla(..)$)	Laplacian operator
$<..>$	Superficial volume-averaged quantity defined in equation 3.2.2 and A.1
$<..>^{\beta}$	Intrinsic β-phase volume-averaged quantity defined in equation 3.2.3 and A.2
$<..>^{\sigma}$	Intrinsic σ-phase volume-averaged quantity defined in equation 3.2.3 and A.2
$\{..\}$	Weighted equilibrium quantity defined in equation 3.4.17 and A.29
$MIN(x_1,x_2,\ldots,x_N)$	Minimum of a series of values $(x_1,x_2,\ldots,x_N)$

Chapter 1. Introduction

1.1 Background

Currently, organ transplantation is still one of the most important surgeries in medicine to replace malfunctioning and diseased organs. However, organs that are suitable for implantation are always far fewer than the demand [1, 2]. According to Organ Procurement and Transplantation Network (www.optn.org), in the United States alone, 101,593 patients as of April 14, 2009 are in the waiting list for organ transplantations whereas the number of donors was only 1,170 as of April 3, 2009. Apparently, the "supply and demand" is totally out of the balance. Furthermore, there are always concerns about transmitted diseases and immune response in autologous transplants [3, 4].

Artificial substitutes made of polymers, metals, ceramics and composites, on the other hand, have been employed as grafts for reconstruction [5] such as the metal alloys and polyethylene used in hip replacement [6]. Although the biocompatibility of these materials has been improving, most of them induce different degrees of foreign body reactions from the host tissue since they do not naturally exist in the human body [7]. Functionally, these materials cannot fully adapt to the changing demands of human activities, accommodate body growth (which is especially true for children) and cover the whole range of functions for replaced tissues. Wear or corrosion during the service time also limits the sustainability of this approach [6, 7]. The use of artificial materials is considered a solution for improving life quality or just prolonging life [8].

In the 21st century, the fast development of tissue engineering possibly offers a potential, complete and permanent solution to the problem of tissue loss and failure. It makes use of knowledge in engineering and life sciences to produce biological substitutes that can restore, maintain or improve tissue functions [1]. Efforts in this area can be dated back to the 1980s when artificial skin was used as skin replacement for burn injuries [9, 10]. At present, tissue engineering of bone [11, 12, 13], cartilage [14, 15, 16], bladder [17, 18], small-diameter blood vessels [19, 20, 21], cardiac muscle [22, 23, 24] and many other organs and tissues is being actively investigated.

Two main approaches are commonly used in tissue engineering in order to develop grafts or substitutes for implantation (or called tissue construct) [25]: (1) *In vitro* type involves association of cells isolated from healthy tissue into biomaterial, a so-called scaffold and culturing in bioreactor, a device to develop tissue construct under controlled environment (Figure 1.1). *In vivo* type involves producing tissue construct inside the human body by implanting cell-included or excluded scaffolds to the site where diseased tissue has been removed.

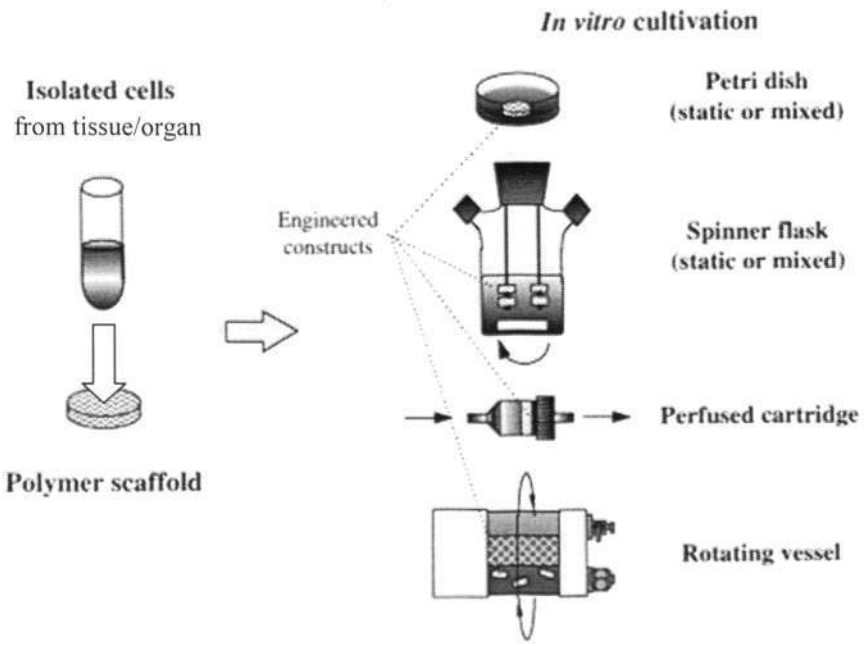

Figure 1.1: *In vitro* Tissue Engineering. Isolated cells are incorporated into polymer scaffold (seeding) and then cultured in bioreactors (in vitro culturing) [31]

Tissue regeneration *in vivo* mainly relies on the induction of natural healing from host tissue by scaffold, resulting in infiltration of cells and capillaries, remodeling, re-organization and concomitant scaffold degradation or resorption. The rate of scaffold degradation becomes critical to the final construct quality. If it is too fast, the construct collapses before complete regeneration due to rapid loss of mechanical strength; if it is too slow, the remaining scaffold material hinders complete regeneration [25]. Therefore, scaffold degradation in timely fashion is critical to the success of the implanted scaffold to progressively regain the functions of the organ or tissue. .

Tissue engineering via the *in vitro* approach, in this regard, provides a potential solution that a controlled microenvironment *in vitro* supplying with appropriate growth signals might probably guide tissue regeneration to completion. This has received increasing attention due to its scale-up potential that functional tissue

constructs can be produced in a well-designed bioreactor to meet the high demand in organ and tissue replacements [26, 27]. Cartilage, bone, small-diameter blood vessels, heart valves and cardiac muscles have been studied intensively in bioreactors. Good progress has been achieved but functional tissue constructs remain unavailable. For example, tissue-engineered cartilage harvested from bioreactors possessed native cartilage-like structures but the biochemical compositions and mechanical properties are still inferior [28]. Tissue-engineered blood vessels produced in pulsatile bioreactor had hierarchically layered structures with comparative collagen content and burst pressure, but the absence of elastin and a low density of smooth muscle cells are still the drawbacks of these constructs [21]. These results are probably due to the lack of understanding of growth signals and ineffective mass transfer. Hence, an optimized bioreactor environment is required to improve the construct quality.

It is recognized that a bioreactor should provide a physiological microenvironment making proliferation, differentiation and morphogenesis possible for cells *in vitro* to grow into tissue-like structure [29]. More specifically, a bioreactor must maintain pH and temperature at physiological level [26, 30], facilitate nutrients and oxygen supply and metabolite removal, or in the general term, mass transfer [26, 31] and deliver growth-mediating chemicals such as growth factors and vitamins [21, 32]. Furthermore, it has been shown in many studies that mechanical stimulations are playing an important role in cell proliferation and differentiation and enhancing the mechanical properties of tissue constructs [21, 33].

Mass transfer in tissues or organs is facilitated by an extensive network of capillaries. Since the technique of building such a network within the construct is still immature

[34], a bioreactor, which is efficient in mass transfer, will be of significant importance to provide continuous nourishment for the construct before implantation. Recognizing this point, the *in vitro* culture technique has evolved from Petri dishes to the more sophisticated systems such as mixed flasks, rotating wall vessels (RWV) and perfusion bioreactors, which incorporated medium flow or mixing (convection) to facilitate mass transfer in tissue constructs [22, 30, 35, 36, 37, 38]. However, most of these bioreactors still cannot effectively eliminate mass transfer resistance within the construct leading to the limitation of construct size [31, 39], necrotic core [31, 40] and uneven cell distribution [36, 38]

There are more than a hundred or a thousand of chemical species (e.g. carbohydrates, growth factors, hormones, salts, amino acids) involved in cell growth and tissue development, it is considered that mass transfer of oxygen (or oxygen transport) is critical to construct development *in vitro* due its low solubility in culture medium. There has been increasing evidence showing the effect of oxygen on the outcome of tissue constructs. Furthermore, cell growth, viability and energetics are all known to be affected under a deprived oxygen environment (hypoxia). It would be logical and important to focus on the oxygen transport in such a complex system. Experimental studies of oxygen measurement in the culture system have been carried out to correlate with the quality of the tissue construct such as cellularity (how many populated cells are in the construct?), extracellular matrix (ECM) molecules secreted by cells (that are specific to target tissue) and biomechanical properties. Earlier studies were focused on the dissolved oxygen in the medium measured by a blood gas analyzer, which is sometimes difficult to be used to interpret the construct outcome since the internal

oxygenation could be totally different and more related to the construct quality. More recent studies focused on the internal oxygenation by the measuring oxygen profile within the tissue construct which correlated well with the spatial distribution of cells and ECM molecules [41]. However, the current methods mostly used oxygen microsensors to profile construct outside the actual culture conditions which could lead to incorrect interpretation.

Mathematical modeling would be useful to study the effect of mass transfer of oxygen on the development of tissue constructs. Earlier studies using a mass transfer model to investigate the limitation of substrate diffusion to cartilage growth *in vitro* showed that there is a strong link between tissue development and mass transfer [42, 43]. However, most of the current studies focused on mass transfer either internally [42, 43, 44, 45, 46, 47, 48, 49] or externally [50, 51] and only a few recent attempts tackled the interaction of mass transfer between the bulk medium and tissue construct (coupled effect) [52, 53, 54], which is believed to be more significant for a dynamic bioreactor with medium flow (convective effect) around the construct. Furthermore, the tissue construct was treated as a single continuum without considering the multiphase and porous nature of the construct. In most of these studies, this simplification in the model might lead to an inaccurate account of internal mass transfer. Taken together, there is a need to understand the effect of hydrodynamics on mass transfer in a bioreactor through a more rigorous approach.

To address the aforementioned issues, it would be important to investigate the implications of the trio: hydrodynamics, oxygen transport and tissue regeneration and identify the operation conditions for the bioreactors that can improve oxygenation for

optimal tissue development. It was believed that the mass transfer in a growing tissue construct (internal) is influenced by the hydrodynamic conditions of bulk fluid medium (external) and that the coupling effects between tissue construct and bulk fluid medium cannot be ignored. It was also believed that enhancement in oxygen transport through controlled uniform hydrodynamic conditions can improve the construct quality, such as cell distribution.

In this study, a numerical approach has been adopted to study mass transfer and cell mass deposition under different bioreactor configurations and hydrodynamic conditions. To take into account the coupling effect in mass transfer, the model domain included both a tissue construct phase and an external medium phase to provide a better understanding of their interactions. Furthermore, more rigorous formulations of the governing equations compared to past model studies have been adopted with the application of the Volume Averaging Method (VAM) to give a more rigorous account of mass transfer in this coupled system. It is expected that this model would be useful to study the hydrodynamic effects on mass transfer and tissue development in a bioreactor system involving different tissue construct geometries, bioreactor configurations and hydrodynamic conditions.

Furthermore, it is important to conduct experiments to validate the mathematical model. A bioreactor system (including incubation unit, bioreactor and oxygen microsensor system) was designed and fabricated in order to facilitate the culture tissue construct and in-situ oxygen profiling outside a conventional incubator. To produce the scaffold for cell seeding in bioreactor culture experiments, a new method using gas foaming was used to create a porous gelatin scaffold. In human physiology,

smooth muscle is considered one of the important muscle types which controls contraction and relaxation of various internal organs such as blood vessels and gastrointestinal tracts. Reconstruction of such organs requires smooth muscle cells as cell source to rebuild the muscle layer. In this study, porcine esophageal smooth muscle cells isolated from porcine esophagus were chosen as a model cell type and seeded into the scaffold. With the current experimental set-up, smooth muscle constructs were cultured under uniform laminar flow and in-situ oxygen profiling with minimal interferences on the culture conditions might result in more realistic spatial oxygen data in the growing tissue constructs compared to that required conducting measurements outside the culture environment in the previous study [45]. Attempt was made to correlate the measured oxygen data with the cell distribution such that the effect of oxygen transport in the bioreactor on the cell distribution can be further analyzed and elucidated.

1.2 Objective

The main objective of this project is to investigate oxygen transport and cell distribution of smooth muscle construct cultured in tissue engineering bioreactor with medium flow registered across the surface(s) of the tissue construct.

The specific goals in this project are:

1. To develop a method to create tissue engineering scaffold with relatively uniform porous properties for cell seeding purpose
2. To develop a method to isolate porcine esophageal smooth muscle cells (PESMCs) as cell source and to adapt the cells under normal air environment.
3. To design and validate a bioreactor system to carry out tissue culture under normal air environment to facilitate in situ oxygen profiling of the tissue construct cultured in the flow bioreactor outside conventional incubator;
4. To establish a mathematical model to study and analyze oxygen transport and cell growth in a PESMCs-seeded tissue construct cultured in the designed flow bioreactor.

1.3 Scope

The flowchart in Figure 1.2 illustrated the main research activities conducted for each stage of research in order to achieve the goals abovementioned.

The first stage involved establishment of mathematical model to study the mass transfer of a bioreactor with bulk medium and tissue construct coupled up as the model

domain. Transport equations (continuity equations, momentum balances and species mass balances) were written for bulk medium and tissue construct. An empirical oxygen-limiting cell mass deposition model (Contois kinetics) was used to describe dependency of oxygen tension on cell mass deposition. The Volume Averaging Method (VAM) was applied in the formulations of these governing equations. Spatial and temporal distributions of oxygen tension and cell-phase volume fraction (implying local cell density) were the main parameters investigated under different bioreactor flow conditions. Commercial Computational Fluid Dynamics (CFD) software, FLUENT® was used solve for the numerical solutions.

Stage 2 involved a detailed design of the bioreactor system. The system involves three important components: (1) an incubation unit, (2) a bioreactor for construct cultivation and (3) an oxygen profiling system. The whole system design involved in situ oxygen profiling within the bioreactor (closed system) with minimal interferences on the culture environment. The bioreactor was designed to deliver a uniform laminar flow field across the construct surface. The geometry and the dimension of the flow chamber were determined by CFD modeling. To facilitate oxygen measurement in the bioreactor, holes were drilled in the top of the bioreactor where the oxygen microelectrode (tip size of 50μm) could be introduced and profiling was enabled by moving the electrode slowly through the system. To ensure a closed system, all access holes for oxygen measurements were first sealed with polydimethylsiloxane (PDMS) which is nontoxic, penetrable and self-sealing. Since the precise movement of the microelectrode requires the control of motorized manipulator which cannot be installed in the conventional incubator, an incubation unit incorporated with a heating

module was designed to carry out the bioreactor experiments independent of the incubator. All the components were purchased and fabricated.

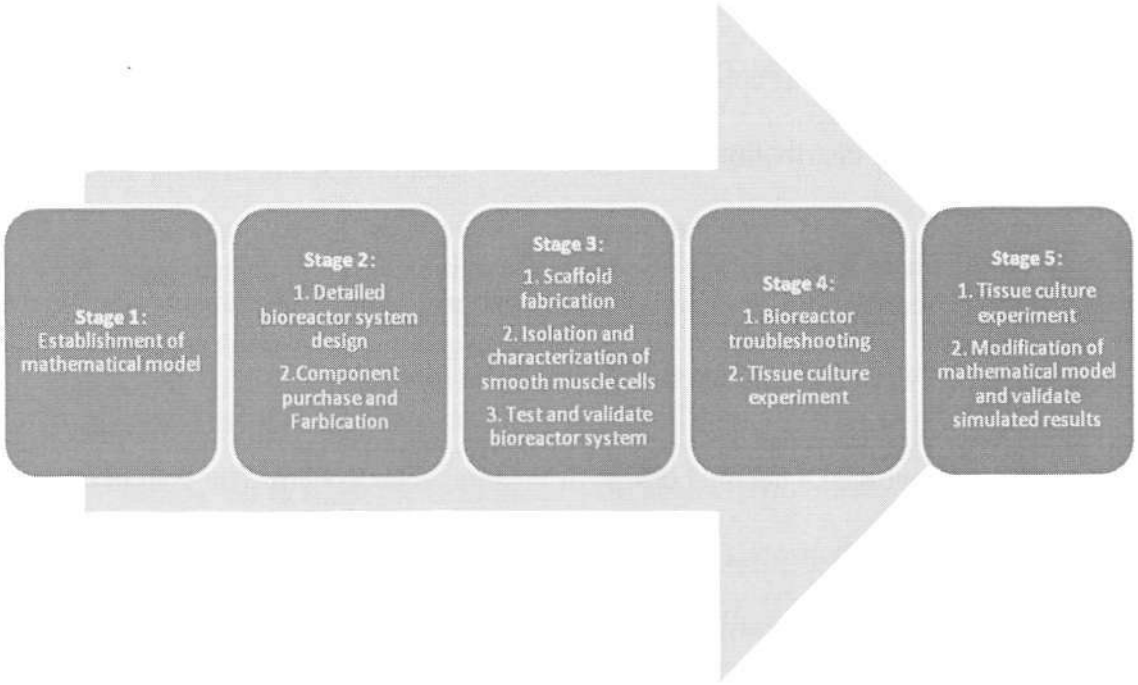

Figure 1.2: Research flowchart

Stage 3 focused on the preparation and characterization of the scaffold and the cell source together with testing the bioreactor system. Gelatin was chosen as scaffold material due to its excellent biocompatibility and it was fabricated into a porous scaffold using a new simple foaming method accompanied by ethanol aggregation to create an interconnected porous structure. The gelatin scaffold was crosslinked by a dehydrothermal (DHT) method to control its degradation rate in an aqueous environment. The scaffold properties were analyzed by scanning electron microscopy (SEM) for pore morphology and pore size, degradation rate and crosslink index, and by a tensile test for mechanical properties.

The cell source was esophageal smooth muscle cells from the pig. Smooth muscle cells were isolated from porcine esophagus using both enzymatic and explant methods and a strict sterile technique was employed in all culture activities due to the susceptibility of mammalian cells to contaminants such as bacteria, mycoplasma, yeast and virus [55]. The cells were then cultured and expanded *in vitro* in a tissue culture dish inside a 5 % CO_2 incubator at 37 ^{o}C. Dulbecco modified eagle's medium (DMEM) supplemented with serum and antibiotics was used as the culture medium to provide a nutrient source and growth promoting factors. Once cells were grown to confluency (cells filling all space of the dish), the cells were split and cultured in new culture dishes (passaged or subcultured). Cell morphology, phenotype and growth kinetics were studied using inverted light microscopy, immunostaining and a commercial cell proliferation assay kit, respectively. Cell-scaffold interaction was also carried out by seeding smooth muscle cells into the scaffold and histology was used to visualize and evaluate cell growth in the scaffold. On the other hand, since in situ oxygen profiling using microsensor cannot be carried out in the conventional 5 % CO_2 incubator due to space limitation and potential equipment breakdown under humid environment, the bioreactor experiment was carried out outside the incubator and an incubation unit (IU) with temperature control was fabricated to facilitate tissue culture and oxygen profiling. Under the normal ambient air condition (consisting of CO_2 as low as 0.03 %) without CO_2 supplementation, the buffer system used in the conventional culture formula (CO_2/bicarbonate) was substituted by 4-(2-hydroxyethyl)-1-piperazineethanesulfonic acid (HEPES) and the osmolality was also adjusted accordingly. Smooth muscle cells were adapted from normal medium (for 5 % CO_2) to modified medium (for air) and cultured in the IU before the bioreactor

experiment. Furthermore, the cellular requirement of oxygen (using oxygen microelectrode) and glucose (using Hexokinase glucose assay kit) and growth rate (DNA quantification) were measured. These data were used as metabolic and growth parameters required in the mathematical model.

From stage 4 to the final stage, smooth muscle cells were seeded into 2-mm thick scaffolds and cultured in the bioreactors registered at different flowrates. Furthermore, two bioreactor flow configurations were used in the culture experiments: (1) Single flow: only the top surface was exposed to medium flow and (2) double flow: both the top and bottom surfaces were exposed to flow. Static culture of the construct was carried out to serve as control. At each harvest time, oxygen profiling was carried out at the end of the experiment and the construct sample was then analyzed. Histology was carried out to qualitatively examine the cell distribution. Cell distribution was also measured quantitatively: A thin section (5 μm thick in cross section) of the construct was made and stained with fluorescence dye to visualize cell nuclei. Microscopic pictures were taken at 5 locations (in accordance with the locations at which oxygen measurements were carried out) under the fluorescence microscope. By running a user-defined macro in the image processing software, Image J, the microscopic image was sliced into regular intervals across the full depth and the cell number was counted in each depth range to create the cell distribution. Both oxygen and cell distribution data were compared with the simulation results to validate the mathematical model.

Chapter 2. Literature Review

2.1 Enabling Technology in Tissue Engineering

Engineered tissue constructs contain two basic elements: Scaffold and cells. The scaffold acts as a template and support cell growth while the cells act like "workers" to build new tissue. Most of the tissues in the human body, except a few such as cartilage, consist of more than one cell types. To produce a specific type of tissue or organ, specific cell types must be recruited. Cells required for a particular tissue type can be expanded *in vitro* and then inoculated ("seeded") into the scaffold. Cell-scaffold construct is either transferred into the body (*in vivo*) or into the bioreactor for further culturing or conditioning (*in vitro*). Either approach requires an appropriate supply of growth signals and facilitation of mass transfer. In this section, some enabling technologies essential to tissue engineering regarding scaffold, cell sources, mass transfer and bioreactors are discussed.

2.1.1 Scaffolds

Success of tissue engineering scaffolds depends on (i) material selection which associates with inherent properties of materials (e.g. molecular composition, thermal and mechanical properties) and (ii) fabrication into structure with suitable physical properties (e.g. designated porous architecture) for tissue regeneration [10, 56, 57]

I. Biomaterial Selection

Both synthetic and natural materials are being developed into scaffolds for tissue engineering.

Synthetic polymers, for example, polyglycolic acid (PGA) and polylactic acid (PLA) are biocompatible and biodegradable. The control of various inherent properties such as mechanical strength, hydrophobicity, and degradation rate are important and these are important areas of current research [58, 59, 60, 61]. Since these synthetic polymers are not naturally occurring materials in the human body, they offer a little or no biological activity for cells to initiate guided tissue regeneration. In this regard, association with growth factors (chemicals that induce cell growth) [25, 32, 62], promotion of vascularization [4, 39, 59, 63, 64] and incorporation of extracellular matrix (ECM) molecules [62, 65] are important aspects of tissue engineering to improve the bioactivity.

Natural materials derived from plants, animals or humans such as collagen, hydroxypatite, chitosan and matrigel have the merit of eliciting specific biologic activity and of being biocompatible. Recently, natural scaffolds have been derived from decellularized tissues (a method to produce matrix after removing cells from the native tissue), such as porcine small intestinal submucosa (SIS) [66, 67], heart valves [68, 69] and blood vessels [70], but concerns over the virus transmission and immune response remain unresolved [71]. A limited range of physical properties, difficulties in isolation and process, expensive production, and large batch-to-batch variations are also drawbacks of using natural scaffolds [61]

II. Scaffold Fabrication

Scaffolds should be porous to facilitate cell delivery and/or induce the ingrowth of desired cell types [61, 63]. They should also be able to regulate proliferation,

differentiation and morphogenesis [25, 31, 62, 63]. Many methods have been developed to fabricate tissue engineering scaffolds including phase separation, particulate leaching, electrospinning [60] and rapid prototyping [72].

By choosing the appropriate polymer/solvent system, solid-solid or liquid-liquid phase separation occurs at reduced temperature resulting in the formation of fibrous structure with fibres in the nanoscale [73]. Nanofibers can also be produced by electrospinning. However, the pore size or fibre-to-fibre distance produced by these two methods are too small for efficient cell delivery. On the other hand, electrospinning, which creates fibres under electric field contours, requires more complicated equipment set-up and the thickness is limited [72] due to the increased electric resistance across the depositing fibre layers.

Although rapid prototyping can produce scaffolds of different physical shapes, most of the current techniques produce only a simple porous structure and they require a complicated set-up. Particulate leaching is a rather simple method that can produce a scaffold with porosity of more than 90 %. Furthermore, pore size is controlled by the particulate size used. Particulates such as salt, sugar and wax microspheres sieved in the desirable size range are mixed with a polymer solution which is then dried and soaked in water or solvent to leach out the porogens (particulates to make pores) leaving a porous structure with uniform pore size. However, this method is mostly limited to synthetic polymers that are associated with solvents [72]. Solvent residue may induce cytotoxicity [74]. Thickness is also limited since porogens in the deep layers of structure might not be able to leach efficiently [74, 75].

III. Gelatin as a Potential Biomaterial for Tissue Engineering

Although there are batch-to-batch variations in naturally derived biomaterials, their bioactivity appears to be attractive to facilitate cell adhesion and guided tissue maturation [56, 76]. One of the potential candidates is gelatin. Gelatin is a natural polymer derived from denaturation and degradation of collagen from a source such as the skin of animals. It has been widely used in the food industry [77, 78, 79] and for medical purposes [80, 81, 82, 83, 84] . Unlike native collagen, gelatin shares a lot of common aspects with rigid-chain synthetic polymers; however, the presence of both acidic and basic function groups, the capability to form a triple-stranded helix and a specific interaction with water make gelatin unique apart from synthetic polymers [85]. For having excellent biocompatibility and no or reduced antigenicity, gelatin has been developed into haemostatic agents in surgery [81], wound dressing [80, 84] and bioadhesive [83, 86].

Although gelatin is a degraded product of collagen, most of the amino acid sequence is retained, which may be important in tissue regeneration *in vivo* or *in vitro* and is advantageous over synthetic polymers that lack biological signals. Studies have shown that gelatin can be used as growth substrates to support growth of a number of cell types *in vitro* [87, 88]. Furthermore, raw gelatin is relatively economical and stable at room temperature compared to collagen. Therefore, gelatin could be a good material choice for tissue engineering scaffolds and that is why it has attracted increasing attention recently [89, 90, 91, 92, 93, 94, 95, 96, 97]. However, its potential to produce tissue engineering scaffolds has not yet been fully developed in contrast of other biopolymers such as collagen and chitosan, mainly due to high solubility in an

aqueous environment, causing rapid degradation by enzyme degradation *in vivo* or by hydrolysis *in vitro*. Therefore, crosslinking has been introduced to improve resistance to degradation.

Current crosslinking methods are categorized into physical and chemical methods. The physical crosslinking is by means of a dehydrothermal (DHT) process involving heating under vacuum condition, Ultraviolet (UV) and electron beam irradiation without introduction of any chemical agent. The chemical crosslinking involves the introduction of chemical agents such as formaldehyde, glutaraldehyde, epoxy compounds, carboiimide, reducing sugar and genipin. Both methods aim to initiate formation of inter- and intra-molecular bonding. Although it has been reported that the chemical crosslinking achieved higher and more stable crosslinking than physical method in collagen [98], it was also claimed that gelatin treated at 140 ^{o}C under a vacuum of 10^{-3} mmHg for 4 days is insoluble in hot water [99]. Furthermore, the toxicity that is introduced by chemical crosslinking has been of concerns when using chemically crosslinked gelatin as biomaterial in medical applications [80, 83, 86, 100] although genipin have been found to be relatively less toxic [80, 86]. Therefore, physical crosslinking is still attractive since no chemical agents are used. Ozeki and Tabata [101] showed that the DHT method resulted in higher a degree of crosslinking in gelatin hydrogel when compared with UV and electron beam irradiation.

2.1.2 Cell source

I. Cell Sourcing Technologies

Cell sources are considered one of the most important "raw" materials in tissue engineering. Cells commonly used in tissue-engineered constructs are mostly allogeneic, xenogeneic or autologous. Ideal cell sources should be non-immunogenic, highly proliferative, easy to harvest and able to differentiate into a variety of cell types with specialized function [2]. However, some cell types such as cardiomyocytes, hepatocytes and pancreatic islet cells [102] are fully differentiated and difficult to proliferate *in vitro*.

Researchers have been turning their attention to fetal, neonatal, genetically manipulated or stem cells [2, 4, 40, 103]. Among them, stem cells, for example, those found in bone marrow and embryo, have the ability to differentiate into lineages of cells under controlled microenvironment with specific cytokines, growth factors, amino acids and spatial cues [104, 105]. In 2001, stem cells were found to be present in every adult tissues [106]. Although adult stem cells are more restrictive in terms of differentiation, these cells harbor a longer growth span and greater regenerative capacity compared with their differentiated counterparts [107, 108]. However, stem cell technology is still immature in practical applications since the differentiation pathway for stem cells are still not well-understood and the use of embryonic stem cells still holds ethical issues [104].

II. Esophageal smooth muscle cells

Smooth muscle is present in various internal hollow organs including blood vessels and gastrointestinal (or digestive) tracts including intestine, stomach and esophagus [109]. Esophagus is a layered muscular canal that consists of smooth muscle which controls the rhythmic peristaltic motion to facilitate food transit from the mouth to stomach. Currently, esophageal cancer is one of the deadliest cancers due to its difficulty of prognosis in the early stage and surgery is one of the treatment options [110]. Reconstruction requires suitable grafts and tissue engineering may provide a potential solution as a tissue substitute. Tissue engineering of esophagus *in vitro* involves seeding of esophageal cells into a scaffold to initiate the process of tissue regeneration. Therefore, in order to rebuild the muscular portion of the esophagus, smooth muscle cells isolated from esophagus are needed to provide cell source for the scaffold seeding and the subsequent *in vitro* cultivation.

Muscular structure in the esophagus is somewhat different from that in blood vessels and other gastrointestinal tracts in that a various proportion of skeletal and smooth muscle is observed along the esophagus and the distribution is different among animal species [111]. Human esophagus is dominated by skeletal muscle in the upper third and smooth muscle in the lower third while a transition of both muscle types is observed in the middle third [111]. The lower third segment near stomach is required to isolate pure esophageal smooth muscle cells.

Isolation of smooth muscle cells from smooth muscle can be achieved by (i) enzymatic and (ii) explant methods [55]. The enzymatic method involves use of enzymes such as

collagenase, elastase or papain to digest the extracellular matrix (ECM) around the cells in order to free the cells. Since the majority of the mammalian cells, including smooth muscle cells, are anchorage-dependent, they require a surface with suitable hydrophilic properties in order to attach (or "anchor") to and then grow in number (proliferate). The smooth muscle cells released from their surrounding ECM can then be cultured on tissue culture wares with a specially treated surface and expanded in culture medium (e.g. Dulbecco's Modified Eagle medium) supplemented with serum (e.g. fetal bovine serum) and antibiotics (e.g. penicillin and streptomycin). The explant method is relatively simple but rather lengthy. The smooth muscle is diced into small pieces (about a few millimeters). The tissue debris is then evenly distributed on the surface of tissue culture wares. Live tissue debris attach on the surface and cells inside start migrating out of the debris (explant) after a period of time. The time required for cell migration depends on the cell type.

Among smooth muscle cells of different origins, vascular smooth muscle cells have been well-studied and characterized [112] due to their importance in vascular physiology and pathology. Both type of smooth muscle cells share a lot of similar features with their counterparts in the gastrointestinal tracts such as antigens (containing smooth muscle actin, desmin and vimentin), functions (contractibility) and morphology (spindle shape) [112]. However, less attention has been placed on esophageal smooth muscle cells so their growth kinetics *in vitro* is not well-known. In order to employ esophageal smooth muscle cells in esophageal grafts, they study their growth kinetics, phenotype and nutrient demands *in vitro* need to be better understand before we can draw useful information for regeneration of esophageal smooth muscle.

2.1.3 Mass Transfer and Vascularization

Mass transfer is another important issue in tissue engineering. Except for cartilage, most human tissues and organs are embedded with a capillary network (or vascularized), so that the transport of nutrients, gases and metabolic wastes are facilitated to meet their metabolic needs [34, 39, 113]. However, most of the current tissue constructs are avascular (i.e., contain no blood vessels). Upon implantation, vascularization of avascular constructs depends entirely on the invagination into the blood vessels of surrounding tissues, which is a slow process and might not match the mass transfer demands [63]. This drawback limits the reconstruction of more complicated and larger organs such as liver, kidney and heart [2, 25, 114]. In these cases, the cell mass in the center dies due to the lack of nourishment.

Techniques such as modification of the scaffold porous structure [61], pre-vascularization [114] and fabrication of vessel network [4, 115] are being explored in order to improve mass transfer in tissue constructs. Although microcirculation of tissue constructs is possible when using *in vivo* or *in vitro* techniques, problems such as regression of capillaries and host-construct vessel integration upon transplantation are still unsolved [34, 116]. On the other hand, the use of the bioreactor has been demonstrated to improve mass transfer, which in turn results in improved qualities of tissue constructs [22, 26, 35, 36, 37].

2.1.4 Tissue Engineering Bioreactors

Bioreactors, which have long been used in biotechnology for biochemical reactions produce desired bioproducts (e.g., antibiotics, insulin and fertilizer). In tissue

engineering, there has been increasing research in bioreactors for the last decade since bioreactors have the scale-up potential as the bioreactor technology becomes mature and economically viable [26, 27]. Bioreactors have been intensively studied in cartilage and cardiovascular tissue engineering and have shown some promising results [11, 21, 28, 117, 118]. However, issues such as mass transfer and signal delivery (both biochemical and biomechanical signals) are to be addressed in the bioreactor design.

2.2 Tissue Engineering Bioreactor

According to the review by Bilodeau and Mantovani [119], bioreactor is defined as "any apparatus that attempts to mimic and reproduce physiological conditions in order to maintain and encourage cell culture for tissue regeneration". Culturing cells in a bioreactor is one of the most critical steps in the *in vitro* approach of tissue engineering. A bioreactor should provide an optimized and well-defined microenvironment for the development of cell-seeded scaffolds into functional tissue substitutes. Specific growth-related factors, such as biochemical stimuli (e.g., cytokines, growth factors and vitamins) and mechanical stimuli (e.g., shear stress, stretch and distension) that are specific to a particular tissue development *in vitro* must be provided. On the other hand, a continuous supply of fresh medium to provide effective mass transfer for transport of chemical species (e.g., nutrients, oxygen and growth factors) and removal of the metabolic waste products generated by cells (e.g., lactate, ammonium and carbon dioxide) are essential in a tissue-engineered bioreactor to maintain the growing environment at the normal physiological level.

Currently, tissue engineering bioreactors have been developed to produce functional tissue constructs as human spare parts *in vitro* for future replacement of diseased or lost parts. Researchers attempt to devise an optimal microenvironment, which provides appropriate chemico-mechanical factors by giving effective mass transfer and specific mechanical stimulations to promote tissue regeneration. There follows a review of the recent *in vitro* culture research.

2.2.1 Static Flask/ Petri Dish

Traditional static tissue culture in a Petri dish is only capable of maintaining a monolayer of cells by diffusion. Aeration of the culture is merely through the dissolution of oxygen at the air-culture medium interface. Nutrients in the medium are progressively depleted and exchange of medium is required every 2 to 3 days. Diffusion is the only way for mass transfer within the system. If a 3D tissue construct is to be built *in vitro* by this technique, some shortcomings would be encountered: (1) lack of any specific tissue regenerative signals [21, 117, 120, 121]; (2) mostly batch operation [23, 35, 117]; and (3) poor mass transfer for 3D tissue culture resulting in a necrotic core [23, 35, 117]. This method in tissue engineering is only considered for expansion of a target cell source [29].

2.2.2 Mixed Flask

Fluid mixing promotes mass transfer in the mixed flask (Figure 2.1b) through convection by continuously mechanical swirling and stirring of the culture medium. Batch operation is normally adopted so that regular medium change is carried out to replenish the culture. Although external mass transfer is improved, diffusion is still the

major mode of mass transfer within the tissue construct. Although the mixed flask, produces better tissue constructs than the static culture [37], still exhibits poor internal mass transfer and high shear stress with the result that a thick cell capsule is grown in the periphery of the construct with comparatively acellular core [22, 37, 38]. Without a well-designed growth environment, it appears that the mixed flask is not an optimal option for culturing of functional tissue constructs.

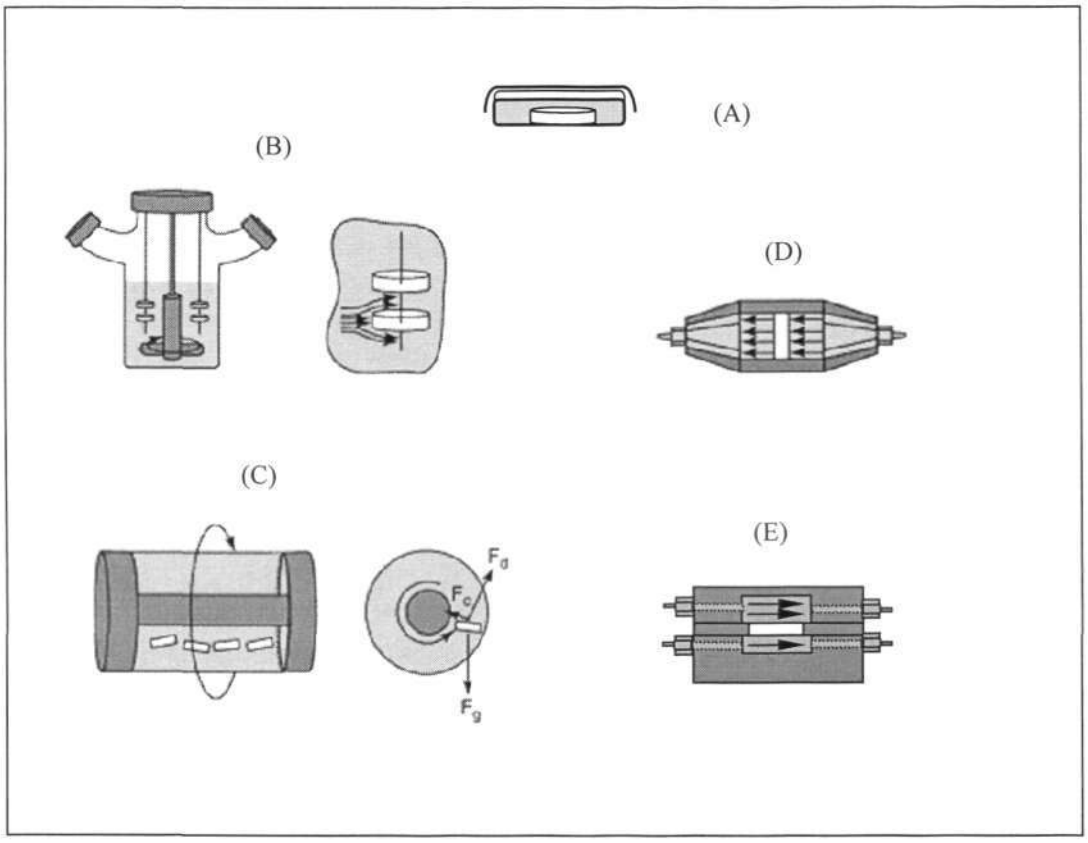

Figure 2.1 Existing Tissue Engineering Bioreactors: (A) Petri dish; (B) Mixed flask; (C) Rotating wall vessel (RWV); (D) Direct perfusion bioreactor; (E) Perfusion bioreactor (Gradient type) (Adapted from [26]).

2.2.3 Rotating Wall Vessel (RWV)

Basically, the rotating wall vessels (RWV), shown in Figure 2.1C, attempts to simulate microgravity so that a three-dimensional (3D) structure can be assembled in a dynamically static environment. It normally consists of two concentric cylindrical vessels with the constructs cultured in the space between the vessels. Wall rotation in a horizontal plane at a rate ranged from 15-40 rpm induces momentum transport in the radial direction, producing a laminar radial flow field [37]. The rotation speed is adjusted for maintaining constructs in suspension by which dynamic equilibrium can be established between three forces: gravitational (F_g), centrifugal (F_c) and drag forces (F_d) [37]. A laminar environment is established to minimize cell damage. Mass transfer in this type of bioreactor depends on the terminal velocity of the suspended construct and the diffusion within the construct [122].

Two geometries can be found in RWVs in earlier times: (1) slow-turning lateral vessel (STLV) [123] and (2) high-aspect-ratio vessel (HARV) [124]. Both require medium exchange, but continuous gas exchange is devised into the design. In STLV, gas exchange takes place at the permeable inner vessel made of silicone whereas gas exchange for HARV is devised at its vessel base.

Most of the recent designs are equipped with continuous medium supply (perfusion system). The Rotary Cell Culture System (RCCS) developed by Synthecon (www.synthecon.com) has a slightly different configuration from STLV and HARV in that fresh or re-circulated medium is continuously delivered through the inner vessel. Another recent design by Johnson Space Center (www.nasatech.com), the

hydrofocusing bioreactor (HFB), adopts rotation and viscosity to induce low-shear environment with controlled bubble formation and construct location in suspension.

RWVs have been used to culture cartilage and cardiac constructs in many studies [35, 37, 125]. Although adequate tissue constructs suitable for further clinical tests have not been produced by RWVs due to inferior biochemical composition, it has shown the capability of improving external mass transfer, ECM synthesis and inducing phenotype development of tissue such as higher glycosaminglycan (GAG) and collagen synthesis in cartilage constructs [37, 41, 125] and the contractility of cardiac constructs [35].

It is noted that this type of bioreactor might be more suitable to tissue "blocks" such as cartilage, bone and cardiac constructs [35, 37, 126]. However, for other tissue or organ types of specific geometries and consisting of different cell types in hierarchical order, such as blood vessels and esophagus in multi-layered, tubular structures or stomach in multi-layered, sac structure, regeneration of these tissue types in the RWV appears to be impossible. On the other hand, collisions between constructs and wall result in cell damage [127]. Furthermore, although increased ECM deposition is found in cartilage constructs, the biochemical composition was still inferior to native constructs. This perhaps is due to the lack of specific growth signals provided by RWV. This will be discussed further in the later sections.

Another rotating type bioreactor is the concentric cylinder bioreactor, which is based on concentric cylinder viscometer [128]. This type of bioreactor also produced encouraging results in culturing cartilage constructs. The objective of this bioreactor is

to produce low shear stress, facilitate seeding and exploit its scale-up potential. In contrast to the RWVs mentioned above, the concentric cylinder bioreactor consists of a fixed, non-permeable inner vessel on which the constructs are attached. The inner-to-outer radius ratio of this bioreactor is 0.941, which is set near unity to ensure stable flow and constant shear stress across the gap.

It has been claimed that cartilage constructs produced by the concentric cylinder bioreactor shows a cell-filled structure with no necrotic core and morphology similar to native cartilage. The analysis of construct composition shows high cell number, GAG and collagen. However, proteoglycan synthesis is still not satisfied and the absence of dynamic compression was suggested as the probable reason [128]. Dynamic compression (found *in vivo*) that is absent in this type of bioreactor and in RWVs previously mentioned could be one of the important factors in producing functional cartilage construct. More broadly, this conclusion implies that a better construct requires the appropriate use of mechanical modules during culture.

2.2.4 Perfusion Bioreactor

Continuous fresh medium flow facilitates mass transfer in the medium, ensuring optimal nutrient supply and removal of metabolites. Perfusion bioreactors of this type apply a continuous flow of medium across the surface of the tissue construct in order to optimize its biochemical environment. This approach eliminates the complications induced by medium exchange and is suitable for long-term culturing [30]. There have been many promising results produced using perfusion bioreactors developed by Minuth and coworkers (www.minucells.de). For example, the gradient-type perfusion

bioreactor, shown in Figure 2.2E, can be used to culture tissue constructs, which require luminal-basal medium gradients such as collecting duct epithelia [129]. The microenvironment that is intended to mimic *in vivo* conditions of collecting duct epithelia has been proven to maintain the differentiated state of the native tissue. Recent studies employing a perfusion bioreactor to develop tissue constructs included bone [11] and cartilage [15].

A monolayer of cells, as the collecting duct epithelia just mentioned, the thickness of which is on the order of 10 μm, can be maintained in a perfusion bioreactor [129]. It is believed that culturing of three-dimensional tissue constructs with thickness on the order of 1000 μm under perfusion should provide better mass transfer than static culture, but there is still a limitation in terms of the highest allowable thickness that can be produced from this system. This is so because as cell mass gradually deposits in the scaffold due to growth and ECM synthesis, internal mass transfer resistance increases while permeation of medium into tissue construct reduces, resulting in poor nourishment in the interior [31]. For thicker tissue constructs, the interior cells might suffer from nutrient and oxygen shortage and metabolite poisoning due to mass transfer limitations.

On the other hand, in addition to shear stress at the construct surface, other specific mechanical stimulations tailored for particular tissues or organs obviously are absent. Nevertheless, the use of a perfusion system to maintain the culture environment at a near physiological state is still attractive and it appears to be more possible in perfusion bioreactor than in other bioreactors mentioned previously to accommodate specific mechanical stimulations for particular tissue types.

2.2.5 Tissue-specific Bioreactors

Some recent designs of tissue engineering bioreactors tend to be more function-oriented to mimic the *in vivo* environment specific to the development of a desired tissue/organ type. It is noted that the conventional bioreactors mentioned so far are unable to create such an environment. It might be also impractical to design a single bioreactor to fit the needs for all tissue types in our body since tissues at different anatomical locations experience very distinct microenvironments in terms of mechanical and biochemical conditions. Therefore, growth signals that drive cells into reorganization are believed to be unique for each tissue type. A good bioreactor design should be able to provide tissue-specific growth signals in order to initiate and guide tissue regeneration [29]. Common concepts of current design of tissue-specific bioreactors are adopted: (1) perfusion is incorporated into the bioreactor design to facilitate mass transfer; (2) imitation of pseudo *in vivo* conditions to guide tissue regeneration.

The mechanical environment *in vivo* is important in tissue morphogenesis and its influence can be traced back to the embryonic period [130]. Recent studies focus on the application of mechanical stimulations to assist tissue regeneration *in vitro*. Many studies proved that appropriate modules of mechanical stimulation improve the construct properties in many aspects, such as ECM deposition, structural organization and mechanical properties [21, 117, 131].

I. Heart Valve

One of the notable results obtained using a specially designed bioreactor is heart valve culturing. Heart valves have the function of preventing backflow of blood, which is especially important in blood circulation in the heart [132]. A heavy hemodynamic loading *in vivo* implies high demand on the mechanical properties of heart valve substitutes. In recent research, incorporation of hydrodynamics into the bioreactor to mimic blood flow *in vivo* for growing heart valve substitutes becomes central in the design. Sodian *et al.* [131] and Schenke-Layland *et al.* [117] seeded vascular cells into a synthetic scaffold, polyhydeoxyalkanoate (PHA) and natural scaffold, decellularized porcine pulmonary valves in their respective experiments and cultured these seeded constructs under designed pulsatile flow conditions using static cultures as controls. Histological, biochemical and mechanical examinations showed that the use of mechanical stimulations completely preserved the ECM integrity, induced proliferations and secretion of ECM that outperformed the static controls. These examples demonstrate that mechanical stimuli such as shear stress and hydrostatic pressure when applied in a time-varying manner via a pulsatile flow are beneficial to heart valve development *in vitro*. It also implies that a mechanical environment that is similar to *in vivo* conditions would be important in the design of a bioreactor. This can be further elucidated in bioreactor studies for vascular tissue engineering.

II. Blood vessel

Niklason *et al.* [21] reported tissue-engineered blood vessels (PGA scaffold seeded with vascular cells) cultured under pulsatile flow conditions similar to fetal

development (165 beats/min and 5 % radial distension) in their specially designed bioreactors. The engineered vessels possessed rupture strengths greater than 2000 mm Hg and these constructs also exhibited contractility. In their experiments, ascorbic acid (vitamin C) known to promote ECM formation, was added into medium leading to a large amount of ECM formation in the vessel constructs as compared with controls. It also showed the importance of the synergistic effect by biomechanical and biochemical factors.

Although the vascular constructs that were produced in their pulsatile bioreactor resulted in better rupture strength and collagen deposition compared with the non-pulsed controls, other mechanical properties and biochemical compositions (cell mitotic rate and cell density) were still inferior to the native vessel. Elastin, which contributes elasticity of the tissue, was coincidently absent in tissue engineered vascular [21] and heart valve [131] constructs that were cultured under pulsatile flow. It appears that many other factors might affect vascular development. Recently, for example, it was recognized that there is a relationship between collagen deposition and pulsed rate [133]; and Isenberg and Tranquillo [118] found that collagen-based vascular constructs preconditioned with cyclic radial distension through a distensible mandrel resulted in strong elastin expression in smooth muscle cells. It is clear that the identification of growth-influencing factors remains an area of great importance in tissue engineering.

III. Cartilage

Cartilage has been actively studied in tissue engineering due to its relatively simple structure (avascular and consisting of a single cell type) and methods have been developed to engineer cartilage *in vitro* [134]. Cartilage is a load-bearing tissue and fibrosis (formation of stiff fibrous tissue) after damage limits the functional recovery of cartilage. Success in engineered cartilage would help patients to regain joint function. Since cartilage constantly bears load during daily activities such as walking, Gooch and Tennant [135] suggested that low-amplitude cyclic compression, which is experienced by cartilage *in vivo*, might help the development of cartilage *in vitro*. Their research showed that such mechanical loads increased production of GAG and collagen (which are major ECM components in cartilage) in freshly excised cartilage. In tissue engineering cartilage, bioreactors equipped with dynamic compression has also shown some promising results in terms of increased ECM deposition and improved mechanical properties [136, 137].

Application of hydrodynamics in bioreactors, as mentioned for heart valve and blood vessel, not only produces specific mechanical stimuli such as pulsatile-flow-induced radial distension for vascular growth but could also improve nourishment within the tissue construct. In a growing soft tissue construct having a poroelastic structure, hydrodynamics induces mechanical strains that could in turn generate interstitial flow within construct, resulting in promotion of convective mass transfer. Load-induced interstitial flow in cartilage case has been found to improve mass transfer in both native [138] and engineered cartilage [139]. In these cases, it is difficult to identify the real factors (mass transfer or mechanical cues or both) behind the final outcome. On

the other hand, although it is known that mass transfer is important in tissue growth, the detailed mechanism has not been completely understood, which limits advances in bioreactor design.

2.3 Mass Transfer in Bioreactor

Tissue engineering bioreactors have shown great progress in tissue regeneration *in vitro*. Most of the constructs harvested from bioreactors possessed the tissue-like structure, but the biochemical composition and mechanical properties are still inadequate. One major cause is insufficient internal mass transfer. Since tissue constructs developed *in vitro* are mostly avascular and diffusion is the major pathway for mass transfer, it limits tissue growth to constructs only about a few millimeters thick. This is especially true for cell types with a high metabolic demand such as cardiomyocytes [37]. In this case, mass transfer becomes one of the major concerns.

2.3.1 Overall Mass Transfer

It has been suggested that 100 μm is the farthest cell-capillary distance in native tissue [31] while Reece and Patrick [3] suggested an even stricter range of 25-50 μm. This cell-capillary distance suggests the importance of mass transfer in tissue, even more so for culturing tissue constructs in a bioreactor. In tissue culture, dissolved oxygen and nutrients such as glucose and glutamine are always critical to cell metabolism; without them, cells cease to grow and cell death will subsequently occur. Furthermore, ineffective removal of metabolites such as carbon dioxide, lactate and ammonium and excessive accumulation of these waste products also adversely affect the cell growth and physiology [140].

Many studies have shown the importance of mass transfer in tissue regeneration *in vitro*, especially for 3D structures. In the past *in vitro* studies, one major drawback of culturing constructs in a Petri dish or a mixed flask was ineffective internal mass transfer through diffusion to meet metabolic needs resulting in a cell-free core and non-uniform cell distribution [3, 31, 37]. Therefore, bioreactor design should also consider delivering more effective internal mass transfer in order to increase cellularity and cell uniformity of the constructs.

The effect of mass transfer in rotating wall vessels (RWV as shown in Figure 2.1C) has been reviewed by Freed and Vunjak-Novokovic [37]. These investigators found that the metabolic indicator, lactate-to-glucose ratio (L/G in molar basis), was greatly reduced in culturing cardiac tissue constructs in a RWV, where they recorded a value of 1.0 compared with 1.6 in mixed flask and 2.0 in static culture, respectively [35]. A lower value of L/G implies more glucose is oxidized in the aerobic pathway (called the tricarboxylic acid cycle or the Kreb's cycle) and this requires effective oxygen transport within the whole construct. This indicator can, in general, be used as an overall measure of effectiveness for mass transfer of oxygen. For example, L/G for cartilage constructs harvested from RWV tended to be slightly anaerobic, which gave a L/G of 1.3, but this was considered to be reasonable because metabolism of native cartilage is slightly anaerobic [37]. Recent follow-up studies on engineered cartilage and bone using bone marrow stem cells showed that culture in a RWV can support the development of tissue constructs with higher cellularity (increase in DNA content), and a higher degree of osteogenesis (increase in calcium or up-regulation of

osteocalcin level) for bone constructs and chondrogenesis (increase in GAG and collagen type II deposition) for cartilage constructs [141, 142].

On the other hand, in cardiac constructs harvested from a RWV, although the L/G was as low as 1.0, the appearance of a relatively acellular core implied that the metabolically active cardiacmyocytes were malnourished due to poor internal mass transfer in this type of bioreactor [35]. The study of cell types with different metabolic activities (chondrocytes and cardiomyocytes) demonstrated that a RWV may not satisfy mass transfer for all cell types with different metabolic demand. Diffusion might be sufficient for the metabolic demand of cartilage constructs but it is often inadequate for cardiac constructs. In order to increase mass transfer within the tissue construct for cell types with high metabolic demands, convection might be required. The follow-up studies carried out by Carrier and coworkers [22, 36] suggested that convection might be important in mass transfer within cardiac construct.

In the studies by Carrier *et al.* [22, 36], cardiomyocytes-seeded PGA constructs (2 mm thick) were cultured either in a bioreactor equipped with direct perfusion or in a mixed flask. Direct perfusion was carried out by forced medium flow through the construct as shown in Figure 2.1D. Direct perfusion of constructs for 10 days resulted in relatively uniform cell distribution within the construct, of thickness up to 1 mm, whereas only approximately 100 μm of peripheral region (only 5 % of total thickness) was filled with cells in the constructs cultured in mixed flasks. In the experiments, increasing the medium perfusion rate reduced the change of metabolic parameters (pH, pO_2, pCO_2, glucose and lactate concentrations) across the constructs, giving a more uniform

nutrient, which is probably the reason that a higher DNA content found in these constructs.

Direct perfusion also showed promising results in engineered bone. Interstitial flow has been known to be important in bone physiology such as communication between different bone cells [143]. For example, direct perfusion from 1ml/min to 3 ml/min in bone constructs observed a remarkable increase in cellularity and upregulation of osteogenesis [144, 145, 146]. In contrast, direct perfusion from 0.1-1 ml/min has been found detrimental to the development of a cartilage construct [147]. Increasing direct perfusion rate from this range showed a reduction in the overall cellularity and GAG deposition [147]. A separate study [148] showed that by applying a direct perfusion rate as low as 0.02 ml/min, a marked increase in cellularity, GAG and hydroxyproline (an amino acid commonly present in collagen) was observed in a perfused cartilage construct. From the recent progress on applying direct perfusion in three tissue types (cardiac, bone and cartilage), it appears that interstitial flow within the construct affects the development of different tissue types each to a different extent. However, the mechanism is still not well-understood due to the complexity of the system, which involves mass transfer (transport of nutrient species) and mechanical stimulation (shear). Furthermore, although direct perfusion has shown promising outcomes in cardiac constructs, Strehl and coworkers [24] pointed that shear stress due to direct perfusion might not be physiological for cardiomyocytes that are not exposed to shear flow *in vivo*. Thus, it is important to identify the effect of isolated factors and their combined effects. In this regard, mass transfer, which is important in maintaining cellularity and cell viability, should become a priority. On the other hand, among all

chemical species involved in maintaining cell growth, energetics and viability [149, 150], oxygen appears to be critical mainly due to its low dissolution in culture medium compared with other more soluble nutrient species.

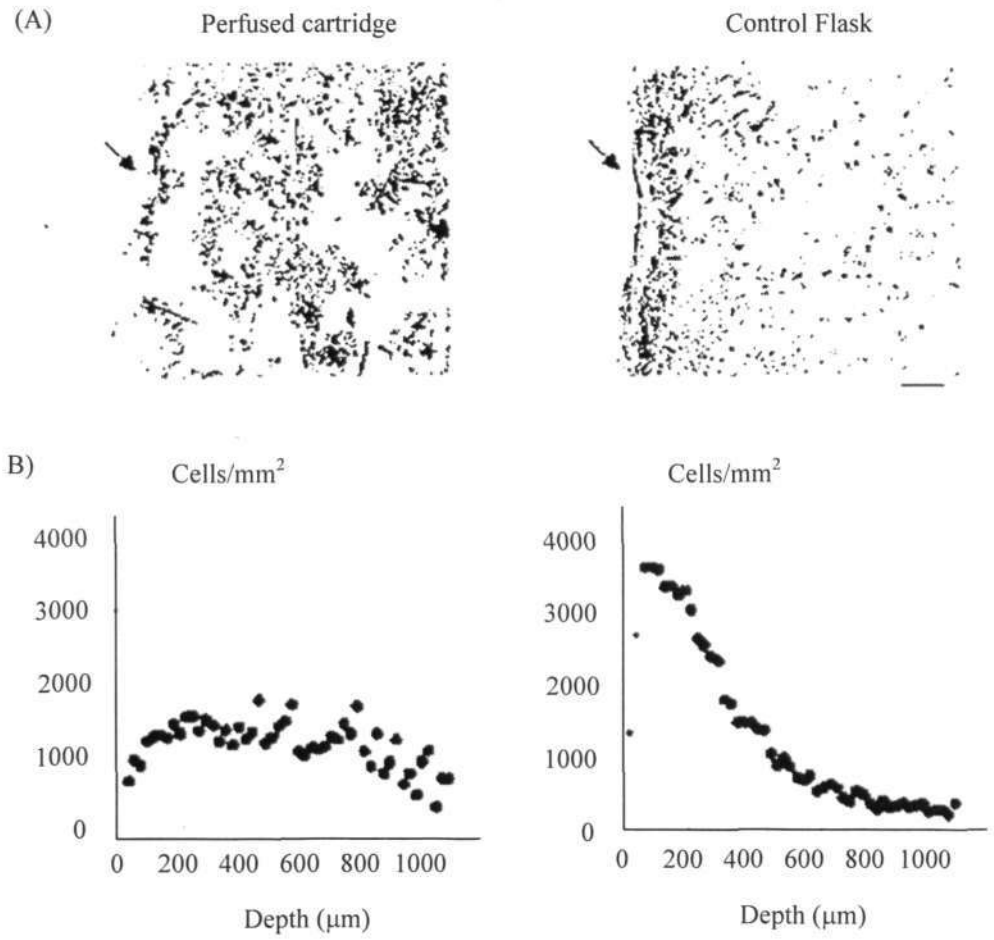

Figure 2.2: Cell distributions of cardiac construct cultured in either direct perfusion at 0.6ml/min (left) or in mixed flask (right): (A) histological micrographs showing qualitative distribution of cell nuclei (black area) and (B) quantification of cell number at different depth of the construct using histological micrograph [36].

2.3.2 Oxygenation

Capillary trees are embedded throughout most of the human tissues, so at normal conditions, oxygen transport can be facilitated, even though oxygen has low solubility

in water [151, 152]. Furthermore, in the presence of hemoglobin as oxygen carrier, blood can carry almost 40 times higher oxygen content than that in the culture medium, which normally contains no oxygen carriers [24]. Low solubility of oxygen in culture medium appears to be an issue in tissue engineering *in vitro* since avascular tissue constructs require an optimal oxygen supply to prevent adverse effects from hypoxia such as cell death due to acidosis [153], low energy conversion from the energy source [154] and activation of hypoxia-induced factor 1α (HIF-1α) causing cell cycle arrest (cessation of growth) [155] or cell death [156] .Elevation of dissolved oxygen in the culture medium by increasing the partial pressure of oxygen might partially alleviate the oxygen supply problem but high level of dissolved oxygen may be toxic to the cultured cells. However, Oller and coworkers [157] showed that mammalian cells cultured *in vitro* are able to proliferate at dissolved oxygen up to 400 μM before growth arrest initiates. This hyperbaric oxygen level, which is twice normal air can saturate in the culture medium, can only be achieved by additional oxygen supplementation in the gas phase.

Due to the versatility of oxygen in cell and tissue physiology, Forster and Estabrook [19, 152] concluded that "oxygen is too important to life to be categorized simply as a nutrient" which implies how essential oxygen is needed. Oxygen is required for most of the organisms during metabolism and it is especially important in order for most of normal human cells to undergo aerobic metabolism.

In medical terms, normoxia, hypoxia and anoxia refer to normal oxygen supply, deprivation of adequate oxygen supply and complete deprivation of oxygen supply, respectively at the cellular level. In the human body, the brain becomes anoxic at

about 2/3 of normal blood flow, initiating body control mechanisms that shut down the vital organs in order to maintain the oxygenation in the brain [158]. A low oxygen environment *in vivo* and *in vitro*, triggers anaerobic metabolism during when glucose converts to lactate resulting in very low and ineffective energy conversion (38 adenosine triphosphate (or ATP) in aerobic compared with 2 ATP in anaerobic metabolism) [154]. Also, lactate accumulation causes a dramatic shift of pH within the tissue by increasing hydrogen ion generated in the anaerobic metabolism, which results in consequent cell death due to acidosis [153].

I. Effect of oxygenation on tissue construct grown in vitro

Freed *et al.* [159] pointed out that oxygen plays an essential role in the regeneration of functional tissue constructs. Experimentally, Obradovic *et al.* [41] showed the implication of this role in cartilage cultured in RWV. These researchers found that the size of the construct without oxygenation was smaller than constructs grown with oxygenation; and an important ECM constituent of cartilage, GAG, only accumulated in the periphery, which gradually decreased towards the center. Furthermore, cell number in constructs grown without oxygenation for 5 weeks had no significant difference from that measured at day 3. Hence, effective oxygenation appears to be important in tissue regeneration *in vitro*. In a later study by Malda and colleagues [160], oxygenation has shown to be important but had to be regulated at a desired level. This study found that 100 % dissolved oxygen in culture medium turned out to be detrimental to cellularity and ECM (GAG and collagen) accumulation, whereas 5 % dissolved oxygen, which was at the *in vivo* level led to better biochemical

composition. An earlier study by another group also confirmed that 5 % dissolved oxygen helped restored differentiation gene expression in chondrocytes seeded in alginate (a seaweed derived biomaterial) [161]. Therefore, regulation of oxygenation is needed for the proper development of cartilage constructs.

As mentioned earlier, cartilage is avascular and diffusion is sufficient to meet the oxygen demand of chondrocytes. However, for other tissue types, which are vascularized, the oxygen requirement of cells is high so optimization of oxygen dissolution is important. It was reported that oxygen consumption rate for cardiomyocytes [162] is at least an order of magnitude higher than that for chondrocytes [163]. This implies that high oxygen delivery is critical in development of cardiac constructs and other tissues with high oxygen demand.

Carrier and colleagues [36], for example, observed the impact of oxygen on the quality of cardiac constructs cultured in direct perfusion connected in series. In their studies, 8 constructs were connected in series and subjected to direct medium flow. At a flowrate of 0.2 ml/min, the oxygen level at the inlet was around 160 mmHg (100 % dissolved oxygen) and the medium subsequently passed through 8 constructs with the oxygen partial pressure dropping progressively down to 60 mmHg at the outlet. An interesting observation was made from the first construct to the last construct: both the DNA content (overall cellularity) and the cellular protein content of the constructs were progressively decreased in correspondence with oxygen partial pressure (Figure 2.4). This study demonstrated the importance of adequate oxygen delivery in the development of cardiac constructs.

Due to high oxygen requirement for cardiomyocytes, optimization of dissolved oxygen in the culture medium could be beneficial for oxygen delivery for the cardiac construct. Since culture medium does not usually contain any oxygen carriers, such as hemoglobin in blood, an artificial oxygen carrier has been proposed to increase oxygen delivery in the culture medium [164]. One of the possible artificial oxygen carriers, perflurocarbon (PFC) was used to improve the oxygen content in culture medium for cardiac construct [24]. For example, 5.4 % (vol/vol) PFC in the medium, the maximum dissolved oxygen could be more than doubled, from 220 μM (medium alone) to 450 μM. In addition, the cardiac constructs obtained had higher cellularity with lower lactate dehydrogenase activity (an indicator to measure cell viability through lactate dehydrogenase released by dead or dying cells with broken cell membrane) in the oxygen-enhanced medium compared with the normal medium. However, the dissolved oxygen with PFC was still less than the hemoglobin level in arterial blood (450 μM vs. 8500 μM; thus a better hemoglobin substitute will be needed in the future.

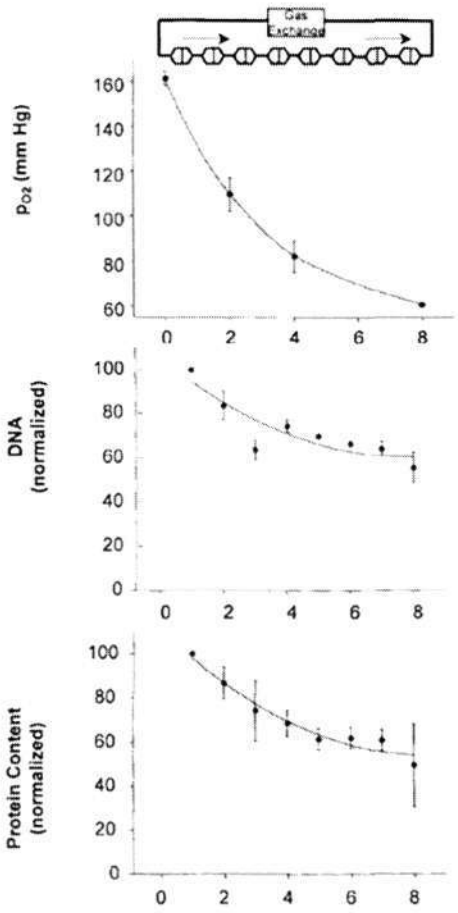

Figure 2.3: Eight cardiac constructs connected in series and cultured under direct perfusion. Cellular DNA (middle) and protein content (bottom) were reduced progressively and concurrently with oxygen partial pressures (pO_2, top), adapted from [22]

II. Internal Oxygen Transport

Most of the earlier studies focused on the correlation of oxygenation in the medium (external transport) with the construct quality and overlooked the local oxygenation within the construct itself (internal transport), which is equally important. Recently, a biomarker pimonidazole was used to correlate with the hypoxic state of cardiomyocytes seeded in collagen-matrigel [162]. At a dissolved oxygen as low as 14 μM, pimonidazole reacts with thiol groups to form adducts which can be detected by immunostaining. By this method, a sharp interface that separates normoxic from hypoxic (red) region can be identified and the diffusion depth for oxygen can be

determined (see Figure 2.4). Thus, this biomarker is a useful tool with which to detect localized hypoxia but the actual oxygen profile remained unknown, particularly within the distance between construct surface and normoxia-hypoxia interface.

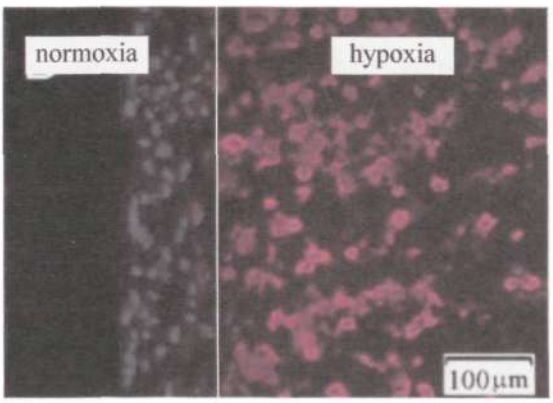

Figure 2.4: Immunofluorescence staining of pimonidazole in cardiomyocytes-seeded collagen-matrigel construct [162].

More recently, there has been an interest in studying the internal oxygenation in engineered tissue, such as, cartilage, bone and cardiac muscle. With the use of an oxygen microelectrode, optic fiber or fluorescence sensor, it became possible to study the diffusion limitation of oxygen transport in cartilage [16, 165, 166] and cardiac constructs [24, 162], and the temporal change of oxygen concentration was monitored at the centre of the bone [13]. Most of these studies also attempted to correlate the oxygen profile with the measured cell distribution, which offers more information to explain the connection between an environment factor (oxygen) and tissue development (cell distribution). However, there are drawbacks in these studies: (1) only the oxygen profiles in cells cultured in the open Petri dishes or open flow systems, were measured, since the measurements require introduction of the microsensor [16, 24, 162, 165]; or (2) only a single point measurement inside the construct in the bioreactor were carried out since the location of the sensor was fixed

beforehand [13]; or (3) only a planar profile was measured due to the limitation of the measurement method [166]. In situ oxygen profiling is still not possible in a closed system, which is normally required for bioreactor culture.

In addition to experimental studies, mathematical simulation of the system can provide insights into the effects of environmental factors on the development of tissue construct.

2.4 Modeling Growth of Tissue Construct

Cell growth and reorganization into a tissue-like structure is affected by many environmental factors such as biochemical and biomechanical stimuli, mass transfer and scaffold-related factors that have been discussed previously. Unfortunately, many of these factors are interrelated and complicated. The phenomena involved are generally complex and cannot be elucidated by available experimental techniques. Mathematical models offer a convenient and useful approach to explain some of these phenomena.

2.4.1 Current Progress

Tissue regeneration *in vitro* is governed by a set of complicated and an unknown set of factors, many of which cannot be easily correlated with each other. Tissue engineering models must predict events such as cell seeding into scaffold, cell proliferation and differentiation, ECM synthesis, scaffold degradation and mass transfer. Many mathematical models have been used to verify experimental results from tissue-engineered cartilage cultivation. For example, Wilson *et al.* [167] proposed a compartmental model to correlate the experimental data of dynamic deposition of

GAG and collagen, and degradation of scaffold (PGA/PLA) in cartilage construct. First order kinetics without diffusion limitation was assumed, so the model found an exponential relation between ECM synthesis and time. With curve fitting of time constants, the model results showed a qualitative agreement with experimental results. However, compartmental models of this kind cannot explain the intrinsic mechanism of the process (such as diffusion limitation to ECM synthesis) and the interpretation of time constants for different experiments appears unclear [168].

It would be useful if tissue regeneration could be correlated with culture conditions. As stated previously, tissue regeneration *in vitro* is mass-transfer dependent and the spatial distribution of growth-affecting solutes (e.g. oxygen, growth factors) appears to influence local cell growth. Obradovic *et al.* [47] suggested that GAG synthesis rate is oxygen limited, a phenomenon which was observed in their previous experimental work [41]. Here, spatial variation in oxygen concentration in the constructs was taken into account to correlate the GAG synthesis with mass transfer. The authors found that the spatial GAG distribution agreed well with the experimental data acquired from cartilage constructs cultured in rotating wall vessel (RWV) under oxygen partial pressure (pO_2) of 40 or 80 mmHg. Recently, Pisu *et al.* [48] attempted to use their own mathematical model to verify the experimental results obtained by Obradovic and coworkers [41]. The results of their simulation showed a qualitative and quantitative match with Obradovic's model [47] and with their experimental results [41]. From these two mathematical models, internal mass transfer (oxygen transport within the cartilage construct), has been shown to correlate with GAG deposition. In light of these recent model studies, it appears that the development of tissue in a bioreactor is

very much depended upon effective mass transfer. However, this parameter has not been fully investigated in these studies.

The treatment of mass balance within the construct in the abovementioned studies was rather simple in that a homogeneous (single-phase) domain was assumed. This assumption might be inappropriate since the tissue construct is a multiphase, porous structure with changing transport properties over time due to cell mass deposition and scaffold degradation. Therefore, it is believed that a more rigorous formulation for mass balance is required to give an accurate description of mass transfer within the tissue construct. Furthermore, a constant bulk concentration ("well mixed" condition) was imposed on the boundary (surface) of tissue construct and this could be an inappropriate boundary condition. Since mass exchange occurs between bulk medium and tissue construct, it is believed that a concentration boundary layer develops at the construct surface, leading to a reduction of species concentration across this layer and to a non-uniform interfacial concentration. Maintaining interfacial concentration at bulk value, therefore, seems to be impossible. Since the construct was considered as the model domain in some previous studies such as the models from Obradovic *et al.* [47] and from Galban and Locke [42, 43, 47], without any information from the bulk medium side, this boundary condition was unavoidably imposed.

Galban and Locke [42, 43] applied the Volume Averaging Method (VAM) to model dynamic chrondrocyte growth in a scaffold. The microscopic mass balance equations for each phase involved in the domain were volume-averaged into macroscopic equations. By using this method, an effective diffusivity and an effective metabolic rate constant can be correlated with the porosity of the construct, so that these

parameters change dynamically with the change of porosity. Various empirical cell-growth kinetic models were adopted to fit the experimental data of cartilage constructs [14, 169] and the consumption rate of only the substrate, glucose was taken as independently of the cell growth. The simulated results were qualitatively fitted with the experiment-derived dynamic volume fraction of cell phase for different construct thicknesses by adjusting kinetic parameters, including growth rate constant and metabolic rate constant [42]. Since the mathematical model established in the first stage of this study is based on VAM, studies from Galban and Locke [42, 43] will be further discussed in section 3.3.

Recently, Lappa [50, 51] applied the analogy of protein crystallization in soft organic tissue growth under fluid flow. He used the method so-called Organic Tissue Growth Volume-of-Fraction Method that assigned a single parameter as an indicator of tissue (= 1), medium solution (= 0) and interface (between 0 and 1) for a computational cell. The rotating wall vessel (RWV), with laminar flow around the cartilage, was modeled. It was assumed that the tissue construct was a highly viscous liquid (homogeneous) and surface deposition accounted for the evolution of the tissue construct. The author claimed that the growth of a cartilage construct is related to the mass transfer and shear stress. Surprisingly, the results showed the evolution of the construct similar to the actual results. The author concluded that there was an interplay between the increasing size of the sample and the structure of the convective field. This study also disclosed a possible disadvantage of the RWV was that the shape of construct cannot be easily controlled due to the non-consistent flow field around the construct. Moreover, the boundary layer established on the construct surface still hindered the mass transfer

from the bulk medium to the construct surface. The model itself neglected mass transfer and cell mass deposition within the tissue construct; it limits the analysis of tissue development to a rather macroscopic view.

The application of hydrodynamics in bioreactors has been proven to enhance mass transfer in many cases. The characterization of hydrodynamics and mass transfer in bioreactors has been carried out using mathematical modeling. The flow field and concentration profile in a concentric cylinder bioreactor [170] and a RWV [171] have been studied using Computational Fluid Dynamics (CFD). A constant consumption rate of oxygen was assumed in the governing equation. Furthermore, the mass transfer within the growing tissue construct was not taken into account in Lappas' studies. The commercial CFD software, FLUENT, was adopted in the former case [170] and it can be extended to study mass transfer in growing tissue constructs. In addition to general fluid flow, FLUENT also provides build-in functions for simulation of transport phenomena within porous materials.

Generally speaking, current mathematical models of growing tissue constructs only deal with mass transfer externally [50, 51] or internally [42, 43, 47, 48] and their coupled effects have not been studied. Hence, in light of the enhancement of mass transfer by hydrodynamics over experimental studies, the investigation of mass transfer in a system containing flowing bulk medium and growing tissue construct is necessary in order to understand their interaction (coupling effect) and the modeling should be a valuable tool to conduct this study. The following sections are dedicated to the application of the VAM to give a more rigorous description of mass transfer within

cellular media and growing tissue constructs. This will serve as a basis for the model established later in this study.

2.4.2 Volume Averaging Method: Modeling Mass Transfer in Cellular Media

Mass transfer (diffusion and reaction) through cellular media such as biofilms has been widely studied recently [172, 173, 174, 175, 176] in a theoretical way, which can be extended to tissue structures [173]. In many publications, tissue is described as a heterogeneous, gel-like structure consisting of a mixture of collagen fiber and proteoglycan which constitute the extracellular space, and cells [132, 177]. Diffusion is the major pathway for solutes to move around the tissue structure and the effectiveness in mass transfer depends mainly on the heterogeneity of the structure and the molecular size [177]. A general structure of a biofilm is similar to tissue in that two phases can be identified: microbe as the cell phase and polysaccharide matrix as extracellular phase [174].

In the past studies, the cellular media was treated as a continuum. Wood and Whitaker [174] pointed out that biofilm (including tissue) is a multiphase system that each phase can be treated as a single continuum and an effective transport coefficient (diffusivity) should be correlated with the structure of the system, that is, the spatial arrangement of each phase. In their analysis [174], the Volume Averaging Method (VAM) was applied to formulate the mass balance for biofilm, through which the microscopic governing equations are transformed into macroscopic ones, which are similar to those used for a homogeneous fluid. Furthermore, the microscopic and cellular information can be linked with the effective diffusivity through the formulation process. This

method provides with a simple but more rigorous way to formulate the mass transfer within a multiphase, porous domain, and it has been applied in this study to formulate governing equations. The following review covers a brief background of VAM and the application of VAM in the mass transfer model of biofilm.

The VAM was first applied over multiphase transport problems (reviewed by [178]). It is applicable when the length scales in a hierarchical system are disparate [179]. By using VAM, the microscopic information can be imparted into the macroscopic level at which the quantities can be measured in the experiments [174]. Hence, the model results can be validated with experiments without difficulties. First of all, for a given domain, a representative elementary volume (REV) must be selected, the characteristic size of which must be set much larger than the length scales of phases in the domain but much smaller than the characteristic length of the domain considered. In the case of the biofilm shown in Figure 2.5, two phases, the cell (σ) and the extracellular (β) phases, were identified in the domain and the mathematical form of this length constraint for VAM can be expressed by:

$$\ell_{bf} >> \ell >> \ell_{\beta}, \ell_{\sigma} \qquad 2.4.1$$

The σ-phase and β-phase have the length scales (ℓ_{β} and ℓ_{σ}) on the order of 10 μm where the characteristic length of the biofilm (ℓ_{bf}), normally taking its thickness, is on the order of 100 to 1000 μm or more [173], which is at least 10 times larger than the phase scales. In this situation, the selection of ℓ is restrictive since its value

selected only ranges from 10 to around 100 μm and is required to fulfill the length constraint given in equation 2.4.1.

Now, considering a physical quantity for a particular phase, Ψ_β or Ψ_σ (at a given point in the domain), the superficial volume-averaging and intrinsic volume-averaging of this quantity can be defined by:

Superficial volume-averaging of Ψ_β or Ψ_σ

$$< \Psi_\beta >= \frac{1}{V} \int_{V_\beta} \Psi_\beta \, dV \qquad 2.4.2$$

$$\text{and } < \Psi_\sigma >= \frac{1}{V} \int_{V_\sigma} \Psi_\sigma \, dV \qquad 2.4.3$$

Intrinsic volume-averaging of Ψ_β or Ψ_σ

$$<\Psi_\beta>^\beta = \frac{1}{V_\beta}\int_{V_\beta} \Psi_\beta \, dV \qquad 2.4.4$$

$$\text{and } <\Psi_\sigma>^\sigma = \frac{1}{V_\sigma}\int_{V_\sigma} \Psi_\sigma \, dV \qquad 2.4.5$$

The only difference between these two definitions is that superficial averaging is the integral divided by the volume of the REV whereas intrinsic averaging is the integral divided by the volume of a particular phase in the REV. The sum of volumes of all phases must equal the volume of the REV (i.e., $V = V_\beta + V_\sigma$) and the volume fraction of each particular phase can be defined as:

$$\varepsilon_\beta = \frac{V_\beta}{V} \qquad \text{and} \qquad \varepsilon_\sigma = \frac{V_\sigma}{V} \qquad 2.4.6$$

$$\varepsilon_\beta + \varepsilon_\sigma = 1 \qquad 2.4.7$$

Most transport equations consist of the divergence or the gradient of, and of the time derivative of a dependent variable (Ψ_β or Ψ_σ which can be a scalar or a vector). The following expressions for superficial volume averaging these terms, for Ψ_β (the same applies for Ψ_σ) and the full derivations of these equations can be found in [179]:

Divergence of a vector: $$<\nabla \cdot \Psi_\beta> = \nabla \cdot <\Psi_\beta> + \frac{1}{V}\int_{A_{\beta\sigma}} \Psi_\beta \cdot \vec{n}_{\beta\sigma}\, dA \qquad 2.4.8$$

Gradient of a scalar: $$<\nabla \Psi_\beta> = \nabla <\Psi_\beta> + \frac{1}{V}\int_{A_{\beta\sigma}} \Psi_\beta \vec{n}_{\beta\sigma}\, dA \qquad 2.4.9$$

Time derivative of a scalar or a vector component:

$$<\frac{\partial \Psi_\beta}{\partial t}> = \frac{\partial <\Psi_\beta>}{\partial t} - \frac{1}{V}\int_{A_{\beta\sigma}} \Psi_\beta \vec{w} \cdot \vec{n}_{\beta\sigma}\, dA \qquad 2.4.10$$

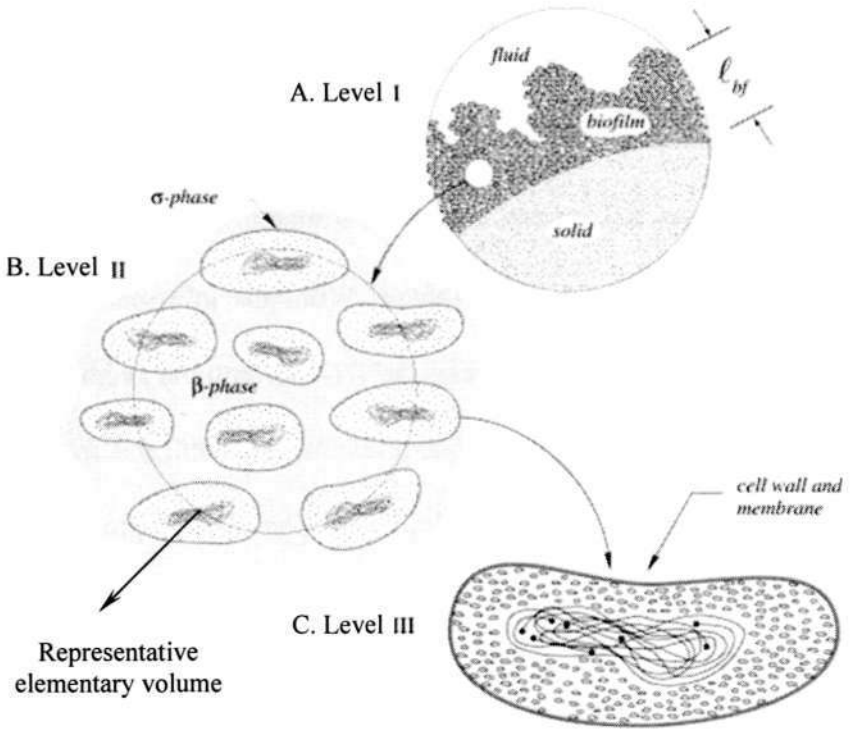

Figure 2.5: Hierarchical structure of biofilm: (A) Level I: Macroscopic domain: biofilm with thickness, ℓ_{bf} ; (B) Level II: A representative elementary volume (REV) with volume, V and characteristic length, ℓ or radius, R. In this view, two phases are identified: β-phase with length scale, ℓ_β and σ-phase with length scale, ℓ_σ ; and (C) Level III: Enlarged view of a cell [176].

All definitions contain area integral terms. In the integral, $A_{\beta\sigma}$ is the surface area of the $\beta\sigma$-interface, $\vec{n}_{\beta\sigma}$ the outward unit normal vector of the interface and $\vec{w}$ the displacement vector of the interface. In most of the analysis, $\vec{w}$ is neglected because its contribution is comparatively small. Furthermore, spatial decomposition can link the intrinsic volume-averaged quantity ($\langle\Psi_\beta\rangle^\beta$ or $\langle\Psi_\sigma\rangle^\sigma$) and the quantity at a given point (Ψ_β or Ψ_σ) through the spatial deviation quantity ($\tilde{\Psi}_\beta$ or $\tilde{\Psi}_\sigma$):

$$\Psi_\beta = \langle\Psi_\beta\rangle^\beta + \tilde{\Psi}_\beta \qquad 2.4.11$$

$$\Psi_\sigma = \langle\Psi_\sigma\rangle^\sigma + \tilde{\Psi}_\sigma \qquad 2.4.12$$

In a biofilm, three dominant processes are identified [174]: (1) diffusion in a continuous β-phase, (2) transport across a membrane into the σ-phase, and (3) transport and reaction inside the σ-phase. With this information, microscopic mass balances can be written for both phases [174]. After volume averaging the microscopic governing equations using the previous relations, a general macroscopic mass balance for substrate, for example, glucose (G), in the β-phase and σ-phase through the biofilm take the forms:

β-phase

$$\frac{\partial}{\partial t}(\varepsilon_\beta < C_{G,\beta} >^\beta) = \nabla \cdot [\mathbf{D}_{G,\beta} \nabla(\varepsilon_\beta < C_{G,\beta} >^\beta) + \frac{1}{V}\int_{A_{\beta\sigma}} \vec{n}_{\beta\sigma} C_{G,\beta}\, dA] + \frac{1}{V}\int_{A_{\beta\sigma}} \vec{n}_{\beta\sigma} \cdot \mathbf{D}_{G,\beta} \nabla C_{G,\beta} dA \quad 2.4.13$$

σ-phase

$$\frac{\partial}{\partial t}(\varepsilon_\sigma < C_{G,\sigma} >^\sigma) = \nabla \cdot [\mathbf{D}_{G,\sigma} \nabla(\varepsilon_\sigma < C_{G,\sigma} >^\sigma) + \frac{1}{V}\int_{A_{\beta\sigma}} \vec{n}_{\sigma\beta} C_{G,\sigma}\, dA] + \frac{1}{V}\int_{A_{\beta\sigma}} \vec{n}_{\sigma\beta} \cdot \mathbf{D}_{G,\sigma} \nabla C_{G,\sigma} dA - \varepsilon_\sigma \frac{r_{G,max} < C_{G,\sigma} >^\sigma}{< C_{G,\sigma} >^\sigma + K_{M,G}} \quad 2.4.14$$

The dependent variable in the mass balance is the concentration of glucose (G), $C_{G,\beta}$ and $C_{G,\sigma}$. Here, $\mathbf{D}_{G,\beta}$ and $\mathbf{D}_{G,\sigma}$ are the diffusivities of glucose in the β- and the σ-phases, respectively. The Michaelis-Menton kinetics with parameters $r_{G,max}$ (maximum consumption rate of glucose, kg/m^{3}s) and $K_{M,G}$ (saturation constant of glucose, kg/m^3) are adopted for the glucose consumption rate. In addition, the assumption of local mass equilibrium in the biofilm can simplify the system into a single-phase continuum [173]. It was stated that with respect to the membrane transport process between the cell (σ-phase) and extracellular space (β-phase), equilibrium of chemical species could be achieved rapidly. Therefore, the concentrations of β-phase and σ-phase can be tied to one another by an equilibrium relationship [173]:

$$\{C_G\} = < C_{G,\beta} >^{\beta} = K_{eq,G} < C_{G,\sigma} >^{\sigma} \qquad 2.4.15$$

where $\{C_G\}$ is called weighted equilibrium concentration of glucose. With this relation, equation 2.4.13 and 2.4.14 can be combined into a single mass balance equation representing the biofilm as a single-phase continuum. This concept has been extended to the model established later in Chapter 4. After solving the closure problem for the effective diffusivity of glucose and rearranging, the single mass balance takes the form:

$$\frac{\partial\{C_G\}}{\partial t} = \nabla \cdot D''_{eff,G} \nabla\{C_G\} - \frac{r''_{G,max}\{C_G\}}{\{C_G\} + K''_{M,G}} \qquad 2.4.16$$

where

$$D''_{eff,G} = \frac{D_{eff,G}}{\varepsilon_\beta + K_{eq,G}^{-1}\varepsilon_\sigma} \qquad 2.4.17$$

$$r''_{G,max} = \frac{\varepsilon_\sigma r_{max,G}}{\varepsilon_\beta + K_{eq,G}^{-1}\varepsilon_\sigma} \qquad 2.4.18$$

$$K''_{M,G} = K_{eq,G} K_{M,G} \qquad 2.4.19$$

The term $D_{eff,G}$ requires some explanation. This parameter refers to the effective diffusivity of a substrate (glucose in this case). It requires solving the closure problem over an REV that is set up from microscopic and macroscopic mass balances in conjunction with the microscopic boundary conditions. The real structure is always complicated, which requires high computational efforts to obtain numerical solutions;

with the use of a theoretical model, such as the unit cell (Figure 2.6A and B) that have been used in many studies. $D_{eff,G}$ can be obtained using this model with a good approximation to the real solution and experimental measurements [173, 176].

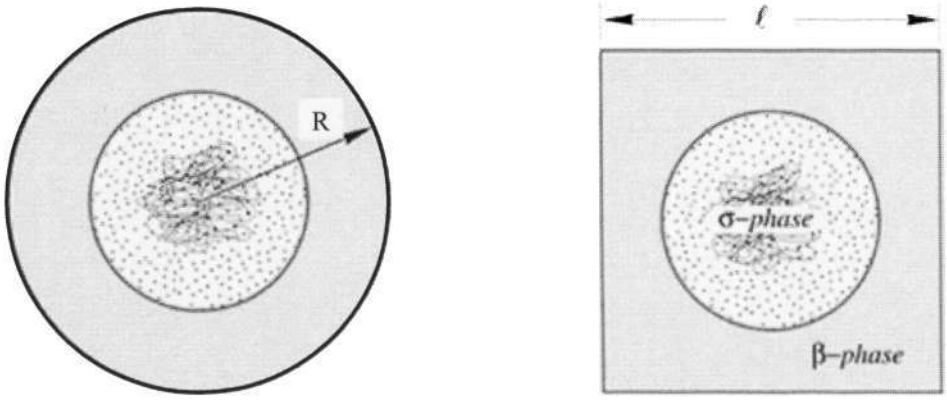

Figure 2.6: Unit cells. (A) Chang's unit cell with radius of R. (B) Unit cell for a spatially periodic system of an array of spheres (3D) or cylinders (2D) [176].

In nature, no isotropic porous structure exists. However, if the biofilm structure is arranged in a random manner that does not have any directional preference in the way the σ-phase distribute in the β-phase , as shown in Figure 2.5B, the diffusion process within this REV can be considered to be isotropic [175]. Under this condition, it was claimed that the detailed information of the microscopic structure such as the actual arrangement and irregularities of the phases are filtered out when solving the closure problem using the real structure and the most important factor that affects the solution is the boundary condition at the σβ-interface [175, 178]. Hence, the effective diffusivity solved using the unit cell gives a good agreement with that using real structure [173]. Keeping in mind that the analytical solution is always useful in the

approximation of effective diffusivity, Chang's model, which is shown in Figure 2.6A, has the analytical solution [176]:

$$\frac{D_{eff,G}}{D_{G,\beta}} = \frac{3\kappa - 2\varepsilon_\beta(\kappa-1) + 2\varepsilon_\beta\varepsilon_\sigma^{-1/3}\gamma}{3 + \varepsilon_\beta(\kappa-1) + (3-\varepsilon_\beta)\varepsilon_\sigma^{-1/3}\gamma} \qquad 2.4.20$$

where

$$\kappa = \frac{D_{G,\sigma}}{K_{eq,G}D_{G,\beta}} \qquad 2.4.21$$

$$\gamma = \frac{\Gamma D_{G,\sigma}}{K_{eq,G}E_o R} \qquad 2.4.22$$

and, Γ (membrane resistance, kg.s/m^3) and E_o (surface concentration of transporter proteins, kg/m^2) are the parameters of the simple carrier model for membrane transport [174]. Through effective diffusivity, the subcellular (membrane transport) and microstructure (porosity) details are transported to the macroscopic governing equations. In this regard, the macroscopic governing equations, derived using VAM are beneficial because the equations are solved without neglecting all the important information from the microscopic level. In tissue engineering, this approach has been recently adopted by Galban and Locke [42, 43] in predicting the dynamics of chrondrocyte growth in porous PGA scaffold. The details of their model are discussed in the next section, which has been used as the basis for the model established in the first stage of this project.

2.4.3 Volume Averaging Method: Modeling Growth of Tissue Constructs

In the model of Galban and Locke [42], a two-phase system was defined that was similar to the one used in the studies by Ochoa *et al.* [172] and Wood and Whitaker [174]: (1) Void phase (β-phase): contains nutrient fluid and polymer matrix, (2) Cell phase (σ-phase): it contains cells, nutrients, ECM released by cells and some polymer matrix. The mass balance of substrate or metabolite was similar to that given in equation 2.4.16, but first-order kinetics (with rate constant, r_G) was used rather than the Michaelis-Menton form. Furthermore, a permeable membrane with a single parameter, k_m (mass transfer coefficient, m/s) was adopted and the membrane transport model was the same as that used by Ochoa's analysis [172]. Hence, the mass balance and the effective diffusivity of substrate (glucose) take the form:

$$\frac{\partial\{C_G\}}{\partial t} = \nabla \cdot D''_{eff,G} \nabla\{C_G\} - r''_G\{C_G\} \qquad 2.4.23$$

where

$$D''_{eff,G} = \frac{D_{eff,G}}{\varepsilon_\beta + K_{eq,G}^{-1}\varepsilon_\sigma} \qquad 2.4.24$$

$$r''_G = \frac{\varepsilon_\sigma K_{eq,G}^{-1} r_G}{\varepsilon_\beta + K_{eq,G}^{-1}\varepsilon_\sigma} \qquad 2.4.25$$

and

$$\frac{D_{eff,G}}{D_{G,\beta}} = \frac{2\kappa - \varepsilon_\beta(\kappa - 1) + \varepsilon_\beta \varepsilon_\sigma^{-1/2}\alpha}{2 + \varepsilon_\beta(\kappa - 1) + (2 - \varepsilon_\beta)\varepsilon_\sigma^{-1/2}\alpha} \qquad 2.4.26$$

where

$$\kappa = \frac{D_{G,\sigma}}{K_{eq,G} D_{G,\beta}} \qquad 2.4.27$$

$$\alpha = \frac{D_{G,\sigma}}{R k_m} \qquad 2.4.28$$

Using equation 2.4.26, the effective diffusivity can be estimated at various times during cell growth. With appropriate boundary conditions [42], solutions were obtained for cultured chrondrocyte-seeded PGA scaffolds with a diameter of 1 cm and four different thicknesses (0.088, 0.116, 0.168 and 0.307 cm) for 30 days. In the first study [42], a one-dimensional (1D) model and quasi steady state ($\frac{\partial\{C_G\}}{\partial t} = 0$) were assumed in the mass balance and different cell growth models (a modified Contois, a Moser and an n-th order models) were used. The predicted kinetics were examined for their agreements with the experimental results of cell density (which was derived from the volume fraction of the cell phase) at 5 different time points until 30 days [14, 169]. For these growth models, a single substrate (glucose) was assumed to limit the growth of the chrondrocytes. The analytical solution for substrate concentration was solved, the area-average of which was substituted into the growth models to solve for the volume fraction of the cell phase (ε_σ). By adjusting the kinetic parameters, all growth kinetics were able to give a qualitative fit to the experimental results for most scaffold

thickness ranges, but the agreement for the thinnest scaffold used in the series (i.e., 0.88mm) was not satisfied for all growth models.

In a follow-up study [43], the temporal and spatial distributions of substrate (glucose) and metabolite (lactate) were taken into consideration and a modified Contois model, accounting growth-inhibition of metabolite, was adopted. In this model, the spatial dependence of cell growth was again modeled for different scaffold thickness.

Although no corresponding experimental data was available to validate their results, this model provided a good beginning with which to study dynamic cell growth in a cell-seeded scaffold in that a more rigorous mass transfer of substrate could be taken into consideration with effective diffusivities being correlated with the volume fraction of the phases. This simple but more rigorous account of mass transfer will be pursued in the model established in Chapter 4. However, a two-phase model might be too simplistic for this system in that an independent scaffold phase was not completely defined in the analysis of Galban and Locke [42, 43]. In mass balance, a first-order reaction expression was adopted, which might not be applicable for the description of cellular consumption; and in this case, Michaelis-Menton kinetics might be a more recommended form [180]. According to extensive studies in the cell behavior [180, 181], cells mobilize in random fashion and move towards concentration gradients of some particular chemicals (chemotaxis), which could be nutrients [181], growth factors and ECM molecules on the scaffold surfaces [182]. Although cell immobilization was assumed in their models, this assumption might be reasonable at this point since limited experimental data is available to support modeling the chemotactic effect on the cell motility within the scaffold. .

In Chapter 4, a model will be established to study mass transfer and cell mass deposition under medium flow (hydrodynamics) that is based on the work of [173, 174, 175, 176, 183], Galban and Locke [42, 43] and past VAM studies [178, 184]. The modifications of the model study from the one used by Galban and Locke [42, 43] to study mass transfer in a growing tissue construct can be summarized into four points:

1. Convective effect due to medium flow is incorporated into the transport equations.

2. The coupled effect of mass transfer in the bulk medium (external) and the tissue construct (internal) is now considered.

3. A three-phase porous construct, rather than a two-phase configuration, is used.

4. Michaelis-Menton kinetics is applied to model the substrate consumption.

With the modifications made, a mathematical model to study hydrodynamic effect in bioreactor on oxygen transport and cell mass deposition of growing tissue construct was established to gain insights on how medium flow influence tissue development through oxygen transport and the simulation can be validated by providing reasonable agreement with the data extracted from the experiments.

In the experimental studies, a flow-type tissue engineering bioreactor was designed and fabricated to provide uniform, laminar flow across the tissue construct surface and in situ profiling was made possible minimizing interferences on the culture environment. Due to the space limitation, an oxygen microsensor system cannot be accommodated in a conventional incubator especially if the incubator is shared within a research team. In this regard, an incubation unit was designed in order to perform

cell and construct culture experiments outside the incubator without external 5 % CO_2 supplementation. Without proper CO_2 supplementation outside the incubator, the conventional CO_2/bicarbonate buffer system cannot be used. An alternative buffer system was adopted to culture esophageal smooth muscle cells under normal air condition (0.03 % CO_2) in which their phenotype and requirement of oxygen and glucose were studied. A porous scaffold was required for cells to attach and grow into a construct. A new gelatin scaffold fabrication method was used to create a porous scaffold with relatively uniform pore size distribution. Esophageal smooth muscle cells seeded scaffolds were cultured in the designed bioreactors at different flowrates and in situ oxygen profiling was carried out before harvesting for characterization (cell distribution). The simulation results were compared with the experimental results This study offered more new insights on the effect of flow-improved oxygen transport on the development of a tissue construct than previous studies available in the literature.

Chapter 3. Methodology

3.1 Research Method

The research approach is summarized in Figure 3.1. It involved both mathematical and experimental studies. In the mathematical studies, a mathematical model was established to simulate mass transfer and tissue construct development under laminar flow conditions. Due to the complexity of the porous constructs, the Volume Averaging Method (VAM) was employed to formulate microscopic governing equations into more general macroscopic equations carrying important microscopic information. Model parameters related to cell physiology required in the model were obtained experimentally. The numerical solution was obtained by the CFD software, FLUENT®. With the use of CFD, a detailed geometry of the bioreactor was determined to fulfill the laminar flow condition within the construct region. This information was then used in the design and fabrication of the bioreactor.

The experimental studies involved three areas: scaffold, cell and bioreactor. A gelatin-based porous scaffold was developed to provide a template for the cells to attach and grow. Characterization of the scaffold was carried out including microstructure observation (with pore size measurement), measurements of degradation rate, crosslink index and mechanical properties, and evaluation of cell-scaffold interaction. Porcine esophageal smooth muscle cells (PESMCs) were isolated from pig esophagus using either the explant or the enzymatic approach. Serial expansion of the cells provided a cell source for seeding into the scaffold. Characterization was carried out including their morphology, cell phenotype and growth kinetics. Since the bioreactor

culture was carried out in normal air, unlike conventional culture in a 5 % CO_2 incubator, PESMCs at passage 4 were adapted under air conditions and cultured in incubation unit designed for this study. PESMCs cultured under normal air were characterized by their cell morphology and phenotype. More importantly, oxygen and glucose requirements, growth rate, cell size and cell weight were measured as parametric inputs for the mathematical model.

The bioreactor is the focus of this project and a special bioreactor system was designed and fabricated. This system is composed of an incubation unit, a bioreactor (including flow loop) and an oxygen profiling system. A 2D (cell expansion) and 3D (tissue construct) cultures were carried out in the system. This system was used for development of esophageal smooth muscle construct in the designed bioreactor. At designated times, the tissue construct was oxygen-profiled in situ, harvested and analyzed. The outcome provided information of the quality of tissue construct such as cellularity, cell phenotype and cell distribution. The oxygen profile and cell distribution obtained from the bioreactor cultured construct were used to validate the mathematical model. The following sections describe the methodology in detail.

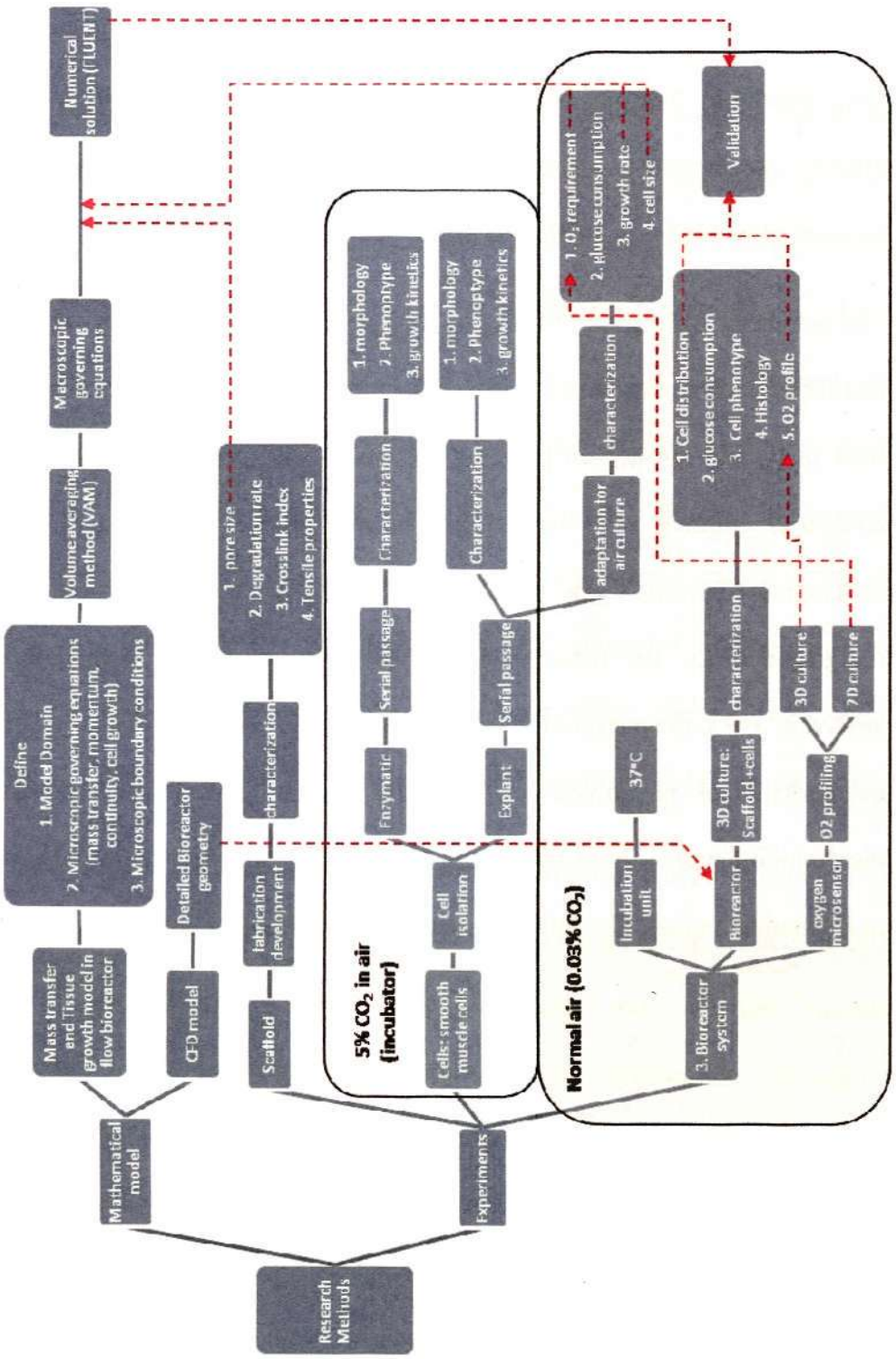

Figure 3.1: Research method flow chart

Chapter 4. Mathematical Model

4.1 Mathematical model of mass transfer and tissue development under laminar flow in flow bioreactor

4.1.1 Model Description

In order to examine the effect of hydrodynamics (medium flow) on the mass transfer in tissue construct cultured in the bioreactor, a mathematical model was established to predict the spatial and temporal cell distribution and the concentration profile of chemical species involved in tissue growth (e.g., oxygen and glucose). The domain of the model is diagrammatically shown in Figure 4.1A, which describes a cell-seeded construct was mounted in a bioreactor where the construct is exposed to a laminar flow of the culture medium across its top surface. **Two subdomains** are defined, namely, (1) bulk medium (**η-subdomain**) with height, H and length, L; and (2) cell-seeded scaffold or tissue construct (**ω-subdomain**) with thickness, h and length, l. Figure 4.1B shows an example of the microscopic structure of a cell-seeded scaffold [185]. **Three phases** can be identified in the ω-subdomain: medium (β), cell (σ) and scaffold (γ) phase shown in Figure 4.1B. Due to the multiphasic nature of the system, the Volume Averaging Method (VAM) [3] was employed to formulate the governing equations including continuity, momentum, mass and cell growth equations. By using VAM, dependent variables (such as velocity) in the governing equations were volume-averaged over a small representative elementary volume (REV). The averaging process converts microscopic equations of all phases in a given domain into a single macroscopic equation which represents the whole domain. The resulting one-equation

model incorporates microscopic information into model parameters such as the effective diffusivity, which avoids the over-simplified homogeneous assumption in a multiphase domain using constant model parameter for the whole domain. To find the effective property, a theoretical model was pursued in a 3-phase Chang's unit cell as shown in Figure 4.1C. This unit cell model was used to solve the closure problem raised by the VAM process [173]. The following assumptions were made to simplify some of the complexities in the model.

4.1.2 Assumptions

I. Bulk medium (η-subdomain)

1. A parabolic velocity profile is imposed along the inlet boundary, consistent with a fully developed laminar flow [186].
2. The inlet concentration of oxygen is maintained constant.

II. Tissue construct or scaffold (ω-subdomain)

1. The pore size and pore interconnectivity is uniform within the scaffold.
2. The construct volume remained is constant over the culture period.
3. Cells are seeded uniformly in the scaffold.

III. Bulk medium-tissue construct interface (ηω-interface)

Continuous boundary conditions are applied neglecting the effect of excess flux due to the abrupt change of the structure through this boundary.

IV. Medium phase (β-phase)

1. Incompressible [187].
2. Dilute solution assumption is applied since the mass fraction of the main component, glucose, is less than 1 % in the culture medium [22].

V. Cell phase (σ-phase)

1. Oxygen (subscript O in all related variables) is considered the limiting chemical species [152]. The consumption rate of oxygen is modeled by the Michaelis-Menton kinetics [174, 180].
2. Oxygen-dependent Contois growth model is used for the cell mass deposition [188].
3. Consumption rates of oxygen are written independent of cell mass deposition [42, 43, 174].
4. Density of cell phase is constant. Cell phase consists of new and old cells and the density of cell phase is assumed to be the average of this mixture [42, 43].
5. Cells are immobilized [42, 43] and spherical.
6. Local mass equilibrium between the cell phase and the medium phase in the ω-subdomain was used to combine the mass balances of the cell and the medium phase into one general form [174, 175].

VI. Scaffold phase (γ-phase)

1. No mass transfer between the cell phase (σ) and the scaffold phase (γ), or between the medium phase (β) and the scaffold phase (γ), or in scaffold phase (γ) itself is assumed. Therefore, no mass balances are written for the scaffold phase.
2. Degradation is neglected because γ-phase takes up less than 5 % of the total volume in a highly porous scaffold.

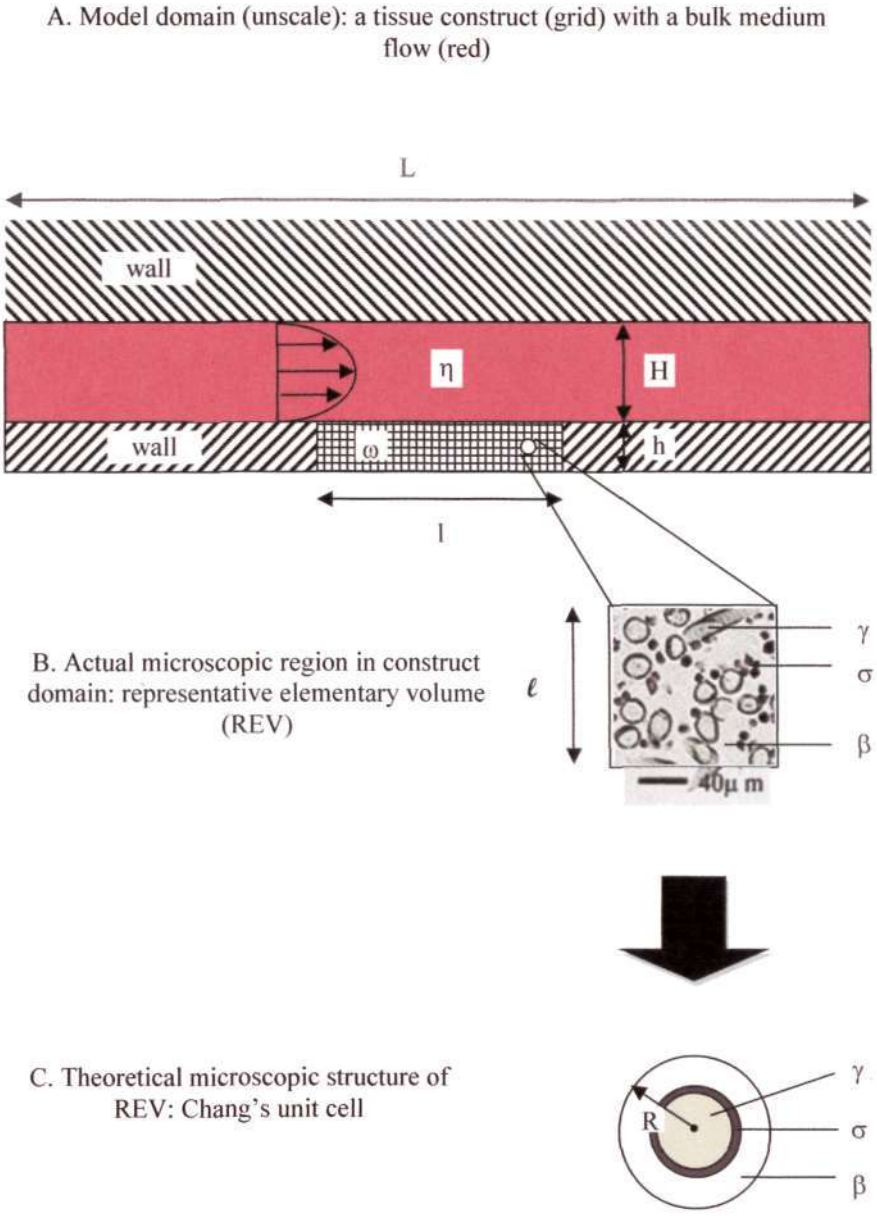

Figure 4.1: Domain description: (A) A laminar flow region of bioreactor was modeled . It contains a bulk medium flow (η-subdomain) and porous scaffold seeded with cells or tissue construct (ω-subdomain) with domain size of H × L and h × l, respectively. (B) Histological cross section of cell seeded PET fibrous scaffold [185]. In the cell-seeded scaffold, 3 phases are defined: medium- (β), cell- (σ) and scaffold- phase (γ). This small subdomain is called representative elementary volume (REV) used in the Volume Averaging Method, having characteristic length, ℓ. (C) Theoretical model of REV: Chang's unit cell, having radius R.

4.1.3 Microscopic Governing Equations

I. Governing Equations at microscale

The major model derivation is presented in this section. The system consists of two subdomains: a bulk medium (η-subdomain) and a cell-seeded scaffold or a tissue construct (ω-subdomain). Inside the ω-subdomain, which is a porous medium, a medium phase (β), a cell phase (σ) and a scaffold phase (γ) are identified. Unlike a homogeneous liquid or gas phase, transport phenomena in porous medium are complex, for example, a porous media, more than one phase co-exist so that transport phenomena are greatly influenced by the interactions between phases. Therefore, application of the VAM becomes very useful in the formulation of transport equations in a porous medium [179, 183].

Since the η-subdomain is considered an homogeneous subdomain, the governing equations can be written without difficulties. The focus is placed on the ω-subdomain, where the VAM is applied in the model formulation. Firstly, a representative elementary volume (REV) is defined in the ω-subdomain. The example of an REV is shown in Figure 4.1B. The requirement is for the characteristic length of the REV, ℓ, being much greater than the length scales of all phases within the REV [179]:

a. Length scale constraints

$$\ell >> \ell_\sigma,\ \ell >> \ell_\beta \text{ and } \ell >> \ell_\gamma \qquad 4.1.1$$

This length scale constraints must be fulfilled when VAM is used. The length scale of the cell, or scaffold, is around 10^{-5} m, which indicates the cell size and fiber diameter

of scaffold, respectively [169, 185] . The value ℓ set in the model will be around an order of magnitude larger so as not to violate this constraint. Furthermore, the order of ℓ has to be much smaller than the characteristic length of the system considered, which is the thickness of the tissue construct (in the order of 10^{-3} m) [36, 42]. Hence, ℓ has to be around 10^{-4} m.

First, the microscopic governing equations for mass and momentum balances are written in the ω-subdomain:

b. Continuity equation (Incompressible fluid)

$$\nabla \cdot \vec{v}_\beta = 0 \qquad 4.1.2$$

c. Momentum balance (Navier-Stokes equation, steady-state, Newtonian fluid with constant properties, without external forces)

$$0 = -\nabla p_\beta + \mu_\beta \nabla^2 \vec{v}_\beta \qquad 4.1.3$$

Mass balances for species i in β-phase and σ-phase

$$\frac{\partial C_{i,\beta}}{\partial t} + \nabla \cdot (C_{i,\beta}\vec{v}_\beta - D_{i,\beta}\nabla C_{i,\beta}) = 0 \text{ for } \beta\text{-phase} \qquad 4.1.4$$

$$\frac{\partial C_{i,\sigma}}{\partial t} + \nabla \cdot (-D_{i,\sigma}\nabla C_{i,\sigma}) = R_i \text{ for } \sigma\text{-phase} \qquad 4.1.5$$

The dependent variables are velocity ($\vec{v}_\beta$) and pressure (p_β) of medium phase, and mass concentration of species i ($C_{i,\beta}$ and $C_{i,\sigma}$). Since an incompressible medium phase was assumed, the divergence of velocity is zero in equation 4.1.2. Steady-state, Navier-Stokes equation, neglecting gravitational force is written for the momentum

balance in Equation 4.1.3. Furthermore, the convective term ($\vec{v}_\beta \cdot \nabla \vec{v}_\beta$) in the original form of the Navier-stokes equation is cancelled because of the continuity equation ($\nabla \cdot \vec{v}_\beta = 0$). Unsteady mass balances of species i for both β-phase and σ-phase are expressed in equation 4.1.4 and 4.1.5. The diffusive term of species i is defined by Fick's law [186] and the convective term is only present in β-phase due to the interstitial flow and immobilized σ-phase. R_i is the sink or source term that represents consumption or production rate of species i. This term only appears in the mass balance of the σ-phase due to the biochemical reactions in the cells. Microscopic boundary conditions of ω-subdomain are:

B.C.1: $\vec{v}_\beta = 0$ at $A_{\beta\sigma}$ 4.1.6

B.C.2: $-\vec{n}_{\beta\sigma} \cdot (D_{i,\sigma} \nabla C_{i,\sigma}) = -\vec{n}_{\beta\sigma} \cdot (D_{i,\beta} \nabla C_{i,\beta})$ at $A_{\beta\sigma}$ 4.1.7

B.C.3: $-\vec{n}_{\beta\sigma} \cdot (D_{i,\sigma} \nabla C_{i,\sigma}) = k_m (C_{i,\beta} - K_{eq,i} C_{i,\sigma})$ at $A_{\beta\sigma}$ 4.1.8

B.C.4: $-\vec{n}_{\sigma\gamma} \cdot (D_{i,\sigma} \nabla C_{i,\sigma}) = 0$ at $A_{\sigma\gamma}$ 4.1.9

B.C.5: $-\vec{n}_{\beta\gamma} \cdot (D_{i,\beta} \nabla C_{i,\beta}) = 0$ at $A_{\beta\gamma}$ 4.1.10

At βσ-interface or $A_{\beta\sigma}$, no-slip condition (equation 4.1.6) is given and interfacial fluxes are set to be identical. The mass flux of species i at the βσ-interface must be matched (equation 4.1.7). Here, $\vec{n}_{\beta\sigma}$ is the outward unit vector normal to the βσ-interface. The third boundary condition (equation 4.1.8) relates the interfacial flux to the constitutive equation, which is proportional to the concentration difference

between the free stream and interface [186]. The k_m is the mass transfer coefficient in m/s while $K_{eq,i}$ is the equilibrium constant of species i. The last two boundary conditions (equation 4.1.9 and 4.1.10) state that no mass transfer takes place at the βγ- or σγ- interfaces. For Chang's unit cell shown in Figure 4.1C, only equation 4.1.10 was used as a boundary condition since the σ-phase was the only phase that was assumed to come into contact with the γ-phase. This microscopic boundary condition was used later to solve the closure form brought about by the volume averaging process to obtain the effective diffusivity, which is elaborated in Appendix A.6.

d. Source or Sink of Chemical Species i

A series of complex biochemical reactions occur in cells for growth and maintenance. Reaction involves consumption and/or production of chemical species. A source or sink term (R_i) can be added into the mass balance equation for the σ-phase (equation 4.1.5) to account for this contribution. A single chemical species involved in the biological system can be highly complex, involving a very large number of reactions. To represent R_i in a simplified way, an unstructured model was applied to assume that the substrate is consumed by "a volume of cells" at a single overall reaction rate, to avoid having to account for the biological details in the cells [189]. This consideration is rather empirical, but useful in the formulation.

Both consumption/production rates, in $kg/m^3.s$, are modeled using the Michaelis-Menton kinetics [174, 180] which can be expressed as:

$$R_i = \pm r_{i,max}\left[\frac{C_{i,\sigma}}{C_{i,\sigma} + K_{M,i}}\right] \qquad 4.1.11$$

where $r_{i,max}$ is the maximum consumption (when negative) or production (when positive) rates in $kg/m^3.s$ and $K_{M,i}$ is the half saturation constant in kg/m^3.

II. Cell Growth Model

Cell growth depends on the availability of growth-related chemical species in the culture environment. Furthermore, cell growth slows down when the growing space is reduced due to continuous cell growth [55]. To account for these phenomena, Contois equation was used to model the cell growth, which depends on the concentration of limiting species ($C_{i,\sigma}$) and is inhibited at high cell density (ρ_σ) [188]. Among all growth-related species, oxygen was assumed to be the growth-limiting species. Therefore, the rate of cell mass deposition, R_σ, which depends on dissolved oxygen concentration ($C_{O,\sigma}$) can be expressed as:

$$R_\sigma = \frac{d\rho_\sigma}{dt} = r_{\sigma,max}\left[\frac{C_{O,\sigma}}{C_{O,\sigma} + K_C\rho_\sigma}\right]\rho_\sigma \qquad 4.1.12$$

where $r_{\sigma,max}$ and K_C are the maximum specific growth rate, in s^{-1}, and the Contois constant, respectively.

4.1.4 Macroscopic Governing Equations

I. Macroscopic Governing Equations in ω-subdomain

Microscopic governing equations (from equation 4.1.2 to 4.1.5) presented in the previous section are volume-averaged over the REV and the results will be shown in the following sections. Detailed derivations can be found in Appendix A.3. It is

necessary now to explain the representations, which are used extensively in the subsequent discussion:

a. Superficial volume-averaged velocity

$$<\vec{v}_\beta>=\frac{1}{V}\int_{V_\beta}\vec{v}_\beta dV \qquad 4.1.13$$

b. Intrinsic volume-averaged pressure

$$<p_\beta>^\beta=\frac{1}{V_\beta}\int_{V_\beta}p_\beta dV \qquad 4.1.14$$

c. Intrinsic volume-averaged concentrations

$$<C_{i,\beta}>^\beta=\frac{1}{V_\beta}\int_{V_\beta}C_{i,\beta}\,dV \qquad 4.1.15$$

$$<C_{i,\sigma}>^\sigma=\frac{1}{V_\sigma}\int_{V_\sigma}C_{i,\sigma}\,dV \qquad 4.1.16$$

d. Weighted equilibrium concentration

$$\{C_i\}=<C_{i,\beta}>^\beta=K_{eq,i}<C_{i,\sigma}>^\sigma \qquad 4.1.17$$

e. Volume fraction of phases

$$\varepsilon_\beta=\frac{V_\beta}{V},\ \varepsilon_\sigma=\frac{V_\sigma}{V}\ \text{and}\ \varepsilon_\gamma=\frac{V_\gamma}{V} \qquad 4.1.18$$

$$\varepsilon_\beta+\varepsilon_\sigma+\varepsilon_\gamma=1 \qquad 4.1.19$$

The superficial volume-averaged dependent variable Ψ in phase j denoted by $<\Psi_j>$ (e.g. $<\vec{v}_\beta>$ in equation 4.1.14), is the average over the REV volume (V). The intrinsic volume-averaged dependent variable Ψ in phase j, denoted by $<\Psi_j>^j$ (e.g. $<p_\beta>^\beta$, $<C_{i,\beta}>^\beta$ and $<C_{i,\sigma}>^\sigma$ in equation 4.1.14, 4.1.15 and 4.1.16), refers to the average over

the volume of phase j within the REV (i.e. V_β or V_σ in this system). These two quantities are exchangeable through $\langle\Psi_j\rangle = \varepsilon_j \langle\Psi_j\rangle^j$. If local mass equilibrium is valid, the weighted equilibrium concentration, $\{C_i\}$ defined in equation 4.1.17 can be used to link concentrations in β- and σ- phases to aid forming one-equation mass balance in the ω-subdomain. More discussion on the local mass equilibrium can be found in Appendix A.5. The volume fraction of each phase is defined in equation 4.1.18 as the ratio of the volume of the specific phase in the REV to the volume of REV, and they must add up to one (equation 4.1.19). The macroscopic governing equations for ω-subdomain are given below:

f. Macroscopic continuity equation in the ω-subdomain

$$\nabla \cdot \langle \vec{v}_\beta \rangle = 0 \qquad 4.1.20$$

g. Macroscopic momentum equation in the ω-subdomain

$$0 = -\nabla \langle p_\beta \rangle^\beta + \varepsilon_\beta^{-1} \mu_\beta \nabla^2 \langle \vec{v}_\beta \rangle - \mu_\beta \mathbf{K}_\beta^{-1} \cdot \langle \vec{v}_\beta \rangle \qquad 4.1.21$$

Equation 4.1.21 above is Darcy's law with first Brinkman's correction (second term on the right hand side) [184]. $\mathbf{K}_\beta$ represents the permeability tensor in Darcy's law. In this study, the Chang's unit cell is used as the theoretical model to solve the effective parameters. As shown in Figure 4.1C, a single Chang's unit cell consists of a spherical γ-core, the outside of which lies a σ-phase, followed by a β-phase. By using this theoretical model, one can visualize the whole ω-domain filled up by an array of Chang's unit cells which are identical to an array of spheres (see Figure A.1 and A.6 in

Appendix A.6 for illustration). In this isotropic array, the Kozeny-Carman equation was used for estimating K_β [190]:

$$K_\beta = \frac{d_{\sigma\beta}\varepsilon_\beta^{\,3}}{180(1-\varepsilon_\beta)^2} \qquad 4.1.22$$

where $d_{\sigma\beta}$ in this equation is estimated from the diameter of combined σ- and γ-phase in Chang's unit cell shown in Figure 4.1C. As ε_β approaches 1, or when β-phase is the only phase present in the domain, it takes on infinity permeability and the sink term (Darcy's law) disappears.

h. Macroscopic one-equation mass balance of species i in ω-subdomain

$$\varepsilon_i \frac{\partial\{C_i\}}{\partial t} + \nabla\cdot(\{C_i\} < v_\beta >) = \nabla\cdot D_{eff,i}\nabla\{C_i\} + \{R_i\} \qquad 4.1.23$$

where

$$\varepsilon_i = \varepsilon_\beta + K_{eq,i}^{-1}\varepsilon_\sigma \qquad 4.1.24$$

In the derivation of this equation through the volume-averaging process, the dispersion effect was neglected and the change rate in volume fraction (i.e. growth rate) was assumed much smaller than that of the species concentration (i.e. $\frac{\partial\varepsilon_\sigma}{\partial t} << \frac{\partial\{C_i\}}{\partial t}$). These details can be found in Appendix A.4. The local mass equilibrium allows the combination of the volume-averaged mass balances of σ- and β- phases into a single equation through the equilibrium relation, equation 4.1.17. The effective diffusivity of species i, $D_{eff,i}$, is derived from the closure problem created through the volume averaging procedure, which can be solved with a known

microscopic geometry (in this case, that is, Chang's unit cell shown in Figure 4.1C) through the procedure described in [191]:

$$\frac{D_{eff,i}}{D_{i,\beta}} = \frac{G_{1,i}(1-\varepsilon_\gamma \kappa_i) - G_{2,i}(\varepsilon_\beta - \varepsilon_\gamma \kappa_i) - G_{3,i}}{G_{1,i} - G_{2,i}} \qquad 4.1.25$$

The derivation of equation 4.1.25 and definitions of $G_{1,i}$, $G_{2,i}$, $G_{3,i}$ and κ_i, which are the functions of volume fractions, can be found in Appendix A.6. Finally, the macroscopic source and sink term of species i, $\{R_i\}$ is defined as follows:

i. Macroscopic Source or Sink of Species i

Applying the volume-averaging procedure together with the local mass equilibrium (equation 4.1.17) over equation 4.1.11, the macroscopic source or sink term of species i, $\{R_i\}$ takes the form:

$$\{R_i\} = \pm \frac{\varepsilon_\sigma r_{i,max}\{C_i\}}{\{C_i\} + K_{M,i}K_{eq,i}} \qquad 4.1.26$$

j. Macroscopic Cell Mass Deposition Model

The same treatment, as for the source or sink term, is carried out to write the cell mass deposition model in macroscopic form. It is convenient to express the result in terms of the change rate of volume fraction of cell phase ($\frac{d\varepsilon_\sigma}{dt}$):

$$\frac{d\varepsilon_\sigma}{dt} = \varepsilon_\sigma \left[\frac{r_{\sigma,max}\{C_O\}}{\{C_O\} + K_C K_{eq,O} <\rho_\sigma>^\sigma \varepsilon_\sigma} \right] \qquad 4.1.27$$

where $<\rho_\sigma>^\sigma$ is the intrinsic volume averaged cell density, which refers to density of a single cell.

k. Macroscopic Governing Equations in η-subdomain

The macroscopic governing equations for the η-subdomain can be simply written using equations 4.1.20, 4.1.21 and 4.1.23 by imposing $\varepsilon_\beta = 1$ and $\varepsilon_\sigma = \varepsilon_\gamma = 0$ with no sink or source term in the mass balance (i.e. $\{R_i\} = 0$):

l. Macroscopic continuity equation in η-subdomain

$$\nabla \cdot \langle \vec{v}_\beta \rangle = 0 \qquad 4.1.28$$

m. Macroscopic momentum equation in η-subdomain

$$0 = -\nabla \langle p_\beta \rangle^\beta + \mu_\beta \nabla^2 \langle \vec{v}_\beta \rangle \qquad 4.1.29$$

n. Macroscopic mass balance of species i in η-subdomain

$$\frac{\partial \{C_i\}}{\partial t} + \nabla \cdot (\{C_i\} \langle \vec{v}_\beta \rangle) = \nabla \cdot D_{i,\beta} \nabla \{C_i\} \qquad 4.1.30$$

Note that the governing equations for η-subdomain are identical to the governing equations for a homogeneous fluid.

4.1.5 Boundary and Initial Conditions

In order to solve the governing equations, boundary and initial conditions must be specified. The boundaries of the system and the location of the xy-coordinate are shown in Figure 4.2. There are three types of boundaries, including the "wall", the "velocity inlet" and the "outflow", and the boundary conditions are:

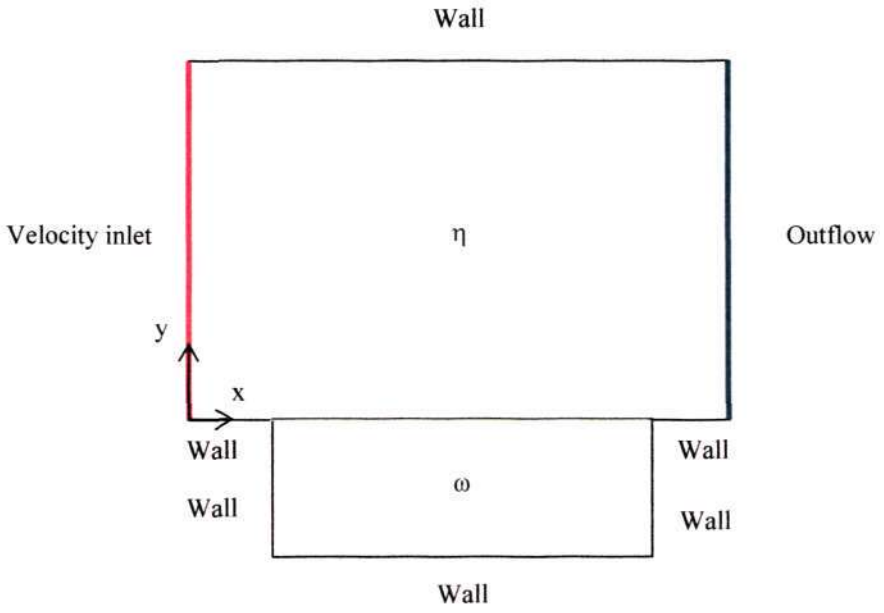

Figure 4.2: Boundary of the sytem: velocity inlet, outflow and wall.

At the velocity inlet, a parabolic profile was defined for the x-velocity (equation 4.1.31) and the concentration of species i was set at a fixed value ($C_{i,o}$) (equation 4.1.32):

$$< v_{\beta,x} >= v_{max}\left[1-\frac{(y-H/2)^2}{(H/2)^2}\right] \qquad 4.1.31$$

$$\{C_i\}=C_{i,o} \qquad 4.1.32$$

where v_{max} denotes the maximum velocity across the profile.

At the "Outflow" boundary, the diffusive flux of momentum (viscous + pressure) and species i normal to the boundary (n) were set to zero since the flow and concentration fields were unchanged near the exit of the domain and the solution can be extrapolated from the interior of the domain near the exit:

$$\nabla_n < \vec{v}_\beta >= 0 \qquad 4.1.33$$

$$\nabla_n \{C_i\} = 0 \qquad 4.1.34$$

At the "Wall" boundaries, no-slip condition was employed and the diffusive flux of species i normal (n) to the boundary was set to zero due to no mass exchange across the impervious boundary:

$$\nabla_n \{C_i\} = 0 \qquad 4.1.35$$

$$<\vec{v}_\beta >= 0 \qquad 4.1.36$$

The initial conditions (t = 0) are also specified. In the η-subdomain, the velocity and concentration fields were set similar to the "Velocity inflow":

$$< v_{\beta,x} >= v_{max}\left[1 - \frac{(y - H/2)^2}{(H/2)^2}\right] \qquad 4.1.37$$

$$\{C_i\} = C_{i,o} \qquad 4.1.38$$

In the ω-subdomain, a static condition was set and the concentration field was constant. The volume fraction of the cell phase was also fixed at a constant value (ε_o) with the assumption of a uniform cell distribution at each point in the scaffold subdomain:

$$<v_{\beta,x} >= 0 \qquad 4.1.39$$

$$\{C_i\} = K_{eqi} C_{i,o} \qquad 4.1.40$$

$$\varepsilon_\sigma = \varepsilon_o \qquad 4.1.41$$

4.1.6 Nondimensionalization

The nondimensionalization of the governing equations was also performed. By using the time scale $\bar{t} = \frac{h^2}{D_{O,\beta}}$, the length scale, $\ell = h$, the scaled velocity, $\bar{v} = \frac{h}{\bar{t}}$ and the scaled pressure, $\bar{p} = \frac{\rho_\beta h^2}{\bar{t}^2}$, all the governing equations, boundary and initial conditions in section 4.1.4 and 4.1.5 can be re-written and generalized into dimensionless forms suitable for both subdomains. Since oxygen is the only limiting factor to be considered, all the subscripts related to species i are dropped for brevity.

a. Generalized dimensionless macroscopic continuity equation

$\nabla \cdot \vec{\varpi}_\beta = 0$ valid for both ω and η- subdomains 4.1.42

Where $\vec{\varpi}_\beta$ is the dimensionless velocity defined as:

$$\vec{\varpi}_\beta = \frac{< \vec{v}_\beta >}{\bar{v}} \qquad 4.1.43$$

b. Generalized dimensionless macroscopic momentum equation in ω-subdomain

$$0 = -\nabla \Pi_\beta + Sc\, \nabla^2 \vec{\varpi}_\beta - \frac{Sc}{K} \cdot \vec{\varpi}_\beta \qquad 4.1.44$$

where

$$\Pi_\beta = \frac{< p_\beta >^\beta}{\bar{p}} \qquad 4.1.45$$

$$Sc = \frac{\mu_\beta}{\rho_\beta D_{O,\beta} \varepsilon_\beta} = \frac{\upsilon_\beta}{D_{O,\beta} \varepsilon_\beta} \text{ for ω-subdomain} \qquad 4.1.46$$

$$Sc = \frac{\mu_\beta}{\rho_\beta D_{O,\beta}} = \frac{\upsilon_\beta}{D_{O,\beta}} \text{ for η-subdomain} \qquad 4.1.47$$

$$K = \frac{K_\beta}{h} \text{ for } \omega\text{-subdomain} \qquad 4.1.48$$

$$K \to \infty \text{ for } \eta\text{-subdomain (infinite permeability)} \qquad 4.1.49$$

Π_β is the dimensionless static pressure, Sc is the Schdmit number, which is the relative measure between viscous and diffusive effects. K is the dimensionless permeability normalized by the length scale, h (i.e. construct thickness). In the η-subdomain, K can be assumed to be infinity, which makes the sink term become zero.

Generalized dimensionless macroscopic mass balance of oxygen

$$\frac{\partial X}{\partial \tau} + \nabla \cdot (X \vec{\varpi}) = \nabla \cdot (\mathcal{D} \nabla X) - Da_I \left(\frac{X}{X + K''_M} \right) \qquad 4.1.50$$

where

$$X = \frac{<C_{O,\beta}>^\beta}{C_o} \qquad 4.1.51$$

$$Da_I = \frac{\varepsilon_\sigma r_{O,max} C_o^{-1} h^2}{D_\beta} \text{ for } \omega\text{-subdomain} \qquad 4.1.52$$

$$Da_I = 0 \text{ for } \eta\text{-subdomain (no consumption)} \qquad 4.1.53$$

$$K''_M = \frac{K_{M,O} K_{eq,O}}{C_o} \qquad 4.1.54$$

$$\mathcal{D} = \frac{D_{eff,O}}{D_{O,\beta}} \text{ for } \omega\text{-subdomain} \qquad 4.1.55$$

$$\mathcal{D} = 1 \text{ for } \eta\text{-subdomain}$$

The parameters are the dimensionless oxygen concentration X, the dimensionless diffusion coefficient, $\mathcal{D}$, the dimensionless modified half saturation constant (K''_M)

and the Damökhler number for oxygen transport (Da_1), which represents the relative measure between consumption and diffusion of oxygen.

c. Generalized dimensionless Macroscopic Cell Growth Equation

$$\frac{d\varepsilon_\sigma}{d\tau} = Da_2\left[\frac{X}{X + K_C''}\right] \qquad 4.1.56$$

Where

$$Da_2 = \frac{r_{\sigma,max}\,\varepsilon_\sigma h^2}{D_\beta} \text{ for } \omega\text{-subdomain} \qquad 4.1.57$$

$$Da_2 = 0 \text{ for } \eta\text{-subdomain (no cell growth)} \qquad 4.1.58$$

$$K_C'' = \frac{\varepsilon_\sigma < \rho_\sigma >^\sigma K_C K_{eq,O}}{C_o} \qquad 4.1.59$$

The volume fraction of the cell phase is not scaled since it is dimensionless already. The cell mass deposition model consists of the dimensionless modified Contois constant (K_C'') and the Damökhler number for cell growth (Da_2) represents the relative measure between the cell growth and the diffusion of oxygen (limiting factor).

Finally, the dimensionless boundary and initial conditions are obtained by nondimensionalization of the conditions listed in section 4.1.5 through equation 4.1.31 to 4.1.41.

d. Dimensionless boundary conditions

Velocity inlet: $$\varpi = \varpi_{max}\left[1 - \frac{(\psi - \phi)^2}{\phi^2}\right] \qquad 4.1.60$$

$$X = 1 \qquad 4.1.61$$

where $$\varpi_{max} = \frac{V_{max}}{\overline{V}} \qquad 4.1.62$$

$$\psi = \frac{y}{h} \qquad 4.1.63$$

$$\phi = \frac{H}{2h} \qquad 4.1.64$$

Outflow: $0 = \nabla_n \vec{\varpi}_\beta$ 4.1.65

$$0 = \nabla_n X \qquad 4.1.66$$

Wall: $0 = \nabla_n X$ 4.1.67

$$\vec{\varpi} = 0 \qquad 4.1.68$$

e. Dimensionless initial conditions

In η-region: $\varpi = \varpi_{max}\left[1 - \frac{(\psi - \phi)^2}{\phi^2}\right]$ 4.1.69

$$X = 1 \qquad 4.1.70$$

In ω-region: $\vec{\varpi} = 0$ 4.1.71

$$X = K_{eqO} \qquad 4.1.72$$

$$\varepsilon_\sigma = \varepsilon_o \qquad 4.1.73$$

4.1.7 Parameter Inputs

In order to solve the dependent variables in the governing equations derived in the last sections, values of model parameters, boundary and initial conditions are specified as inputs. Inputs required in the model can be classified into 5 categories:

(i) Domain and subdomain: Dimension of model domain and each subdomain

Height of η-domain = 0.55 mm;

Length of η-domain = 5.2 cm;

Height of ω-domain = 0.2 mm;

Length of ω-domain = 3.2 cm.

(ii) Fluid properties: medium density, viscosity, flowrate (applied conditions)

Density of medium = 1030 kg/m^3

Viscosity of medium = 0.7 cp

Flowrate = 0.272 and 0.545 ml/min (experimental conditions)

(iii) Scaffold properties: porosity and pore size

Porosity = 0.95

Pore size = 141.4μm

(iv) Dissolved oxygen: diffusivity of oxygen in water and dissolved oxygen at inlet

Diffusivity of oxygen in water ($D_{O,\beta}$) = 2.00×10^{-9} m^2/s

Dissolved oxygen at inlet (C_o) = 7.04×10^{-11} kg/m^3 (100 % saturation)

(v) Cell properties: density of a single cell, cell growth parameters, oxygen utilization parameters and initial cell seeding density.

Density of a single cell ($<\rho_\sigma>^\sigma$) = 1475 kg/m^3

Maximum oxygen consumption rate ($r_{max,O}$) = 2.77×10^{-10} $kg/m^3.s$

Half saturation constant of oxygen ($K_{M,O}$) = 6.81×10^{-9} kg/m^3

Equilibrium constant of oxygen between cell and medium ($K_{eq,O}$) = 1.0

Maximum specific growth rate ($r_{max,\sigma}$) = 1.33×10^{-5} s^{-1}

Contois constant (K_C) = 5.70×10^{-11} kg O_2/kg cells

Initial cell density (N_o) = 2 million cells/cm^3

4.1.8 Numerical Solution

A numerical solution was obtained using segregated solver in FLUENT 6.0.2 (FLUENT Inc., 2003a). The physical domain and mesh were created in GAMBIT 2.0. A grid of 25,000 cells was generated. Spatial discretization of FLUENT is based on finite volume method and in the model simulations, second-order upwind discretization and first-order implicit time discretization were used [192]. Since the oxygen diffusion is the critical process in this system, the time scale, $\bar{t}$, provides an estimate of the time step. For a 2-mm thick scaffold with the oxygen diffusivity in the culture medium of 2×10^{-9} m^2/s, the time scale is 2,000 s. Therefore, the time step selection should be less than 2,000 s. On the other hand, tissue growth is a dynamic process, which is time-dependent; a stricter time step of 2s was used and the simulation results were verified the results using even a smaller time step of 0.2s. Furthermore, the grid was also refined to 50,000 cells to verify the solution. The model results of 25,000-cell grid with 2-s time step is found to have a maximum 4.8 % difference from the results obtained using the 50,000-cell grid with 0.2-s time step.

FLUENT solved mass, momentum and mass balance of oxygen; and cell growth equations to obtain medium velocity, pressure, dissolved oxygen concentration and the

volume fraction of cell phase. Since there is no built-in transport equation for cell growth model, the volume fraction of cell phase was defined as "user defined scalar" (or UDS) in FLUENT. In this manner, a transport equation consisting of an unsteady term, a convective term, a diffusive term and a source/sink term was generated in FLUENT to solve for the volume fraction of the cell phase. However, the cell growth defined in equation 4.1.56 does not contain a convective and a diffusive term. In order to solve this equation, both terms were manually switched off by setting diffusivity of the cell phase to zero and disabling the convective option in the UDS control menu. A similar approach has been used in pyrolysis of solid species in biomass [193]. At each time step, the segregate solver solved the governing equations sequentially and iteratively until the convergence criterion of 10^{-6} was fulfilled.

A macro file in C language was created with user defined functions (UDFs) to specify the momentum sink in x- and y- direction, the sink term of oxygen, cell growth rate, diffusivities of oxygen and user defined scalar (UDS), viscosity, density, inlet velocity profile, initial volume fraction of cell mass and time steps used in the simulation (FLUENT Inc., 2003b). This file was linked with FLUENT which was then used in the solving process. A sample UDF file can be found in Appendix B.

The mathematical model assumed a fully-developed laminar flow region in the bioreactor. When designing the bioreactor, an adequate geometry and entrance length must be adopt for the flow field to fully develop. Therefore, the flow field in the bioreactor chamber has to be studied in detail to provide design information for the chamber geometry and dimension.

4.2 CFD for bioreactor geometry design

4.2.1 Design Criteria of Flow Field

The overall design criteria of the bioreactor are detailed in section 5.3.3I. CFD studies were conducted to determine the geometry and dimension of a chamber for delivery of the desired flow pattern.

It is required that the flow pattern is a uniform, fully-developed, laminar flow across the construct surface. This leads to a parabolic profile on the plane perpendicular to the construct surface and plug on the plane parallel to the construct surface. In order to provide a fully-developed flow, a sufficient entrance length has to be given to allow flow development as the medium enters the chamber through a small chamber inlet. On the other hand, the purpose of plug flow is to achieve a uniform flow across the construct width such that 2D analysis can be achieved as intended in the mathematical model.

4.2.2 Geometry Study

A parallel plate configuration was considered to provide designated flow for the construct. The geometry was then determined to finalize the chamber design in terms of flow pattern and chamber volume. The latter is to reduce the cost (including chamber materials and culture medium) and space by building an oversized chamber. Three geometries of chamber enclosure were investigated and their top views are shown in Figure 4.3:

1. Rectangular chamber (Figure 4.3A).

2. Pill-shaped chamber with semi-circular (radius = 2 cm) entrance and exit portions (Figure 4.3B).
3. Pill-shaped chamber with semi-ellipsoid (long axis = 4 cm and short axis = 2 cm) entrance and exit portions (Figure 4.3C).

All the chamber width is fixed at 4 cm and a 6-cm long rectangular area (shaded area in Figure 4.3) in the centre portion is the area of interest in which the construct is to be mounted in the bioreactor. A first estimate of the entrance length (L_E) is obtained using the empirical correlation by Atkinson *et al.* [194].

$$\frac{2L_E}{H} = 1.25 + 0.088\ \mathrm{Re} \qquad 4.2.1$$

where

$$\mathrm{Re} = \frac{v_{av} H}{\nu_\beta} \qquad 4.2.2$$

This correlation estimates L_E for a parallel plate channel with height of H and width of W if $H/W << 1$. Re is the Reynolds number with v_{av} as the average velocity and ν_β as the kinematic viscosity ($=\frac{\mu_\beta}{\rho_\beta}$). From the equation and given chamber height (H), a higher velocity requires a longer entrance length for full development of the flow. An average velocity of 10^{-3} m/s is used to estimate the entrance length together with ρ_β = 1030 kg/m^3 and μ_β = 0.7 cp for culture medium [36]. By using 4.2.1 and 4.2.2, the Reynolds number and the entrance length were 8.093 and 5.4 mm, respectively. Since H/W = 0.14 in the current configuration, it may not fully fulfill the condition of the correlation of H/W << 1. A slightly longer L_E may be required and this estimate

provides us with the magnitude of the entrance length. Simulation of flow fields were carried out on the proposed geometries to investigate the entrance length required and the location of the construct. The final chamber design was based on the flow pattern, chamber volume and fabrication cost.

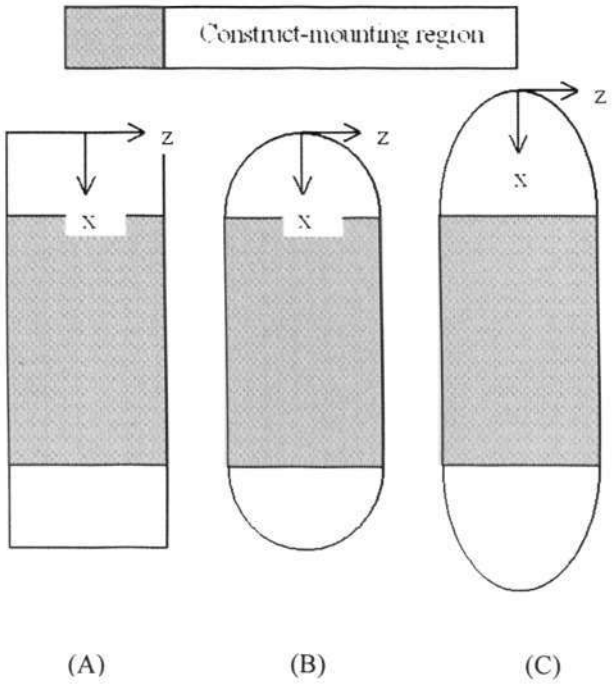

Figure 4.3: Top view of three chamber geometries studied: (A) rectangular; (B) pill shape with semi-circular entrance and exit region and (C) pill shape with semi-oval entrance and exit region. x-z coordinate was set at the entrance of the chamber. The flow fields in the grey areas were investigated for the proper location of the construct mounting

Since only the flow field was solved, the governing equations for this system only involved continuity and momentum balance for culture medium:

4.2.3 Governing equations

a. Continuity Equation (Incompressible fluid)

$$\nabla \cdot \vec{v}_\beta = 0 \qquad 4.2.3$$

b. Momentum Balance (Navier Stokes equation without external force)

$$\frac{\partial(\rho_\beta \vec{v}_\beta)}{\partial t} + \nabla \cdot (\rho_\beta \vec{v}_\beta \vec{v}_\beta) = -\nabla p_\beta + \mu_\beta \nabla^2 \vec{v}_\beta \qquad 4.2.4$$

Subscript β is used here intends to maintain the consistency in the nomenclature and does not imply the participation of other phases. Boundary conditions were given as follows.

4.2.4 Boundary conditions

To avoid abrupt change of flow condition after entering the chamber, a 2-cm tubular segment was added to the inlet and the exit of the chamber geometries in the simulation shown in Figure 4.3. The inlet of the chamber is a circular port of 1.5-mm internal diameter. A parabolic profile for circular channel was imposed to the velocity inlet (x = -0.02m):

$$v_\beta(x = -0.02\,m) = v_{max}\left(1 - \frac{y^2}{R_p{}^2} - \frac{z^2}{R_p{}^2}\right) \qquad 4.2.5$$

R_p is the radius of the inlet port with y ∈ [0, 0.0075m] and z ∈ [0, 0.0075m]. For a circular tube, maximum velocity in the profile, v_{max} is simply twice of the average velocity, v_{av}:

$$v_{max} = 2v_{av} \qquad 4.2.6$$

The outlet boundary was imposed with outflow condition with diffusive flux to be zero:

$$\nabla_n \vec{v}_\beta = 0 \qquad 4.2.7$$

This completes the problem specification.

4.2.5 Numerical solution

A 3-dimensional model was built in Gambit with mesh. Since the geometry is symmetrical in both xy- and xz-plane, only a quarter of the geometry was simulated as shown in Figure 4.4. The numerical solution was obtained by FLUENT® with the convergence criterion set at 10^{-6}. The only inputs for the simulation were the density and viscosity of medium, which were 1030 kg/m^3 and 0.7 cp, respectively, according to Carrier *et al.* [36].

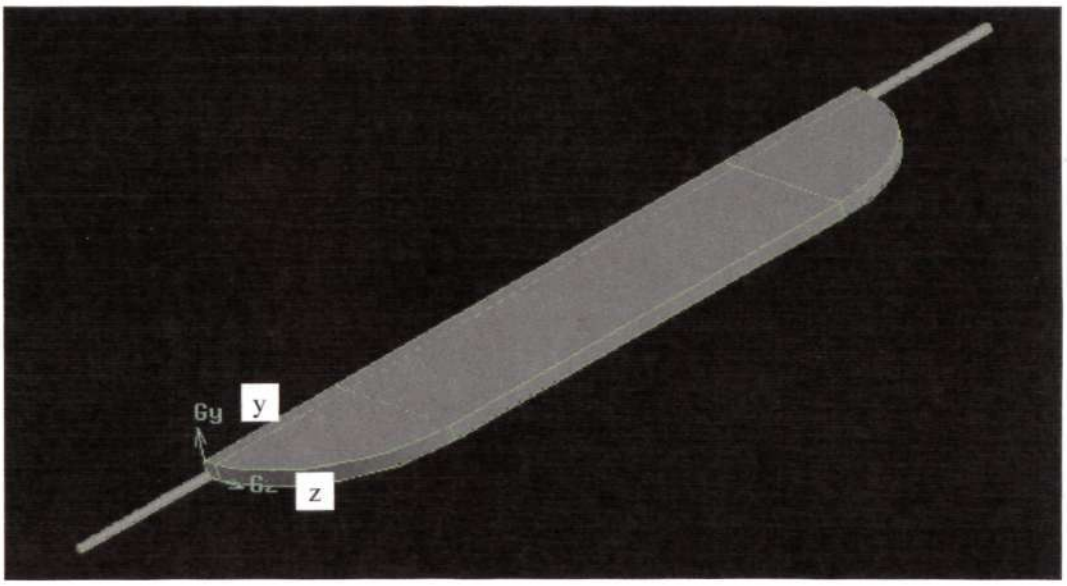

Figure 4.4: A quarter portion of pill-shaped geometry created in GAMBIT®

Chapter 5. Experimental Studies

5.1 Scaffold

5.1.1 Scaffold preparation

Materials: Gelatin derived from porcine skin (Type A, Bloom 175) and ninhydrin were purchased from Sigma-Aldrich. Liquid nitrogen (Soxal).

Equipment: Magnetic stirrer (Heidolph), water bath, freezer, freezer dryer, vacuum oven.

Procedure: 1 gram of gelatin was dissolved in deionized water to make 5 % (wt/wt) solution at 40 ^{o}C water bath for 30 minutes. The solution was then continuously stirred at 1500 rpm in room temperature for 10 minutes to foam. At 25 ^{o}C, a continuously stirred gelatin solution becomes stable foam which was then transferred to a mold made of silicone rubber followed by rapid freezing in liquid nitrogen. Frozen scaffolds were freeze-dried for at least 18 hours. Scaffolds were then crosslinked by dehydrothermal (DHT) method for 5 days at 140 ^{o}C under vacuum of 10^{-3} mmHg.

5.1.2 Scanning Electron Microscopy (SEM)

Equipment: Gold sputtering machine and Scanning electron microscope (SEM, Jeol, JSM-5600LV).

Procedure: Cross section of gelatin scaffold was gold-sputtered at 10 mA for 90 seconds under vacuum pressure between 8 and 9 psi. Microstructure of gelatin sponge was observed using scanning electron microscopy (SEM, Jeol, JSM-5600LV) at 10kV. To measure mean pore size of the scaffold, SEM micrographs of scaffold cross-

sections were converted into binary format (black and white) in ImageJ such that the pore area and scaffold area appeared in black and white, respectively. Pore size analysis was conducted using the ImageJ built-in function to measure the area in black (pore).

5.1.3 Crosslink index

Ninhydrin test was used to determine the extent of crosslinking colorimetrically [86]. Briefly, 0.35 % (wt/vol) ninhydrin in ethanol was mixed with crosslinked (n = 3) and uncrosslinked scaffolds (n = 3) and allowed to react at 70 ^{o}C for 30 minutes. Ninhydrin reacts with free amino acids to produce purple-colored product. During crosslinking, it is expected that the amount of free amino acids decrease resulting in lower degree of ninhydrin-amino acid reaction. The absorbance (Ab) of product solution was read at 460 nm in microplate reader (Tecan) and crosslink index (CL%) can be calculated using the formula below:

$$CL\% = \frac{Ab_{UNCL} - Ab_{CL}}{Ab_{CL}} \times 100\% \qquad 5.1.1$$

Ab_{UNCL} and Ab_{CL} are absorbance of non-crosslinked scaffold and cross-linked scaffold, respectively.

5.1.4 Degradation study

Crosslinked scaffolds were cut in 0.5 × 0.5 × 0.2 cm^3 pieces and soaked in culture medium (DMEM with 10 % FBS) at 37 ^{o}C for up to 14 days. The medium was changed for every 2 days. The scaffolds were weighed dry before and after soaking. The dry weight before soaking was 1.243 ± 0.215 mg. After soaking, the scaffolds

were rinsed with distilled water five times to remove medium residue before drying in convection oven (55 °C). Degree of degradation, DD% after time t (n = 3 for each time point) in culture medium can be calculated by [100]:

$$DD\% = \frac{W(t) - W_o}{W_o} \times 100\% \qquad 5.1.2$$

W_o and W(t) are dry weight of scaffold before and after soaking in medium for time t, respectively.

5.1.5 Tensile properties

The tensile properties of dry (n = 3) and wet sponges (n = 3) after 5-day DHT treatment (described in section 5.1.1) were tested by Instron tensile testing machine (Instron 5566) at room temperature. All the samples were cut according to ASTM (American Society of Testing and Materials) standard D638-03 with gauge length of 7.62 mm. A total of 6 samples were tested. For wet samples, dry sponges were pre-soaked in phosphate buffered saline (PBS) overnight before testing and kept moistened during test by spraying with PBS regularly. The sample was pulled at strain rate of 10 mm/min [83] until broken. The stress-strain relationship was obtained and ultimate tensile stress (MPa) and strain (mm/mm) were determined at the point of breaking.

5.2 Cells

5.2.1 Isolation of porcine esophageal smooth muscle cells (PESMCs)

I. Tissue collection and preparation

Materials: Dulbecco's phosphate buffered saline (DPBS), antibiotic-antimycotic solution (AAS, 100×, Sigma), kanamycin sulfate (Sigma), Dulbecco's modified eagle medium (high glucose DMEM, HyClone), fetal bovine serum (FBS, research grade, HyClone), Styrofoam box, transport medium, sterile forceps and surgical scissors and ethanol (75 %). Transport medium contains DMEM with 20 % FBS and 2 % AAS and 1mg/ml kanamycin.

Procedure: Porcine (Pig) esophageal smooth muscle cells (PESMCs) were isolated from the esophagus near the stomach where is abundant in smooth muscle cells within the muscularis externa (or outer muscle layer). Porcine esophagus was collected in local abattoir (approved by AVA, Singapore) less than half an hour after the pig was slaughtered. A 2-cm length of esophagus was dissected about one inch above the stomach and rinsed in 75 % ethanol, followed by rinsing in DPBS with 1 twice. The esophageal segment was transferred in transport medium back to the lab in ice-filled Styrofoam box. Muscularis externa was dissected from the submucosa and washed in DPBS with antibiotics three times. The muscle layer was cut into small cubes (about 2 × 2 mm^2) and two methods were employed for cell isolation.

II. Enzymatic method

Materials: 4-(2-hydroxyethyl)-1-piperazineethanesulfonic acid (HEPES, Gibco), sodium bicarbonate ($NaHCO_3$, Sigma), soya trypsin inhibitor (Gibco), Hank's Balanced salt solution (HBSS), bovine serum albumin (BSA, tissue culture tested, Sigma), collagenase type II (Sigma), papain (Sigma), tissue culture flasks (Nunc), tissue culture dish (Greinier Bio-one) hemocytometer, serological pipettes, antibiotic-AAS (100×, Sigma), kanamycin sulfate (Sigma), Dulbecco's high glucose DMEM, (HyClone), FBS (research grade, HyClone), 40-μm cell strainer (BD), 0.2-μm polypropylene filter (Satorious), sterile forceps and surgical scissors and ethanol (75 %). Complete culture medium contains DMEM with 20 % FBS (for primary culture) and 1 % AAS and 0.5 mg/ml kanamycin.

Equipment: Biosafety cabinet, 5 % CO_2 incubator and centrifuge

The tissue sample was handled in a biosafety cabinet after transfer from the abattoir. Muscle cubes were digested in 10 ml of enzyme solution containing 10 U/ml papain, 1 mg/ml collagenase II, 2 mg/ml BSA, 2 mg/ml soya trypsin inhibitor, 10 mM HEPES and 4 mM $NaHCO_3$ in HBSS. The solution was filter-sterilized by 0.2-μm polypropylene filter before use. After a 30-minute digestion, the solution was triturated with 1-ml pipetter for 10 minutes to release the cells from the extracellular matrix. After 3-minute settling, the supernatant was collected and passed through a 40-μm cell strainer. The filtrate was centrifuged at 3000 rpm for 5 minutes and the supernatant was removed and the cell pellet was resuspended in 1-ml complete medium. Suspension of PESMCs was transferred to 25-cm^2 tissue culture flasks and 4-ml

complete medium was added. This culture was considered passage 0 (or p0). Medium was changed the next day and every other day after that. Cells were cultured in 5 % CO_2 incubator at 37 ^{o}C for 10 days to reach confluence. The confluent culture was then subcultured.

III. Explant method

Muscle cubes were distributed evenly on tissue culture dish (about 5 cubes/10 cm^2) and allowed attachment on the dish surface by drying them with the dish open in the biosafety cabinet for one hour. One to two drops of complete medium were then added onto each cube and the culture dish was transferred to 5 % CO_2 incubator at 37 ^{o}C. On the next day, any detached muscle cube or contamination was checked. Contaminated culture was discarded immediately. Any detached muscle cube was removed from the culture dish by sterile forceps and a thin layer of medium was added just enough to partially submerge the cubes. Medium was then changed for every 3 days. About 10-12 days, cells started migrating from the muscle cubes. 2 days after the first sign of cell migration, the muscle cubes were removed carefully by sterile forceps and cells were subcultured once the culture reached confluency.

IV. Subculture

Subculture or passage of cells is a routine operation to expand mammalian cells. Once cells grow and fully occupy the area in the culture dish or flask, the cell culture is considered to reach confluency. Upon confluency, cells can be detached from the culture dish by the enzyme trypsin. This process is also called trypsinization. Trypsin

was then deactivated and the resulting cell suspension was centrifuged. Finally, cells were counted and seeded to new culture dishes or flasks for further culture. This process is called subculture. The passage number of the new culture is increased by 1 each time this process is carried out.

Materials: Tissue culture flasks (Nunc), Trypan blue solution (Sigma), hemoctyometer, serological pipettes, AAS (100×, Sigma), kanamycin sulfate (Sigma), high glucose DMEM (HyClone), FBS (research grade, HyClone), 0.25 % trypsin/EDTA (ethylenediaminetetraacetic acid) solution (Sigma) and ethanol (75 %). Complete culture medium contains DMEM 10 % FBS and 1 % AAS and 0.5 mg/ml kanamycin.

Equipment: Biosafety cabinet, 5 % CO_2 incubator and centrifuge.

Procedure: Once PESMCs at p0 were confluent, cells were washed with sterile PBS three times. Cells were then incubated in 0.25 % trypsin/EDTA solution for 3-5 minutes at 37 ^{o}C. Cells were checked under the inverted microscope for detachment. Since trypsin is a strong protein enzyme, overexposure of cells to trypsin (more than 5 minutes) is not advisable due to digestion of cell surface proteins which would damage the cells. To deactivate trypsin activity in practice, 1 part of trypsin solution was neutralized with 1 part of complete medium in which serum contains trypsin inhibitor. The cell suspension was triturated repeatedly using a sterile serological pipette against the culture surface to dislodge the undetached cells. The suspension was then collected in a sterile centrifuge tube and centrifuged for 3,000 rpm for 5 minutes to pack the cells into pellet form at the bottom of the tube due to cell density.

The supernatant was removed carefully without disturbing the cell pellet. Next, 1 ml of complete medium was added and mixed gently by a 1-ml pipettor. A sample of cell suspension (2-10 μl) was mixed with trypan blue in the ratio ranged from 1:9 to 1:1 and 10-μl of the mixture was injected into the hemocytometer. Under the inverted microscope, the live cells were reflective while the dead cells were appeared blue due to infiltration of the dye through damaged cell membrane. With the aid of the grids in the hemocytometer, the number of live cells in the cell suspension could be estimated. Cells were re-seeded into new tissue culture flasks at 10,000 cells/cm^2 and reached confluency after 5 days. The subculture process was repeated whenever the cells were confluent and the passage number was conventionally increased by one after one subculture. Immunocytochemisty and cell proliferation assays were conducted on PESMCs at p1, p3, p5 and p7 to confirm cell identity and examine cell proliferation state over serial subculture, respectively. Furthermore, compatibility of the scaffold with PESMCs was carried out.

a. Immunocytochemistry

Materials: Trypan blue solution (Sigma), hemoctyometer, tissue culture dishes (35-mm diameter, Grenier Bio-one), complete medium, PBS, 0.25 % trypsin/EDTA solution (Sigma), methanol (stored at -30 ^{o}C), serological pipettes, Tween 20 (Sigma), goat serum (DAKO), monoclonal mouse anti-human smooth muscle alpha actin (Clone 1A4, DAKO), mouse immunogloblulin-1 (IgG_1, DAKO), ImmunoCruz^{TM} staining system for mouse (Santa Cruz Biotechnology, Inc.), Gill's No.2 hematoxylin, gelatin (pig skin, Bloom 300, Sigma), and glass coverslip (No.1). Washing buffer contains 0.05 % Tween 20 in PBS. ImmunoCruz^{TM} staining system included detection reagents

(biotinylated goat anti-mouse IgG, streptavidin-horseradish (streptavidin-HRP), 3,3'-diaminobenzidine (DAB), hydrogen peroxide and substrate buffer). Gelatin mounting medium was made up with 1 % (wt/vol) gelatin in deionized water.

Equipment: Biosafety cabinet, 5 % CO_2 incubator, centrifuge and light microscope (Axioskop 4, Carl Zesis)

Procedure: Cells at p1, p3, p5 and p7 were stained for alpha-smooth muscle actin to confirm cell identity. A 3-step indirect immunostaining method was used. PESMCs were seeded at 10,000 cells/cm^2 on a 35-mm tissue culture dish and allowed to attach for 1 to 2 days. Cells were then washed in sterile PBS three times, fixed in cold methanol (-20 ^{o}C) for 10 minutes and washed with PBS three times. To avoid antibody from binding with other cellular antigens, non-specific binding sites were blocked by a serum block solution consisting of 2 % goat serum (vol/vol) for 30 minutes. Monoclonal mouse anti-human alpha-smooth muscle actin antobody (DAKO) was diluted at 1:500 with primary antibody diluent and incubated with fixed cells for 1 hour at room temperature. Concurrently, a separate cell sample was incubated with mouse IgG_1 diluted in the same ratio as the primary antibody to serve as negative control. It is important to establish a negative control to avoid false positive results. The cells were then washed three times with washing buffer for 10 minutes.

Secondary antibody, biotinylated goat anti-mouse IgG (diluted at 1:500) was then added and incubated for 1 hour to bind with primary antibody. Samples were washed again three times with washing buffer for 10 minutes. Since the secondary antibody was conjugated with biotin (i.e., biotinylated), biotin-avidin link could be used as the

detection system for the antigen. Streptavidin-HRP was then added on the sample for 30 minutes to link with biotinylated secondary antibody followed by washing steps. Finally, DAB was added and HRP catalyses conversion of DAB to a brown-colored product with hydrogen peroxide as the substrate. The color was allowed to develop for 5 minutes before washing with deionized water twice for 2 minutes.

The cells were then counterstained with Gill's Hematoxylin for 5 minutes and washed with deionized water twice. A few drops of gelatin mounting medium were then applied on the cells and a round-shaped glass coverslip was overlaid on the mounting medium. Pressure was applied on the coverslip to spread the mounting medium evenly beneath the coverslip. After air-drying, cells were observed under light microscope. The actin filaments inside any cell that were stained in brown confirmed the presence of smooth muscle actin and its cell identity as smooth muscle cell. This can be further confirmed with the negative control which should show little or no stain.

b. Proliferation assay

Materials: Complete medium, PBS, 0.25 % trypsin/EDTA solution (Sigma), trypan blue solution (Sigma), hemoctyometer, MTS assay kit (CellTiter 96® Aqueous One Solution Cell Proliferation Assay, Promega), 24-well plate and 96-well microplate.

Equipment: Biosafety cabinet, 5 % CO_2 incubator, centrifuge and microplate reader (Ultra Evolution, Tecan).

Procedure: Cell proliferation of PESMCs derived from both isolation methods were tested at alternate passage (p1, p3, p5 and p7). After subculture, cells were seeded at 10,000 cells/cm^2 in 24-well microplate (n = 12 for each group). Medium was changed

every 2 days. At day 1, 3, 5 and 7, cell viability of cells (n = 3 from each group at each time point) were measured using the MTS assay kit according to manufacturer instructions. Briefly, 40 µl of MTS solution was mixed with 200 µl of culture medium and the mixture was then added into each well. The mixture was incubated with the cells for 2 hours in 5 % CO_2 incubator at 37 ^{o}C and colour was developed in the presence of viable cells. Absorbance at 490 nm in the product solution is proportional to the number of viable cells. A 100 µl sample of product solution was transferred into 96-well microplate and the absorbance was measured by microplate reader (Tecan) at wavelength of 492 nm. Cell Proliferation state over time at specific passage was observed by plotting absorbance at 492 nm against time.

V. Cell-scaffold Cytocompatibility test

Materials: Complete medium, PBS, 0.25 % trypsin/EDTA solution (Sigma), trypan blue solution (Sigma), hemoctyometer, Petri dish (35-mm diameter, Greinier Bio-one) and porous gelatin scaffold.

Equipment: Biosafety cabinet, 5 % CO_2 incubator and centrifuge.

The gelatin scaffold was sterilized in 70 % ethanol for 15 minutes followed by washes in sterile PBS three times for 15 minutes. PESMCs at p4 were used in the cytocompability experiment. Approximately 1 million cells per cm^3 scaffold were seeded onto 1 × 1 × 0.2 cm^3 gelatin scaffold placed in Petri dish. After 0, 1, 3, 5, 7 and 14 days, the seeded scaffolds were harvested for DNA quantification and histology (hematoxylin and eosin) were conducted on day 3, 7 and 14.

a. DNA quantification

Materials: Papain (Sigma), PBS, cysteine (Sigma), disodium ethylenediaminetetraacetate (Na_2EDTA, Fisher Scientific), 0.2-μm polypropylene filter (Satorious), Deoxyribonnuclease I (DNase I, Sigma), magnesium chloride ($MgCl_2.6H_20$, Sigma), Hoechst 33258 (Sigma), Tris-EDTA buffer (100×, pH 8.0, Sigma), sodium chloride (NaCl, Pancreac), white 96-well microplate (Greinier Bio-one) and calf thymus DNA (Sigma).

Equipment: Freezer dryer (Christ) and microplate reader (Tecan, Genios).

Procedure: DNA quantification of the construct followed the method given in [195]. Briefly, seeded or unseeded scaffolds at different harvest times (n = 3 each time) was freeze-dried and digested in papain (125 μg/ml) in PBS, pH 6.0 containing 5 mM cysteine and 5 mM Na_2EDTA. Enzyme solution was filter-sterilized with a 0.2-μm polypropylene filter. After papain digestion, further treatment was conducted: (A) One volume of papain-digested sample was mixed with one volume of DNase I (100 μg/ml in PBS with 125 mM $MgCl_2$, pH 7.0) and 1 volume of PBS; (B) One volume of papain-digested sample was mixed with 2 volumes of PBS. Both (A) and (B) were incubated at 37 ^{o}C for 1 hour. (A) and (B) were diluted 1:10 in 0.1 μg/ml Hoechst 33258 in 1× Tris-EDTA buffer containing 0.1 mM NaCl (pH 7.4). A 200 μl of sample was transferred to a white 96-well microplate which was read by microplate reader at excitation/emission wavelength of 365/460 nm. DNA digested by DNase I in (A) was served as sample background. The net fluorescence enhanced by Hoechst-DNA complex in the sample was calculated by the difference of Fluor unit of (B) and Fluor

unit of (A). A DNA standard from calf thymus DNA was prepared (0, 0.02, 0.05, 0.2, 0.5 and 2 μg) to establish a standard curve to correlate between fluorescence enhancement and DNA content such that DNA content (in ng DNA/scaffold) in the seeded scaffold was estimated. An unseeded scaffold cultured and treated in a similar way served as the negative control.

b. Histology

Materials: Glutaraldehyde (40 % in water, Sigma) PBS, Optimal Cutting Temperature (OCT) freezing compound (Leica), hematoxylin and eosin Y.

Equipment: -86 ^{o}C deep freezer (NuAir) and cryostat microtome (Leica) and light microscope (Olympus)

Procedure: The harvested sample was washed with PBS three times and fixed with 2.5 % glutaraldehyde in PBS, pH 7.4, for 10 minutes followed by rapidly freezing in OCT freezing compound at -80 ^{o}C. The frozen sample was cut into 5-μm thick sections in cryostat (Leica) at -18 ^{o}C. Each section was then air-dried in room temperature overnight and rehydrated in deionized water for 5 minute. The section was first stained with Weigert haematoxylin solution for cell nuclei. The stained section was washed in running tap water for 5 minutes followed by deionized water wash for 1 minute. It was then counterstained by 5 dips in eosin solution for ECM and cytoplasm. The excess eosin solution was rinsed in 1 dip of deionized water and ethanol for 5 minutes. The stained section was air-dried overnight without coverslipping and observed under light microscope. Under the microscope, the gelatin scaffold was stained in pink while cytoplasm and cell nucleus appeared purplish and bluish, respectively.

5.2.2 Adaptation of cell culture in air environment

I. Conditioned medium makeup

Materials: Tissue culture dish (10-cm diameter, Iwaki), powdered DMEM (high glucose and no bicarbonate, Gibco), $NaHCO_3$ (Gibco), deionized water (with resistivity = 18.2 MΩ.cm that complies ASTM D1193), 0.2-μm filter unit (Nalgene), HEPES (1M, Gibco), AAS (100×, Sigma), kanamycin sulfate (Sigma), FBS (research grade, HyClone), PBS, 0.25 % trypsin/EDTA solution (Sigma), trypan blue solution (Sigma) and hemocytometer (Marienfeld).

Equipment: Biosafety cabinet, incubation unit (IU), pH meter (Fisher Scientific), freezing point depression osmometer (Wescor 5500) and deionized water system (ELGA, Maxima)

In order to adapt PESMCs to normal air (containing about 0.03 % CO_2 compared with 5 % in conventional incubator), which is required for the bioreactor system, PESMCs were cultured using conditioned DMEM to maintain pH and osmolality in the incubation unit used for bioreactor culture (see section 5.3.2). Powdered DMEM without bicarbonate (Invitrogen) was reconstituted in deionized water and buffered with $NaHCO_3$ and HEPES. Since no literature documented the required amount for DMEM, 4mM $NaHCO_3$ and 10mM HEPES buffer for Eagle's balanced salt solution used in normal air [1] was taken as a starting point. The pH was measured on day 2 and day 10 after incubation in IU (n = 3 for each time). The osmolality of medium was measured using an osmometer based on freeze point depression (n = 3). With this buffer combination, the osmolality was lower than the original formula. Therefore,

extra sodium chloride (NaCl) was added to increase the osmolality to be comparable to normal DMEM (336 mOsm/kg). The osmolality-adjusted medium was sterile-filtered through a 0.2-μm filter and a 4 ml of medium from each batch was incubated in the culture condition to check its sterility and pH. When PESMCs reached confluent at p2 in CO_2-supplemented culture, subculture was carried out and 1 million cells were transferred into a 10-cm tissue culture dish. After that, cells were cultured either in normal air using the conditioned DMEM described above (n = 3) or CO_2 incubator using normal DMEM (n = 3). The cell morphology was observed and the doubling times were compared between both culture environments for 4 passages.

II. Growth characteristics of PESMCs in air culture at high/low glucose environment

In order to obtain cell physiological data to understand cell growth and nutrient requirements in cells incubated under normal air conditions, cell culture experiments were conducted at high (4.5 g/L) and low (1 g/L) glucose concentrations to investigate the effect of glucose concentration on oxygen requirement, glucose utilization and growth rate. These data were used as model parameters for the mathematical model established in section 4.1.

Materials: 24-well plate (Greinier Bio-one), Conditional high glucose DMEM (refer to section 5.2.2(I) for the preparation), conditioned low glucose DMEM, antibiotic-antimycotic solution (100×, Sigma), kanamycin sulfate (10 mg/ml, Sigma), PBS, 0.25 % trypsin/EDTA solution (Sigma), trypan blue solution (Sigma), hemoctyometer. Conditional low glucose DMEM was prepared from powdered low glucose DMEM

(without bicarbonate) using similar method described in section 5.2.2(I). Complete conditioned medium was made up by low or high glucose conditioned DMEM with 10 % FBS and 1× AAS and 0.5 % kanamycin.

Equipment: pH meter, biosafety cabinet, centrifuge and incubation unit.

Procedure: PESMCs at p5 were grown on 24-well plate at 10,000 cells/well in either high (4.5 g/L) (n = 18) or low (1 g/L) (n = 18) glucose environment. Upon seeding, 1-ml medium from each group was added to each well and the cells were allowed to attach for 24 hours. At hour 24 (day 1), the medium from each group (n = 3) was collected and replaced with fresh culture medium. Glucose concentration of the collected medium was determined by Glucose (Hexokinase or HK) assay kit. Approximately 3 hours later after the fresh medium was added, the oxygen profile from the medium surface to the bottom of the well (on which the cells were grown) was measured using an oxygen micronsensor. After oxygen measurement, the cells in the well were harvested and the DNA content was quantified for correlation with cell number. This procedure was repeated every 24 hours until day 6 (144 hour). Using data extracted from this experiment, cell growth rate, glucose consumption rate and respiration rate (oxygen consumption rate) were estimated.

a. O_2 requirement of PESMCs

Equipment: Oxygen microsensor system (Unisense) and incubation unit.

Procedure: Microsensor was calibrated in both de-oxygenated and oxygen-saturated medium before use (see 5.3.4II) for detailed calibration method). Before measurement, the lid of a 24-well plate was replaced by another lid with holes of 2-mm diameter pre-

made at the centre of each well location. The location of the microsensor was manually adjusted near the level of the lid and slowly targeted the centre of the hole. The sensor was moved down slowly at a controlled speed of 0.2 mm/s by motorized manipulator. Once the sensor reached the medium surface, a sharp drop of oxygen was noticeable and this point was defined as "depth = 0". The measurement was taken moving downward at every 100 μm downward until reaching the bottom (depth = 4000 μm). The oxygen measurements were taken in three separate wells for each group.

To estimate the respiration rate (oxygen consumption rate) of PESMCs using obtained data, a pseudo steady state 1-dimensioanl mass balance was solved for the oxygen concentration field to correlate with the oxygen consumption rate. For a static system, shown in Figure 5.1, the mass balance of oxygen can be written:

$$D_{O,\beta}\frac{d^2C_{O,\beta}}{dz^2}=0 \qquad \textbf{5.2.1}$$

where $D_{O,\beta}$ is the diffusion coefficient (m^2/s) of oxygen in culture medium, $C_{O,\beta}$ is the dissolved oxygen concentration in the medium (mol/m^3) and z is the direction perpendicular to the medium surface as seen in Figure 5.1.

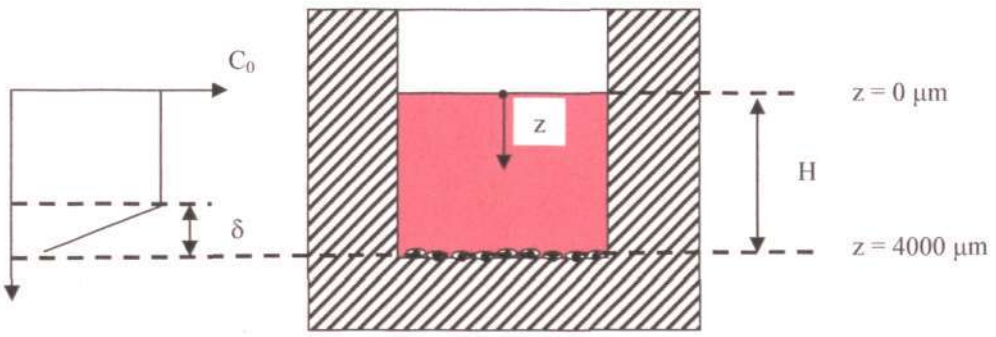

Figure 5.1: static culture of PESMCs in a well of 24-well plate. 2-ml of medium was added to register a medium height of 4 mm. Oxygen profiling was carried out from z = 0 to z = 4000 μm.

Equation 5.2.1 was solved with two boundary conditions at z = H - δ with known concentration C_0, and at the cell surface (or well bottom, z = H) with surface reaction (i.e., oxygen consumption):

$$C_{O,\beta}(H-\delta) = C_0 \qquad 5.2.2$$

$$-D_{O,\beta}\left.\frac{dC_{O,\beta}}{dz}\right|_{z=H} = \frac{r_{max,O}V_c C_{O,\beta}(H)}{C_{O,\beta}(H)+K_{M,O}}N_\sigma = R'_O \qquad 5.2.3$$

In equation 5.2.3, V_c is the volume of a single cell (m^3) while $r_{max,O}$ and $K_{M,O}$ are the maximum oxygen consumption rate and half saturation constant defined in equation 4.1.11, respectively. N_σ refers to the number of cells per culture area. R'_O is defined as the oxygen consumption flux (kg/m^2s) at z = H. The solution of equation 5.2.3 is valid within the boundary layer is simply:

$$C_{O,\beta}(z) = C_0 + R'_O[z-(H-\delta)] \qquad H-\delta \le z \le H \qquad 5.2.4$$

$$\text{or } R'_O = \frac{C_{O,\beta}(z) - C_0}{z - (H - \delta)} \qquad 5.2.5$$

$$\text{At } z = H,\ R'_O = \frac{C_{O,\beta}(H) - C_0}{\delta} \qquad 5.2.6$$

The boundary thickness (δ) and dissolved oxygen at the well bottom or $C_{O,\beta}(H)$ varied due to the changing oxygen demands from the cells. Due to a limitation of resources, the culture was only carried out under normal oxygen composition (21 %). The experiment results showed that there was only a 6 % difference in $C_{O,\beta}(H)$ when cells were cultured at the 1 g/L (low) and the 4.5 g/L (high) glucose levels, which suggests a weak dependence of $C_{O,\beta}(H)$ on the glucose level; and it is at least true when the glucose is still abundant in the medium. Therefore, the $C_{O,\beta}(H)$ was assumed to be constant. The only unknowns in equation 5.2.3 are now R'_O and N_σ.

In order to calculate the consumption parameters ($r_{max,O}$ and $K_{M,O}$). First, the expression of R'_O in equation 5.2.3 is rearranged to give:

$$-\log(R'_O) = -\log(N_\sigma) - \log\left(\frac{r_{max,O} V_c C_{O,\beta}(H)}{C_{O,\beta}(H) + K_{M,O}}\right) \qquad 5.2.7$$

Then, $-\log(R'_O)$ was plotted against $-\log(N_\sigma)$, which produced an intercept ($-\log\left(\frac{r_{max,O} V_c C_{O,\beta}(H)}{C_{O,\beta}(H) + K_{M,O}}\right)$). Since there are two unknowns ($r_{max,O}$ and $K_{M,O}$) to be solved, two equations (arisen from two intercepts at two glucose levels) were solved simultaneously.

b. Growth rate

To estimate cell growth rate, cells were harvested from 3 wells on each day (n = 3). Cells were lyzed and cellular DNA was isolated and purified. DNA content was measured and was proportional to the cell number present in the well. The data was used to estimate the parameters in the growth model established in Chapter 4.

Materials: 2-ml polypropylene microcentrifuge tube (Greinier Bio-one), black 96-well microplate (Greinier Bio-one), sodium dodecyl sulfate (SDS, Sigma), Tris-base (USBiological), protease K (10 mg/ml, Qiagen) phenol-chloroform-isoamyl alcohol (25:24:1) (Molecular Probes), 7.5 M ammonium acetate (Sigma), PicoGreen$^{(R)}$ (Molecular Probe, Invitrogen), ethanol (>99 %, non-denatured, Sigma).

Equipment: Pipetter, biosafety cabinet, fume hood, microcentrifuge, orbit shaker (Heidolph), concentrator and microplate reader (Tecan Evolution)

Procedure:

Cell Lysis: Cells on each well were added with 100 µl PBS and 100 µl lysis buffer. After mixing with the cells, 10 µl of protease K (10 mg/ml) was added and the cells were lyzed in 37 ^{o}C overnight. The next day, lyzed cells were collected in a 2-ml microcentrifuge tube. To clean up the residue cells in the well, 100 µl of PBS followed by 200 µl of lysis buffer were added and the rinses were also collected in the same tube. The collected suspension was further digested in 55 ^{o}C for 1 hour. Following these steps, the nucleic acid should be free from the nucleic protein.

DNA isolation and purification: The downstream purification was carried out to separate DNA from cellular proteins. The digest was first mixed with equal volume (500 µl) of phenol/chloroform/isoamyl alcohol (25:24:1) solution. The mixture was then shaken for 20 minutes at room temperature followed by centrifuge at 13,000 rpm for 20 minutes. The supernatant (aqueous phase) was collected carefully and transferred to a new 2-ml microcentrifuge tube (about 500 µl). It was further centrifuged at 13,000 rpm for 10 minutes. Half of the volume (250 µl) was transferred to a new 2-ml microcentrifuge tube for high quality DNA. 250 µl of 7.5 M ammonium acetate was added to neutralize the charge of the nucleic acid followed by adding 1.25 ml of cold 95 % ethanol to precipitate DNA by dehydration. To facilitate DNA precipitation, the sample was kept in -30 ^{o}C for at least 1 hour. The precipitated DNA sample was then centrifuged at 7,000 rpm for 15 minutes and the supernatant (including acetate and ethanol) was poured off. The DNA sample was washed with 70 % ethanol followed by centrifuged at 7,000 rpm for 15 minutes. The ethanol was poured off and the DNA was dried in concentrator under vacuum for 20 minutes. The dried DNA was re-dissolved in 100 µl of TE buffer at 55 ^{o}C for 1 hour. The sample was kept at 4 ^{o}C for temporary storage.

DNA quantification: DNA quantification was carried out using PicoGreen® kit. DNA sample was diluted with Tris/EDTA buffer in 1:50 or 1:100 and DNA standards with known concentration (provided in the kit) was prepared at 0, 1, 10, 100 and 1000 ng/ml. Both diluted samples and standards were mixed with PicoGreen® dye in 1:1 ratio. After mixing with the dye, 200-µl solution from each sample and standard was added to 96-well microplate. The fluorescence enhancement of the DNA-dye complex

was measured using a microplate reader at excitation/emission wavelength of 485/535nm. A standard curve of DNA can be drawn (Fluorescence unit vs. DNA concentration) with the trend line equation which was used to determine unknown DNA amount in the samples. Based on DNA content per PESMC determined previously, cell number in each well was estimated.

Estimation of growth rate: The cell growth model equation 4.1.12 is required to estimate cell growth rate and growth parameters:

$$R_\sigma = \frac{d\rho_\sigma}{dt} = r_{\sigma,max}\left[\frac{C_{O,\sigma}}{C_{O,\sigma} + K_C\rho_\sigma}\right]\rho_\sigma \qquad 5.2.8$$

Since the cell monolayer grew on a flat culture plate rather than in 3-D scaffold, a 2-dimensional version was written for cell number per area (N_σ):

$$R'_\sigma = \frac{dN_\sigma}{dt} = r_{\sigma,max}\left[\frac{C_{O,\beta}(H)}{C_{O,\beta}(H) + K'_C N_\sigma}\right]N_\sigma \qquad 5.2.9$$

It was assumed the maximum specific growth rate (s^{-1}) was unchanged for cell growth on a 2-D substrate or a 3-D scaffold. It is noted that $C_{O,\sigma}$ was converted to $C_{O,\beta}(0)$ in 2-D version because it was assumed that oxygen transport resistance through the cell membrane is negligible [18]. Therefore, oxygen concentration at the well bottom was assumed to be similar to that in cells. The Contois constant in 2-D (K'_C) has the unit of kg O_2/m.cell while its counterpart in 3-D (K_C) has different unit (kg O_2/m^3.kg cells). Therefore, a correlation was made to connect K_C and K'_C for dimension consistency:

$$K'_C = m_c\left(\frac{A_w}{V'_{\sigma,max}}\right)K_C \qquad 5.2.10$$

m_c, A_w, $V'_{\sigma,max}$ are the mass of a single cell, well bottom area and maximum allowable volume occupied by PESMCs in monolayer culture. By reciprocating equation 4.1.9 with re-arrangement, a linear relationship between $1/R'_\sigma$, $1/N_\sigma$ and $1/C_{O,\beta}$ was written as follow:

$$\frac{1}{R'_\sigma} = \frac{1}{r_{\sigma,max}}\left(\frac{1}{N_\sigma}\right) + \frac{K'_C}{r_{\sigma,max}C_{O,\beta}(H)} \qquad 5.2.11$$

In order to apply this equation to calculate the growth parameters ($r_{\sigma,max}$ and K'_C), N_σ was first plotted against time and the estimation of the instantaneous gradient of the curve using a spline approximation resulted in R'_σ. To obtain growth parameters, a similar constant $C_{O,\beta}(H)$ assumption was made as in oxygen consumption Then $1/R'_\sigma$ was plotted against corresponding $1/N_\sigma$. The plot was provided with linear regression of the data and the gradient ($\frac{1}{r_{\sigma,max}}$) and intercept ($\frac{K'_C}{r_{\sigma,max}C_{O,\beta}(H)}$) were used to estimate $r_{\sigma,max}$ and K'_C.

III. Determination of Glucose concentration

Materials: 2-ml polypropylene microcentrifuge tube (Greinier Bio-one), 96-well microplate (Greinier Bio-one), Glucose (HK) assay kit (Sigma), hydrochloric acid (HCl, 37 %, Pancreac)

Equipment: Pipetter, biosafety cabinet, 37 °C incubator (Sanyo) and microplate reader (Tecan Evolution)

Procedure: Each day, 1 ml of culture medium was removed from the culture and collected in a microcentrifuge tube. A glucose (HK) assay kit was used for this analysis and adapted for microplate reader instead of spectrophotometer. The reagent (consisting of hexokinase) was mixed with 20 ml of sterile distilled water as instructed in the manual. Since the culture medium contains phenol red as a pH indicator, which is commonly known to interfere the assay, the medium was pre-treated with 1N HCl in medium-to-HCl ratio of 100:1 to change the pH to around 4 estimated using pH indicator stick (i.e., medium color changed from red to pale yellow). It was hoped that the de-colorization could reduce or eliminate the interference.

A comparative study was first conducted between control medium (red color) and pH-adjusted medium (pale yellow color). A calibrated glucose solution (1 mg/ml) provided in the assay kit was used to set up standards (0, 0.01, 0.05, 0.1 and 0.25 mg/ml) and PBS containing the identical amount of phenol red as in DMEM (0.0159g/L) was used as diluent. The standards were either pH-adjusted or pH-unadjusted and 5 µl of standards from both groups were mixed with 500 µl of reagent solution. The mixture was incubated in water bath at 37 ^{o}C for 15 minutes. In this assay, glucose is first phosphrylated by ATP in the presence of hexokinase followed by conversion of phosphrylated glucose (glucose-6-phosphate) and nicotinamide adenine dinucleotide (NAD+) to 6-phosphogluconate and NADH (reduced form of NAD+) with glucose-6-phosphate dehydrogenase as catalyst.

The absorbance at 340 nm in the product solution is directly proportional to glucose concentration. A 150 µl sample of the solution was transferred to a transparent 96-well microplate and the absorbance of solution was measured by microplate reader (Tecan)

at wavelength of 340nm. It was found that medium without the pH adjustment reduced the absorbance and that the standard curve was not in a good fit. On the other hand, the pH-adjusted medium resulted in better sensitivity and an almost perfect linear curve fit. Therefore, glucose analysis was carried out on the medium after pH adjustment. A similar method was used to determine glucose concentration in the medium samples when they were then calculated (in mg/ml) using the standard curve.

IV. Measurement of cell size and cell mass

a. Cell size

In cell culture, cell size is difficult to estimate because the aspect ratio is large (length compared to cell width and thickness) when cells attach to the substrate. In order to facilitate the determination of cell size of PESMCs, cell size was estimated when they are in unattached (round-up) form which is close to spherical shape. It was assumed that unattached and attached cells are similar in size although they adopt different morphologies.

Materials: PBS, complete medium, 0.25 % trypsin/EDTA solution (Sigma), hemoctyometer.

Equipment: Biosafety cabinet, pipetters, centrifuge and microcentrifuge.

A PESMC suspension after trypsinization (refer to section 5.2.1(IV) for details on trypsinization) was made in 4 ml of PBS. A 10 μl aliquot of cell sample was injected into hemocytometer. Micrographs were taken outside the grid area at 40× with scale bar shown Figure 5.2A. The micrograph was opened in image software, ImageJ. The

local length scale was set based on the scale bar in the micrograph. A clean-up of image was carried out to remove the scale bar, unfocused spots, dead cells, or cells crossing the micrograph boundary (Figure 5.2B). The micrograph was then converted to an 8-bit black and white micrograph (Figure 5.2C). In this image, the black area represents the cell area which was measured by the built-in "particle analysis" function to measure cell area (mm^2) and the total of 301 cells was counted. A histogram was plotted for the cell area distribution and the mean cell area (± SD) was determined. By assuming that the cells were spherical particles, the cell radius and the cell volume were calculated.

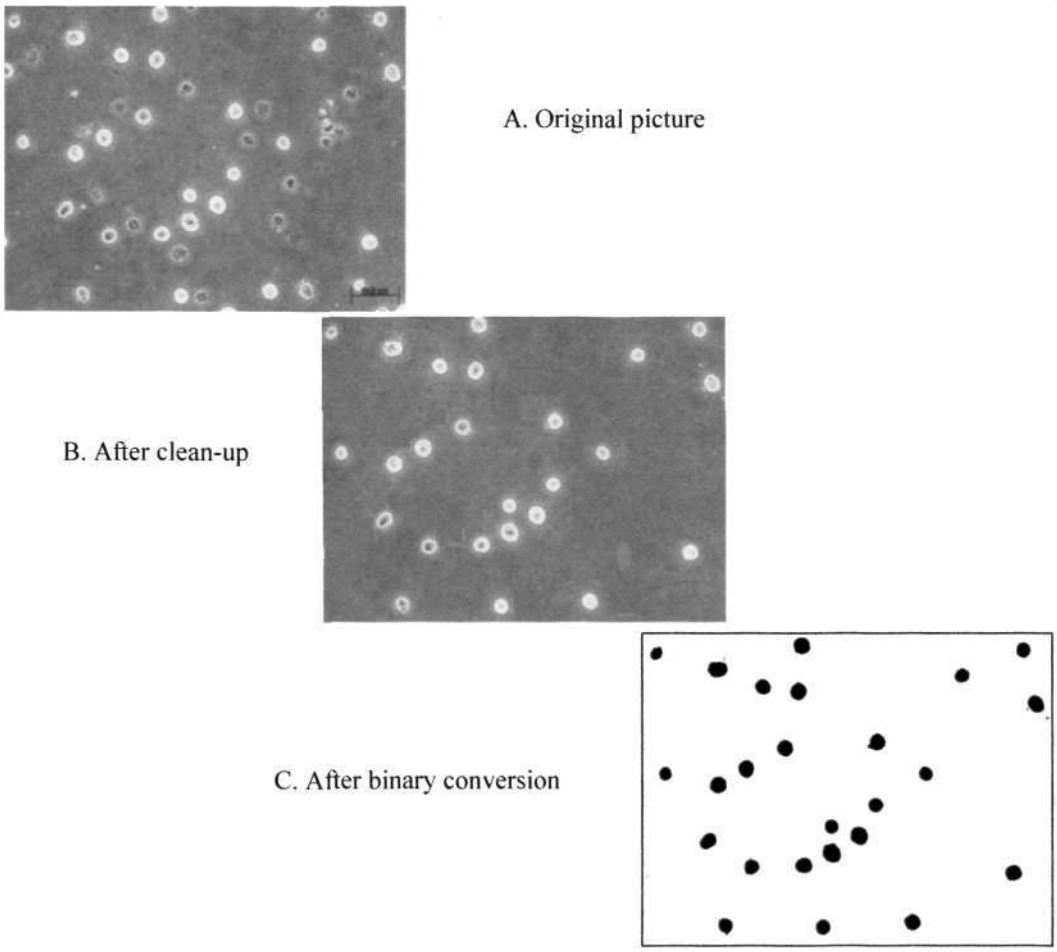

Figure 5.2: Image convesion process in Image J for cell size estimation: (A) the original micrograph was open in Image J; (B) All the dead cells, unfocused points and cells crossing the border were cleaned up; (C) Binary conversion of the micrograph into 8-bit picture led black and white differentiation between cells and background.

b. Cell mass

Materials: 1.5-ml microcentrifuge tube (Greinier Bio-one), PBS, complete medium, 0.25 % trypsin/EDTA solution (Sigma), hemocytometer, concentrator and electronic balance.

Equipment: Biosafety cabinet, pipetters, centrifuge and microcentrifuge.

Cell density of PESMCs suspension used in cell size measurement was determined using hemocytometer. Samples containing 25,000, 50,000, 75,000 and 1 million cells (n = 3 for each cell number) were transferred in 2-ml pre-weighed microcentrifuge tubes in triplicates. Cells were centrifuged in a microcentrifuge at 10,000 rpm for 5 minutes to form a compact cell pellet. The supernatant was decanted and the tube interior was blotted dry by a cotton bud (or swab) without touching the cell pellet at the bottom. The cell samples were briefly dried in a concentrator at vacuum for 1 minute to remove moisture from the tube. The samples (cells + tube) were weighed and the cell mass of specific cell number was estimated by subtracting the mass of the sample (cells + tube) from the mass of tube alone. Cell mass was plotted against cell number and a linear fit was used to obtain cell mass per cell (i.e. gradient in mg). With the data of cell mass and cell volume, density of a single PESMC was also determined (= cell mass/cell volume).

5.3 Bioreactor

5.3.1 Concept of Bioreactor System

Most of the mammalian cell and tissue cultures, including bioreactor operations, are carried out in a conventional CO_2 incubator, which is operated nominally at 37 ^{o}C for normal cell physiology, humidified to avoid the culture from drying out and more importantly, supplemented with CO_2 (mostly 5 %) to support the pH buffer system (CO_2/sodium bicarbonate) in the culture medium. This environment works well for cell culture in culture dishes or flasks that are designed with ventilation for gas exchange and humidification. For bioreactor operation, however, a closed system is important especially for bioreactors involving medium flow to avoid any leakage from

the system. For this case, humidification is not required and gas exchange can always be facilitated by oxygenator or medical grade gas-permeable silicone tubing with sufficient length. A closed system also ensures higher level of sterilization. On the other hand, some bioreactor operations require extra set-ups or accessories or auxiliary equipment, which are not compatible with the standard incubator due to the space limitation and sensitivity of specialized equipment to the warm and humid environment. Although a custom-made incubator can be made to meet all the needs of different systems (such as access ports for tubing and metabolic sensors), but an extra cost is incurred.

There are commercial fermentators and bioreactors (e.g., Biostat from B. Braun Biotech. Inc.) available for algae cultivation and suspension culture that operate outside an incubator with controls for pH, temperature and dissolved gas compositions. It appears that tissue culture can also be carried out independent of the CO_2 incubator provided that important culture parameters (nutrients, gas exchange, pH and temperature) are maintained at normal physiological levels. In tissue engineering and biomaterial testing, Minucells and Minutissue Vertriebs GMBH founded by Professor Will W. Minuth has produced a series of mini-scale perfusion chambers that can run on a benchtop. This new design expands the concept of operation for a tissue engineering bioreactor from the conventional incubator to the benchtop with a concomitant (e.g., monitoring equipment) to increase in the flexibility of the bioreactor operation.

Since gas exchange and humidification are not the primary problems for closed unit operation in air condition laboratory, the remaining major concerns for successful

tissue culture outside the incubator are pH and temperature stabilization. In the perfusion systems developed by Minucells and Minutissue, cultures are carried out on a hot plate operated at 37 °C and gas exchange is facilitated either in gas exchange chamber with gas with pre-mixed gas composition (e.g. 5 % CO_2/95 % air) or through gas-permeable silicone tubing. For mini-scale chambers at slow perfusion rates, the hot plate may be sufficient for temperature stabilization. However, temperature has to be strictly controlled within a tolerable range ± 0.5 °C to ensure reproducibility [1]. For bioreactors of larger size, heat loss to the surrounding could be significant and the heat flux provided by a hot plate does not provide an even heating and temperature stabilization in the bioreactor. On the other hand, the use of a pre-mixed gas is simply another way of CO_2 supplementation that still relies on the CO_2/bicarbonate system. The alternative for this is to use normal air with the adjustments made to the pH buffer system.

Most of the culture medium formulations (except Leibovitz formula) are traditionally pH-buffered by CO_2/bicarbonate, which require supplementation of gas-phase CO_2 in the incubator (2-10 %) [55]. The buffering capacity by this system can be described by the reversible reaction below:

$$CO_{2\,(g)} \leftrightarrow CO_{2\,(aq)} \leftrightarrow H_2CO_3 \leftrightarrow H^+ + HCO_3^-$$

When acidic metabolites accumulate (e.g. lactate), bicarbonate (HCO_3^-) neutralizes the acid (H^+) to maintain the pH of the medium. The reaction is driven from right to left and gaseous CO_2 is released from the culture. Since the culture wares are designed

with ventilation, partial pressure of CO_2 does not build up and the gas phase CO_2 is always maintained at 5 % with the control of the incubator.

The prolonged exposure of medium in normal air (through routine handling cell culture) would cause irrecoverable depletion of bicarbonate due to low CO_2 in air (only 0.03 %) which is continuously weakening the buffering capacity. Newly developed medium formulas use complementary buffer such as HEPES to stabilize the medium pH in a way that is independent of gas composition. In industrial scale operation (e.g., cultivation of mammalian cells to produce recombinant proteins), the neutralization of acidic metabolite such as lactate is required by adding sodium bicarbonate. However, the ongoing pH adjustment causes build-up of CO_2 which in turn adversely affects cell turnover. Other alternatives, such as the use of other buffer systems such as MOPS-histidine, is found to be promising for preventing CO_2 build-up [196].

In this project, in-situ oxygen profiling of the tissue construct cultured inside the bioreactor was carried out. Due to the size of the oxygen microsensor system, it was impossible to carry out oxygen profiling in situ inside a conventional incubator. Therefore, a bioreactor system was designed to carry out a bioreactor culture and oxygen profiling from outside the incubator. A schematic diagram of the new system is shown in Figure 5.3.The system consists of an incubation unit (1 and 2) to provide enclosure for tissue culture at the designated temperature, a bioreactor alongside flow loop components for tissue culture under specified flow conditions (3, 4 and 5) and an oxygen microsensor system (6, 7 and 8) for oxygen profiling. The detailed descriptions of each component will be presented in the following sections.

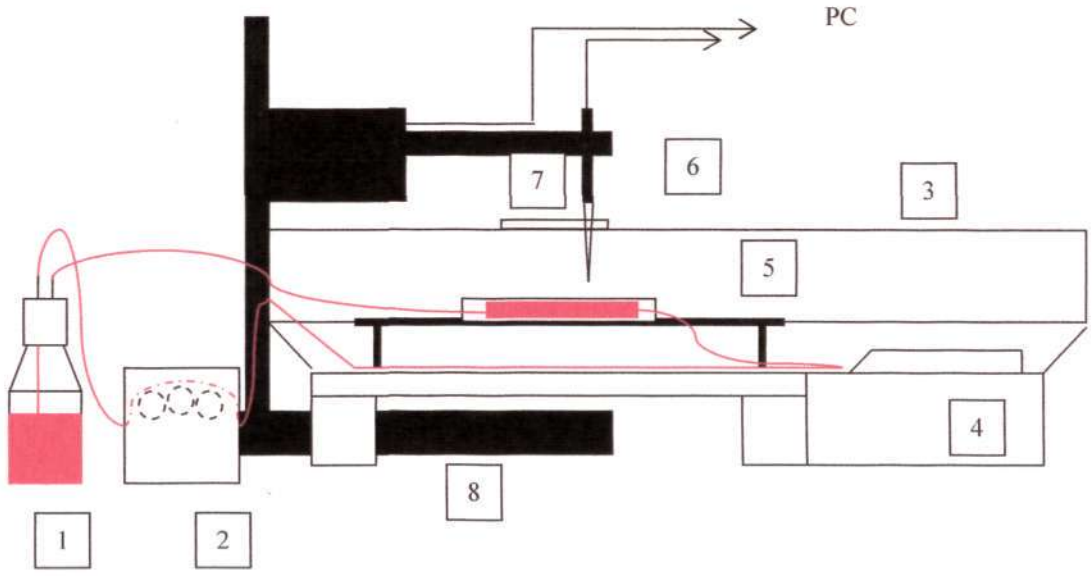

1	Medium reservoir	6	Oxygen microsensor
2	Peristaltic pump	7	Manipulator
3	Incubation unit (IU)	8	Lab stand
4	Heating module	—	Medium flow loop
5	Bioreactor chamber		

Figure 5.3: Schematic diagram of bioreactor system: The system contains (1) medium reservoir; (2) peristaltic pump to register designated flow rate of medium; (3) incubation unit (IU) where tissue culture is carried out; (4) heating module to maintain IU temperature; (5) bioreactor chamber to culture tissue construct under designated flow field; (6) oxygen microsensor to conduct oxygen profiling for the tissue construct in the bioreactor; (7) motorized micromanipulator to control the movement of the oxygen microsensor and (8) Lab stand to mount and secure the micromanipulator and the microsensor The red line represents the flow loop which starts from the medium reservoir and is allowed to warm up and equilibrate with surrounding air in the IU with 140-cm long tubing before entering chamber. The medium flowed through the chamber and recirculated to the medium reservoir.

5.3.2 Incubation Unit

The incubator unit (IU) is a specially made enclosure that is incorporated with the temperature-controlled heating module (Inkubator 1000, Heidolph, Germany) to maintain its interior temperature at around 37 ^{o}C. Tissue culture in the bioreactor chamber was carried out inside the IU at a controlled temperature under normal air condition (containing 0.03 % CO_2). The material used to fabricate the IU is polycarbonate which is transparent and allows visualization of tissue culture from outside. Validation of the IU was carried out on temperature distribution and adaptation studies of cells in such environment.

I. Temperature distribution and stabilization

Since the heating module is on one side as shown in Figure 5.3, temperature distribution may be uneven. Therefore, a 9-point temperature measurement within the area for tissue culture (nodes in Figure 5.4) was carried out to ensure temperature variation was acceptable. Temperature was taken using digital thermometer with short sensor (Thermo digital) with accuracy of ± 0.1 ^{o}C which has been widely used in monitoring temperature in water baths and incubators. The thermometer has a short epoxy sensor which was secured at the designated positions shown in Figure 5.4. The flexible cable connected to the sensor was extended out of the IU through the lid edge of the IU and the readout outside the IU was taken after the temperature was stabilized. After 9-point temperatures were taken, SigmaPlot 9.0 was used to create an estimated temperature contour of the culture area.

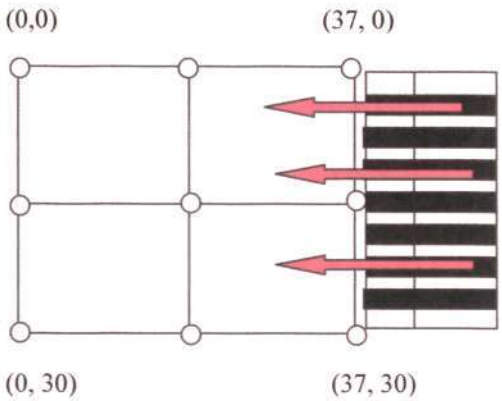

Figure 5.4: 9-point temperature measurement within culture area. The coordinate values are in cm. Warm air blows from the right hand side of the IU to the culture area (red arrow).

Occasional opening or closing the IU is unavoidable and how soon the heating module can response and resume the set temperature is important to maintain the culture temperature. In order to investigate the temperature recovery after the disruption, the unit was intentionally opened for two minutes and then closed and the temperature was recorded for every 5 seconds in the first 20 minutes and then for 30 seconds in the next 30 minutes until the temperature was recovered (or stabilized).

In order to examine the potential overheating in the chamber interior by the temperature overshooting, a simple heat transfer analysis was conducted across the wall of the bioreactor. Considering a simplified system as illustrated in Figure 5.5: Initially, both the surrounding and the bioreactor temperatures are stabilized at 37 ^{o}C (t = 0). The surrounding temperature is suddenly raised to a maximum overshoot temperature, T_{os} ^{o}C, for a time period of t and the bioreactor wall starts heating up due to an abrupt change in the surrounding temperature and heat transfer occurs from the

surrounding through the wall to the culture medium. For an unsteady, one-dimensional heat transfer without external heat source, energy equation can be written as:

$$\frac{\partial T(t,y)}{\partial t} = \alpha_{pc} \frac{\partial^2 T(y,t)}{\partial y^2} \qquad 5.3.1$$

where

$$\alpha_{pc} = \frac{k_{pc}}{\rho_{pc} \hat{C}_{p,pc}} \qquad 5.3.2$$

Polycarbonate was used as the material for constructing bioreactor. k_{pc}, ρ_{pc} and $\hat{C}_{p,pc}$ are the conductivity, the density and the specific heat capacity of polycarbonate, respectively. To solve the governing equation, initial and boundary conditions are given:

Initial condition : $T(0,y) = 37\ ^{0}C$ 5.3.3

Boundary condition 1 : $T(t,0) = T_{os}$ 5.3.4

Boundary condition 2 : $T(t,\infty) = 37\ ^{0}C$ 5.3.5

Here, a semi-infinite slab is assumed since polycarbonate is a poor conductor with conductivity (k_{pc}) as low as 0.2 W/m.K and any temperature perturbation from the surrounding might require a longer time to propagate into the medium side. The solution of equation 5.3.1 has been given in [186]:

$$\frac{T - 37}{T_{os} - 37} = 1 - \text{erf} \frac{y}{\sqrt{4\alpha_{cp} t_{os}}} \qquad 5.3.6$$

where erf is known as the error function. Here, it is of the interest to determine the penetration depth at which the temperature has reached 38.5 °C, which has been discussed previously as the highest physiological temperature limit for most of the cell culture [55]. In this case, T = 38.5 °C, T_{os} is the highest overshoot temperature recorded in the experiment and the overshoot period, t_{os}, which is defined as the time interval that the temperature exceeds 38.5 °C, was used for the value of t. Given these values together with ρ_{pc} = 1200 kg/m^3 and $\hat{C}_{p,pc}$= 1300 J/kg.K, y was solved for the penetration depth required to reach 38.5 °C after the surrounding temperature overshoots to T_{os} for time t.

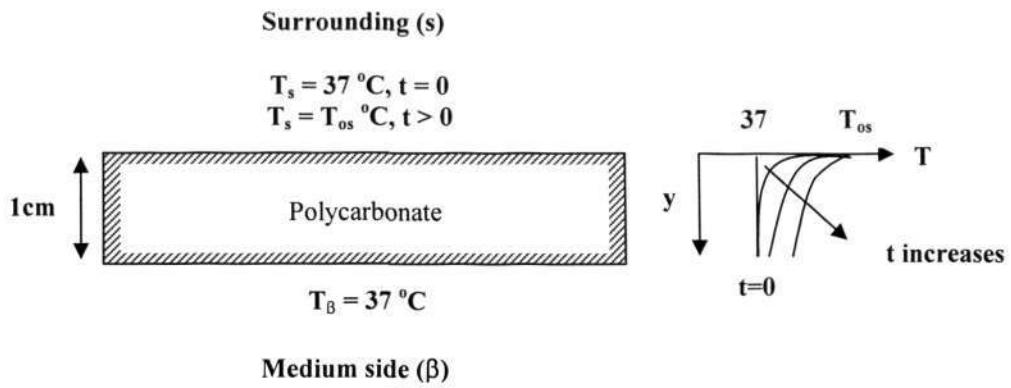

Figure 5.5: Heat transfer from the surrounding to the medium as the the surrounding temperature is increased suddenly increased.

II. Validation of culture environment

In order to conduct cell or tissue culture in the IU, pH and contamination of conditioned medium was checked after equilibration in the IU. In addition, PESMCs were cultured in the IU to validate the culture environment. The details have been

described in section 5.2.2 where adaptation of PESMCs to normal air environment was studied.

5.3.3 Bioreactor

I. Design Criteria

The bioreactor chamber design in this study fulfilled the design criteria below:

a. Flow pattern:

The flow pattern calls for a uniform, fully-developed laminar flow across the construct surface. This involves a parabolic flow profile in the plane perpendicular to the construct surface and a plug flow is in the plane parallel to the construct surface (Figure 5.6). The purpose of the plug flow is to render a constant flow across the construct width (w) such that a 2D analysis can be achieved as intended in the mathematical model established in section 4.1. In order to provide fully-developed flow, a sufficient entrance length has to be given to allow flow development as the medium enters the chamber through a small chamber inlet.

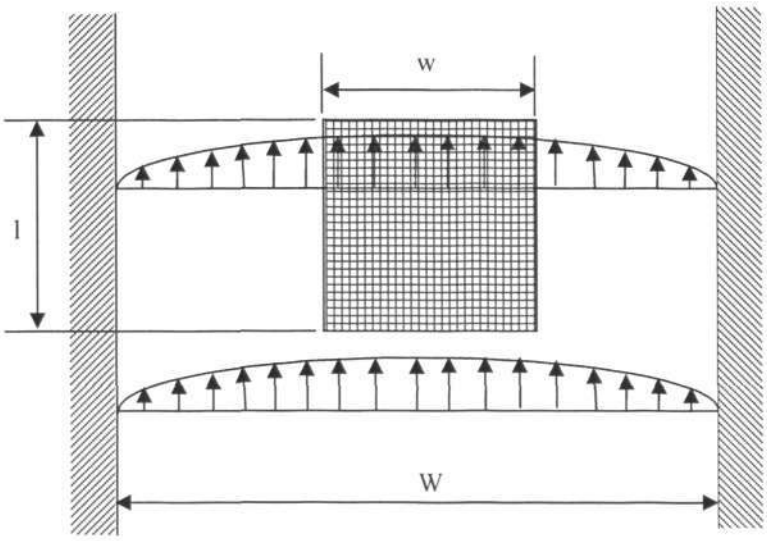

Figure 5.6: Flow profile required in the bioreactor chamber design with given width W. The grid area represents the tissue construct (l × w).

b. Modular design:

A chamber is an assembly of modules. This allows the replacement of any module if it is broken. The modular design allows easy manufacturing, quick assembling and dissembling, leakage prevention and facilitation of in-situ measurements.

c. Selection of materials:

In order for the system components to be used for tissue culture, the chamber must be sterilized using the methods available in the lab, e.g. autoclaving and exposure chemicals such as ethanol. Hence, the materials should be either heat- or chemical-resistant. Biocompatibility is another concern when selecting materials. It would be desired that the materials used for constructing the chamber walls be a good insulator,

so that any perturbation due to surrounding temperature changes can be minimized. A transparent material is also preferable for visual observation of the culture.

Cost: The volume of the chamber determines the start-up medium required for the experiment and materials for chamber construction. Optimal design requires that the star-up medium and chamber materials be minimized while the desired flow pattern still be achieved. Furthermore, the manufacturing cost of the bioreactor has to be considered.

II. Chamber design

Design of the internal geometry of flow chamber was based on CFD simulations described in section 4.2. The simulated flow field allows the determination of the shape and the dimension of the chamber. With these data, flow development was understood and the placement of the tissue construct can be determined. For manufacturability, a simple pill-shaped chamber enclosure with semi-circular entrance and exit portions was used to achieve the desired flow pattern. Polycarbonate and medical-grade stainless steel were used to fabricate the bioreactor chamber. Polycarbonate was used in most of the chamber fabrication because it is easily fabricated, resistant to ethanol sterilization and transparent, which enables visual observation.

III. Modular design

A modular configuration was employed for the design of bioreactor chamber so that replacement of any broken module is possible. The explosion view of a single flow

bioreactor configuration was shown in Figure 5.7. The scaffold seeded with cells was sandwiched between two scaffold plates and the assembly was positioned on the base plate. The pill-shaped chamber enclosure (with inlet and outlet ports on both ends) was overlaid on the scaffold plate 1 to create the flow area together with the top plate. The top plate was drilled with five holes which project over five centreline positions of the tissue construct to facilitate introduction of the oxygen microsensor. To close up the holes during culture experiments, a layer of polydimethylsiloxane (PDMS) was applied on the whole bottom surface (including hole areas) of the top plate. The oxygen microsensor can be pushed through the PDMS to enter the bioreactor interior. The sealing ability of PDMS provides sealing between PDMS and penetrating sensor which avoids introduction of air-borne particles even when oxygen profiling is underway. All the modules were assembled with six M4 screws. To ensure sealing, O-rings or gaskets were applied between modules wherever necessary.

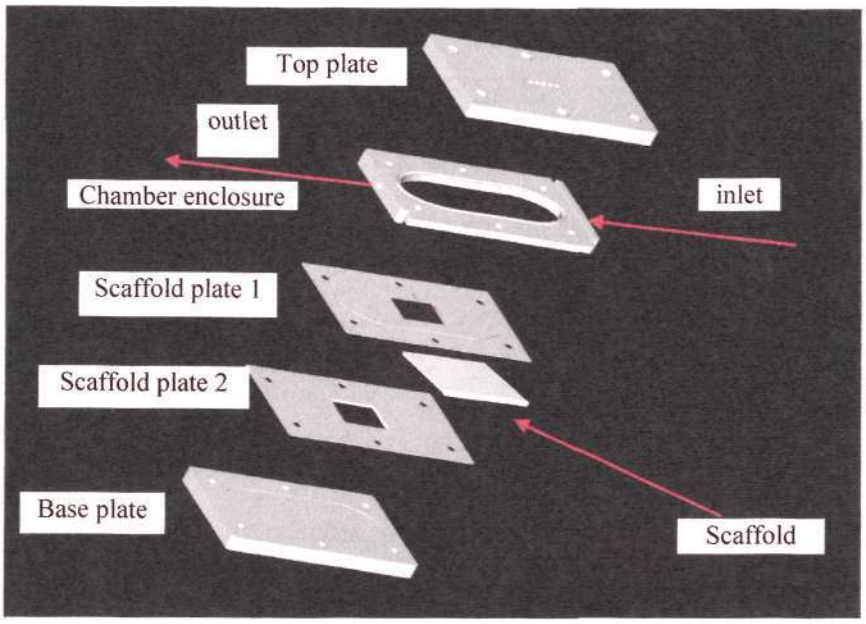

Figure 5.7: Explosion view of modular bioreactor chamber: Chamber enclosure is a pill-shaped geometry for flow to fully develop before crossing the scaffold region. Ports from each side allowed medium flow in and out of the chamber. Scaffold was sandwiched between 2 mounting plates with gasket to secure the position of the scaffold. All the bioreactor modules were assembled with six M4 screws.

IV. Flow loop design

A flow loop (Figure 5.8) constructed by non-cytotoxic silicone tubing and polypropylene fittings provided for the recirculation of medium from the reservoir to bioreactor chamber and from bioreactor back to medium bottle to establish a closed circuit. Medium flow is precisely regulated by a peristaltic pump (Ismatec, IPC high precision multichannel dispenser). The pump was calibrated each time before use according to the manufacturer's instructions. Silicone tubing was used for the medium transport pipeline. With a tubing inner diameter of 1.02 mm, the peristaltic pump can register a flowrate as low as 0.0140 ± 0.0005 ml/min (or 14.0 µl/min) according to the operating manual. Hence, all flowrate values used in this thesis are expressed in three

significant figures (e.g., 0.272 ml/min). Gas exchange of O_2 and CO_2 takes place between gas-permeable silicone tube wall and air surrounding. A length of 140-cm of tubing (1-mm internal diameter) from medium bottle to bioreactor provides sufficient gas exchange area and temperature stabilization. At the exit of the bioreactor, a short length of tubing (50 cm) was connected to the medium reservoir to complete the closed flow loop and a relatively short return line to avoid high back pressure in the bioreactor.

V. Sterilization

Bioreactor modules were made of polycarbonate and medical-grade stainless steel. All the components were washed thoroughly in de-ionized water and dried at 45 °C. Before assembling for tissue culture, they were sterilized in filtered 70 % ethanol for 1 hour and dried inside the biosafety cabinet for 2 hours. All silicone tubings, polypropylene tube fittings and medium bottles used in the flow loop are autoclavable. The internal surface of the tubing was sterilized and washed by continuously pumping ethanol for 3 hours followed by de-ionized water three times for 3 hours. Tubing and fittings were dried in oven, packed in autoclave pouch and autoclaved at 121 °C for 20 minutes.

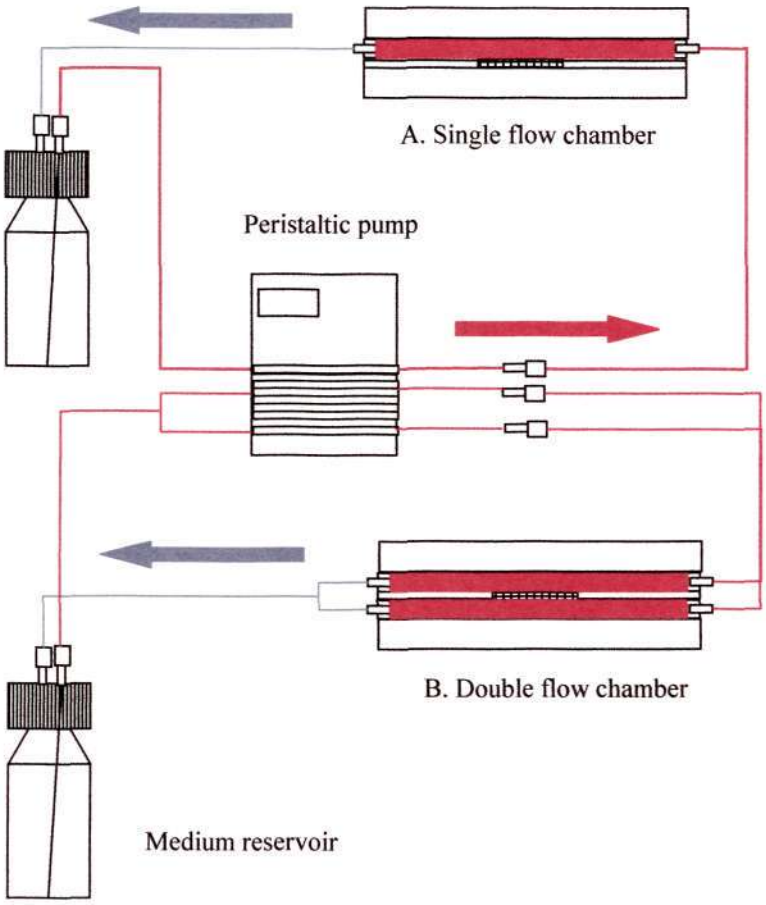

Figure 5.8: Flow loop of bioreactor culture: Medium is drawn from the medium reservoir by peristaltic pump. Medium enters the bioreactor chamber (A. single or B. double) and returns to the medium reservoir.

5.3.4 Oxygen microsensor system

I. System components

The oxygen microsensor system was purchased from Unisense, Denmark. The system includes components are listed below:

Oxygen microsensors: The oxygen microsensors are Clark-type sensors (or polarographic sensors). They are based on diffusion of oxygen through a silicone

membrane to an oxygen reducing cathode which is polarized against an internal Ag/AgCl anode by a voltage of -0.8 V [167]. The flow of electrons from the anode to the oxygen reducing cathode is proportional to the oxygen partial pressure around the sensor tip. The electron current is measured by a high quality picoammeter. The tip size of 50 μm was used in the experiment as a tradeoff between the need for high spatial resolution and strength and stiffness with the 50-μm diameter sensor being less fragile than the 10 μm-diameter sensor.

Dual channel picoammeter: Since the currents measured by a Clark-type sensor is pico-scale, the signal was transmitted and measured using picoammeter.

Lab stand: It provides support for the micromanipulators.

Micromanipulator stage with motor controller: The motorized stage enables controlling the movement of micromanipulator in small well-defined steps using an encoded DC motor. The motorized stage is used in conjunction with motor controller that connects to a PC via the RS-232 serial port. The motor controller acts as a signal receiver and sender in that it receives the location of the micromanipulator while sends the signal to the motor to move to the registered height. The control was carried out by the manufacturer software Profix (see below).

Dual analogue channel A/D converter (USB): This converts two analogue signals from the picoammeter into digital signals. This conversion allows the microsensor measurements to be read directly into specific data acquisition programs, Profix (for microsensor profiling) where analysis, plotting and storing of the microsensor data is performed.

Software for control and data acquisition: Profix is a Windows-based program for automated oxygen profile measurements. Profix can read data from up to two microsensor amplifiers via the A/D converter that is connected to the parallel port of the personal computer, and the program allows control of the motorized micromanipulator. The program functions include recording, calibration, plotting and storage of measured oxygen profiles.

II. Calibration

Materials: Complete medium and nitrogen tank (Soxal)

Equipment: Oxygen microsensor system (Unisense) and fish tank air pump and thermocouple.

A 2-point calibration was carried out in the medium of interest under anoxic (0 % oxygen saturation) and air-saturated (100 % oxygen saturation) conditions at 37 ^{o}C. To produce anoxic condition, culture medium was pumped with nitrogen for 10 minutes to de-oxygenate. Cooling may occur through compressed nitrogen. The medium temperature was continuously monitored and adjusted by controlling the heating element in the water bath. To produce air-saturated condition, the air was continuously injected by air pump for 10 minutes with temperature adjustment. Once the calibration condition was achieved, the microsensor was dipped into the medium immediately and the calibration can be carried out with Profix calibration function to convert a measured voltage value into calibrated units (% saturation). After calibration, the microsensor was used to conduct the oxygen measurement.

5.3.5 Tissue culture

Strategies of tissue culture in this study included static and dynamic mode (Figure 5.9). Static culture of tissue constructs was carried out in Petri dish while dynamic culture involves cultivation in the designed bioreactor. For bioreactor culture, two configurations were employed: single and double flow. This strategy allowed registration of medium flow across either the top surface or both the top and bottom surfaces of the construct. Furthermore, two levels of flowrates were adopted for both configurations: 0.272 and 0.545 ml/min. Before culture experiments started, PESMCs were expanded in routine practice as described in section 5.2.1IV.

Once the cells had proliferated sufficiently for experiments, porous gelatin scaffolds were prepared and bioreactor and flow loop components were sterilized and assembled using asceptic technique in biosafety cabinet. Cells were then seeded into scaffold, mounted in the bioreactor, and the construct was cultured in the bioreactor for 5 or 10 days. On the harvest day, oxygen profiling of tissue construct was carried out and the construct was harvested to measure cell distribution. The detailed methods and procedure of tissue culture will be given in the next sections.

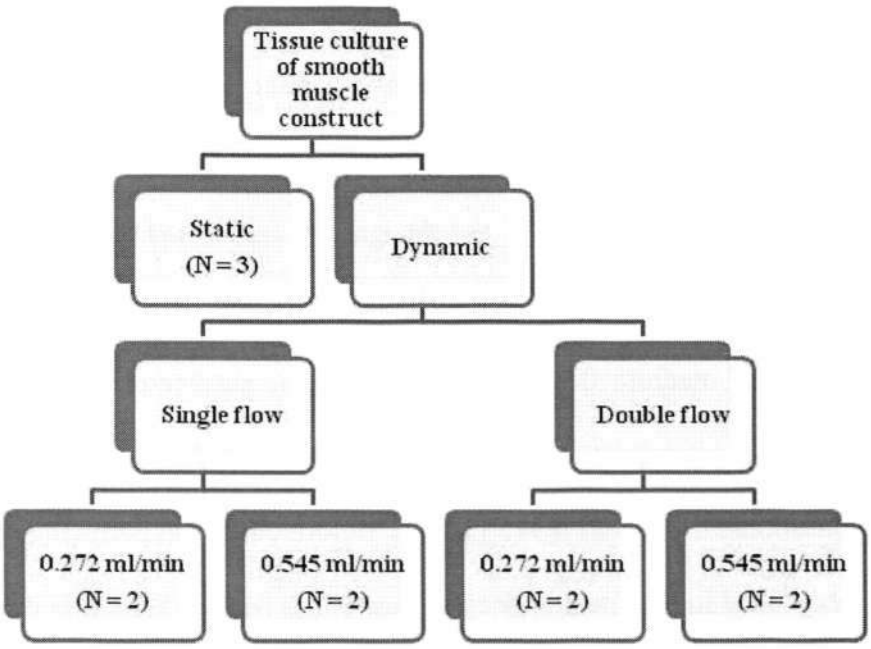

Figure 5.9: Tissue culture strategies used in this study. N represents the repetition of each experiment condition.

I. Scaffold preparation

The porous gelatin scaffold developed in this project (see section 5.1.1) was cut into $3.2 \times 2 \times 0.2$ cm^3. The scaffolds were sterilized in 70 % ethanol for 15 minutes followed by 3 washes in sterile PBS for 15 minutes. After the last wash, PBS was discarded and the scaffold was briefly dried in the biosafety cabinet for 2 hours to facilitate cell seeding.

II. Bioreactor assembly

To assemble the single flow configuration, all the ethanol-sterilized bioreactor components were dried in the biosafety cabinet before use. The lower scaffold plate was first laid on the base plate covered with a silicone sheet. Another silicone sheet

was applied on the first scaffold plate. The scaffold was carefully transferred to the rectangular opening in the centre of the scaffold plate by two pairs of forceps and then sandwiched by the second scaffold plate. Two O-rings were fixed into the grooves on both sides of the chamber enclosure which was placed on the second scaffold plate. The cells can be seeded at this stage (see section 5.3.5III below). The bioreactor was finally closed by adding the top plate. It is important to make sure that the edges of all the components were flush and all the screw holes were aligned from the top plate to the base plate. The bioreactor assembly was then screwed together at six locations of the assembly and then connected to the flow loop. The double flow configuration assembly was carried out in a similar manner with one more chamber enclosure that was inserted between the base plate and the lower scaffold plate.

III. Cell seeding

After PESMCs were confluent, the cells were trypsinized and counted using hemocytometer. Cells were seeded at the density of 2 million cells per cm^3 of scaffold. To facilitate seeding over the area of the scaffold, the suspension volume was adjusted to 120 µl which was evenly separated into six parts (i.e. 20 µl each) and then dropped onto six locations of the scaffold. A briefly dried scaffold was used here to facilitate cell suspension to seep into scaffold by capillary action. The small suspension volume was used to avoid overflow of suspension to the surrounding and contained the cells within the scaffold.

IV. Flow loop connection

After cell seeding and bioreactor assembly, all the autoclaved components involved in the flow loop were transferred into biosafety cabinet. The original screw cap of the sterile 250-ml glass bottle was replaced by a specially made 2-port screw cap which was connected to one 140-cm long silicone tubing for medium delivery to bioreactor and one 50-cm long silicone tubing for medium return from the bioreactor. Finally, these delivery and return tubing segments were then connected to the inlet and the outlet of the assembled bioreactor, respectively to form the complete flow loop. 80-ml of culture medium bottle was then added to glass bottle and the whole set-up (bioreactor and flow loop) was transferred to the IU.

V. Tissue Culture

The cell-seeded construct was left undisturbed for 6 hours to allow cell attachment. After 6 hours, the long silicone tubing segment was mounted into the cassette of the peristaltic pump which was then switched on and the flowrate was adjusted to designated values (0.272 or 0.545 ml/min). Since there is no prior knowledge on the suitable flowrate for culture of smooth muscle construct *in vitro*, the selection of flowrate was based on the values between 0.1 and 1ml/min used in the bioreactor literature [22, 24, 36, 147]. The culture was carried out for 5 or 10 days. On each day, 10 ml of medium was collected from the medium reservoir to monitor glucose and pH. Same amount of fresh medium was replenished. The pH was measured by pH meter (Fisher Scientific). On the harvest day (day 5 or 10), in situ oxygen profiling was conducted at 5 locations along the centerline of the tissue construct under medium

flow. The bioreactor was then dissembled and the construct was washed with sterile PBS three times and about 5 mm width of tissue construct was cut along the centerline. The sample was then processed for histology and measurement of cell distribution.

VI. Oxygen profiling

To facilitate oxygen profiling in the bioreactor system, an observation slit was made on top of the IU to allow introduction of oxygen microsensor into the system. Since a 5-point measurement along the centerline of the construct was intended, the bioreactor was placed such that the access holes on the bioreactor were aligned with the observation slit. The calibrated oxygen microsensor was then mounted on the motorized manipulator positioned above the observation plate. The microsensor was manually moved through the observation slit and reached near the first access hole. Its position was adjusted to the level of the top plate. By using manipulator controlled by Profix software, the microsensor was first moved down 1 cm to pierce through the PDMS sheet bound with the downside of the top plate. The medium interface was then to be located by moving the sensor down stepwise by 50 μm each. Once the interface was reached, a sudden signal fluctuation was observed and this point was set as "depth = zero". The microsensor was moved down slowly at 50 μm/s and five measurements were taken at every 100 μm until reaching the bottom (depth = 7,500 μm for single flow and depth = 13,000 μm). At each x-location, oxygen profiling was carried out three times (n = 3) and the oxygen saturation fraction at each depth were averaged over three measurements to calculate the mean. The plot was generated for oxygen

saturation fraction against depth. Since the data points were taken within very close distance, the addition of the error bars onto the plot causes a severe masking of the oxygen profiles. Instead of assigning the error bar to each data point, only the maximum standard error of mean (i.e. maximum SEM) is given for each culture condition to indicate the data spread.

VII. Histology

a. Sample Processing

The sample was then fixed in buffered 10 % formaldehyde, serially dehydrated in graded ethanol, which was exchanged with xylene and finally embedded in paraffin. All the steps were carried out in the automated tissue processor (Leica TP1020) through the steps shown in Figure 5.10. The embedded sample was cut in 5-μm thick section by microtome (Leica RM2125RT). The section was straightened in water bath at 37 ^{o}C and picked up by Polysine® slide (Menzel-Gläser, Thermo Scientific). In order to increase adherence of section onto the slide, 1 part of tissue adhesive (Microm) was added into 100 parts of water in the water bath. The slide was then dried on a hot plate (Leica HI1220) at 42 ^{o}C for 1 hour and stored in room temperature before staining.

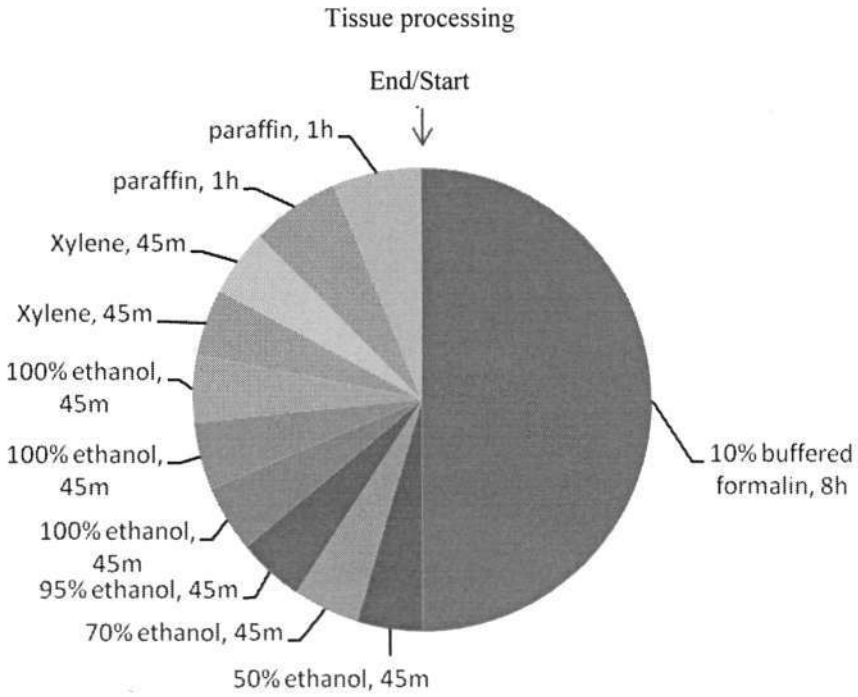

Figure 5.10: Steps of tissue processing

b. Staining

All the slides routinely required deparaffinization in xylene and rehydration before staining. Unless stated, all the slides were de-hydrated in and cleared in xylene. The staining process is summarized in Figure 5.11. All the solvents used in the process were contained in Coplar jars. In the final step, coverslipping was carried out by adding a few drops of Clarion® mounting medium (Sigma) on the slide followed by applying a cover glass (No.1, Marienfeld) on top. A pressure was then applied on top of the cover glass in order to spread the mounting medium evenly over the section and also removed trapped air bubbles.

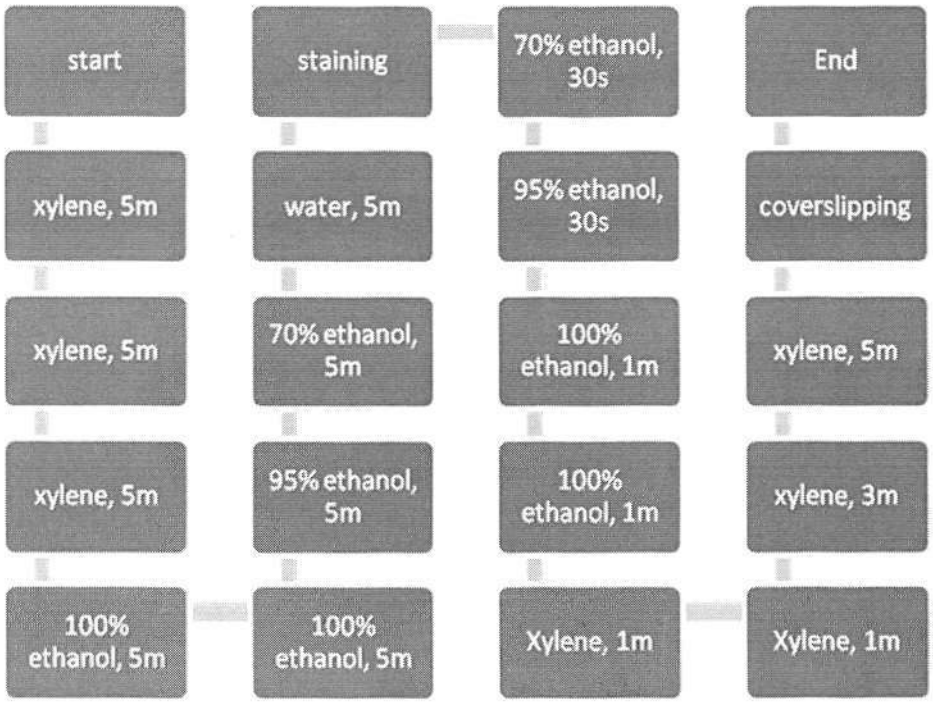

Figure 5.11: Detailed process of pre- and post-staining process.

c. Hematoxylin and eosin (H&E)

The protocol established by Rosen Lab was adapted and Figure shows the detailed procedure. The slides were deparaffinized and rehydrated as stated above. The slides were stained in Harris Hematoxylin solution (ACCUSTAIN®, Sigma) for 3 minutes to stain cell nucleus. The stained sections were then soaked in tap water for 5 minutes followed by differentiation in acid-alcohol (0.25 % vol/vol concentrated hydrochloric acid in 70 % ethanol) to remove excessive dye. It was completed by staining in the eosin solution for 30 seconds for cytoplasm and ECM. The stained section was then de-hydrated, cleared and cover-slipped. After being dried, the section was observed under light microscope. Nuclei were appeared blue while cytoplasm and ECM were stained in pink.

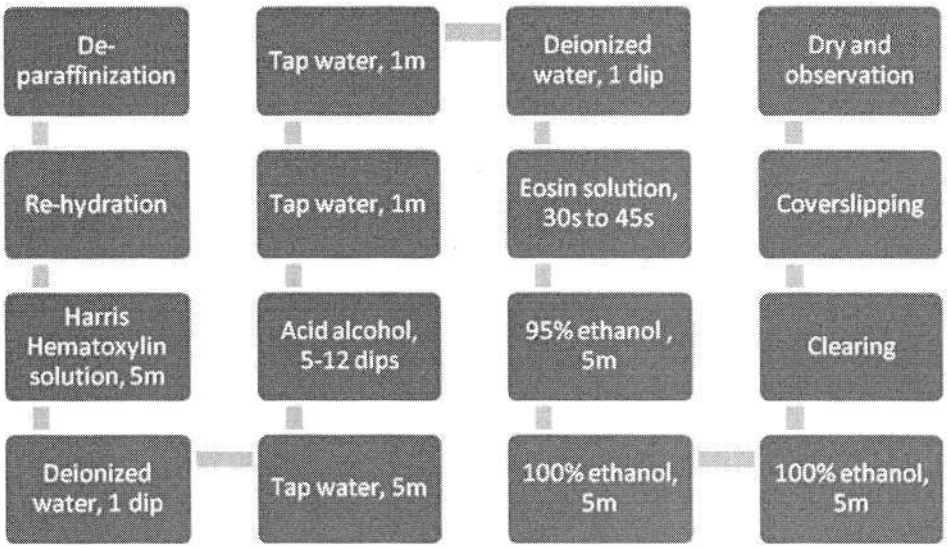

Figure 5.12: Detailed steps of H&E staining

VIII. Cell Distribution

a. DAPI staining

A Deparaffinized and rehydrated section of tissue construct was stained in DAPI (4',6-diamidino-2-phenylindole, Molecular Probes) diluted in PBS at 1:1000 for 5 minutes, washed in deionized water twice for 2 minutes. The section was coverslipped with a few drops of fluorescence mounting medium (DAKO) without dehydration and clearing in xylene. From DAPI staining onwards, all the sections were handled in dark environment to avoid photobleaching. The sections were dried in the fume hood in dark before observation.

b. Image capture and processing

Cell nuclei stained with DAPI was visualized through DAPI channel of fluorescence microscope (Carl Zesis). Serial pictures were taken from top to bottom at the five oxygen profiled locations (Figure 5.13A). Micrographs in vertical sequence were open in ImageJ version 1.40g, open-source image processing program developed by National Institutes of Health, USA (http://rsb.info.nih.gov/ij/). Images were combined vertically using "Stack combiner" Plugin to form a single image (Figure 5.13B). A group of 20 segments were created throughout the whole thickness of the construct using macros program written by the author (Figure 5.13C). The cells were counted in each segment ($100 \times 1200\ \mu m^2$) to represent cell number at each depth position and four sections at each x-location ($n = 4$) were counted and averaged. The cell distribution was created by plotting cell number against depth position and the mean cell density ± SEM ($cells/mm^3$) are expressed at each depth position of the construct

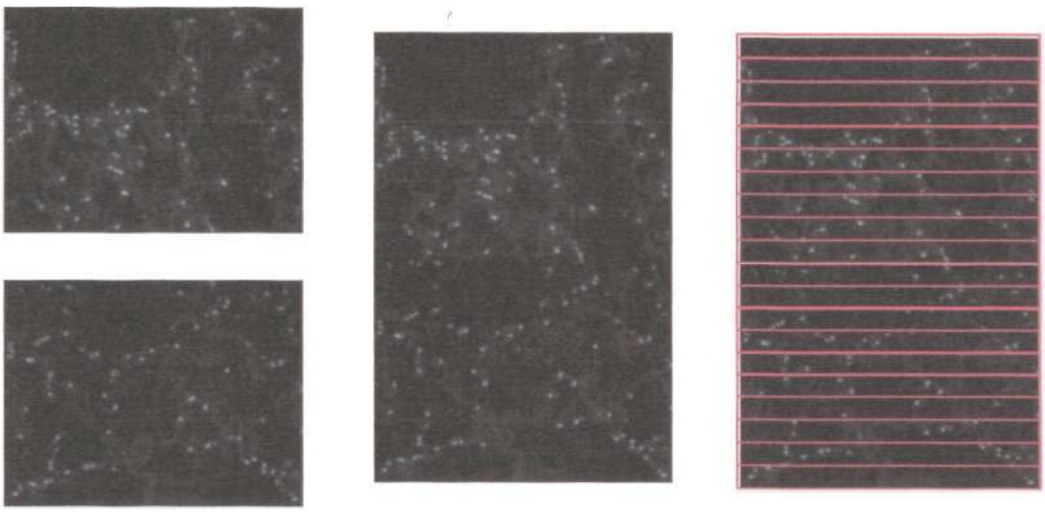

A. Top down serial micrographs taken from DAPI-stained section

B. Combine micrographs into single image

C. Partition combined micrograph into 20 portions

Figure 5.13: Image processing for measurement of cell distribution: (A) The micrographs were taken from the top surface to the bottom surface of the construct section and opened in Image J as a stack; (B) All micrographs were combined into a single image using "stack combiner" and (C) A macro was written to partition the image into 20 even portions. The height of each portion is 100 μm.

5.4 Validation of Mathematical Model

The mathematical model for the culture environment has been described previously in section 4.1. In order to validate the predicted results simulated by the model, the model was used to simulate the tissue culture in the bioreactor experiments. Since oxygen profiles and cell distribution profiles at 5 positions (x = 5, 10, 15, 20 and 25 mm) were measured experimentally after tissue culture was carried out for 5 days and 10 days, the corresponding simulation results were extracted and compared with the experimental results to examine the validation of the results. In order to summarize the difference between experimental and simulation results, discrepancy (Δ) was calculated by:

$$\Delta = [\Psi_{sim}(t,x,y) - \Psi_{exp}(t,x,y)] \times 100\ \% \qquad 5.4.1$$

where $\Psi_{sim}(t,x,y)$ and $\Psi_{exp}(t,x,y)$ are the physical quantities extracted from the model simulation and measured from the experiment, respectively at time t and coordinate (x,y). Both experimental and simulation profiles (in this case, oxygen saturation fraction against depth for oxygen profiles and cell volume fraction against dimensionless depth for the cell distributions) were plotted at all studied locations and time points. A bar chart was also created to summarize the discrepancy averaged over the construct depth (y) for each x-position (x = 5, 10, 15, 20 and 25 mm). Average discrepancy for underestimation ($\Psi_{sim}(t,x,y) - \Psi_{exp}(t,x,y) < 0$) and overestimation ($\Psi_{sim}(t,x,y) - \Psi_{exp}(t,x,y) > 0$) were calculated separately and the maximum discrepancies were also indicated in the chart.

Chapter 6. Experimental results

6.1 Results organization

To facilitate the flow of results presentation, the experimental results will be presented first to provide the actual observations of the studied system and the measured data required for the mathematical model. The results are organized as shown in Figure 6.1:

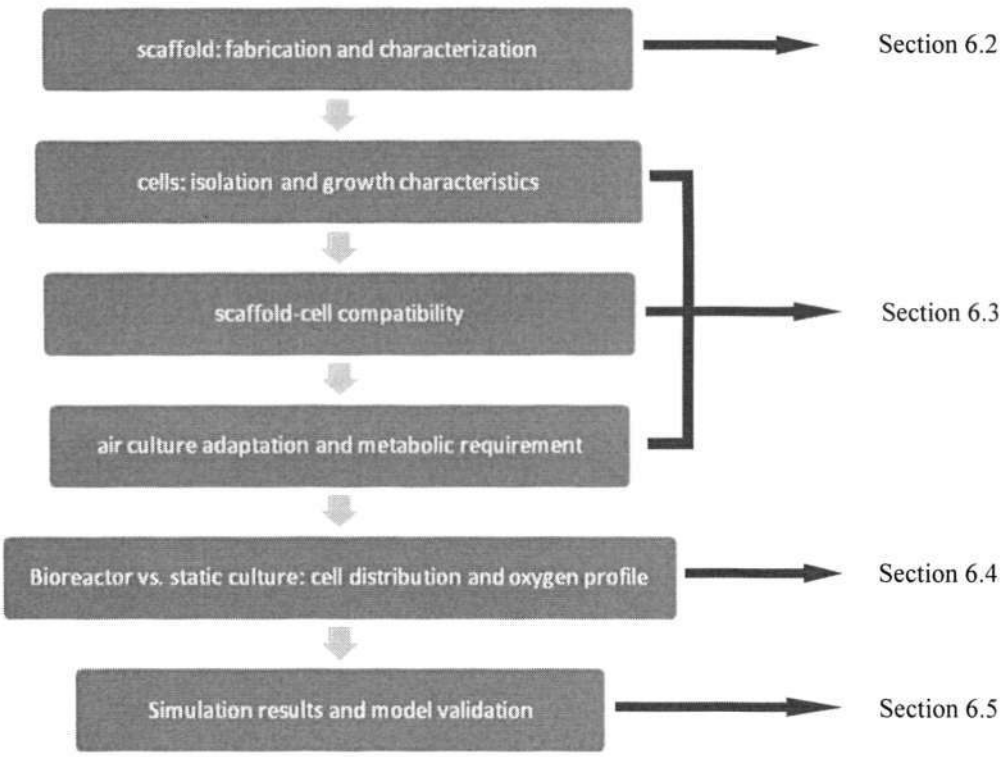

Figure 6.1: Flowchart of result presentation

Briefly, results of two important elements (scaffold and cells) will be first presented followed by their interaction *in vitro*. PESMCs were first adapted in normal air composition and the results of their metabolic requirements will be presented next.

The cell and oxygen distributions of bioreactor culture of cell-seeded scaffold under different flow conditions will next be given and compared with static culture. Finally, the simulated cell and oxygen distributions will be shown and the simulated results was compared and validated with experimental results to complete the study.

6.2 Scaffold

6.2.1 Microscopic structure

Figure 6.2, Figure 6.3 and Figure 6.4 show the SEM images (50×) for a gelatin scaffold from its top, bottom and cross-section, respectively. From these 3 microscopic perspectives, it is found that sponge prepared by this method produced a structure with a relatively uniform pore size range. The pore formation depends on the entrapped air bubbles which are uniformly distributed throughout the foaming gelatin solution. Based on the measurements of 92 pores on the binary micrographs of the cross section using ImageJ, the pore size was ranged from 37 to 359 μm with average pore size of 141.4 ± 78.4 μm (mean ± SD) while 77 % of pores in the range between 50 and 250 μm which showed relatively good pore size uniformity. Another two batches of experiments confirmed this microstructure and pore size range.

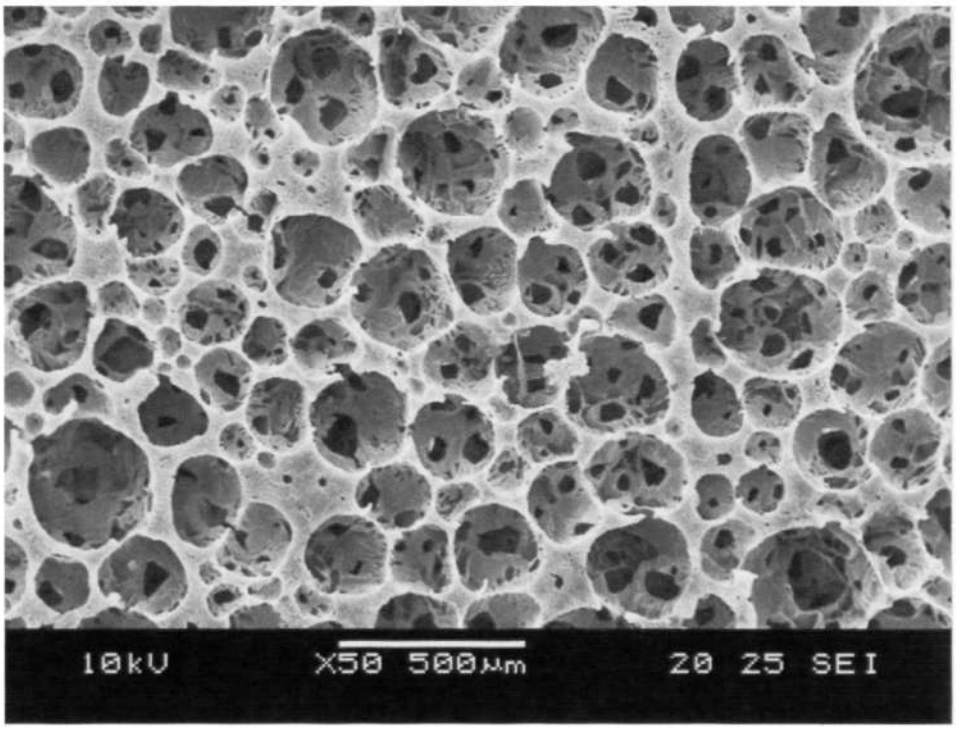

Figure 6.2: SEM micrograph (50×) of top surface of gelatin sponge.

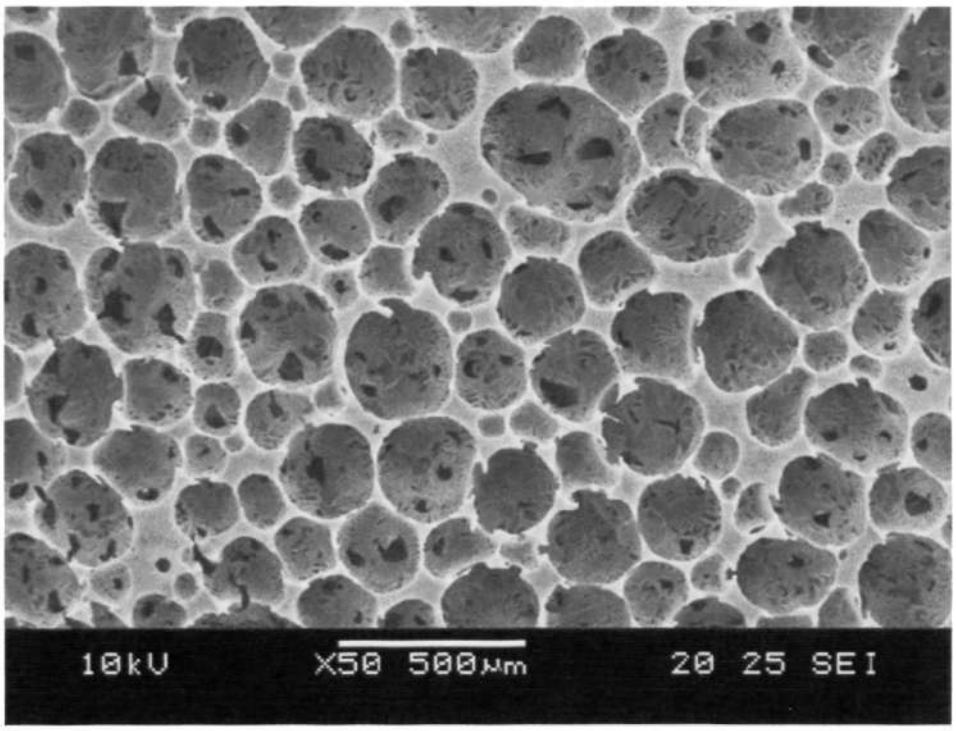

Figure 6.3: SEM micrograph (50×) of bottom surface of gelatin sponge.

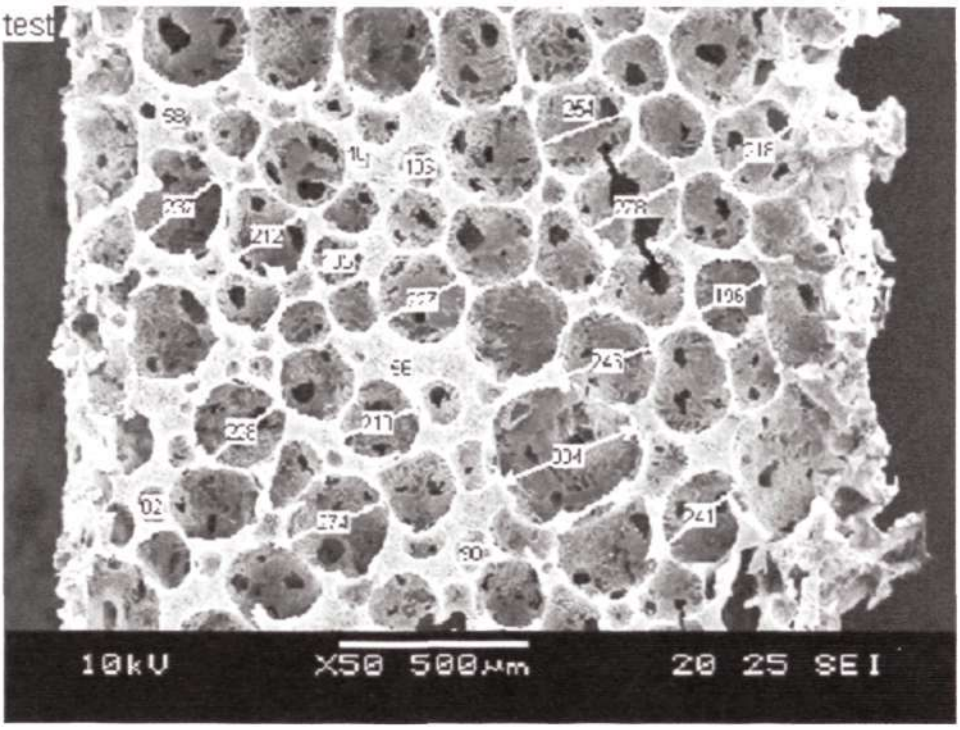

Figure 6.4: SEM micrograph (50×) of cross-section of gelatin sponge.

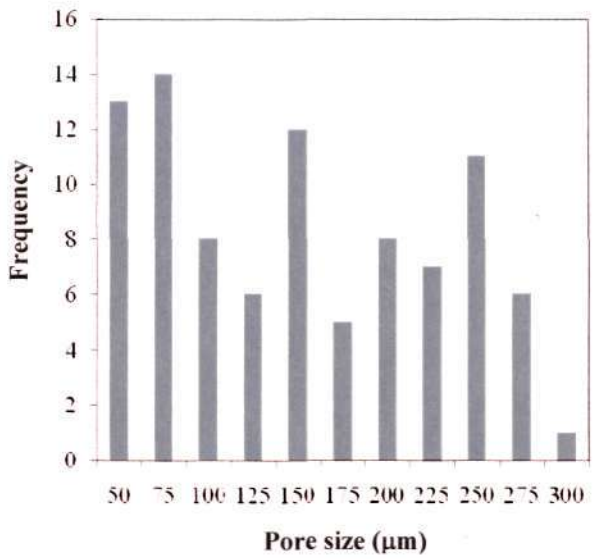

Figure 6.5: Histogram of pore size measurements on the SEM micrographs using ImageJ (n = 92).

6.2.2 Crosslink Index

Dehydrothermal (DHT) crosslinking was carried out for 4 days. A crosslink index (CL%) based on Ninhydrin test was calculated by equation 5.1.1 [90] and is shown in Figure 6.6 (i.e., the reduction of free amino-acid groups over time). The increasing trend in CL% appears to be exponential with respect to the treatment time and the CL% reached 55.55 ± 1.64 % on day 4. This result showed that the DHT method chemically crosslinked free amino acid groups in the gelatin structure. This crosslinking action was hoped to slow down the hydrolysis during culture. To test the rate of hydrolysis, a degradation study was carried out.

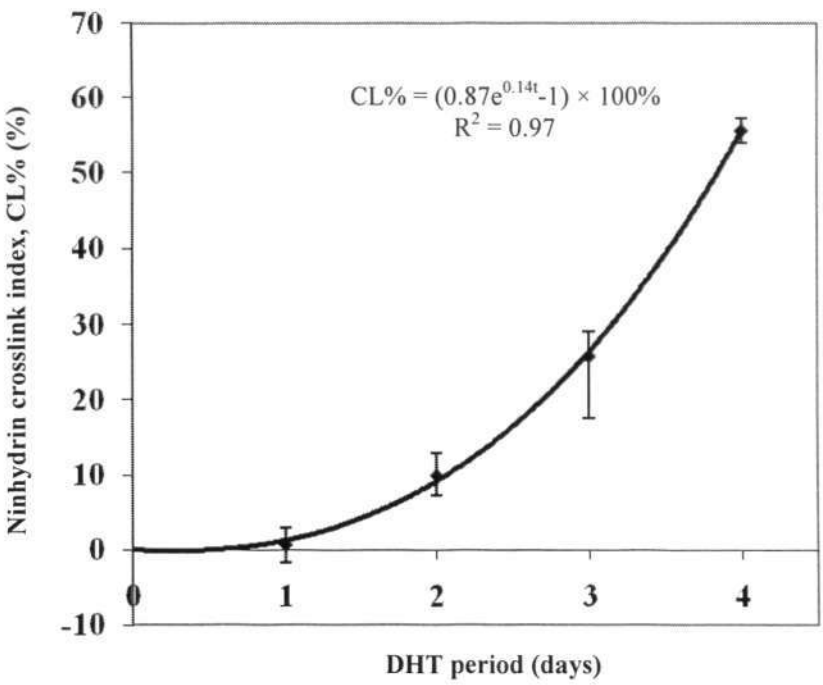

Figure 6.6: Crosslink index (mean ± SEM, n = 3) of DHT-treated gelatin sponge based on Ninhydrin test.

6.2.3 Degradation study

Figure 6.7 shows the degree of degradation over 14 days of a gelatin scaffold crosslinked by a 4-day DHT crosslinking. A rapid degradation was observed on the first day (43.35 ± 6.78 %). Subsequently, the degree of degradation remained between 34 and 48 % for the remainder of the testing period. Thus, the uncrosslinked part of the gelatin was dissolved rapidly on the first day and after that, crosslinked part of gelatin was resistant to dissolution during the testing period.

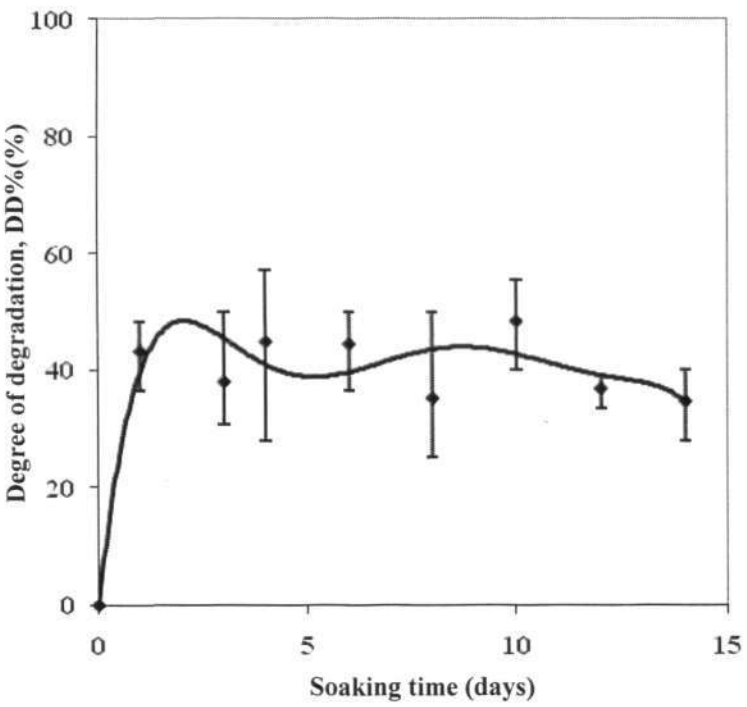

Figure 6.7: Degree of degradation (mean ± SEM, n = 3) after incubation in culture medium at 37 °C over a time course of 14 days

6.2.4 Mechanical test

Table 1 shows the tensile properties of dry and wet gelatin sponge. The ultimate tensile stress and tensile strain at fracture of the dry sample were 0.09 ± 0.02 MPa and 2.32 ± 0.49 %, respectively. The elastic modulus of the dry gelatine sponge was 0.028 ± 0.009 MPa. Surprisingly, once wet, the tensile strain at fracture was increased by almost 15 times (31.36 ±.2.36 %) and the elastic modulus increased by a factor of 2.Thus, the wet sponge material is considerably more elastic and deformable than the stiffer dry sponge.

Table 6.1: Tensile properties of dry gelatin sponge

Tensile properties:	Ultimate tensile stress (MPa)		Tensile strain at break (%)		Elastic Modulus (MPa)	
State	Dry	Wet	Dry	Wet	Dry	Wet
Mean ± SEM	0.092 ± 0.024	0.063 ± 0.010	2.32 ± 0.49	31.36 ± 2.36	0.028 ± 0.009	0.063 ± 0.019

6.3 Cells

6.3.1 Isolation of Porcine Esophageal Smooth Muscle Cells

I. Enzymatic Method

After cell isolation from esophageal smooth muscle by the enzymatic method, PESMCs were found to be attached and spread on the culture

dish on day 3 (Figure 6.8A). The cell morphology was elongated with dense cell cytoplasm and an oval-shaped nucleolus. Tissue debris is visible as scattered in the medium. Therefore, the media was replaced with fresh medium for further culture. Over time, the cell number was increased gradually and some fibroblasts (red circle) were occasionally observed in the dish (Figure 6.8B). On day 10, PESMCs reached confluency and subculture can be carried out.

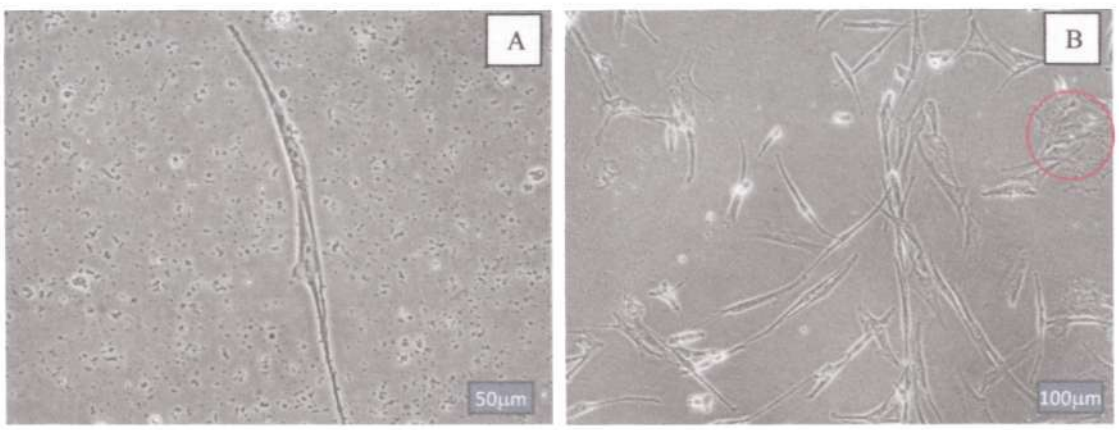

Figure 6.8: PESMCs isolated by enzymatic method: (A) on day 3 and (B) on day 5. On day 5, a few fibroblasts were observed (red circle).

II. Explant Method

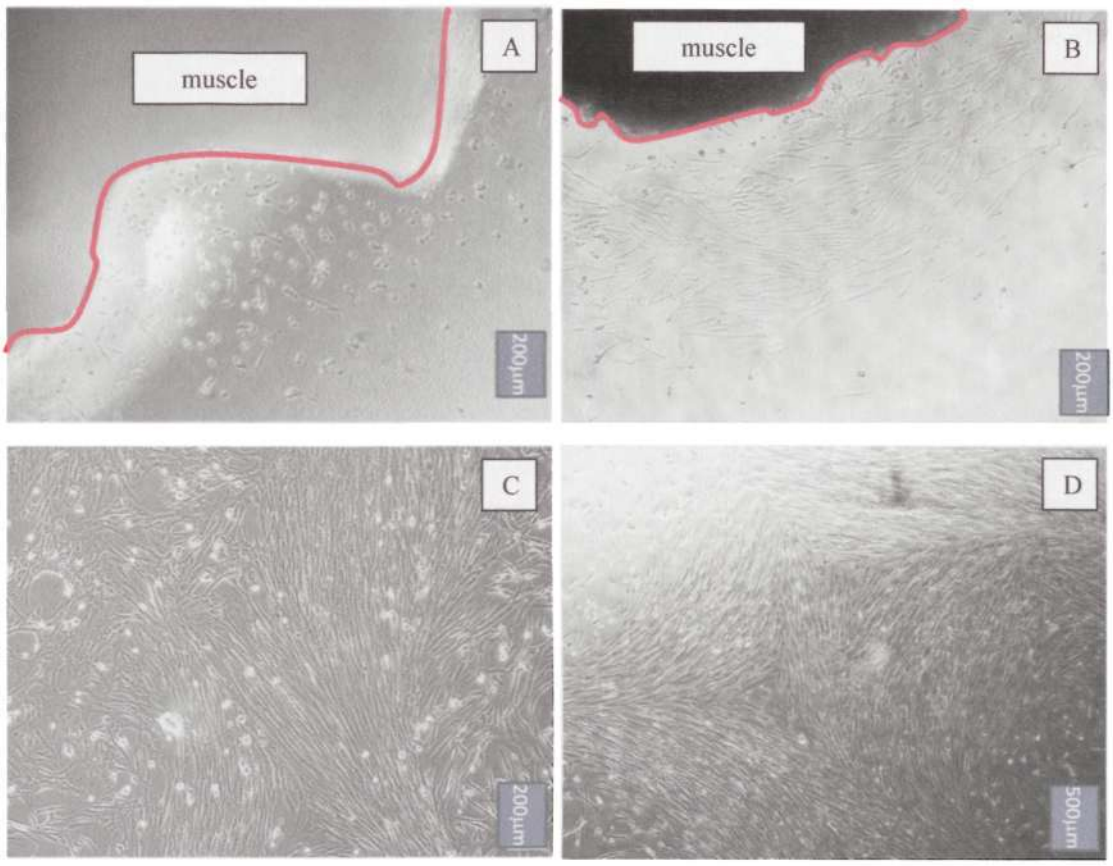

Figure 6.9: PESMCs isolated by explant method: (A) on day 7; (B) on day 10; (C) day 12 and (D) on day 20

The enzymatic method requires the use of an enzyme derived from bacteria while the explant method makes use of the property of cell migration. On day 7, there were some cells migrating from the tissue and scattering around the periphery of the muscle explant (Figure 6.9A). Some of the cells were still not fully spread at this stage. By day 10, cells scattering around the tissue were fully spread and adopted the normal smooth muscle cell morphology (Figure 6.9B). After removal of the muscle tissue (explant), the cells continued to expand and occupy the empty space of the culture dish (Figure 6.9C). On day 20, the cells were confluent and the PESMCs exhibited the

"hill-and-valley" pattern that is different from of the pattern exhibited by fibroblasts upon confluency (Figure 6.9D).

III. Immunohistochemistry

In order to confirm the identity of PESMCs, a molecular marker, smooth muscle-alpha actin, was checked at different passages of cells (p1, p3, p5 and p7). Figure 6.10 and Figure 6.11 show that all passages of PESMCs derived from both methods stained positive for the marker (in brown color).

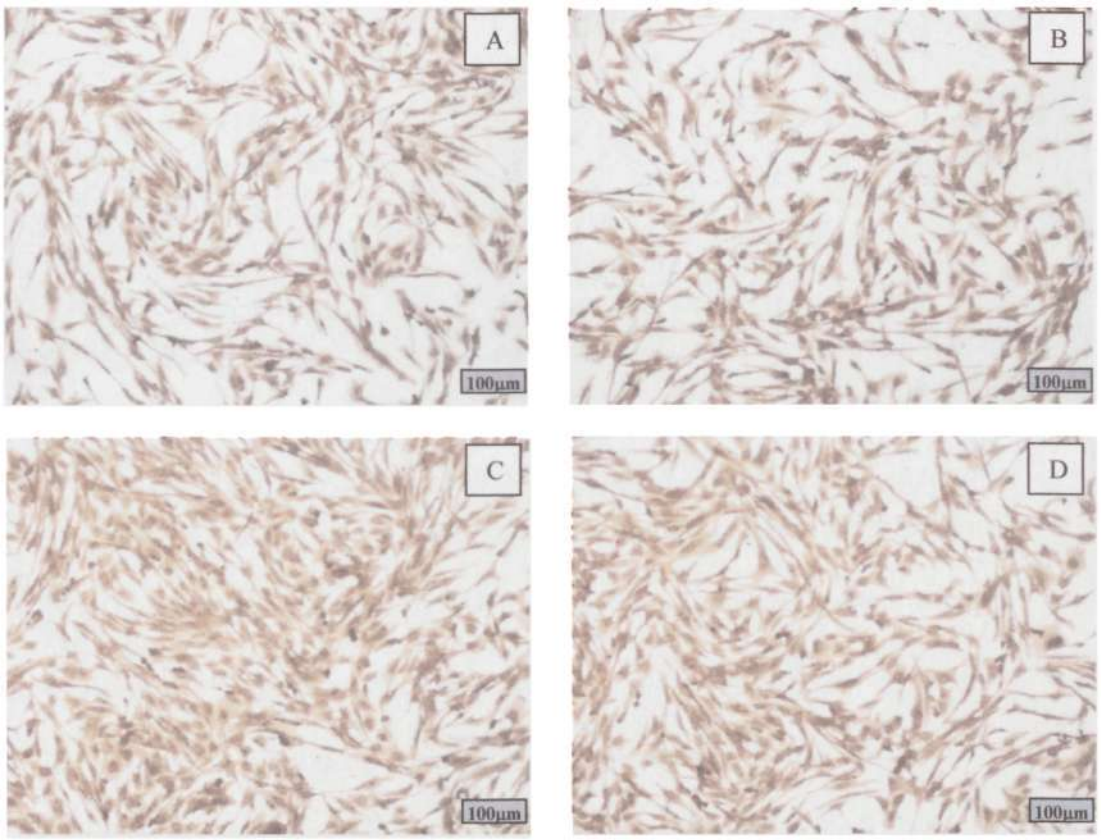

Figure 6.10: PESMCs isolated by enzymatic method positive for smooth muscle alpha actin in serial passage: (A) p1; (B) p3; (C) p5 and (D) p7

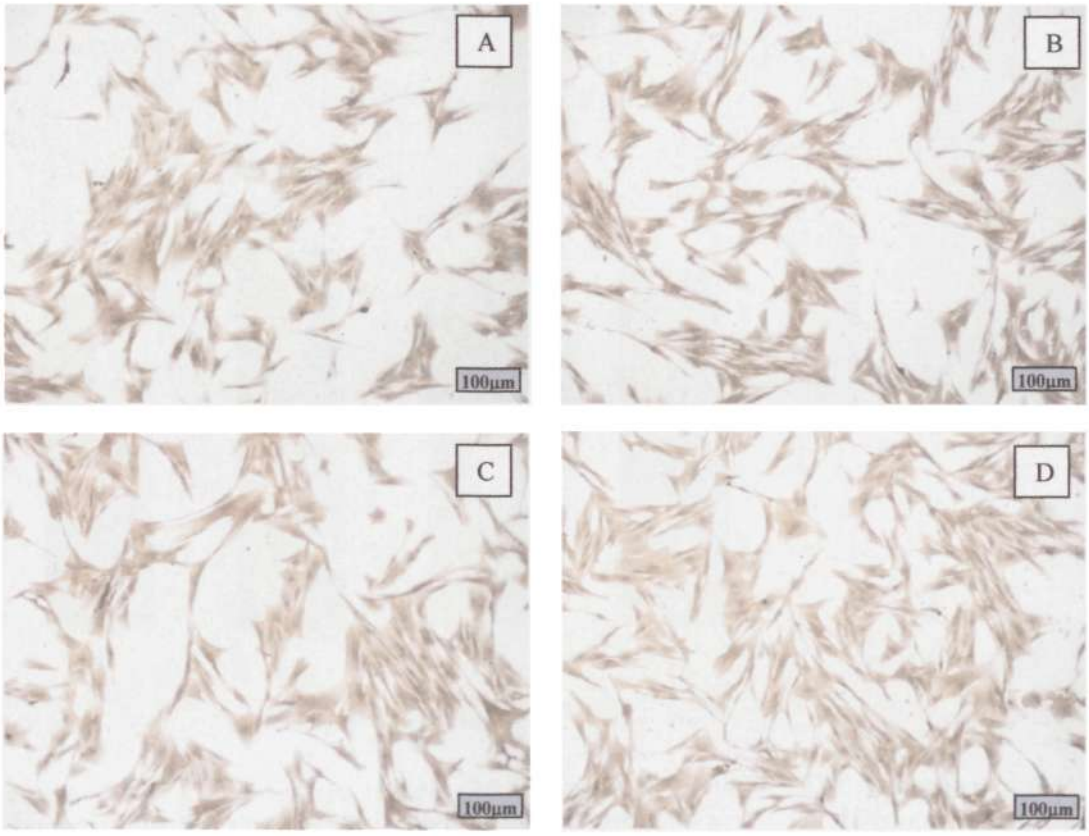

Figure 6.11: PESMCs isolated by explant method positive for smooth muscle alpha actin in serial passage: (A) p1; (B) p3; (C) p5 and (D) p7

IV. Cell Growth Characteristics of Subcultured PESMCs

PESMCs isolated from tissue had a limited proliferation capacity. After serial subculture of PESMCs, cell growth rate was reduced and finally, the cells were no longer able to subculture. Cells for tissue engineering should be able to proliferate so it is necessary to identify how many cell passages could be used for cell seeding experiment before the cell growth was significantly reduced.

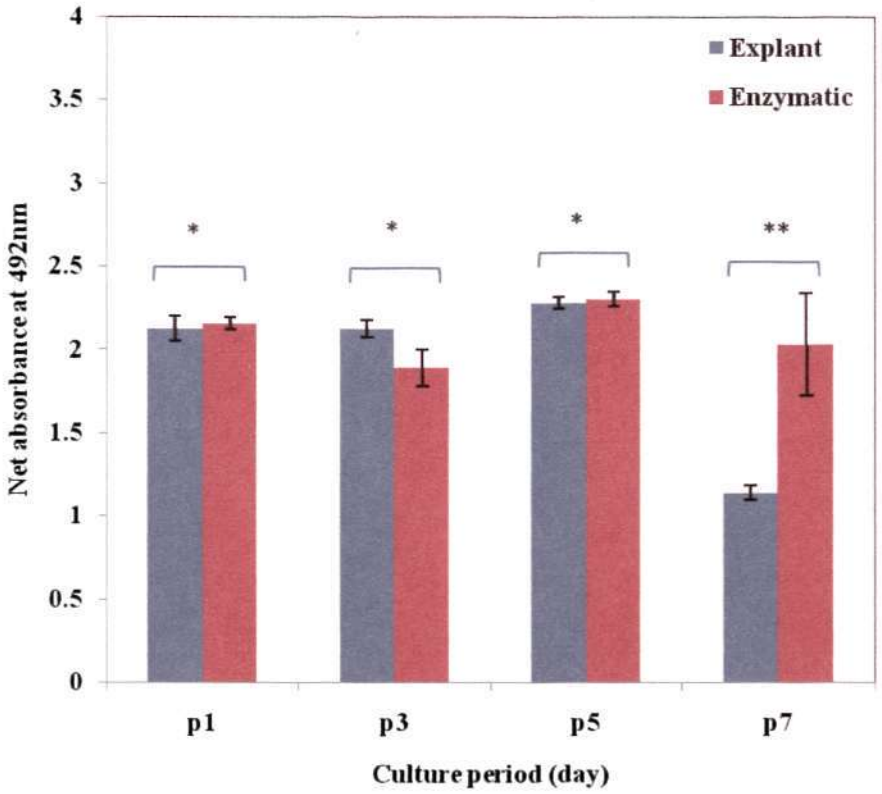

Figure 6.12: MTS proliferation results of PESMCs at passage 1, 3, 5 and 7: Net absorbance (mean ± SEM, n = 3, repeating twice) at wavelength of 492 nm over the culture period. * and ** represent the insignificant and significant difference between explant and enzymatic method, respectively ($p < 0.05$).

As shown in Figure 6.12, the net absorbance at 492 nm provides a measure of cell viability and proliferation on day 7 for different passages of PESMCs derived from two different isolation methods. No significant difference between explant and enzymatic method was observed for PESMCs up to p5 ($p < 0.05$). At p7, absorbance from both methods dropped and the reduction for the explant method was almost by one half compared with the previously passage indicating the stage of cell senescence. Therefore, all the cell study experiments were limited between p2 and p5 to confirm their proliferation capacity.

6.3.2 Cell-matrix Interaction

The phenotype and growth characteristics of PESMCs were characterized in the previous sections. In order to develop constructs for esophageal smooth muscle, the interaction of cells and scaffold developed was studied by seeding PESMCs into the gelatin scaffold and culturing the cell-scaffold construct for 14 days.

I. Histology: Hematoxylin and Eosin (H&E)

Figure 6.13A, B and C show H&E stained sections of PESMCs-seeded gelatin sponges after cultured for 3, 7 and 14 days, respectively. On day 3, cell attachment was complete but only a small number of cells (blue dots representing the cell nuclei) scattered across the scaffold (Figure 6.13A). By day 7, the cells grow rapidly near the surface and populated the scaffold to a depth of 200 μm from the surface (Figure 6.13B). During the following week, the shrinkage of the tissue construct was observed, probably due to the contraction force exerted by the cells on the scaffold. On day 14, the surface cells continued to grow denser but compared with day 7, there was no significant internal cell growth or cellular advance from the surface into the construct interior (Figure 6.13C).

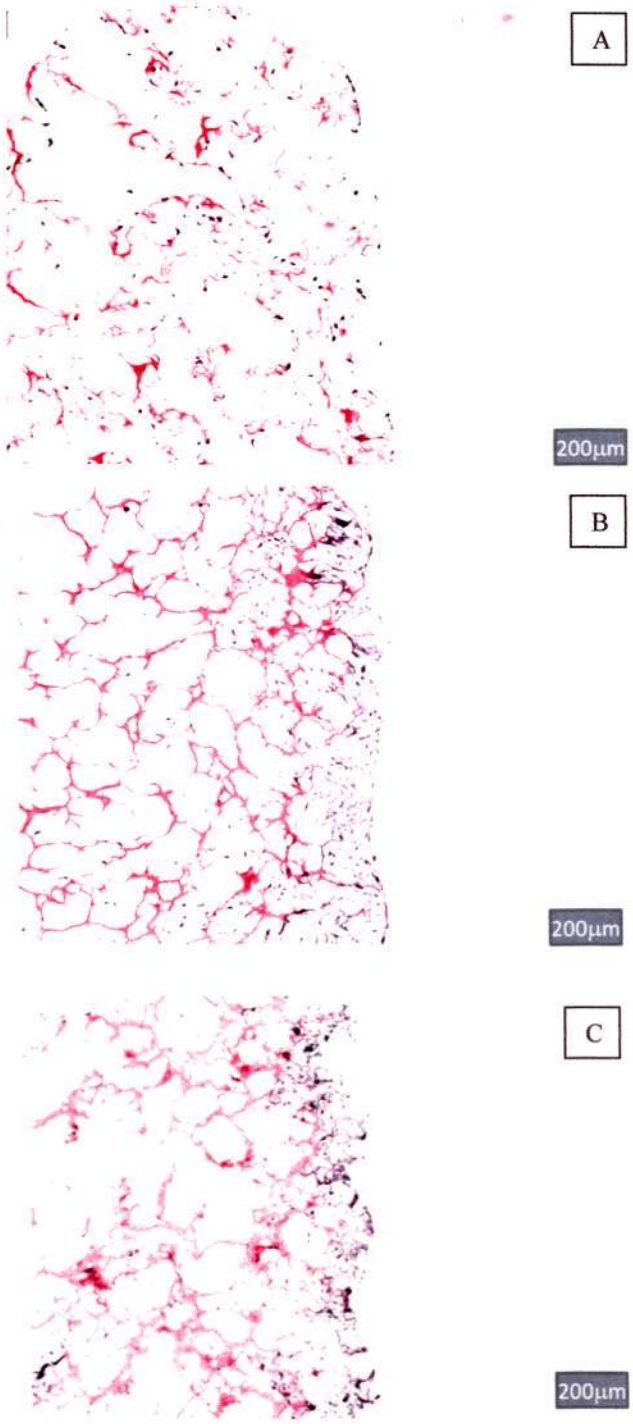

Figure 6.13: H&E micrographs for PESMCs seeded gelatin scaffolds after culturing them for (A) 3 days; (B) 7 days and (C) 14 days.

Figure 6.14 presents DNA data from DNA measurements on seeded scaffolds over a two week time period. The content of DNA gives a measure of number of cells in the construct at the harvest point. The control column on the far right shows that the DNA content detected in a scaffold without cell seeding is insignificantly small. For the cell-seeded scaffolds, the DNA content decreased slightly over the first 3 days due to the lag phase (non-growth period). After the lag phase was passed and cells started to adapt to the new ECM environment, SMCs started to proliferate rapidly from day 3 to day 7. The increase in DNA content in the scaffolds from day 3 to day 7 was greater than a factor of three. From day 7 to 14, the increase was relatively small which implies that the growth had reached a plateau in the given culture environment. This study demonstrates the gelatin scaffold developed in this study provides a good interaction environment for the proliferation of PESMCs.

Up to this point, all the cell and construct culture experiments were conducted in the 5 % CO_2 incubator, which is the conventional culture. To implement the designed culture system, PESMCs have to adapt, and expand in the designed incubation unit with a conditioned medium. To test the feasibility of the new incubation unit, it was tested in terms of temperature distribution and temperature response since temperature stabilization is essential for cell culture, and the composition of the culture medium was adjusted to stabilize both pH and osmolality so that cells could adapt in the new culture environment.

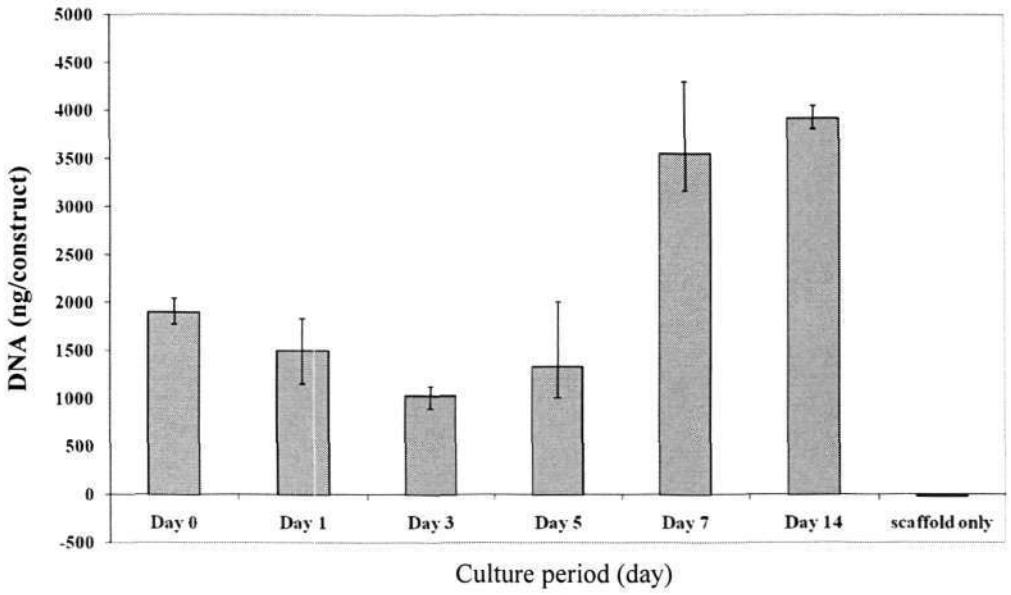

Figure 6.14: DNA content (mean ± SEM, n = 3) of PESMCs seeded gelatin scaffold after culturing for different times.

6.3.3 Adaptation of Cell Culture in Air Environment

To conduct the proposed bioreactor experiment in this project, PESMCs must be cultured in the designed incubation unit (IU), which was validated in term of temperature response of the system.

I. Temperature response of IU

a. Spatial temperature distribution

Temperature is important to maintain normal cell physiology. Any cold spot in the culture unit may induce uneven or unhealthy cell growth. Figure 6.15 shows the temperature distribution of the culture area in the IU. The maximum and minimum temperatures were 36.8 and 36.3 ^{o}C, respectively. The temperature was reduced from

the right (where the warm air vent is located) to the left and the heat front advanced diagonally towards both left corners. Despite the slight unevenness of the temperature, the overall temperature difference of 0.5 °C (or ± 0.25 °C) was considered small enough and fell within the acceptable limit (± 0.5 °C) suggested by Freshney [55] to ensure repeatability of the cell growth.

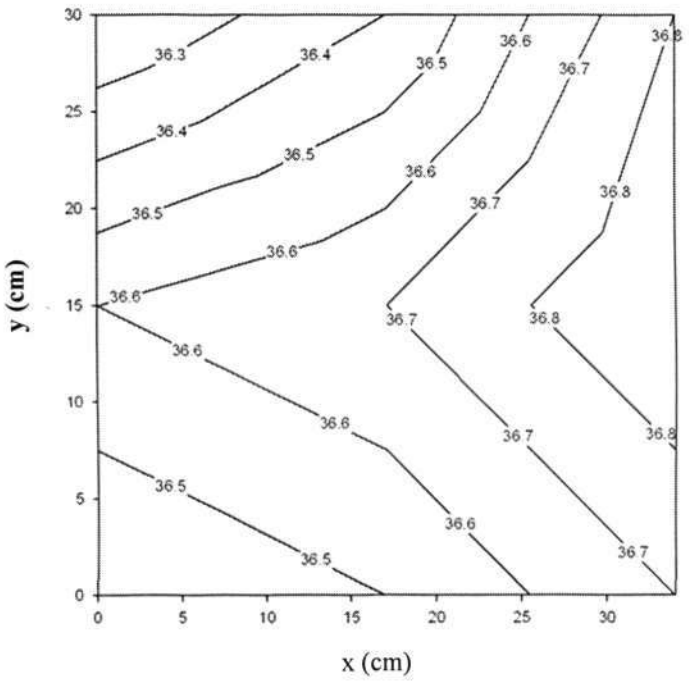

Figure 6.15: Temperature distribution of culture area in the incubation unit

b. Temporal stabilization of temperature

After any disruption of the IU such as opening and closing the unit during handling, temperature was abruptly changed and the feedback control of the heating module adjusted the temperature of the unit. Prolonged thermal overshooting beyond the physiological temperature (> 38.5 °C) or lack of temperature stabilization could cause cell death or uneven cell growth [30, 55]. The top lid of the unit was intentionally

lifted up for two minutes to create a thermal disruption and then closed. The temperature was measured at the centre of the IU over time and the result is shown in Figure 6.16.

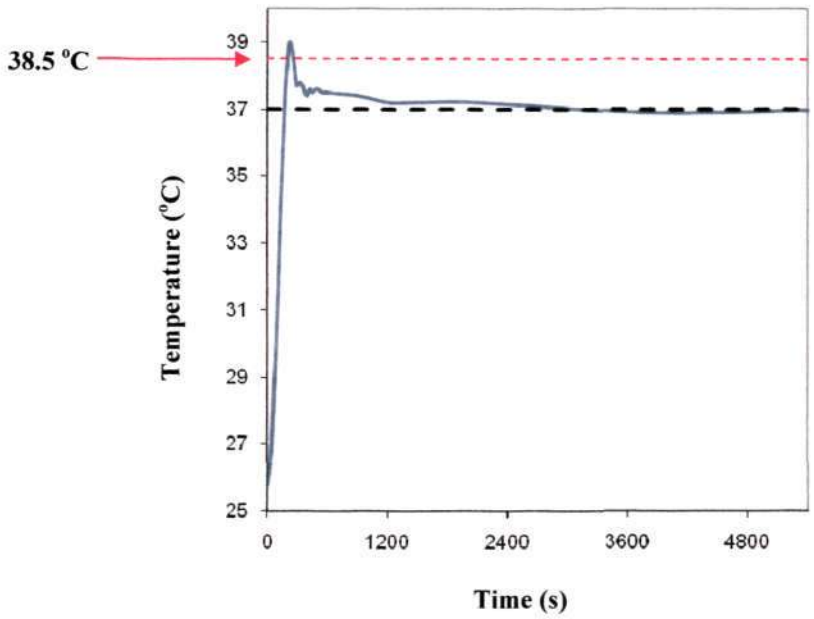

Figure 6.16: Temperature recovery after the incubation unit was open for two minutes before it was closed.

After the lid was closed, the temperature was restored and overshot slightly to 39 °C at t = 225 s and the temperature returned to 98 % and 99.5 % of the set point (37 °C) at t = 285 s (4.75 minutes) and t = 1200 s (20 minutes), respectively. The overshoot period was less than 45 s. With the overshoot temperature (T_{os} = 39 °C) and the overshoot period ($t \approx 45s$) measured, the penetration distance to reach 38.5 °C after the overshoot period was estimated at about 1 mm from the top surface of the polycarbonate top plate using equation 5.3.6. It accounted for only about 10 % of the thickness of the top plate, which is 1 cm thick. By using the same equation, the temperature on the medium

side is 37.00654 °C, the rise of which from 37 °C is relatively small. Therefore, the interior of the chamber was able to maintain below 38.5 °C over the overshoot period. Furthermore, the temperature stabilization was considered reasonable that heating module took about 3 minutes to reach around the set point whereas the conventional incubator in the lab (Sanyo MCO-17AIC) required about 11 minutes reaching the set point with the similar disruption. In addition to regulating the temperature of the culture environment, the culture medium has to fulfill the requirement of normal pH and osmolality in the air environment.

II. Conditioning culture medium

a. pH

The conventional cell culture DMEM contains 44 mM bicarbonate and gradually becomes alkaline after long term exposure in an air environment. It is therefore necessary to reduce the amount of bicarbonate in order to adjust the pH around set point (pH = 7.4) in air environment without supplementation of CO_2. Furthermore, a second buffer needs to be added as a substitute for the reduction of bicarbonate. To vary the buffer recipe for air environment, a combination of bicarbonate and HEPES was tested on the medium without pre-adding bicarbonate beforehand. Figure 6.17 shows the pH measured after stabilization in the IU for 2 and 10 days.

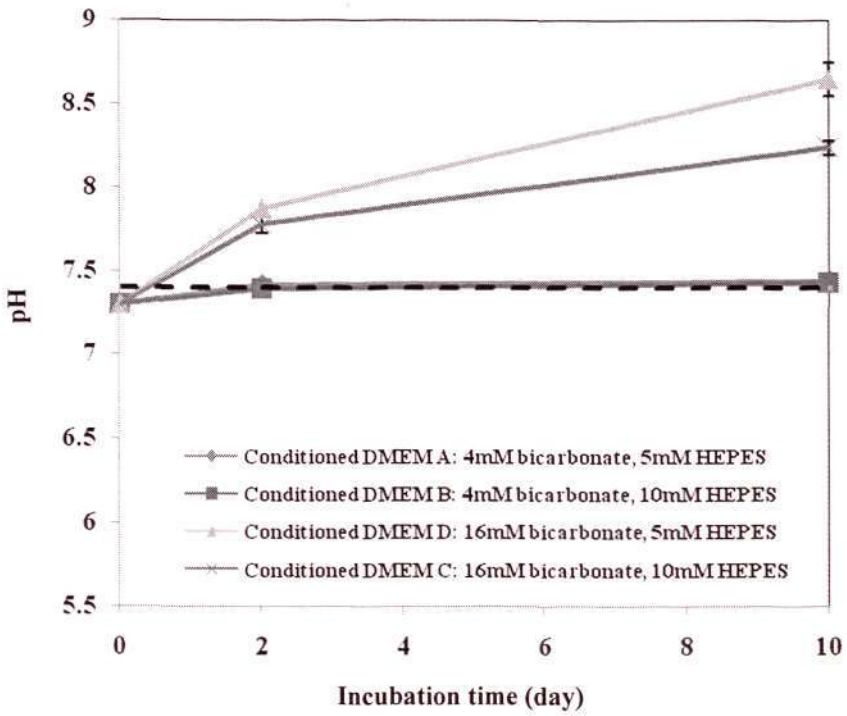

Figure 6.17: pH (mean ± SEM, n = 3) of different conditioned medium with bicarbonate and HEPES at different times in the incubation unit.

Even when bicarbonate was reduced from 44 to 16 mM, the HEPES buffer was not able to stabilize pH at 7.4 in air culture although the pH had been adjusted to 7.3 before incubation. On the other hand, reduction of bicarbonate to 4 mM, with 5 or 10mM of HEPES stabilized the pH around 7.4 for the test period. However, the osmolality of new buffer system was too low to match that of the conventional DMEM. Extra sodium chloride (NaCl) was added to raise the medium osmolality to the desired level.

b. Osmolality

NaCl was added during medium preparation to adjust osmolality. Figure 6.18 shows the increasing trend of osmolality by adding NaCl into conditioned media buffered with 4 mM bicarbonate and two levels of HEPES.

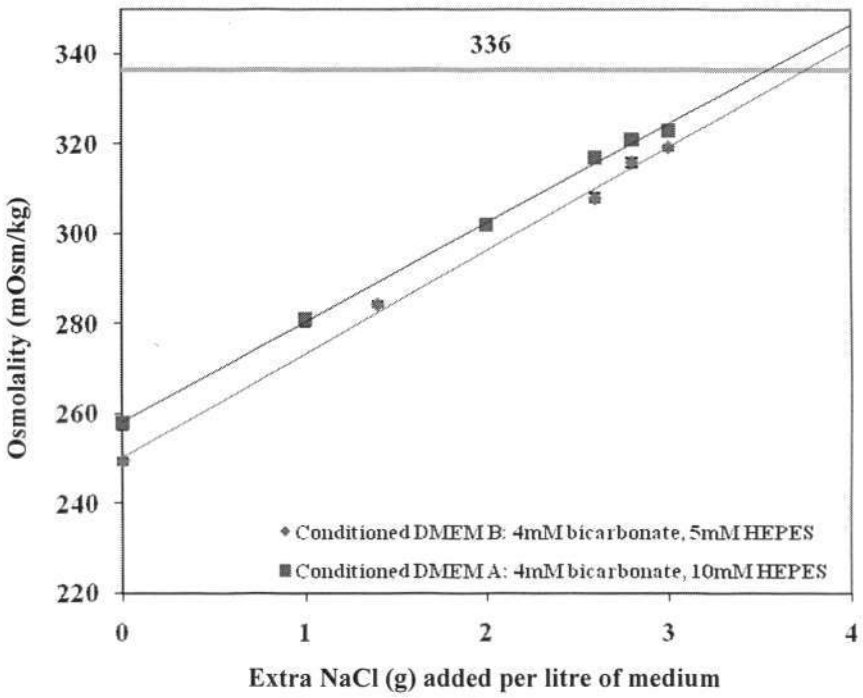

Figure 6.18: Osmolality (mean ± SEM, n = 3) of conditioned medium vs. extra salt added per liter of medium

The conventional DMEM has an osmolality of 336 mOsm/kg while the medium buffered with 4mM bicarbonate and HEPES was as low as between 250 (5 mM HEPES) and 256 mOsm/kg (10mM HEPES) which was at least 25 % lower than the conventional level. For both media, a linear relationship was observed between the quantity of salt added and the osmolality. By using this relationship, an estimate of NaCl per liter of medium was made in order to match the required osmolality (336 mOsm/kg). The pH and osmolality were re-confirmed for the final conditioned

medium. Since pH was tested in a cell-free environment, the higher HEPES concentration (10 mM) was used with 4 mM bicarbonate to increase buffer capacity for cell culture and 3.45 g of NaCl was added per liter of medium. Figure 6.19 shows the adoption of normal cell morphology of PESMCs cultured in the IU with the conditioned medium.

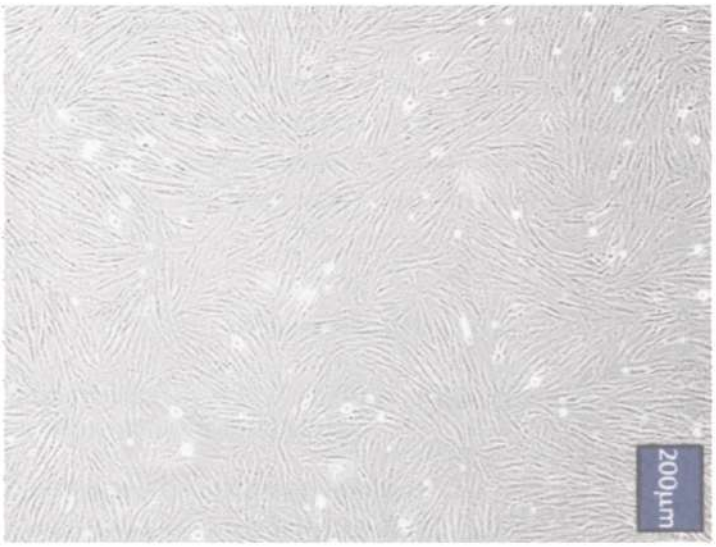

Figure 6.19: An example of PESMCs cultured with conditioned medium in the designed incubation unit.

c. Cell mass and size

Cell mass and size were measured for PESMCs under air culture to complete the study of their physical characteristics. Different cell numbers were weighed without drying the cells since more than 90 % of cell mass is contributed by water and the real mass of a cell should be measured at wet state rather than dry state. Figure 6.20A shows the wet mass verse cell number and the linear trend line gives the gradient which we can estimate the mass per single PESMC. In this case, cell mass of PESMC is approximately 4.6 ng/cell. The rather large standard deviation was due to the degree

of drying of the sample because it is difficult to just remove the water content outside the cells. It may cause either insufficient drying or slight dehydration of the cell sample. On the other hand, cell size was obtained by measuring more than 300 cells captured in micrographs and the cell area histogram is shown in Figure 6.20B. The results show that cell area of PESMCs ranged from 1.17 to 5.38 × 10^{-4} mm^2 and the mean area was 2.30 ± 0.59 × 10^{-4} mm^2. By assuming a perfect circle for each cell in unattached form, the cell radius was 8.55 μm with corresponding cell size (volume) to be 2.6 × 10^{-6} mm^3.

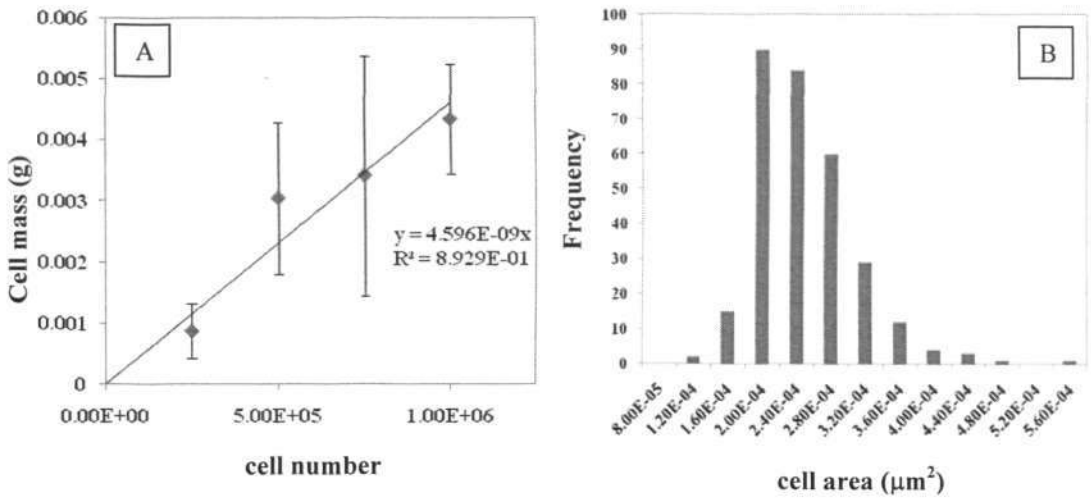

Figure 6.20: Estimation of (A) cell mass (mean ± SEM, n = 3) and (B) size distribution of the PESMCs (n = 301).

III. Culture of PESMCs in High/Low Glucose Environment

a. O_2 requirement of PESMCs

Oxygen profiles were measured from the medium surface down to the well bottom on which cells attached. In order to show the oxygenation state of the cells, Figure 6.21A

summarizes the oxygen concentration at the well bottom or $C_{O,\beta}(H)$ on each day. $C_{O,\beta}(H)$ decreased over time due to an increase in cell number. The distinction between two levels of glucose (1 g/L as low glucose and 4.5 g/L as high glucose) did not appear until day 4 where the $C_{O,\beta}(H)$ for high glucose reduced below that for the low glucose and $C_{O,\beta}(H)$ appeared to reach plateau. The $C_{O,\beta}(H)$ for high and low glucose were recorded on day 6 at 93.64 ± 0.69 % and 95.97 ± 1.10 %, respectively. However, a student t-test showed that the oxygen level at the well bottom over all 6 days was insignificantly different ($p>0.05$). This was expected since only a monolayer of cells was cultured and the cellular oxygenation is usually not a major problem even if cells are confluent. Diffusion is sufficient to supply oxygen to the cells on the well bottom as long as the medium height is sufficiently low.

The oxygen consumption rate per cell at different cell density (shown in Figure 6.21B) appeared to be dependent of the confluency of the culture. At the onset after subculture, cell density was low and cell attachment and spread required higher oxygen demand, which may cause the increase in oxygen consumption per cell. After cells attached and spread; however, oxygen consumption rate per cell was reduced gradually with increasing cell density.

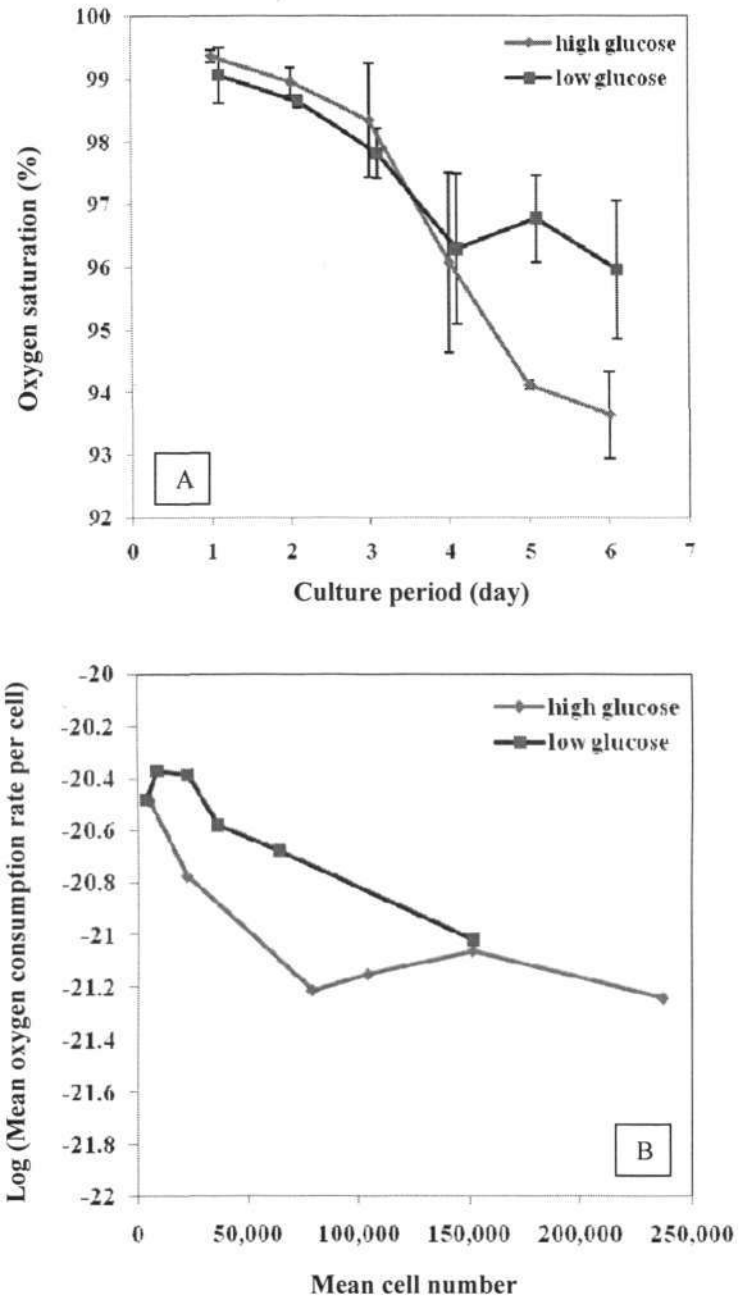

Figure 6.21: (A) Oxygen saturation (mean ± SEM, n = 3) at well bottom over culture period in high (4.5 g/L) and low glucose (1 g/L) DMEM (n = 3 for each day). (B) Log(mean oxygen consmuption rate per cell) versus mean cell number.

b. Glucose Consumption

The glucose concentrations were also measured in the medium after the oxygen measurements. As shown in Figure 6.22A, the change in glucose concentration was shown to be negligibly small over the culture period at two levels of glucose in medium (1g/L as low glucose or 4.5g/L as high glucose). These data implies that glucose is also not the limiting growth factor in the monolayer culture of PESMCs. Estimates of glucose consumption rate per cell (Figure 6.22B) showed a resemblance to its counterpart for oxygen in that cells at low density after subculture required a higher energy source for cell attachment, cytoplasmic reorganization and spreading, which cause increases in both oxygen and glucose requirement per cell. Similarly, the glucose consumption rate per cell was gradually reduced to a lower level as the cells were increasing in number.

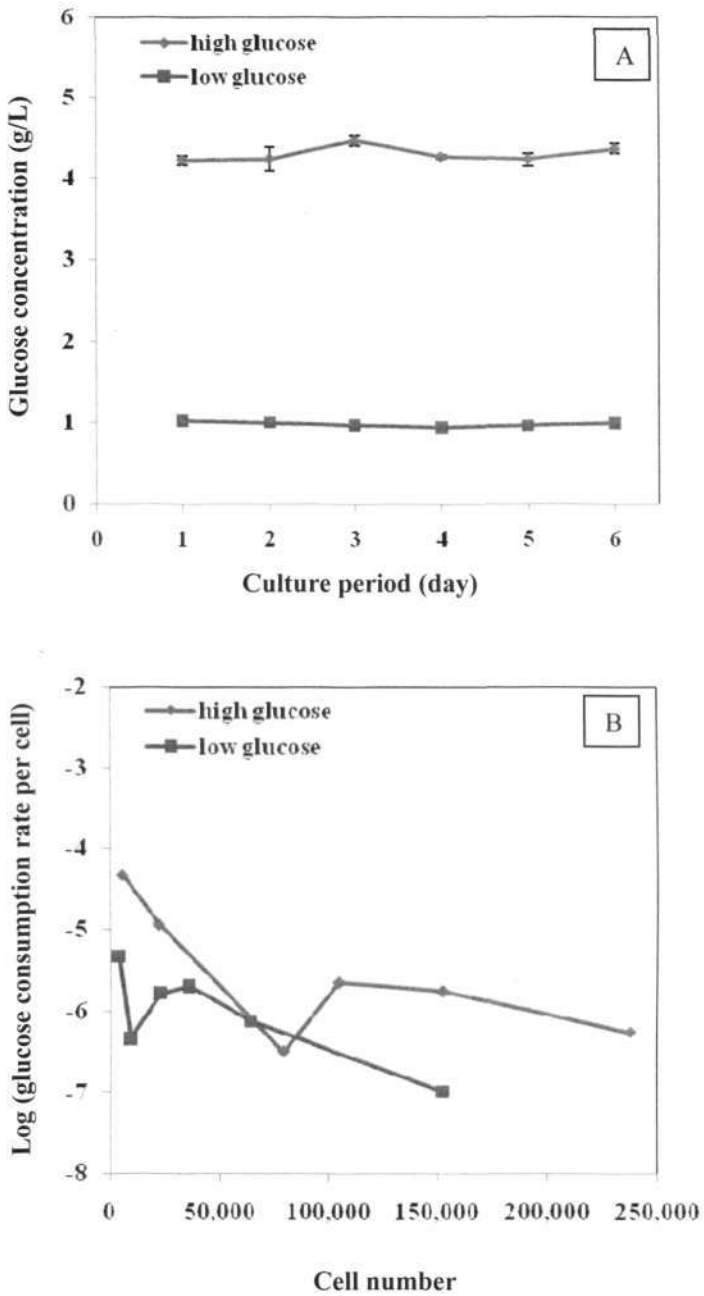

Figure 6.22: Glucose consumption for PESMCs cultured in the high (4.5 g/L) or low (1.0 g/L) glucose DMEM. (A) Glucose concentration (mean ± SEM, n = 3) in medium over culture period and (B) log(glucose consumption rate per cell) versus cell number.

c. Cell Proliferation

On the other hand, the glucose level affected cell growth as shown in Figure 6.23. Except the day 1, cell proliferation from the high glucose group was significantly higher than that of low glucose ($p < 0.05$). This occurred when oxygen is not limiting in the culture so that other nutrient sources could affect the growth rate. If oxygen is scarce in the system, growth would cease even if glucose was in excess. Under sufficient oxygenation, however, glucose availability may cause cellular adjustments in the glucose utilization pathways for cell growth, as suggested in this result.

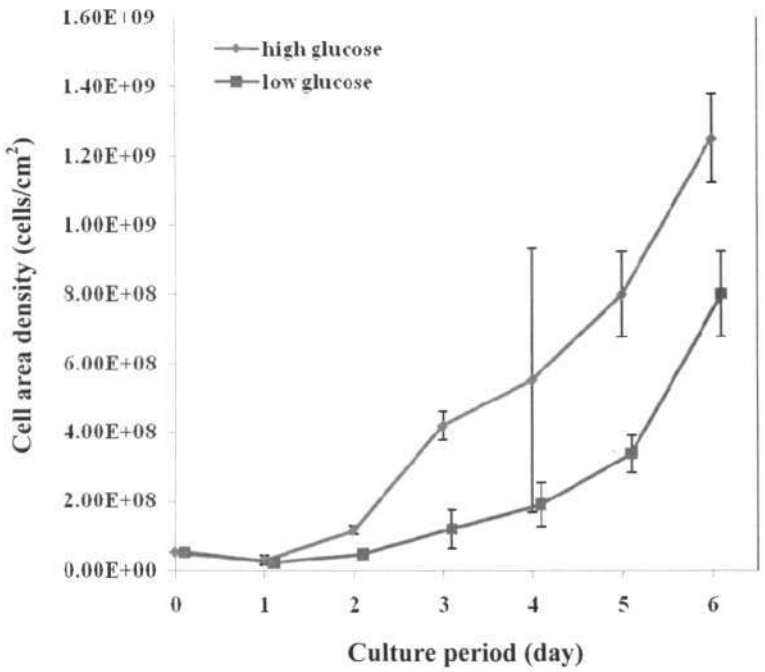

Figure 6.23: Increase in cell density (mean ± SEM, n = 3) over culture period in high (4.5 g/L) or low (1.0 g/L) glucose DMEM.

6.4 Bioreactor Culture

6.4.1 Histology

PESMCs-seeded gelatin scaffolds were cultured under static condition, and under single- or double-sided flow configurations with flowrates of 0.272 and 0.545 ml/min for up to 10 days. Histological staining allowed a visual examination of cell distribution across the thickness of the construct. Figure 6.24, Figure 6.25, Figure 6.26, Figure 6.27 and Figure 6.28 are the micrographs of sections of the tissue constructs stained by Hematoxylin and eosin (H&E) under static condition (no flow), one sided flow (0.272 ml/min), one-sided flow (0.545 ml/min), two-sided flow (0.272 ml/min) and two-sided flow (0.545 ml/min). Since gelatin was also heavily stained during the process which severely masked the stained cells when observing at lower magnifications, the micrographs was enhanced by lightening the heavily dyed scaffold area using "subtracting background" in ImageJ. In these micrographs, blue dots represent the cell nuclei with purplish pink-colored cytoplasm.

I. Static Culture

In the static culture, the construct was placed in the Petri dish and suspended in the culture medium. As shown in Figure 6.24, the top surface of the construct (Figure 6.24A and B) was consistently more populated with cells than the area within the core and bottom regions (Figure 6.24C and D) at both time points. On day 10, a higher cell proliferation was observed and the cell layers (see red triangle in Figure 6.24B) were regularly observed over the top surface (Figure 6.24B). However, the cellularity

remained relatively low in the bottom region of the construct after 10 days of culture (Figure 6.24D) compared to the top region where is close to the air-medium interface.

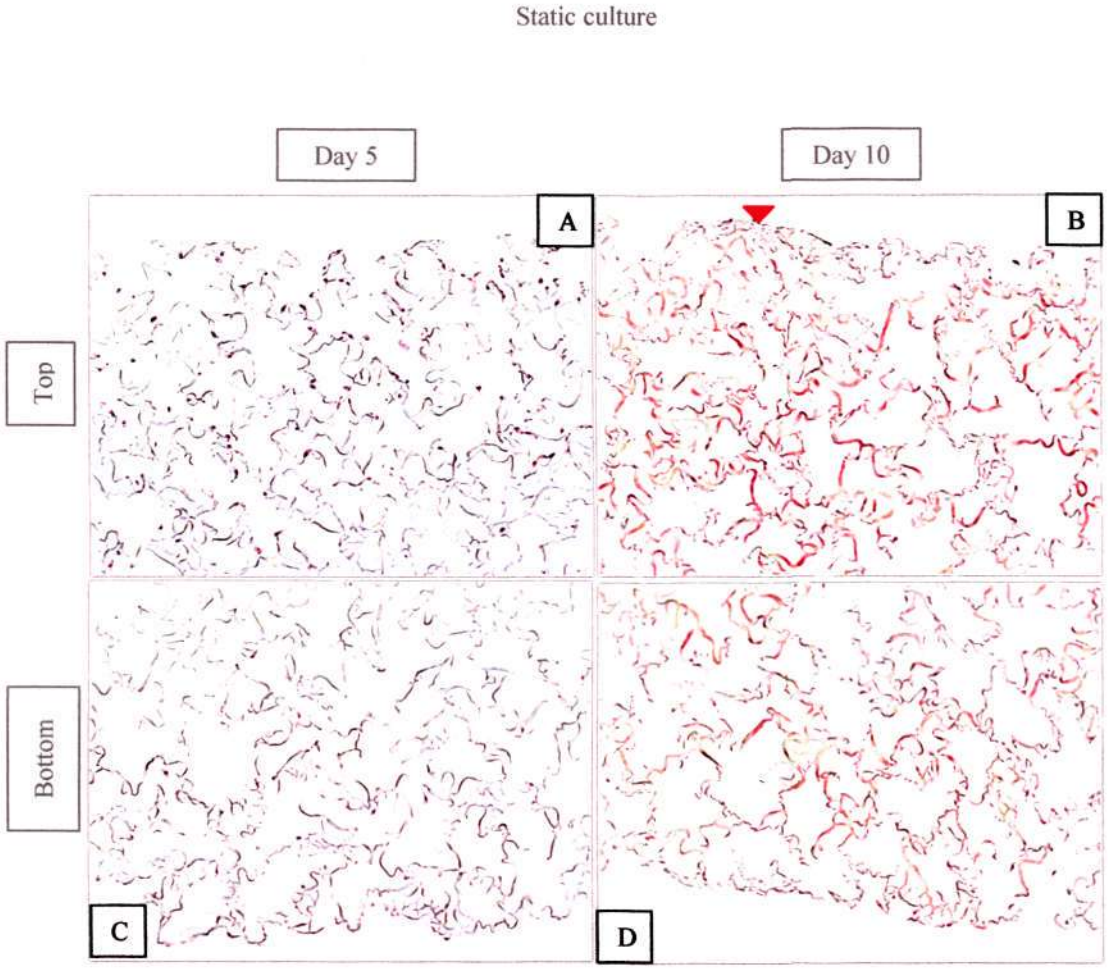

Figure 6.24: H&E micrographs of tissue constructs seeded with PESMCs cultured under static culture: (A) top portion, 5-day culture; (B) top portion, 10-day culture; (C) bottom portion, 5-day culture and (D) top portion, 10-day culture.

II. Single Flow Configuration

As shown in Figure 6.25 and Figure 6.26, under bioreactor culture with one side of the construct exposed to medium flow (single flow), cells proliferated faster near the top surface with medium flow at both time points compared with the bottom surface with no flow. Instead of dense cell layers coverage over the top surface observed in the static culture on day 10 (Figure 6.24B), cells penetrated deeper into the scaffold for both flowrates in the top portion of the construct (Figure 6.25B and Figure 6.26B). However, cells were less detectable near the bottom portion of the construct beneath which was an impervious surface (Figure 6.25C and D and Figure 6.26C and D). By comparing the H&E micrographs between two applied flowrates, it is still not obvious to identify their difference in terms of cell distribution.

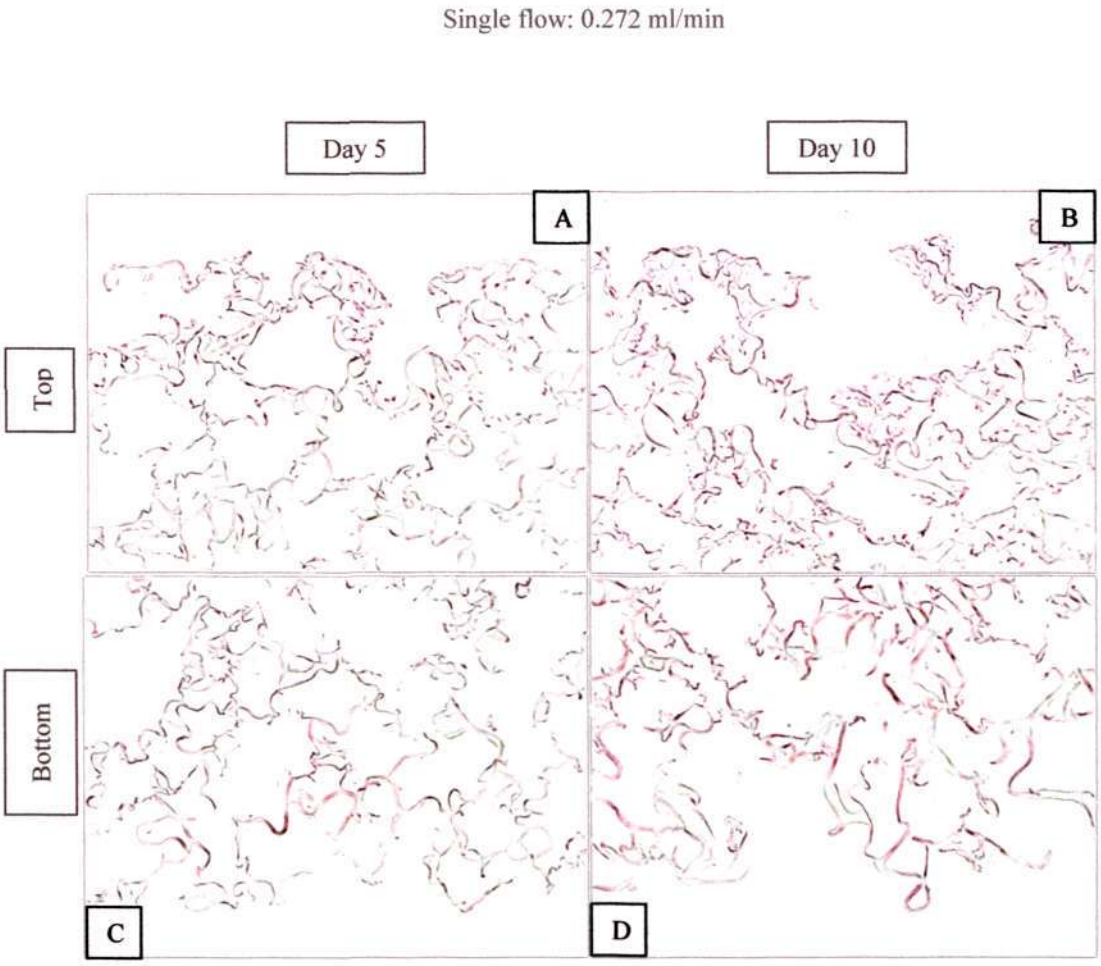

Figure 6.25: H&E micrographs of tissue constructs seeded with PESMCs cultured in a single flow configuration at a flowrate of 0.272 ml/min: (A) top portion, 5-day culture; (B) top portion, 10-day culture; (C) bottom portion, 5-day culture and (D) top portion, 10-day culture.

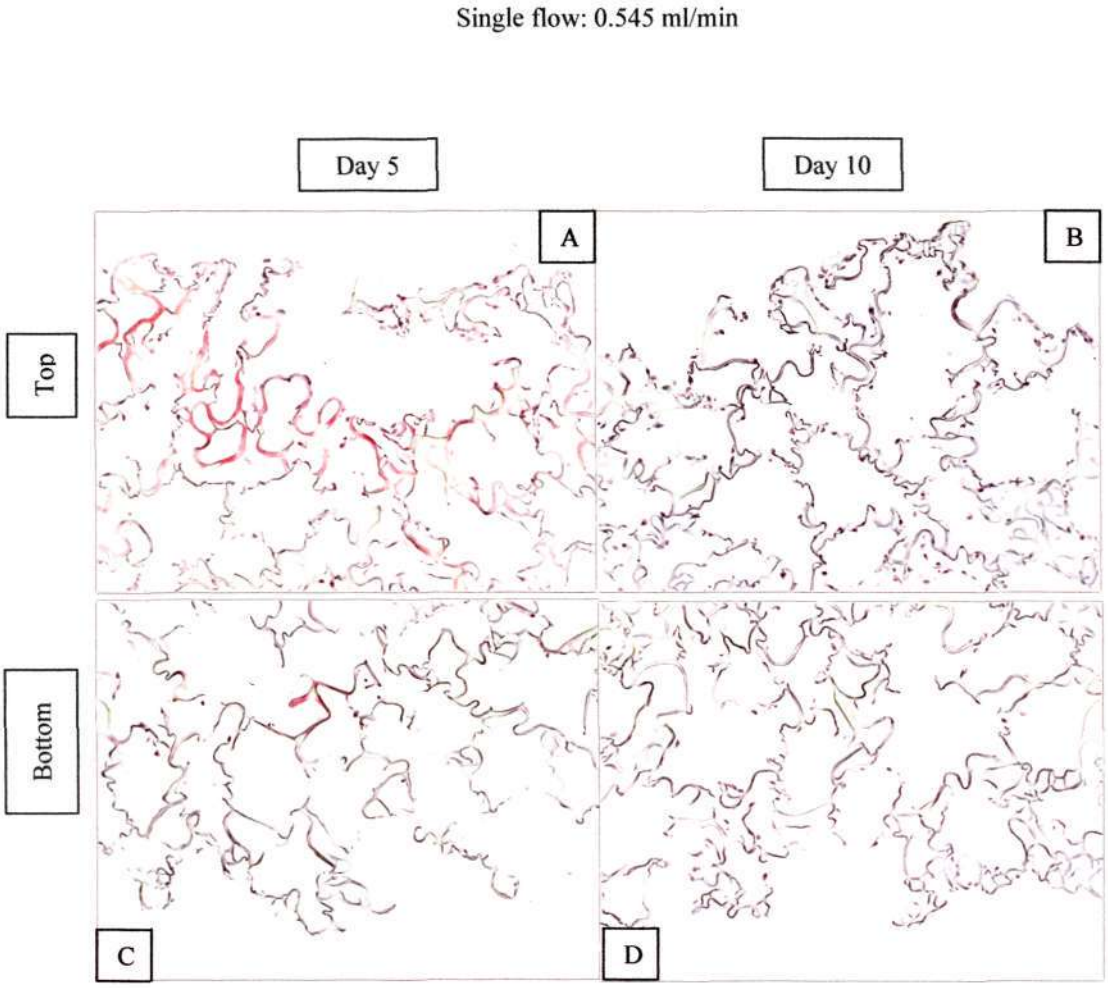

Figure 6.26: H&E micrographs of tissue constructs seeded with PESMCs cultured in a single flow configuration at a flowrate of 0.545 ml/min: (A) top portion, 5-day culture; (B) top portion, 10-day culture; (C) bottom portion, 5-day culture and (D) top portion, 10-day culture.

III. Double Flow Configuration

In order to increase the surface area of the construct exposed to the oxygen-rich medium, both surfaces were exposed to medium flow in the double flow configuration. As shown in Figure 6.31 and Figure 6.32, such a configuration appeared to result in a higher cellularity and a more uniform cell distribution compared with the static culture and single flow configuration. Flowrate also showed an effect on the cell

growth in the construct: 0.545 ml/min led to a more substantial growth from day 5 to day 10 than did to 0.272 ml/min.

These images demonstrate that different culture conditions can cause very distinct pattern of cell distribution. Low local cellularity consistently occurred in both static culture and in the single flow configuration in the core region and near the bottom side of the construct; and locations are believed to be mass transfer-related. With medium on both sides of the constructs in the double flow configuration, this limitation appeared to be reduced and cell proliferation was more uniform. Since H&E micrographs only provided a rather qualitative observation on the cell distribution, a more quantitative study was undertaken to correlate the spatial oxygen distribution with cell distribution to gain more insights on their interrelationship. H&E procedure stained all the features in the construct (e.g., cells, ECM and gelatin materials) and it could be difficult to perform an image analysis with the interferences of the other features (mainly gelatin scaffold). Therefore, sections were stained in DAPI which is a fluorescence nucleus marker and under a fluorescence microscope, only the cell nuclei are shown in blue fluorescence on a dark background (as shown in Figure 5.13) such that cell counting can be facilitated easily using the procedure described in section 5.3.5VIII. The cell distribution will be presented in 6.4.3.

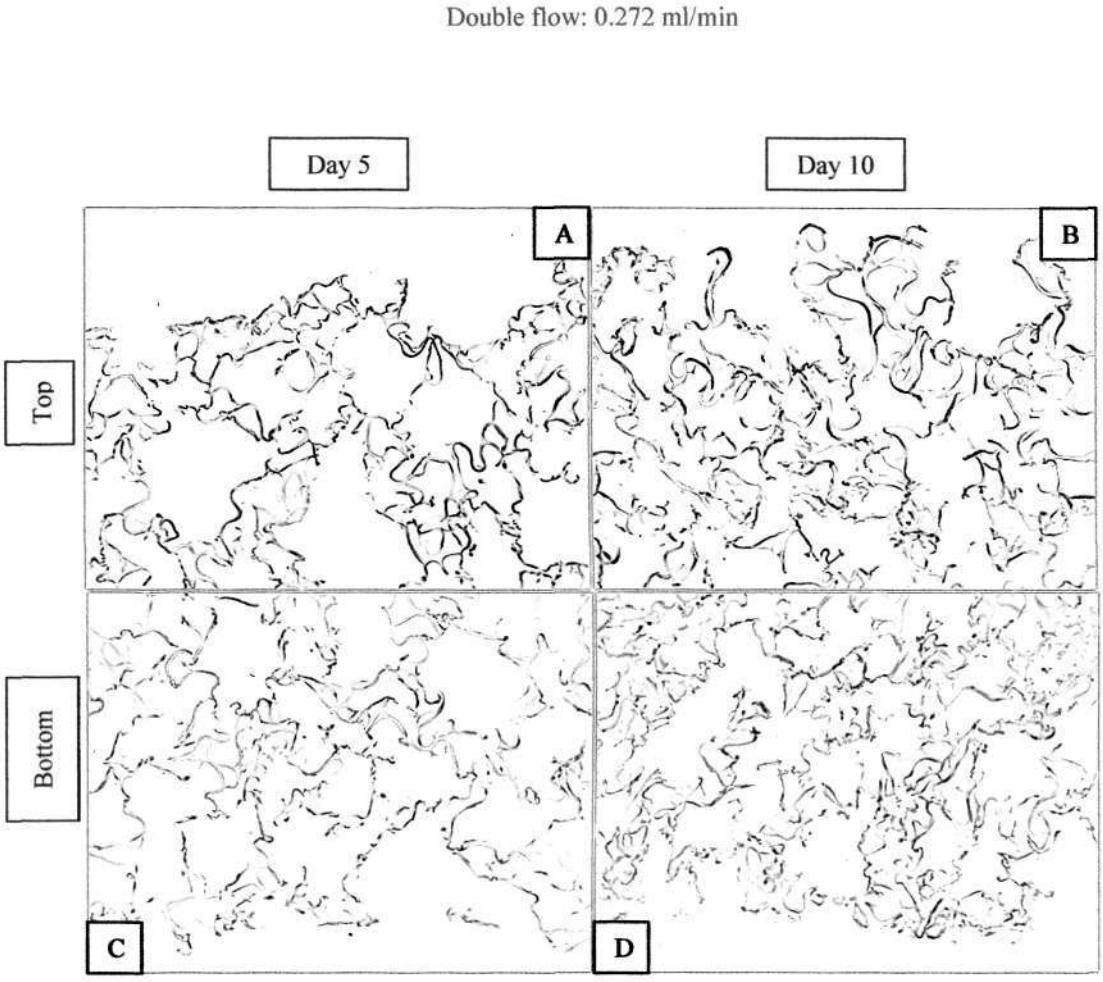

Figure 6.27: H&E micrographs of tissue constructs seeded with PESMCs cultured in a double flow configuration at a flowrate of 0.272 ml/min: (A) top portion, 5-day culture; (B) top portion, 10-day culture; (C) bottom portion, 5-day culture and (D) top portion, 10-day culture.

Double flow: 0.545 ml/min

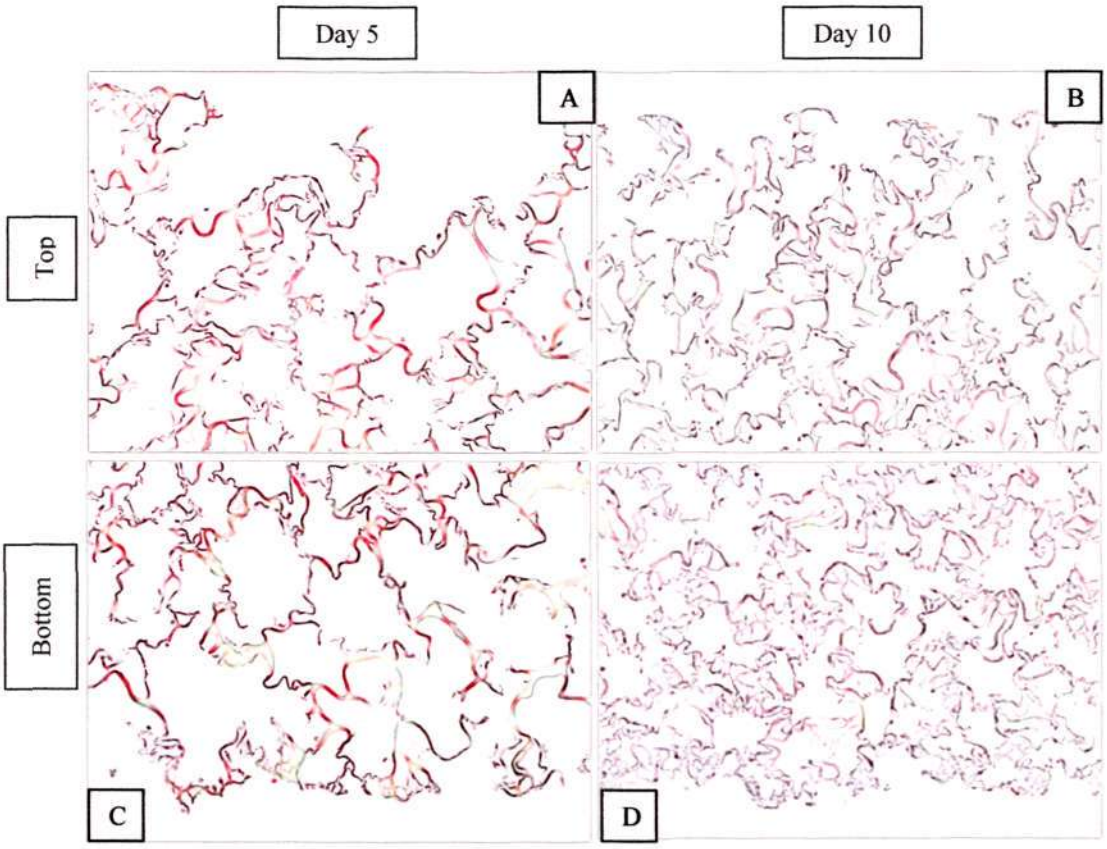

Figure 6.28: H&E micrographs of tissue constructs seeded with PESMCs cultured in a double flow configuration at a flowrate of 0.545 ml/min: (A) top portion, 5-day culture; (B) top portion, 10-day culture; (C) bottom portion, 5-day culture and (D) top portion, 10-day culture.

6.4.2 Oxygen Profile

Most of the previous studies required different degrees of disruption of the system, which could lead to the incorrect conclusion on the oxygenation of the culture system. In this study, oxygen profiling in situ in a closed system (bioreactor) was conducted with a minimal disruption of the system. Tissue culture was carried out in two bioreactor configurations (single or double flow) under two flow rates (0.272 or 0.545

ml/min) for 5 or 10 days. The oxygen profiles at five locations along the flow direction within the construct region were measured and shown in Figure 6.29 and Figure 6.30. In these figures, the region shaded in blue color represents the construct region while red box indicates the region of oxygen saturation fraction of less than 0.2. This region is hypoxic (low oxygen) and one where most cell growth normally ceases in this region.

Figure 6.29 shows the oxygen profiles in the single flow configuration. Oxygen saturation begins to decrease near the surface of the construct. It was reduced more rapidly once entering the construct and reached the minimum at the bottom side of the construct, which is adjacent to an impervious surface. From day 5 to day 10 for the low flowrate, the results showed that as cell growth proceeded, the oxygen utilization would be expected to increase and cause an increase in the steepness of the oxygen profile within the tissue construct. At the higher flowrate, the steepness of the oxygen profile was reduced at day 10, which in turn improved internal oxygenation. At 0.272 ml/min, the oxygen saturation at the bottom of the construct was at least above 40 % on day 5 but fell within hypoxic region on day 10. This hypoxic condition did not occur at 0.545 ml/min where the minimum oxygen level was well above 40 % over the 10-day period. Thus, doubling the external flowrate from 0.272 to 0.545 ml/min dramatically improved the internal oxygenation for extended periods.

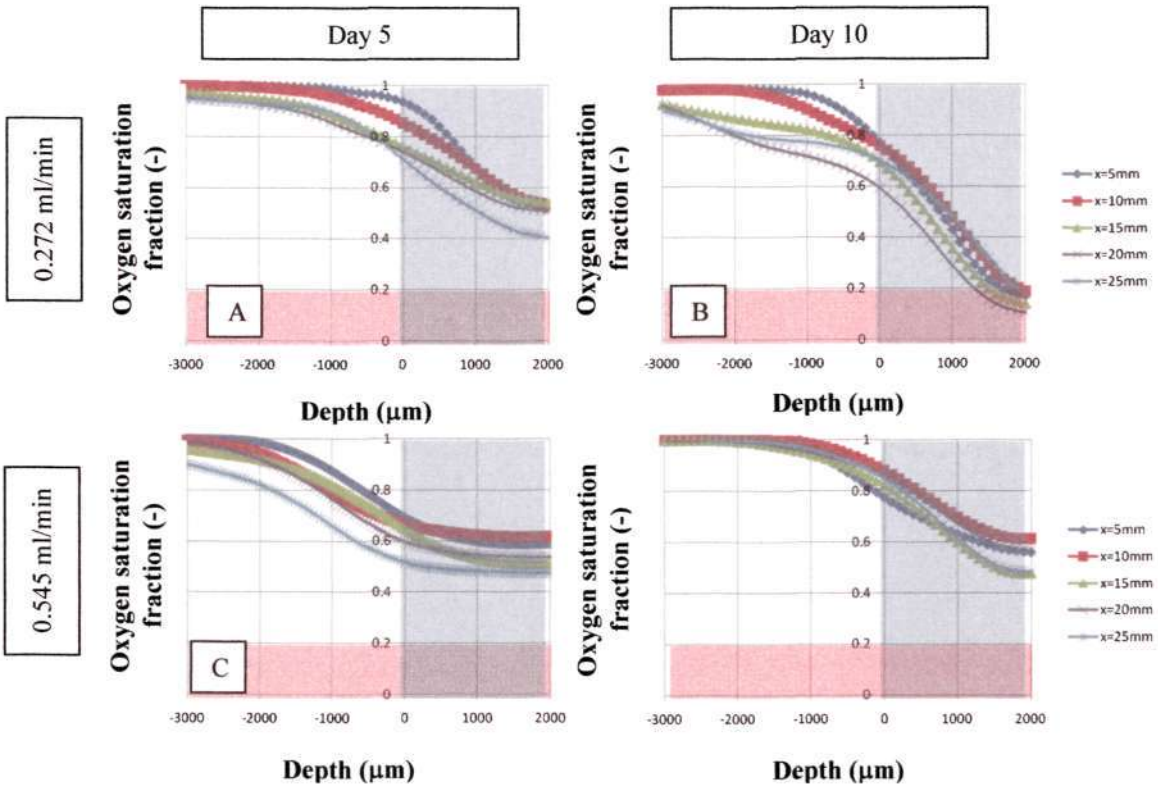

Figure 6.29: Oxygen profiles (mean value, n = 3) of tissue constructs seeded with PESMCs cultured in single flow configuration at a flowrate of (A) 0.272 ml/min for 5 days, max. SEM = ± 4.18 %; (B) 0.272 ml/min for 10 days, max. SEM = ± 23.03 % ; (C) 0.545 ml/min for 5 days, max. SEM = ± 0.78% and (D) 0.545 ml/min for 10 days, max. SEM = ± 3.94 %. Left side is the top surface which exposed to flow.

In Figure 6.30, the oxygen profiles under double flow configuration exhibited a symmetrical pattern. Both sides of the constructs were in contact with medium flow and the oxygen was able to penetrate from both sides. Oxygen was reduced symmetrically from external medium to the midpoint of the tissue construct. In this case, flowrate again played an important role in internal oxygenation. Oxygen profiles within the construct region at 0.272 ml/min were distinctly steeper than those at 0.545 ml/min. For example, on day 5 at the 0.272 ml/min flowrate, the mid-point oxygen level ranged from 30 % to 80 % while its counterparts at the 0.545 ml/min flowrate were well above 50 %. From day 5 to day 10, the steepness of the oxygen profiles

increased for both flowrates and the 0.272 ml/min flowrate resulted in near-zero oxygen saturation at the construct core while 0.545 ml/min flowrate still maintained the mid-point oxygen level well above the hypoxic level (>20 %).

The values of maximum standard errors of means (SEM) are given for each culture in the caption of each figure. All the maximum SEMs are found to be less than 5 %, except for two cases, the single and double flow configurations at the flowrate of 0.272 ml/min after 10 days of culture (Figure 6.29B and Figure 6.30B), in which oxygen dipped below the hypoxic region. The maximum SEMs for both cases are 23.03 % and 51.24 %, respectively, which are found in the hypoxic regions where the oxygen tension measurement fluctuated, probably due to the fast local variation in oxygen tension within the hypoxic regions.

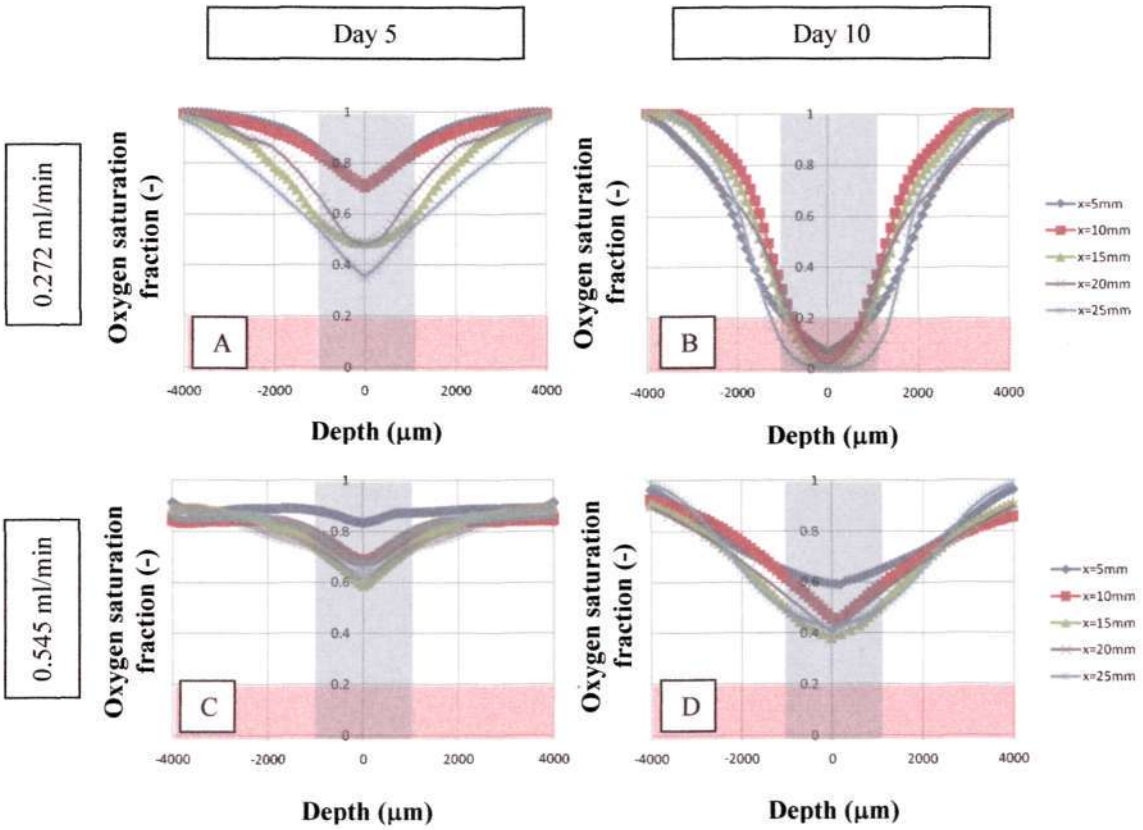

Figure 6.30: Oxygen profiles (mean value, n = 3) of tissue constructs seeded with PESMCs cultured in double flow configuration at a flowrate of (A) 0.272 ml/min for 5 days, max. SEM = ± 3.78 %; (B) 0.272 ml/min for 10 days, max. SEM = ± 51.24 % ; (C) 0.545 ml/min for 5 days, max. SEM = ± 3.44 % and (D) 0.545 ml/min for 10 days, max. SEM = 2.04 %. Both sides were exposed to medium flow.

6.4.3 Cell Distribution

At each oxygen profiling location, the cell distribution was estimated along the thickness of the construct. Figure 6.31 shows the cell distribution of a tissue construct cultured in the single flow configuration. All distributions in this configuration exhibited similar decreasing trend. Cells mostly grew near the top surface over time and did not significantly increase near the bottom. The trend generally agreed with the oxygen profiles and the increase in flowrate improved the internal oxygenation which also appeared to improve the uniformity of cell distribution.

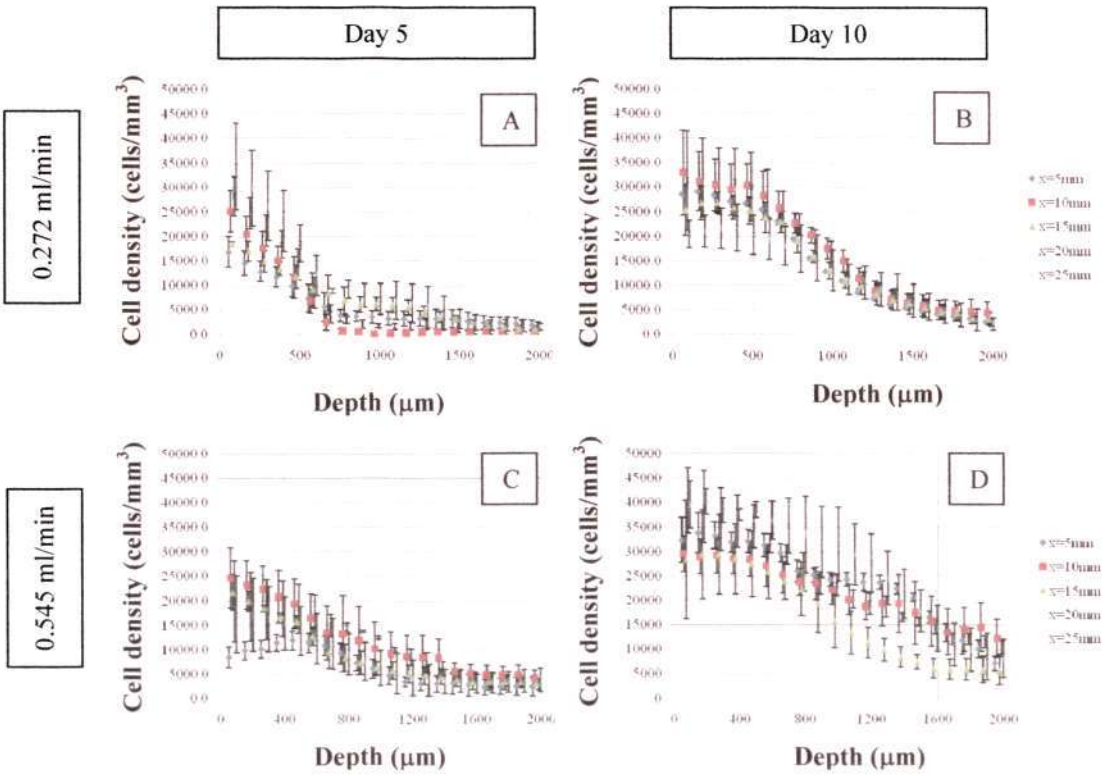

Figure 6.31: Cell distributions (mean ± SEM, n = 4) of tissue constructs seeded with PESMCs cultured in single flow configuration at a flowrate of (A) 0.272 ml/min for 5 days; (B) 0.272 ml/min for 10 days; (C) 0.545 ml/min for 5 days and (D) 0.545 ml/min for 10 days. Left side is the construct surface exposed to flow.

Figure 6.32 shows the cell distribution of a tissue construct cultured in the double flow configuration. With both construct surfaces exposed to flow, cell distribution was more uniform than that in the single flow cases. However, at the flowrate of 0.272 ml/min, although the cells distributed uniformly for both time points, it appeared that this condition did not support proliferation since the cell number was not significantly increased from 5 and 10 days. From the experiments being repeated twice times with two different PESMC stocks isolated at different times, poor cell stock may not be the cause of the problem. On the other hand, the poor growth observed in the lower

flowrate could be due to PESMCs gradually adapting to hypoxic state between day 5 and day 10, which led to cell growth arrest. A further investigation will be required.

When referencing the oxygen profiles for these two cases, the internal oxygenation was severely limited especially on day 10 when the oxygen level was near zero in the core. On the other hand, by increasing the flowrate in the double flow configuration, the cell number was comparatively less uniform but cell proliferation was observed over time. The corresponding oxygen profiles showed sufficient oxygenation over both time points which might explain continued cell proliferation in the construct over 10 days. The trend of cell distribution also appeared to follow the corresponding oxygen profiles. Although the slope of cell distribution was not as dramatic as shown in oxygen profiles, a general symmetrical distribution was observed in all cases. Furthermore, a minimum point was found at the core except for the case of 0.545 ml/min for 10 days where a maximum instead of a minimum was observed. This result might be due to the consequence of uneven cell seeding or shear stress near the construct surface, which induces cell death.

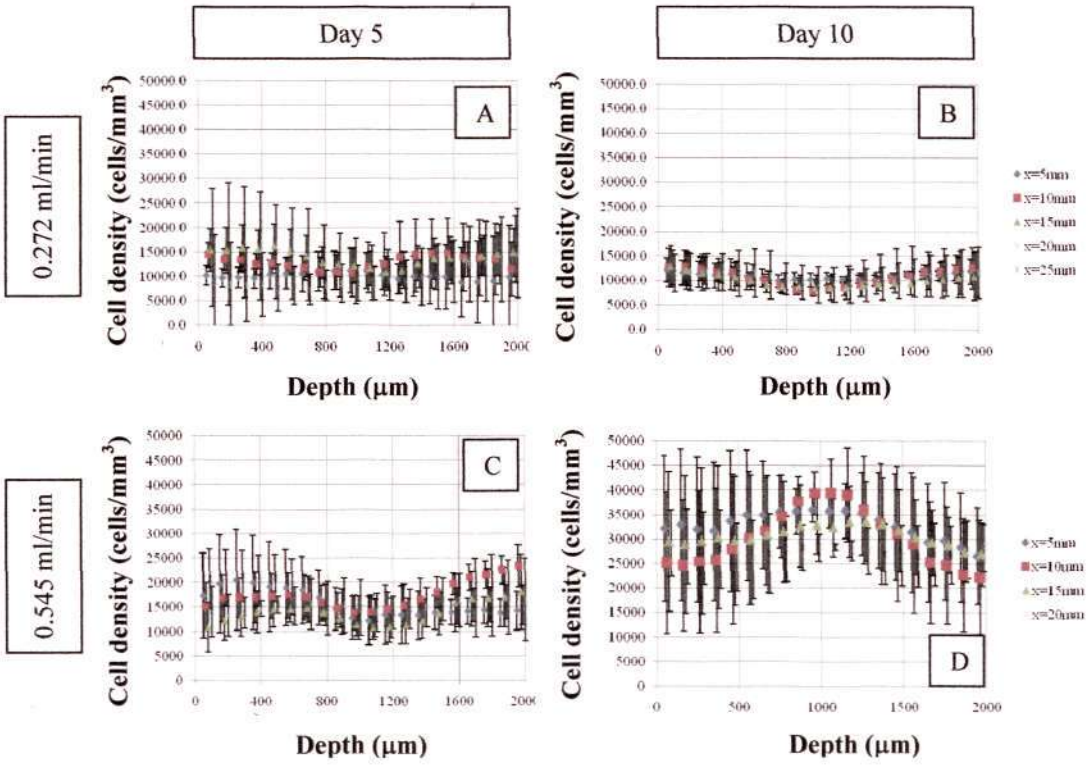

Figure 6.32: Cell distributions (mean ± SEM, n = 4) of tissue constructs seeded with PESMCs cultured in double flow configuration at flowrate of (A) 0.272 ml/min for 5 days; (B) 0.272 ml/min for 10 days; (C) 0.545 ml/min for 5 days and (D) 0.545 ml/min for 10 days.

To compare the improvement of cell distribution with the conventional case, cell distribution of construct cultured statically in the Petri dish was also measured and the results is shown in Figure 6.33. Since the tissue construct was suspended in the medium, both top and bottom surfaces were exposed to medium. Day 5 results showed the core region with lower cellularity which was further intensified on day 10 when more cells populated near both surfaces while the inner core growth was retarded probably due to poor internal oxygenation.

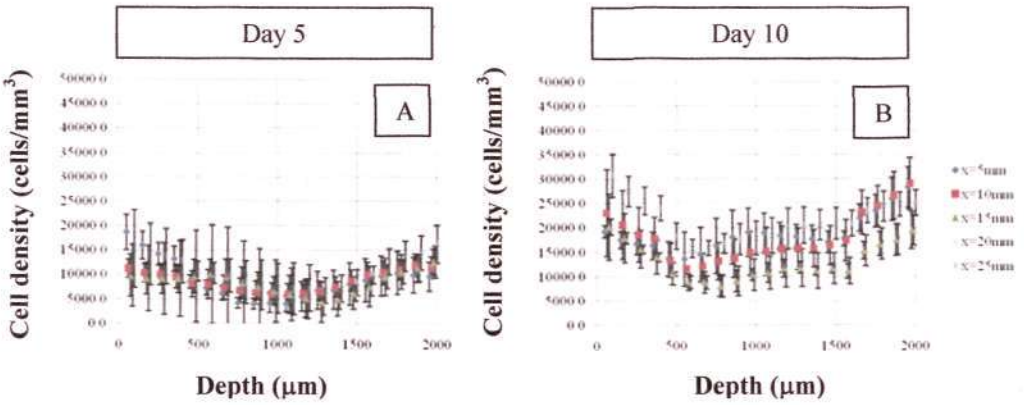

Figure 6.33: Cell distributions (mean ± SEM, n = 4) of tissue constructs seeded with PESMCs cultured in petri dish (A) for 5 days and (B) for 10 days.

In order to understand and predict the process of development of a tissue construct in the designed bioreactor environment, a mathematical model was established to simulate the experimental settings as closely as possible so that the model can be used as an analytical and optimization tool for the system. The simulation results were compared with the experimental results to validate the mathematical model.

6.5 Validation of Simulation Results

In the experimental studies shown in previous section, 5 locations of the construct along the flow direction were taken for the measurement of cell distribution and oxygen profile. Due to the limitation of instrumentation, it is difficult to conduct a full temporal and spatial measurement of the tissue construct. The mathematical model allowed full simulation of the spatial distribution of both properties at any time point. To validate the model, the simulation data was extracted from these five locations as shown in Figure 6.34 and compared with the experimental data in this section.

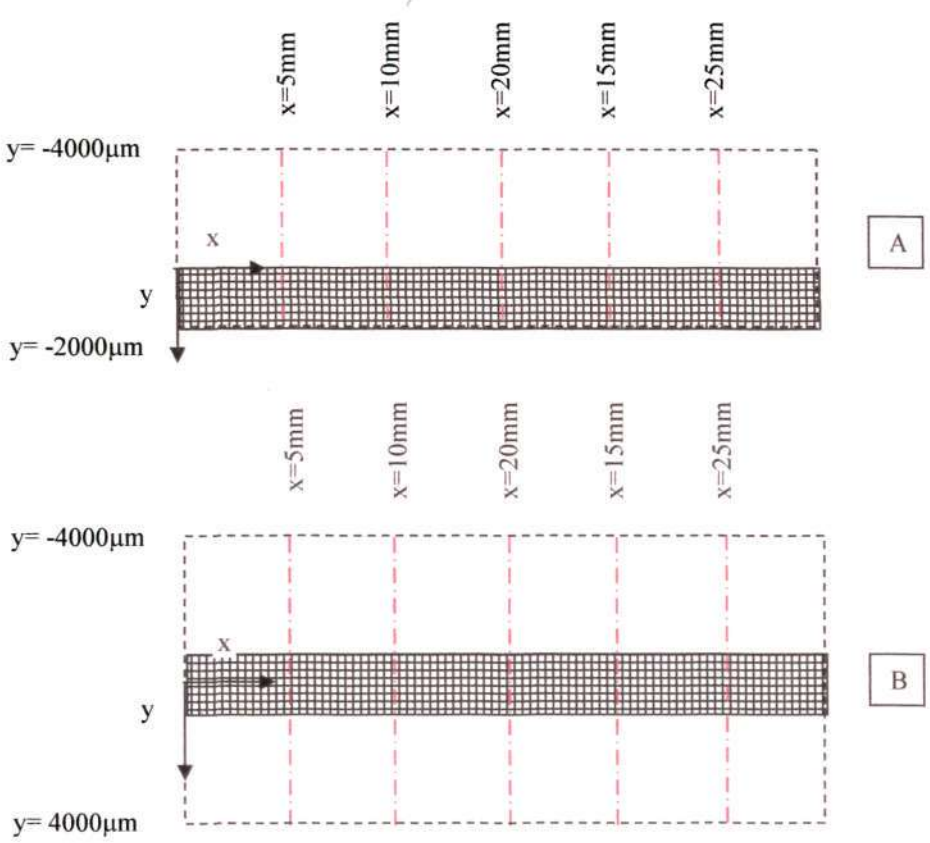

Figure 6.34: Illustrations of spatial locations of measurements for (A) single flow and (B) double flow bioreactor configuration. Red dotted lines are the locations where oxygen profiles and cell distribution were taken experimentally.

6.5.1 Oxygen profile

Figure 6.35 through Figure 6.38 show the oxygen profiles for the single and double flow configuration at low (0.272 ml/min) and high flow rates (0.545 ml/min) obtained experimentally and mathematically. Each figure presents both experimental and simulation profiles at particular x positions to show the degree of agreement. All simulated oxygen profiles for both bioreactor configurations provided good qualitative agreement with the experimental results.

When comparing simulation and experimental results, discrepancies were observed in the medium and in the construct phase. In general, the oxygen concentration was underestimated within the construct and overestimated in the bulk medium. This result could be attributed to experimental errors such as uneven cell seeding and anisotropicity of the porous structure and also errors in estimation of model parameters or assumptions. The discrepancies were summarized in Figure 6.39. The bars in this figure show the mean values for both overestimated and underestimated discrepancies and the extended black lines indicate the highest discrepancies for both sides. This model prediction showed the highest discrepancies of +33 % and -40 % in overestimation and underestimation in all cases, respectively. An overall average of 6.6 % discrepancy (for both over- and underestimation) demonstrated good overall agreement between the simulation and experimental results in oxygen profile.

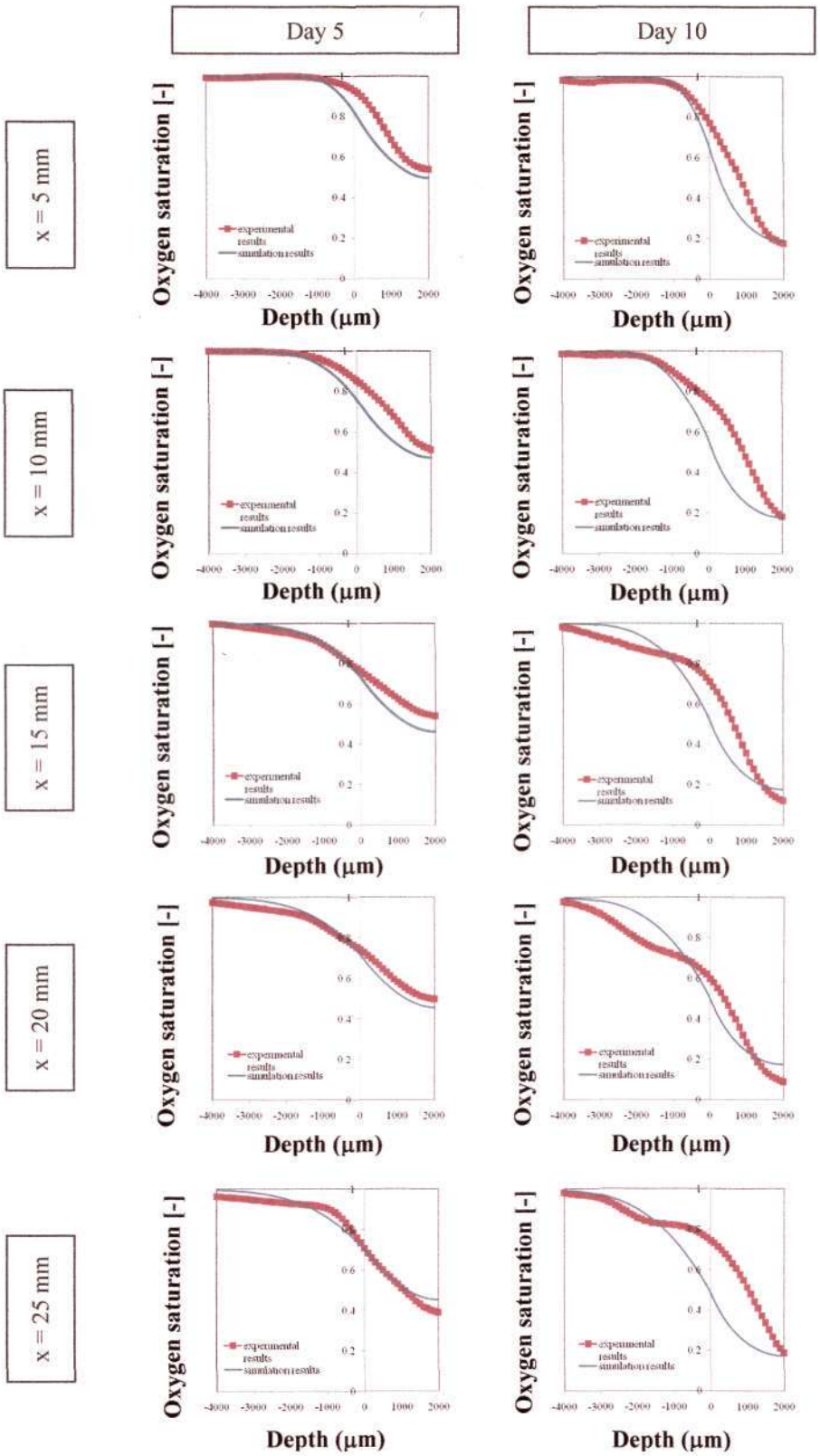

Figure 6.35: Comparison of simulation (blue curves) and experimental (brown squares) results of oxygen profiles in the single flow bioreactor at 0.272 ml/min.

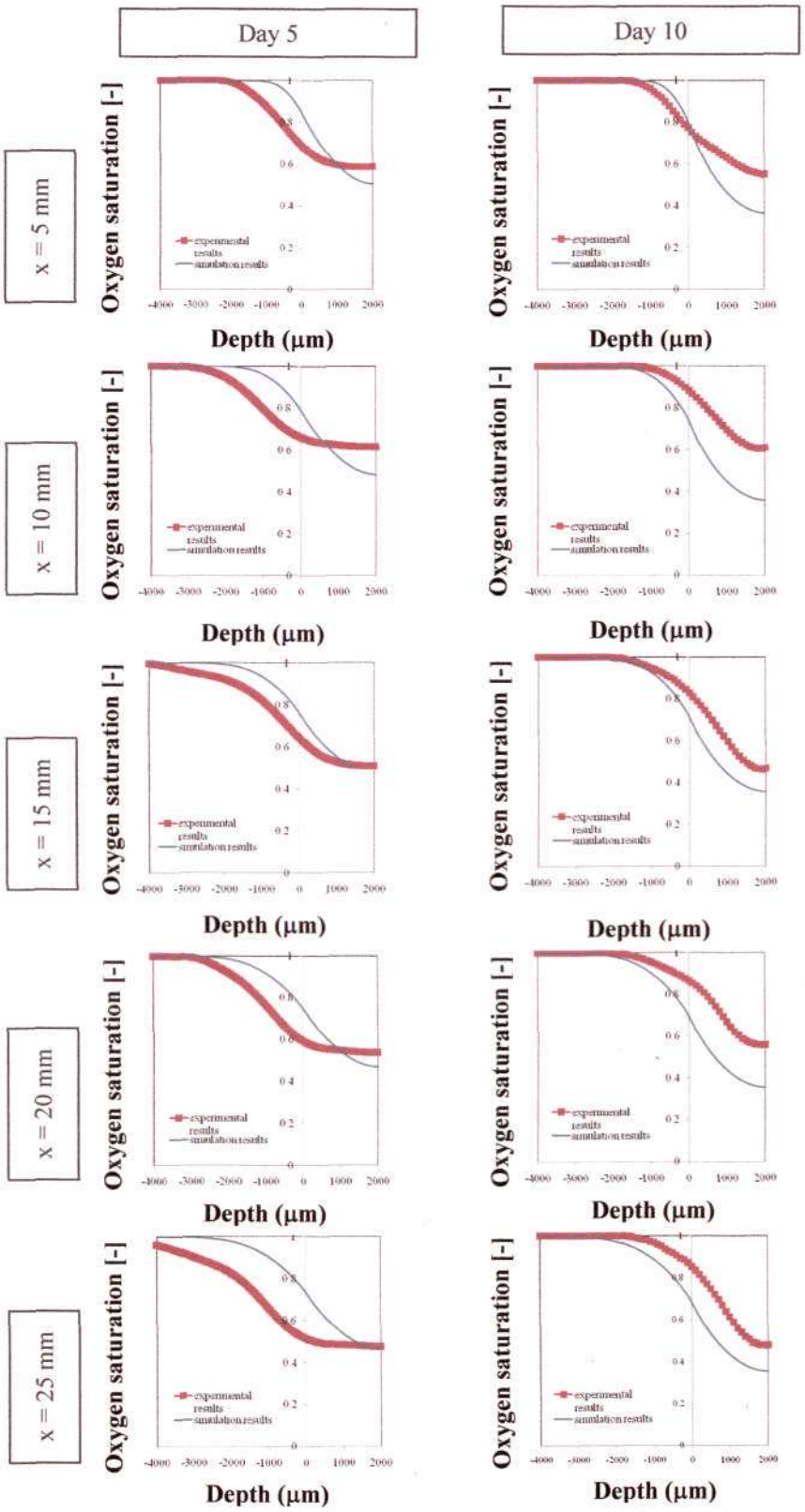

Figure 6.36: Comparison of simulation (blue curves) and experimental (brown squares) results of oxygen profiles in the single flow bioreactor at 0.545 ml/min.

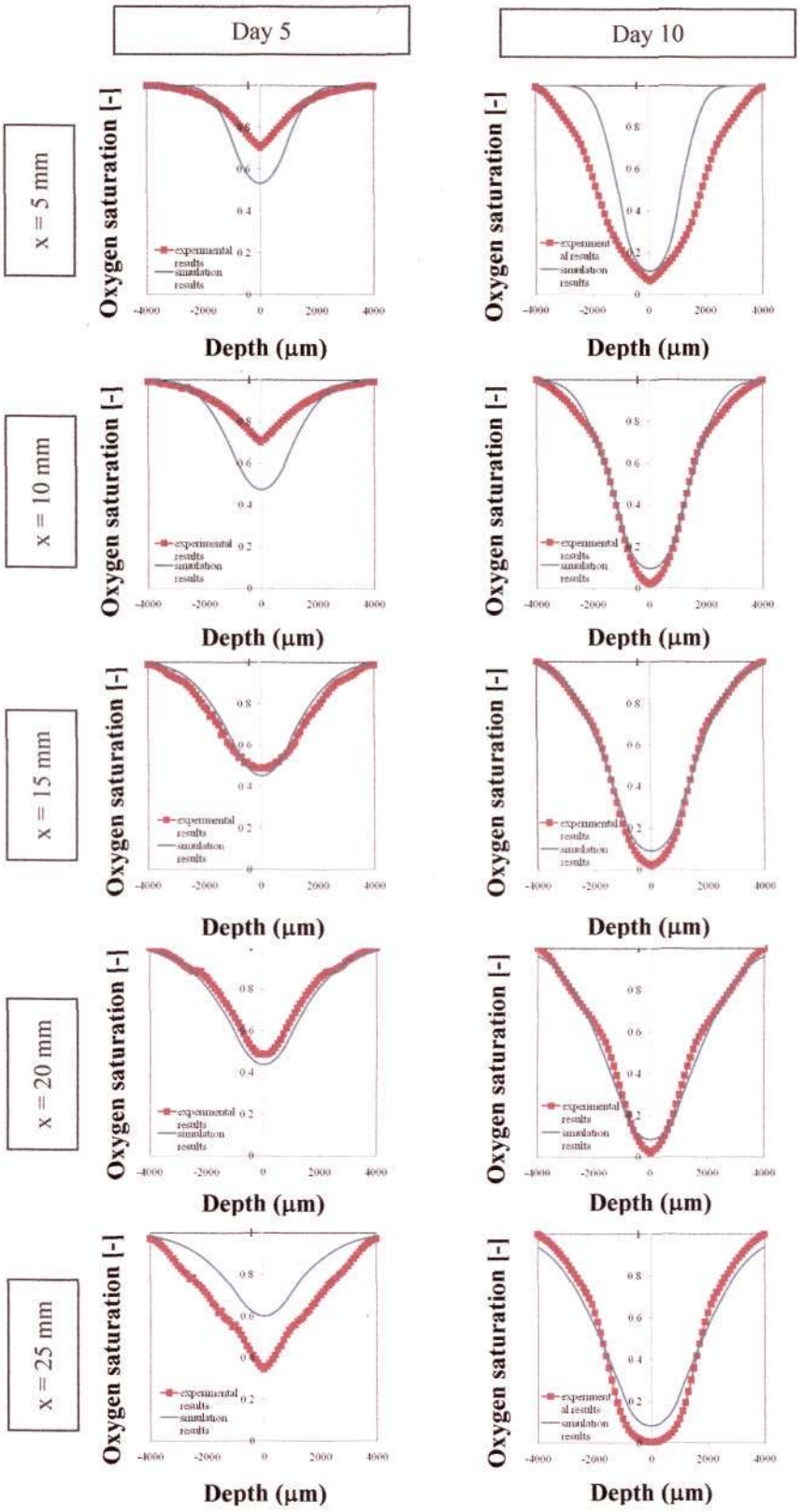

Figure 6.37: Comparison of simulation (blue curves) and experimental (brown squares) results of oxygen profiles in the double flow bioreactor at 0.272 ml/min.

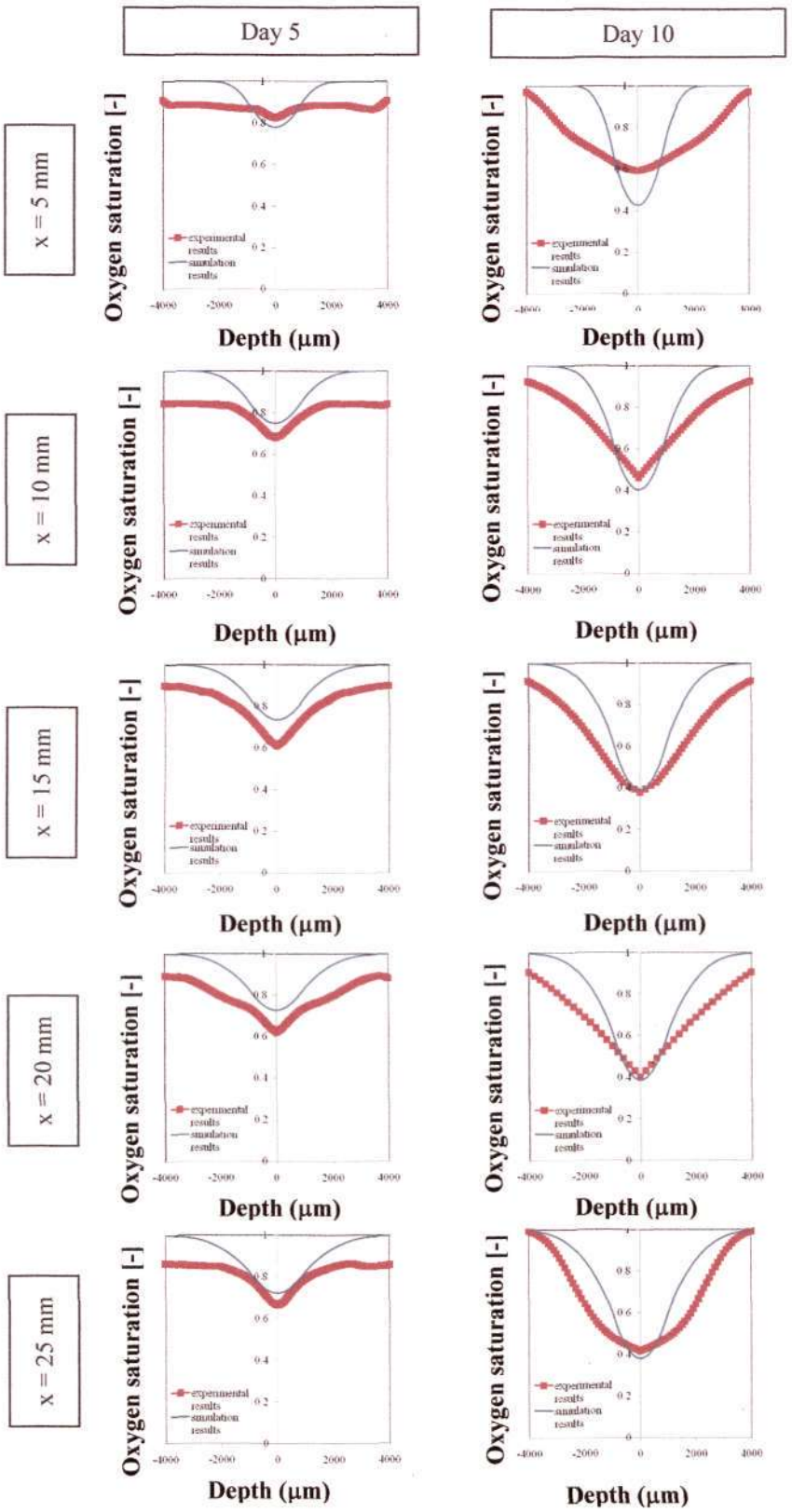

Figure 6.38: Comparison of simulation (blue curves) and experimental (brown squares) results of oxygen profiles in the double flow bioreactor at 0.545 ml/min.

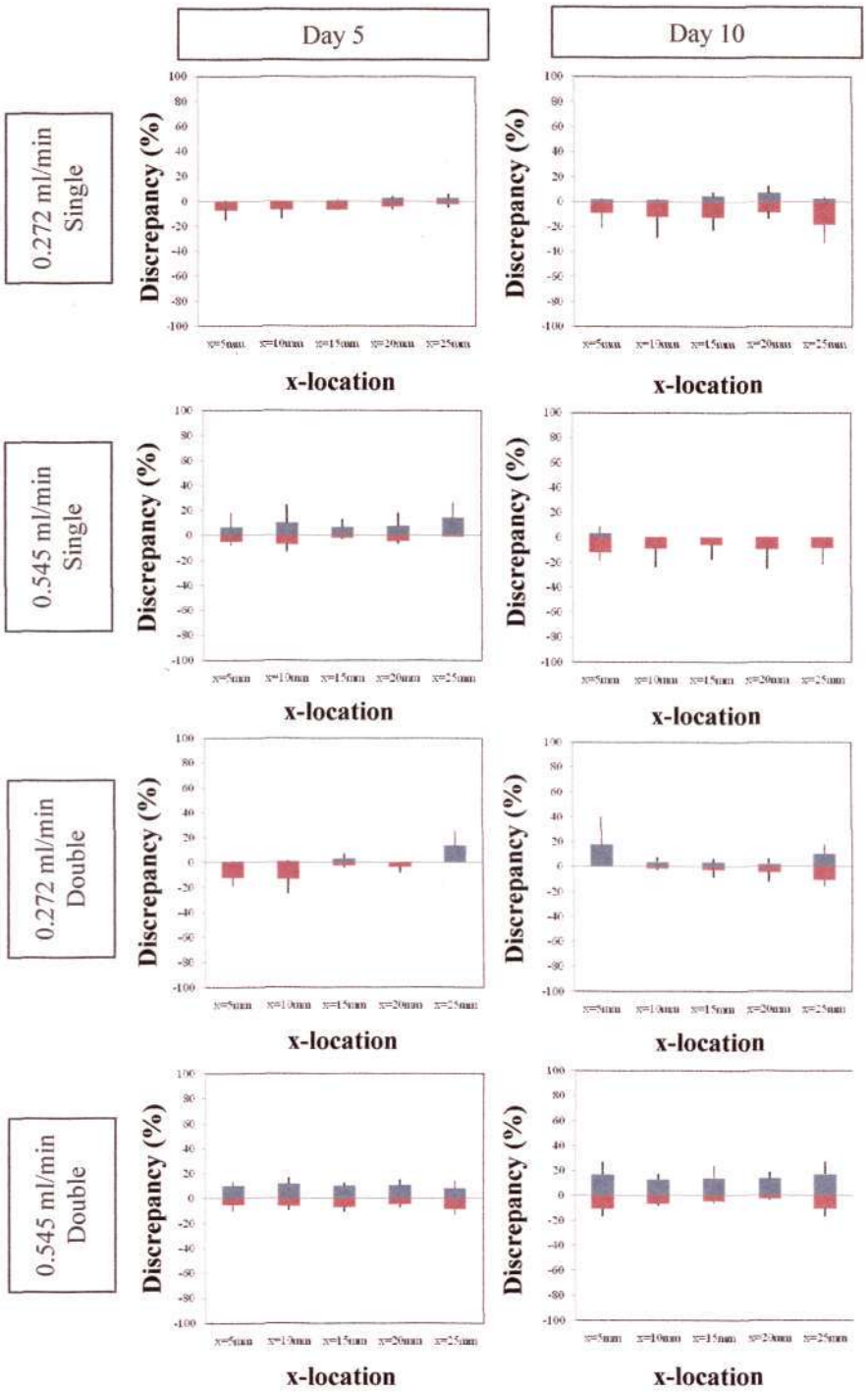

Figure 6.39: Summary of average discrepancies between simulation and experimental results of oxygen profiles. Blue bar and brown bar represent average overestimation (positive value) and average underestimation (negative value) of the simulation results from the experimental results, respectively. The black lines extended from both sides of the bars show either the maximum over- or under-estimation value within the profile.

6.5.2 Cell distribution

Figure 6.40 through Figure 6.43 show the oxygen profiles for the single and double flow configuration at low (0.272 ml/min) and high flow rates (0.545 ml/min) obtained experimentally and mathematically. The simulation results provided an explanation close to the experimental data with decreasing cellularity towards the bottom of the construct in the single flow configuration (Figure 6.40 and Figure 6.41) and towards the core of the construct in the double flow configuration (Figure 6.42). Furthermore, the model results also provided an accurate prediction of the cell growth over time near the construct surface in that a gradual formation of a thick cell layer around the periphery was predicted by the current model. Exception was observed in double flow configuration at 0.545 ml/min after 10-day culture which showed an increased cellularity towards the centre of the construct compared to the simulation results which exhibited a decreasing trend (Figure 6.42). Lower cellularity near both surfaces observed in experimental studies might be due to shear stress damage. Similar observation was also observed in Carrier *et al.* [36] that the myocardium construct showed lower cellularity near the surface when a flow of 1 ml/min of medium flow was applied and tissues of both cases (myocardium and smooth muscle) are not physiological exposed to flow environment unlike endothelium or epithelium found on the lining of most of the internal organs. Therefore, shear stress even at low level may cause damage of these cell types.

The local discrepancies between simulation and experimental results were also calculated and are summarized in Figure 6.44. In all cases, the highest discrepancies were 5 % (overestimation) and -3.4 % (underestimation) while the overall mean

discrepancies were as low as 0.62 % and -0.78 %, respectively, which showed good overall agreement.

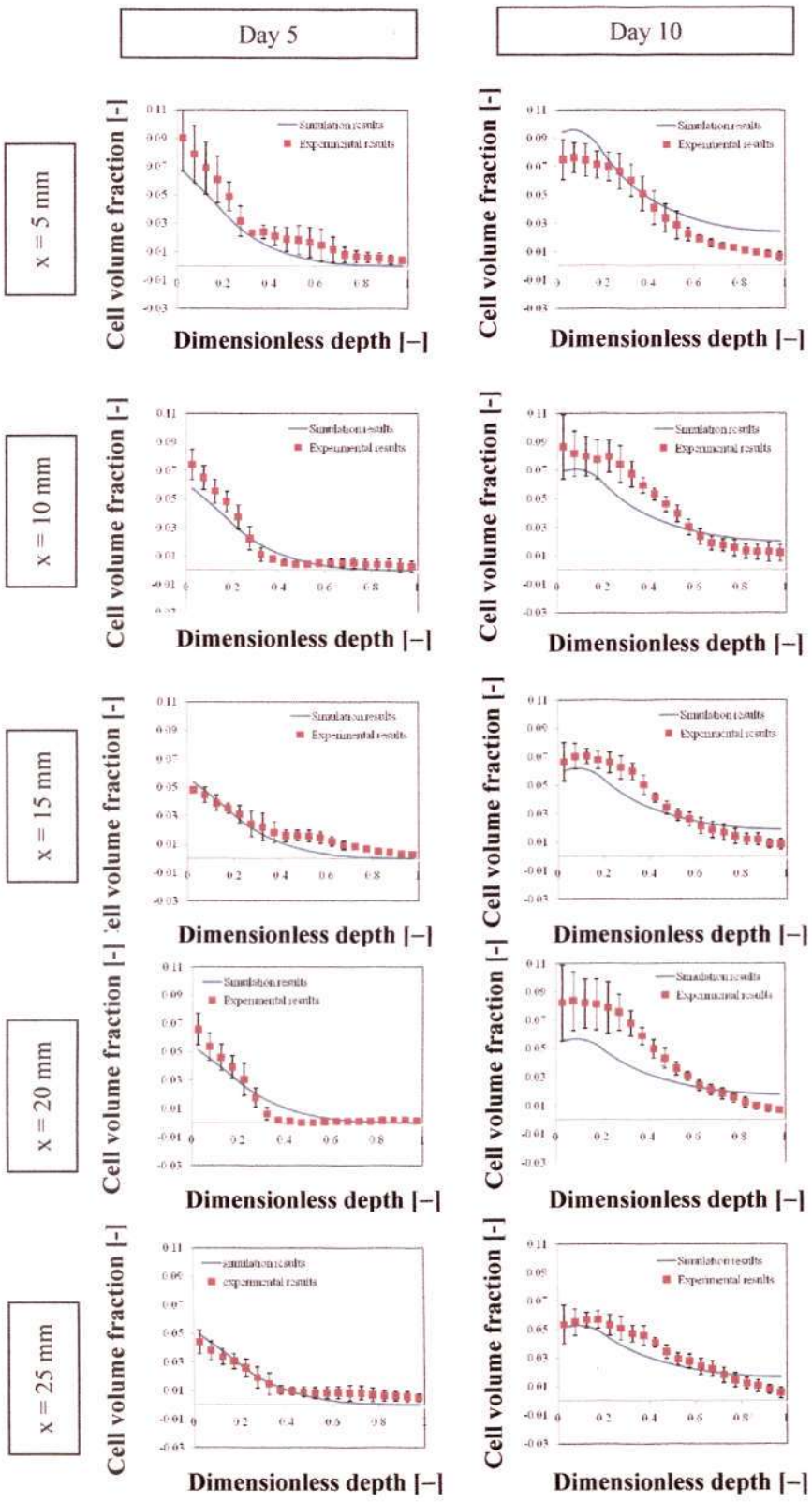

Figure 6.40: Comparison of simulation and experimental results of cell distributions single flow bioreactor at 0.272 ml/min.

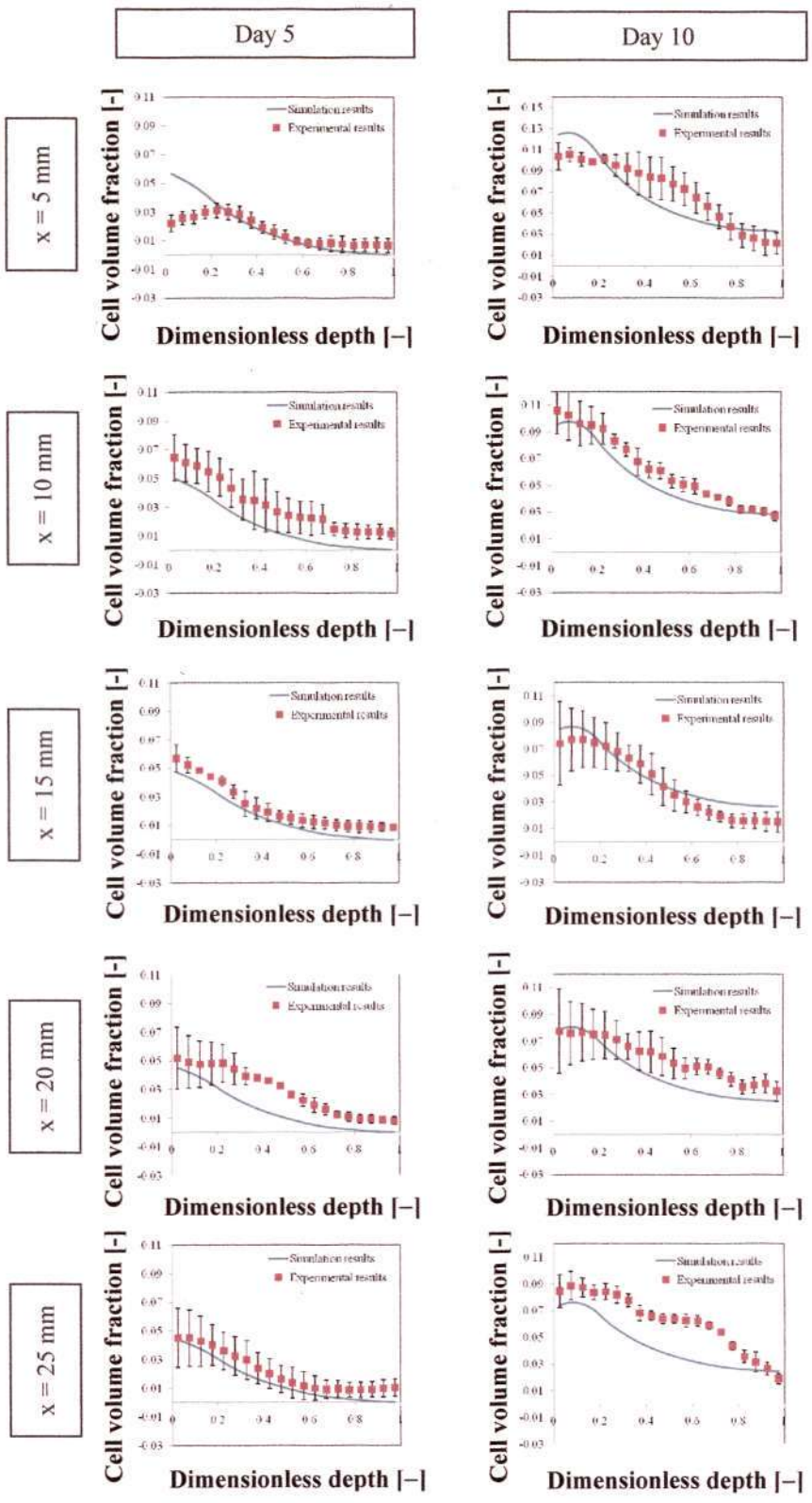

Figure 6.41: Comparison of simulation and experimental results of cell distributions in single flow bioreactor at 0.545 ml/min.

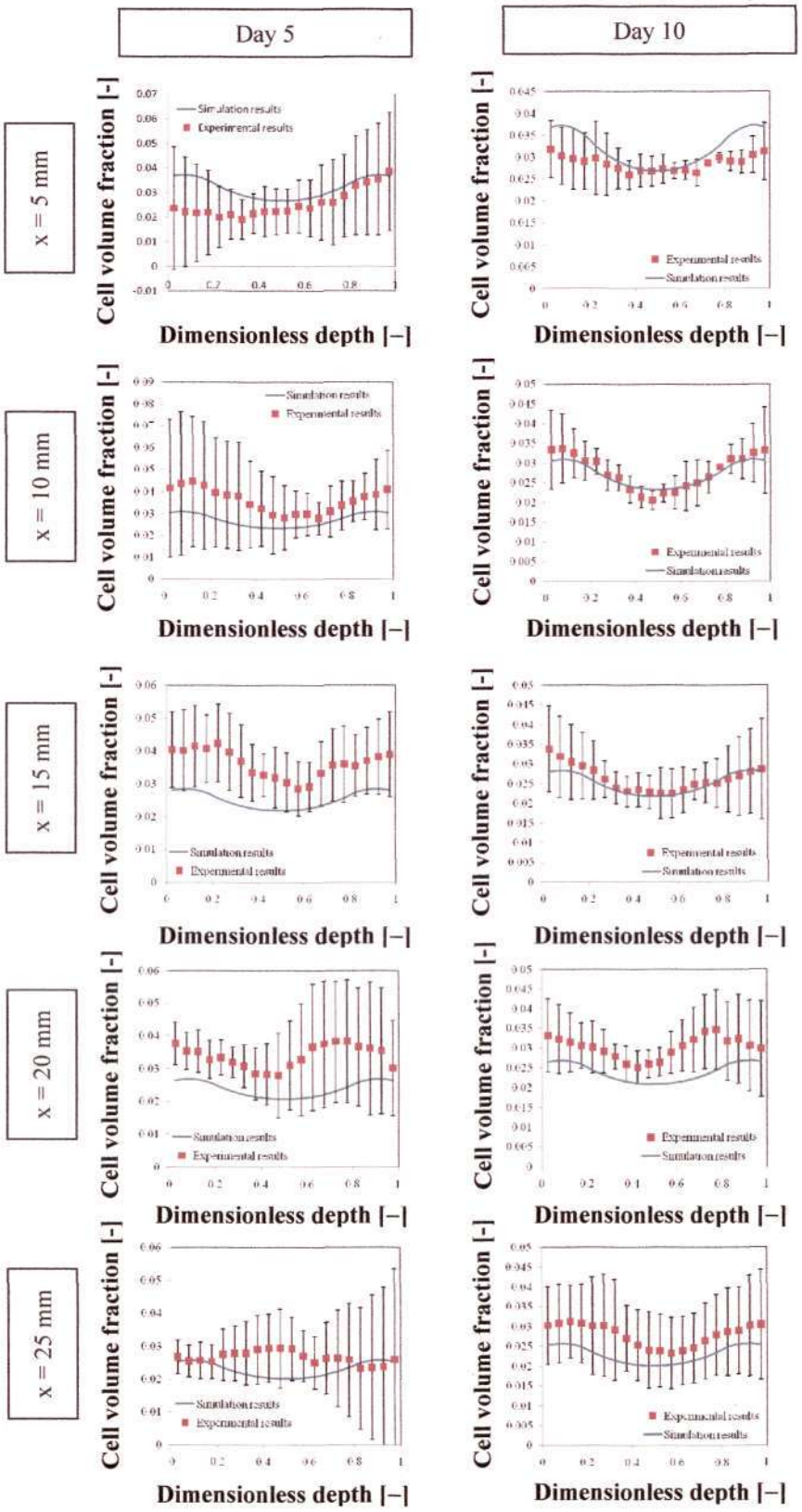

Figure 6.42: Comparison of simulation and experimental results of cell distributions in double flow bioreactor at 0.272 ml/min.

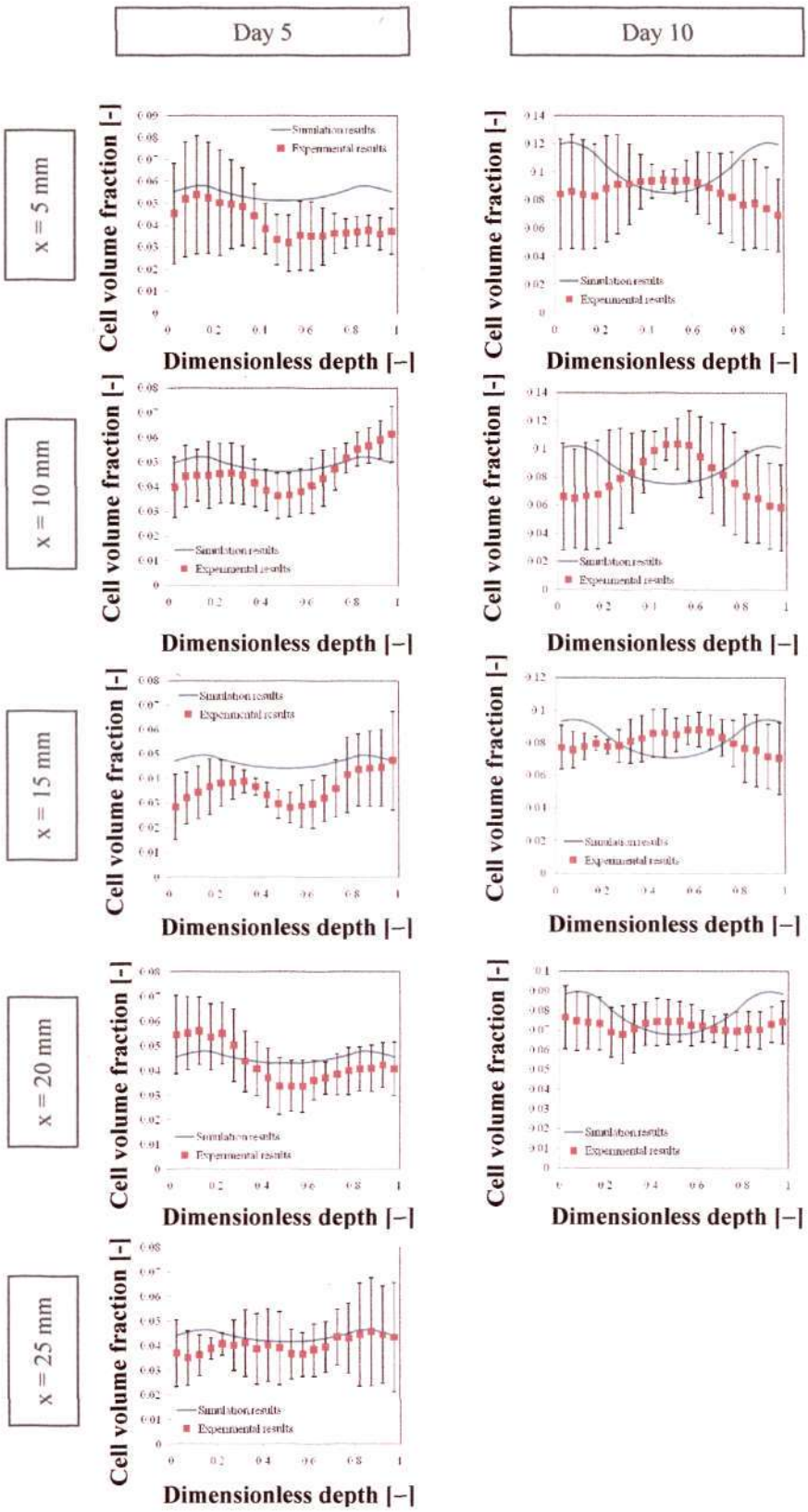

Figure 6.43: Comparison of simulation and experimental results of cell distributions in in double flow bioreactor at 0.545 ml/min. Ommision of x = 25 mm results for day 10 was due to sample loss during processing

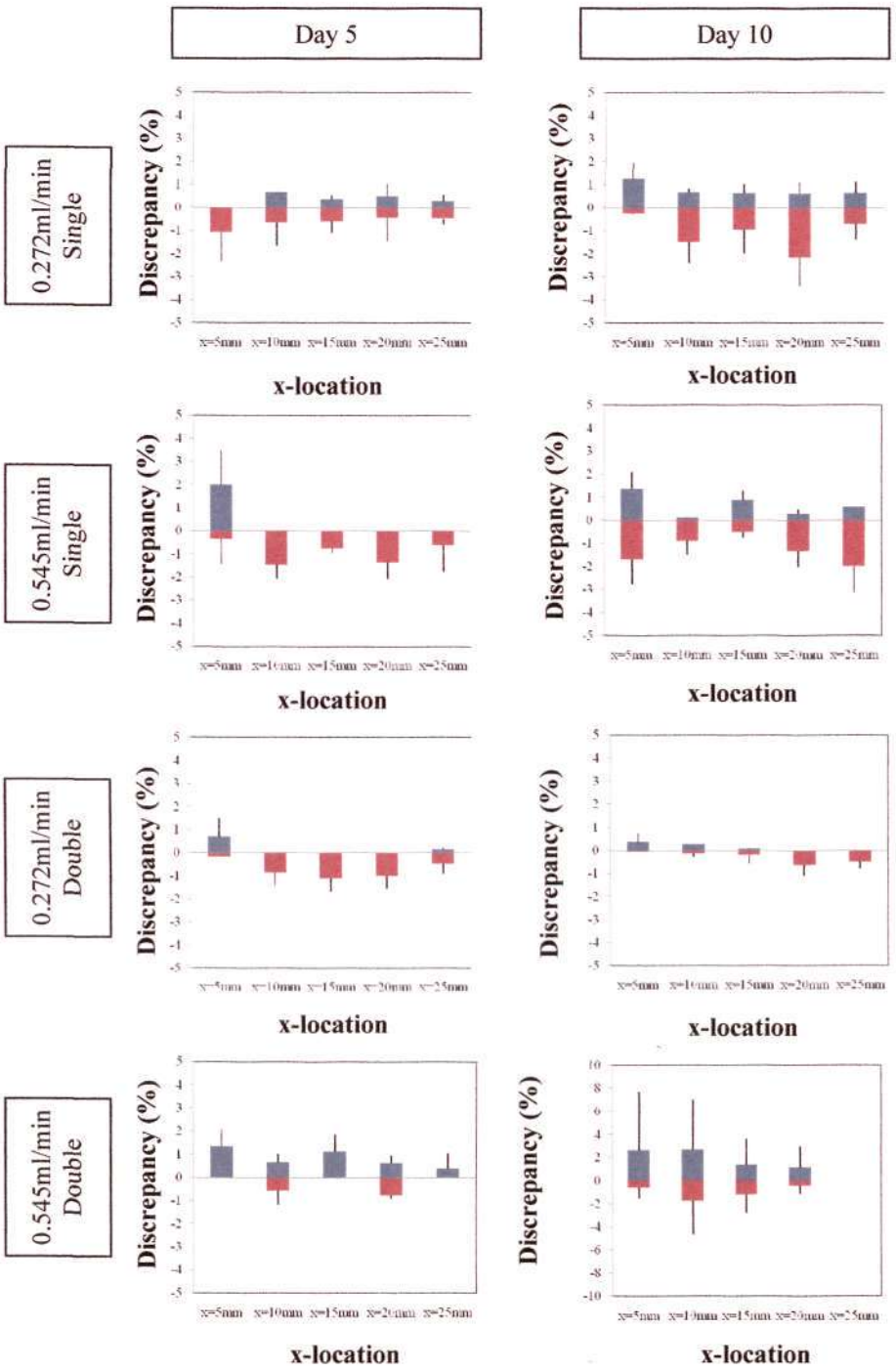

Figure 6.44: Summary of average discrepancy between simulation and experimental results of cell distributions. Blue bar and brown bar represent average overestimation (positive value) and average underestimation (negative value) of the experimental results, respectively. The black lines extended from both sides of the bars show either the maximum over- or under-estimation value within the distribution.

Chapter 7. Discussion

7.1 Scaffold

Gelatin is a natural proteineous material derived from collagen that is abundant in native extracellular matrix such as skin, bone and connective tissues. Gelatin has been used for medical purposes since the 1940s [81]. It has been shown that gelatin has better compatibility with the host *in vivo* than collagen [82], probably due to its reduced antigeneicity that has been of a main concern with collagen-based biomaterials [197]. Furthermore, gelatin is cheaper and the powder form has a prolonged shelf life compared with collagen, which is relatively costly and restricted in its storage conditions.

Using the simple method proposed in this work, a porous matrix with a relatively uniform pore size distribution, was produced by making use of a foaming nature of gelatin solution. Several methods to produce porous gelatin structures have been proposed, such as freeze drying [91, 94, 96], emulsion/ freeze drying [89], salt leaching [93], overrun/ particle leaching [90] and electrospinning [97]. Pore formation in freeze drying relies on ice formation. Kang and Ikeda [91] showed that the pore size is related to the freezing temperature, and that lower freezing temperatures cause smaller ice crystals which produce smaller pore sizes after freeze drying. However, this technique requires the introduction of the chemical crosslinker (glutaraldehyde) to prevent dissolution before the swelling step, which increases water uptake for a higher porosity in the resulting scaffold.

Van Vlierberghe *et al.* [96] manipulated the freezing gradient during freezing of gelatin to control the pore morphology. A matrix with tubular and polygon pores can also be made by this method. The photoinitiator, Irgacure 2959, associated with UV was used to crosslink gelatin before freezing. However, a study of six different cell lines showed that a low degree of cytotoxicity can be induced at concentrations as low as 0.03 % without UV exposure and that UV-initiated crosslinking was found to induce even higher toxicity [198]. Furthermore, scaffolds with polygon pores were mostly not interconnected which might hinder efficient cell delivery and cell distribution.

Salt leaching was also adopted for making gelatin scaffolds. Since the gelatin solution is aqueous, which also dissolves salt, pore formation is due to undissolved salt after reaching the solubility limit and recrystallization during drying. Since salt is partly dissolved when a solution is seeping into the salt bed, local differences due to distinct degree of salt dissolution at different depths might generate a non-uniform porous structure. Although Kang *et al.* [90] combined particle leaching and gas foaming with N_2 to increase pore connectivity, particles in the deep layer might not be able to fully leach out. This combined method, on the other hand, improved slightly pore interconnectivity.

Zhang *et al.* [97] produced nanofibrous gelatin scaffold by electrospinning. However, electrospun scaffold was relatively thin (about 100 μm) and the organic solvent 2,2,2-trifluroethanol was used in dissolution of the gelatin for nanofiber production, which would cause cytotoxicity at low level. Commercial gelatin sponges such as Gelfoam® and Surgifoam® which have been used as haemostatic agents and wound dressing,

have a porous structure formed by irregular polygon grids. Although this material is highly porous and interconnected for cell infiltration, its low surface area might cause low effective surface area for cell attachment in the early stage of tissue construct development.

Although foaming technique has been introduced by Ulubayram *et al.* [84, 100] to produce porous gelatin sponge, the casting temperature at 60 ^{o}C reduced pore size uniformity and foam stability resulting in a thick nonporous bottom due to the collapse of foam. It is also known that protein in solution can lower surface tension of water causing protein foaming. This foaming property has been widely studied in the food industry [78, 79]. Many methods have been developed to modify the properties of foam (e.g., foamability, foam stability and bubble size) by adding surfactants and alcohol [77, 95, 199]. It is believed that change of foaming properties can modify the porous structure of this resulting scaffold. This area requires further studies.

In order to improve the resistance to degradation of gelatin scaffolds *in vivo* and *in vitro*, crosslinking has to be introduced. Yao *et al.* [200] reported a crosslink index (CL%) of 75 % of the maximum based on a ninhydrin test when the crosslinker genipin was used. Using the same test, Lien *et al.* [94] recorded a higher CL% for genipin-crosslinked gelatin scaffolds. In their studies, the CL% of genipin-crosslinked scaffold was between 75 and 87 %, which is comparable to glutaraldehyde-crosslinked scaffolds (82 to 85 %).

In the current study, the CL% was 55.6 % for scaffolds crosslinked by a 4-day DHT treatment compared with 40.1 % for genipin-crosslinked scaffold. The DHT-treated

scaffold resulted in a lower degree of crosslinking compared with the genipin- or the glutaraldehyde-crosslinked gelatin in the previous studies by 20 to 30 % carried out by Yao *et al.* [200] and Lien *et al.* [94], but it was still 15 % higher than that of the genipin-crosslinking carried out in the current study. The deviation of the CL% in genipin-crosslinking between the current and the previous studies might be due to the process adopted in the crosslinking. In these two previous studies, crosslinking was carried out in an aqueous mixture of gelatin and genipin in contrast with soaking a solid gelatin sponge in genipin solution for the current study. The former obviously resulted in a higher degree of mixing between gelatin and genipin molecules which in turn caused higher amount of crosslink reactions between free amino acid and crosslinker.

Water uptake (or swelling ratio) has been used in many studies to investigate the degree of collagen crosslinking and its effect on degradation of the foam matrix. Lien *et al.* [94] and Van Vlierberghe *et al.* [96], for example, found that crosslinking and degradation were not always changing in parallel with the findings of water uptake data. However, for porous gelatin scaffolds, both authors believed that pore morphology plays a more important role. For example, scaffolds with tubular pores were found to degrade the faster than scaffolds with polygonal pores [96]. This increase is probably due to the unit tortuosity (=1) of tubular pores where water diffusion in gelatin is faster compared with other, more tortuous, porous structures. Due to this reason, water uptake was not conducted in the current study and rather, a degradation test was performed. From the crosslink index based on ninhydrin test and degradation test, it appears that the percentage of amino acid being crosslinked (55.6

%) is parallel with the percentage of undissolved gelatin (an average of 40.8 % over a period of 14 days), as shown in the sample after 4-day DHT treatment. Further investigation is required to verify this observation. In addition, it has been reported that DHT crosslinking causes collagen to be more susceptible to collagenase degradation [98], an effect that may be a major concern when the gelatin sponge is used *in vivo*. Such degradation can be overcome by *in vitro* tissue engineering where the cell seeding and culture is first carried out outside the body prior to implantation. Although there was no quantitative data included in the current study, it was found that the cell-seeded scaffold required at least 24 to 48 hours to be completely digested in papain, strong proteolytic enzyme, whereas the unseeded scaffold was completely digested in less than an hour. Furthermore, the digestion time increased with the culture time. Therefore, *in vitro* cell seeding might improve the resistance of gelatin scaffolds to degradation *in vivo*.

The tensile properties of gelatin sponge in its dry state revealed a relatively inelastic and brittle material. But once hydrated, the sponge becomes more pliable and elastic due to the plasticizing effect of water. The inherent properties of dry gelatin can be modified. Yannas reported that a cast film of gelatin with a plasticizer of glycerol can undergo a reversible deformation of 700 % [201]. Therefore, gelatin scaffold can be modified by incorporation of non-toxic agents to improve their mechanical properties.

7.2 Cells

7.2.1 PESMCs

Porcine esophagus is a layered structure surrounded by two layers of muscle (called "muscularis externa"), which mainly controls the peristalsis of the esophagus. Regeneration of the esophagus requires rebuilding of this layered structure from smooth muscle cells, fibroblasts and other neurovascular stem cells. The first step in this process is to facilitate *in vitro* growth of porcine esophageal smooth muscle cells (PESMCs), which are used as "building blocks" for the smooth muscle constructs.

This study showed both enzymatic and explant methods successfully derived PESMCs. The morphology of the isolated cells exhibited the normal characteristics of typical smooth muscle cells, e.g., dense cytoplasm, oval-shaped nucleolus and hill-and-valley pattern upon confluency [112]. However, most of the recent investigations of esophageal smooth muscle cells focused on the cell contraction [202, 203], which did not require subculture and proliferation and the subculture capability was rather unknown compared with its counterpart in vascular tissues [112, 204]. This information is important because: (1) although vascular smooth muscle cells (VSMCs) in some ways are similar to esophageal smooth muscle cells, there are still many subtle differences such as their respective receptors and ion channels [205] but the previous growth studies in VSMCs can still be served as reference data, and (2) tissue engineering *in vitro* requires cells that are able to proliferate and maintain viability in scaffolds and identification of such cell population is essential for the construct development. The MTS cell proliferation study conducted in serial PESMC subcultures demonstrated the PESMCs isolated using both methods allowed subculture

of PESMCs at least 6 times, which was similar to the subculture capability found in vascular SMCs [112] and that at p7, explant cells began dying in significant numbers. Therefore, all the cell experiments were carried out before p7.

One major problem of producing SMCs from the esophagus is fibroblast contamination. In mammalian cell culture *in vitro*, fibroblasts are a concern because they prevalently outgrow the target cell type [55]. This can be problematic since both fibroblasts and smooth muscle cells co-exist in esophageal smooth muscle—unlike vascular smooth muscle which only consists of pure vascular SMCs [112]. In our results, fibroblasts were occasionally found in the primary culture but immunohistological staining showed that fibroblasts did not overgrow the culture and a majority of cells in all subcultures were stained with smooth muscle actins, the specific cell marker for smooth muscle cells.

The method of isolation and subculture of PESMCs established in this work provided a cell source for seeding into scaffolds, but it is also necessary to study the compatibility between cells and scaffold.

7.2.2 Cell-matrix Interaction

Cell seeding experiments demonstrated that PESMCs attached and proliferated in the gelatin scaffold. The histological micrograph on day 3 showed a low number of cells scattered within the scaffold. This observation was parallel with the DNA measurements on day 3, which appeared that cells had been adapting to the new ECM environment. In fact, over the first 3 days, the DNA content was at the lowest level. In the following days, the cells started proliferating and by day 7, more cells near the

scaffold surface were observed, a result that was quantitatively correlated by an almost a 3.5-fold increase of DNA content. However, due to this thick cell cover (about 100 to 150 μm thick), mass transfer deep inside the scaffold was hindered and cells were found to be sparser in the interior. Thus, after day 7, mass transfer becomes a limiting factor and based on the measured DNA content in the sample on day 14, the cell growth appeared to have reached the plateau phase and the cell distribution did not advance further into the scaffold. From this result, the gelatin scaffolds developed were shown to provide a good environment for PESMCs but an improvement in the culture environment is needed for better construct development. In this study, a bioreactor system was designed and built to improve mass transfer in the culture environment.

7.2.3 PESMCs under normal air (without external CO_2)

The bioreactor system designed to enable in situ oxygen profiling using a microsensor system that is not compatible with a conventional incubator. The system consists of an incubator unit (IU), which serves as an incubator to stabilize the temperature around 37 ^{o}C. It has been well-known that the temperature for cell culture *in vitro* has to be monitored at the temperature close to the host to maintain normal functions. Optimal growth of mammalian cells has been observed between 33 and 38 ^{o}C [206]. In practice, any temperature lower than 38.5 ^{o}C would not impose any adverse effects on the cultured cells [55, 206] while lowering temperature from the host temperature would lead to reduction in cell growth and metabolism, which are normally reversible as the normal temperature resumes [206]. However, the latter effect has not been widely studied. Jorjani and Ozturk [206] found that the oxygen consumption of murine

hybridoma was reduced by 10 % for a degree drop in temperature. The authors believed the oxygen requirement can be lowered slightly by a small reduction in the culture temperature such that a higher cell concentration can be maintained. It might be beneficial to develop a tissue construct at high cell density with lower oxygen requirement but the effect on the cell phenotype and the lowest allowable temperature depression are still unknown.

In this study, both spatial and time response tests of the IU showed that the variation of temperature was small (± 0.25 °C in the IU compared with ± 0.2 °C in the conventional incubator [207]) and response time (3 minutes in the IU compared with 11 minutes in the conventional incubator) was sufficiently fast to maintain culture temperature around 37 °C. After a temperature disruption was introduced, there is no temperature overshoot in the conventional incubator while a brief overshoot up to 39 °C (< 45s) was observed in the IU. One may concern the overshoot would cause overheating in the bioreactor culture. However, a heat transfer analysis suggests that such effect might be minimal (less than 0.01 °C temperature rise in the medium side after the temperature disruption) for a bioreactor constructed by 1-cm thick polycarbonate walls.

On the other hand, no external CO_2 was employed for the new system since (1) it can simplify the overall design which does not require gas mixing and CO_2 sensor and (2) over-relying on CO_2-$NaHCO_3$ buffer has shown to adversely affect cell growth in closed system [196] and (3) the buffering capacity of such system is considered weak and may not be able to stabilize pH at high cell density when cellular metabolism is high [55].

The abandoning of the conventional buffering system prompted a change of buffer especially if the culture was conducted under normal air environment with only 0.03 % CO_2 in air. Addition of HEPES has already been shown to be beneficial in stabilization of pH in the conventional CO_2-$NaHCO_3$ system [208] and some other saline-based formula have also attempted to reduce bicarbonate by substituting HEPES to improve pH stabilization when used in normal air [55].

In this study, a HEPES-bicarbonate combination was used and it was found that 5 or 10 mM HEPES and 4 mM bicarbonate were sufficient to maintain pH stabilization suitable for cell culture. Although a higher amount of HEPES could be added for a higher buffer capacity, the lower concentration of 10mM was used due to (1) cytotoxicity at high concentration (>25 or 50 mM) and (2) radical formation under light which adversely affects cell growth [209]. The latter was resolved by lowering the concentration of HEPES to its lowest effective level and by avoiding long-term exposure of the culture medium to light.

Finally, the osmolality of the culture medium was adjusted to maintain the buffer as close as possible to the original formula since cell growth may be altered by a change of osmolality (although mammalian cells can survive a wide range of osmolality) [55]. The osmolality of the conventional formula with 44 mM bicarbonate is approximately 336 mOsm/kg as compared with 256 mOsm/kg in the formula containing 4 mM bicarbonate and 10 mM HEPES. The 25 % deficiency was corrected by addition of 3.45 g/L of NaCl into the culture medium. The successful culture of PESMCs verified the feasibility of performing culture experiments in this modified cell culture environment.

7.2.4 Culture of PESMCs in high/low glucose environment

In order to study cell growth associated with oxygen transport, PESMCs were cultured under two levels of glucose (1 or 4.5 g/L). Experiments were conducted to estimate oxygen and glucose consumption and the growth rate of PESMCs, which provided information on the nutrient requirements and growth kinetics in the new culture environment. The data collected included parameters for oxygen consumption (maximum consumption rate and half-saturation constant) and growth kinetics (maximum growth rate and Contois constant) were obtained and used as parameters in the mathematical model.

The mathematical model in this study requires inputs from the cellular utilization of oxygen and oxygen-dependent growth kinetics. For oxygen or glucose consumption, most of the studies were conducted in cell suspension [210]; such conditions are believed to be different from those influencing attached cells. For example, cells in suspension were found to be low in ATP production which implied lower glucose and oxygen utilization [211]. In order to retrieve such information in attached cells, special sensors were used for all measurements for cells attached on the tissue culture surface.

It was found that both oxygen and glucose transport were not limited in monolayer culture of PESMCs since the oxygen level was higher than 90 % saturation while the glucose level was almost unchanged over time. There were significant differences in oxygen consumption and growth rate for cells growing at the two different levels of glucose. High glucose resulted in a lower oxygen level (implying higher oxygen

consumption) at the latter days of the culture and a significantly higher cell growth. In an oxygen-rich environment, cellular utilization of glucose was altered such that the growth rate was promoted by increase in glucose level.

Estimation of the daily glucose and oxygen consumption per cell showed that higher energy was required after subculture. Foy *et al.* [212] showed that cells required higher oxygen consumption in the attachment phase which implied higher energy consumption for attachment, spreading and cytoskeletal re-arrangement. This explained the rise of both glucose and oxygen consumption in the first 2 days of the culture.

High cell growth occurs when oxygen transport is maintained at a high level, which is not expected in the case of 3D tissue construct, within which oxygen transport could be limited due to diffusion within the construct. Compared with glucose, which is more soluble in aqueous environment, oxygen transport appeared to be more essential in tissue development.

7.3 Bioreactor culture

One of the major bottlenecks for tissue engineering *in vitro* is mass transfer which limits building thicker tissue constructs; that is, the constructs whose dimensions exceed the static diffusion limit, may not be able to match the metabolic requirement for the cells deep inside the construct. Insufficient mass transfer of growth-related species may accelerate cell death or lead to a non-uniform cell distribution. In this study, oxygen was assumed to be the growth-limiting factor due to its low solubility in the culture medium compared with the other factors such as glucose, glutamate and

amino acids. To improve mass transfer in the culture environment, a flow-type bioreactor with two configurations was designed and used in this study. Flowrate was also believed to be important factor for flow bioreactor since it enhance convective mass transfer and two levels of flowrate were studied (0.272 and 0.545 ml/min).

Oxygen transport (both external and internal) was improved by increasing flowrate and, the improvement was even greater in the double flow configuration than single flow configuration. As shown in the experimental data, the lowest oxygen level was observed at the bottom side (full thickness) and at the core (half thickness) of the construct when cultured in the single and the double flow configurations, respectively. The double flow configuration also appeared beneficial in cell distribution studies as the cells distributed more uniformly in the construct, particularly at the higher flowrate. In this study, a slightly lower cell density (2 million cells/cm^3) was used intentionally to observe a progressive decrease in oxygenation and to avoid premature deprivation of oxygen in the first few days at high cell density, which may not be easy to measure.

Fluid flow induces shear stress. It has been well-known that both cells and tissues respond to shear stress *in vitro* and *in vivo* which relates to physiology and pathology [135]. Most of the studies on the effect of shear stress on smooth muscle cells are mainly focused on vascular smooth muscle cells (VSMCs) due to the heavy research on the vascular diseases. For VSMCs, exposure of cells to shear stress was found to affect cell proliferation and phenotype. Sherpetti *et al.* and Fitzgerald *et al.*[213, 214, 215] showed that shear stress between 3 and 11 dyn/cm^2 inhibited proliferation and induce cell apoptosis. Alshihabi and coworkers [216] stimulate short-term secretion of

prostaglandin E2 (PGE2) and prostaglandin I2 (PGI2). The former relates to the smooth muscle relaxation while the latter is known to inhibit VSMC proliferation. At a shear stress of 0.5 dyn/cm^2 led to the highest release of PGI2. Recent findings also showed that shear stress at a level of 15 dyn/cm^2 induced VSMCs to transdifferentiation into endothelial-like cells with upregulation in all the gene expressions of endothelial cells [217]. However, there is currently no research on the effect of shear stress on esophageal smooth muscle cells. Furthermore, most of these studies [213, 214, 215, 216, 217] focused on the higher levels of shear stress, which is probably due to the relevance to the hemodynamics *in vivo*.

In the bioreactor culture conducted in this study, the shear stresses at the construct surface were estimated as low as 3.2×10^{-4} and 1.6×10^{-4} dyn/cm^2 for 0.545 and 0.272 ml/min, respectively using wall shear stress calculation for a flow in a parallel plate chamber (shear stress = $\frac{6Q\mu_\beta}{H^2 W}$)[186] with Q = flowrate, μ_β = medium viscosity, H = chamber height and W = chamber width. The effect of shear stress at this level (10^{-4} dyn/cm^2) has not been widely studied. However, at the level of 10^{-1} dyn/cm^2, studies had shown cell damage in cardiomyocytes [218] and release of growth-inhibiting substance in VSMC [216]. Therefore, cell damage or growth inhibition may be induced even at a low shear stress level, especially for the cell types, which are not physiologically exposed to an external flow like endothelial and epithelial cells. In the cell distributions measured in this study, lower cell densities near the construct surface were occasionally found in some locations, especially at the flowrate of 0.545 ml/min. The cell loss near the construct surface could be due to high local shear stress, which was not able to measure in the experiments.

There are many current designs of tissue engineering bioreactors with direct flow through the tissue construct which have been shown to improve cell distribution and architecture by improving oxygenation [24, 36, 147, 218]. However, interstitial flow may be physiological and beneficial for bone but not for other tissue types such as kidney and myocardium as discussed by Dvir *et al.*[218]. Therefore, direct flow may not be physiological for tissue development, which was the rationale of this research where we only applied flow on top of the construct surface(s). Furthermore, even with direct perfusion, mass transfer resistance increases with time due to cell growth and deposition of extracellular matrix (ECM). To overcome these effects, the future direction of bioreactors should also incorporate angiogenesis into bioreactor design and culture strategy [219].

Oxygen transport has been identified as an important factor in the tissue engineering of constructs and previous experimental studies have not be able to capture important and accurate information about the local oxygen data because: (1) only the oxygen profiles in the tissue constructs cultured in the open Petri dish or an open flow system were measured since construct oxygen data requires introduction of microsensor [24, 162, 165]; or (2) only a single point measurement inside the construct in the bioreactor was carried out since the location of the sensor was fixed beforehand [13]; or (3) only a planar profile was measured due to the limitation of the measurement method [166]. In this study, the bioreactor system design enabled in situ oxygen profiling outside a conventional incubator and the measured oxygen profiles showed high correlation with the cell distribution. Furthermore, the culture system was independent of CO_2 which has not been widely used since it requires an adjustment of culture medium

formula. This study showed that with a simple adjustment of buffer system and osmolality, tissue culture can be easily adopted in air condition without compromise of the performance.

7.4 Validation of Mathematical Model

In order to predict oxygenation and cell growth in the tissue construct grown in the bioreactor, a mathematical model was established and validated. A validated model can serve as a prediction tool for bioreactor operation such that the number of experiments can be minimized.

The simulation results for four bioreactor culture conditions: two levels of flowrates (0.272 and 0.545 ml/min) × two bioreactor configurations showed that the established model not only qualitatively but also quantitatively agreed with the experimental results. This model adopted the Volume Average Method (VAM) in formulation of the complex domain consisting of cells, medium and scaffold. VAM has been used in theoretical studies in biological systems [172, 174, 175, 176] and tissue engineering [42, 43]. In VAM, the governing equations of a domain with a mixture of different phases can be formulated into a single equation by which the microscopic information is absorbed into parameters in the macroscopic equation. In order to simplify the microscopic details to obtain an analytical solution for these parameters, a theoretical model was proposed and Chang's unit cell model was adopted. The two-phase Chang's unit cell has been solved [172] and applied in tissue engineering calculations. However, in our case, the real structure is a three-phase domain with cells, scaffold and medium. This requires special consideration in the theoretical model. In this study,

the closure problem arisen from the VAM formulation was solved using a three-phase theoretical model (see Appendix A) for effective diffusivity to account the variation of oxygen diffusivity due to the increase in local cell number (in terms of cell volume fraction). This approach may provide a better estimation for the parameters rather than just assuming a constant [22, 24]. When compared alongside the model parameters measured from the cells actually used in the experiments, the simulation results showed relatively good agreement with the experimental results (e.g., oxygen profiles, cell distributions).

The coupled system used in the model establishment has advantages over the system modeled using single domain. In the studies of Galban and Locke [42, 43], a well-mixed condition was assumed and caused the overestimation of the surface concentration of nutrients. The well-mixed condition assumes that the surface concentration is fixed at the bulk value. However, as shown in our experimental results, the assumption is overly underestimated even if a flow is applied. Therefore, the use of their model would lead to an incorrect estimation of the nutrient concentration at the construct surface. Lappa *et al.* [50, 51] only studied the outward growth of tissue construct and neglected entirely the internal cell growth and nutrient nourishment. A comparison between the model used by Lappa *et al.* and the model developed was not possible since the experiment culture condition showed a significant outward growth of tissue under simulated gravity condition in rotating wall vessel (RWV) and their established model attempted to simulate such "outward growth" phenomena. However, such outward growth might not be observed in other tissue constructs cultured under different conditions and our experimental results also

showed no sign of outward growth. Due to this reason, the "outward growth" model proposed by Lappa *et al*. was unable to compare with the model used for internal cell growth.

The discrepancies between the model and the experimental data may be due to several factors: (1) experimental errors: since the chamber height was 5.5 mm and flow might not be as uniform as simulated due to unevenness on the scaffold. Any irregularities at the surface of the scaffold would interfere with the flow field to some extent, which in turn, may alter the oxygen profile. Since cell seeding depended on the capillary effect of a small drop of cell suspension seeping into the porous scaffold, there is some degree of inhomogeneity in cell distribution. Furthermore, some blind pores in the scaffold may also prevent cell penetration, which could cause local low cellularity. (2) Model parameters: there may be an over-estimation on the sink term in the momentum equation due to the permeability estimation of the construct using the Carman-Kozeny equation. This turned out to be an underestimation of internal medium flow and oxygen level in some cases. Furthermore, studies suggested that cells react to their surrounding environment and accordingly altered their oxygen utilization and growth rate [22, 24]. Such alterations were not included in the model. Furthermore, as discussed earlier, energy consumption was higher in the cell attachment phase and oxygen consumption is believed to be different from the cells during growth phase. In order to account for this, a separate mathematical treatment may be required for the first few days after seeding. This treatment should also be applied in cell growth since cell growth was normally in lag phase in the first few days during which the cells adapt the new culture environment [55].

Both experiment and simulation suggested that oxygen transport in the culture system is interrelated between external and internal transport. Ignoring either one of them may lead to wrong prediction. In many early studies, the lactate-to-glucose ratio (L/G) was taken as an indicator of aerobic/anaerobic metabolism. Since both lactate and glucose concentrations were measured from the medium samples (external), low L/G value sometimes misled the actual internal oxygenation [35] since lactate may be high in the interior of the construct due to poor internal oxygenation but it could not be transported out of the construct due to a thick cell layers around the periphery. The accumulation of lactate led to cell death in the core region. When studying such a system, it is important to couple both the internal (construct) and external (bulk medium) effect to avoid underestimation or overestimation of the actual situation. As shown in the results, substantial external and internal boundary layers were observed implying overall oxygen transport in the system was not controlled single-sidedly.

The rationale of using the two flow configurations (single and double flow) was simple but important. Like all other transport phenomena such as heat or momentum transfer, an increase in effective surface area implies enhancement of transport of these properties. As discussed before, the location of the lowest oxygen tension was shifted from bottom (full thickness) to the core (half thickness) when the exposure surface was increased from "top only" to "both top and bottom". It is noted that although the diffusion length is reduced, one may also expect an increase in the minimum oxygen level. However, it is not necessarily so in this case since the modeled system is a dynamic process with cell continuously growing. Better oxygenation within the construct led to higher internal cell growth which also in turn increased oxygen

demand. Such an increase in oxygen demand definitely reduced the internal oxygen level. Hence, not only is the oxygen consumption increased, but also the reduction in diffusion further hindered oxygen transport caused by the increase in steric hindrance from the increase in cell mass. Therefore, in order to meet such demands, an increase in effective surface area for oxygen transport is important. This ultimately only can happen if a capillary tree is also grown into the construct to increase the surface area for oxygen transport and reduce the diffusion distance. Therefore, in order to succeed in growing a thicker tissue construct, reconstructing capillaries is necessary to meet the metabolic demand of the tissue construct.

In this project, a new method to prepare a gelatin scaffold for smooth muscle construct has been developed and the created scaffold demonstrated good compatibility with PESMCs. It is also the first time to study growth kinetics and metabolic requirements of PESMCs adapted in the normal air condition, which allowed determination of the cell passage suitable for the tissue culture experiments and the estimation of cell growth and metabolic parameters. The current tissue growth models in literature required curve fitting to ensure reasonable fit with the experimental data since limited data was gathered for the cell growth and metabolism for the particular lineage of cell types. With the cell growth and metabolic parameters estimated from the experiments as model inputs, the mathematical model established was showed reasonable fit with the experimental data. This work was also the first attempt to demonstrate the potential to develop smooth muscle constructs in the designed bioreactor under normal air condition independent of external CO_2 supplementation. Finally, a bioreactor system compatible to full-thickness oxygen profiling during tissue culture which has not been

established in the previous research was developed in this study to perform in-situ oxygen measurement in a growing tissue construct. The results showed the internal oxygenation was influenced by the external flow in the bioreactor and the patterns of cell distribution found in most of this study were highly oxygen dependent.

Chapter 8. Conclusion

1. Dehydrothermally crosslinked gelatin scaffolds have relatively uniform porous properties and showed good interaction with esophageal smooth muscle cells.
2. Porcine esophageal smooth muscle cells (PESMCs) were successfully isolated and able to subculture for more than six times.
3. Culture medium conditioned by 3.45 g/L NaCl and 10 mM HEPES/ 4 mM bicarbonate buffer allowed PESMC culture under normal air.
4. Increasing medium flowrate across the surface of smooth muscle construct improved internal oxygen transport that consequently increased cellularity and improved uniformity of cell distribution
5. Exposing the top surface of tissue construct to flow (single flow configuration) resulted in both decreasing oxygen and cell density across the construct thickness.
6. Exposing both the top and bottom surface of tissue construct to flow (double flow configuration) resulted in better internal oxygen transport than single flow configuration and the uniformity of cell distribution was greatly improved.
7. Mathematical model assuming oxygen-dependent growth showed a good agreement with the experimental data in most of the culture conditions, suggesting a strong correlation between cell distribution and oxygen transport.

References

1. Langer, R. and Vacanti, J.P., *Tissue engineering.* Science, 1993. **260**(5110): p. 920-6.

2. Fuchs, J.R., Nasseri, B.A. and Vacanti, J.P., *Tissue engineering: a 21st century solution to surgical reconstruction.* Ann Thorac Surg, 2001. **72**(2): p. 577-91.

3. Reece, G. and Patrick, C., *Tissue engineered construct design principles*, in *Frontiers in Tissue Engineering*, Patrick, C., Mikos, A., and McIntire, L., *eds*. 1998, Elsevier Science Inc.: NY. p. 166-96.

4. Vacanti, C.A. and Vacanti, J.P., *The History and Scope of Tissue Engineering*, in *Principles of tissue engineering*, Lanza, R.P., Langer, R.S., and Vacanti, J., *eds*. 2000, Academic Press: San Diego. p. 3-8.

5. Park, J., *Biomaterials*, in *The Biomedical Engineering Handbook (Vol. 1)*, Bronzino, J.D., *eds*. 2000, CRC Press: Boca Raton. p. IV-1-IV-8.

6. Bennett, D., Humphreys, L., O'Brien, S., et al., *Wear paths produced by individual hip-replacement patients--A large-scale, long-term follow-up study.* J Biomech, 2008. **41**(11): p. 2474-2482.

7. Freud, E., Efrati, I., Kidron, D., et al., *Comparative experimental study of esophageal wall regeneration after prosthetic replacement.* J Biomed Mater Res, 1999. **45**(2): p. 84-91.

8. Galletti, P.M. and Nerem, R.M., *Prostheses and Artificial Organs*, in *The Biomedical Engineering Handbook (Vol. 2)*, Bronzino, J.D., *eds*. 2000, CRC Press: Boca Raton. p. XIII-1-XIII-11.

9. Bell, E., Ehrlich, H.P., Sher, S., et al., *Development and use of a living skin equivalent.* Plast Reconstr Surg, 1981. **67**(3): p. 386-92.

10. Burke, J.F., Yannas, I.V., Quinby, W.C., Jr., et al., *Successful use of a physiologically acceptable artificial skin in the treatment of extensive burn injury.* Ann Surg, 1981. **194**(4): p. 413-28.

11. Uemura, T., Dong, J., Wang, Y., et al., *Transplantation of cultured bone cells using combinations of scaffolds and culture techniques.* Biomaterials, 2003. **24**(13): p. 2277-86.

12. Botchwey, E., Ferrante, E. and Humphrey, J., *Bioreactor-based bone tissue engineering.* J Biomech, 2006. **39**(Supplement 1): p. S218.

13. Volkmer, E., Drosse, I., Otto, S., et al., *Hypoxia in Static and Dynamic 3D Culture Systems for Tissue Engineering of Bone.* Tissue Eng Pt A, 2008. **14**(8): p. 1331-1340.

14. Freed, L.E., Vunjaknovakovic, G., Biron, R.J., et al., *Biodegradable Polymer Scaffolds for Tissue Engineering.* Biotechnology, 1994. **12**(7): p. 689-693.

15. Sittinger, M., Bujia, J., Minuth, W.W., et al., *Engineering of cartilage tissue using bioresorbable polymer carriers in perfusion culture.* Biomaterials, 1994. **15**(6): p. 451-456.

16. Malda, J., Woodfield, T.B.F., van der Vloodt, F., et al., *The effect of PEGT/PBT scaffold architecture on oxygen gradients in tissue engineered cartilaginous constructs.* Biomaterials, 2004. **25**(26): p. 5773-5780.

17. Oberpenning, F., Meng, J., Yoo, J.J., et al., *De novo reconstitution of a functional mammalian urinary bladder by tissue engineering.* Nat Biotechnol, 1999. **17**(2): p. 149-55.

18. Cheng, E.Y. and Kropp, B.P., *Urologic tissue engineering with small-intestinal submucosa: potential clinical applications.* World J Urol, 2000. **18**(1): p. 26-30.

19. Weinberg, C.B. and Bell, E., *A blood vessel model constructed from collagen and cultured vascular cells.* Science, 1986. **231**(4736): p. 397-400.

20. L'Heureux, N., Paquet, S., Labbe, R., et al., *A completely biological tissue-engineered human blood vessel.* FASEB J, 1998. **12**(1): p. 47-56.

21. Niklason, L.E., Gao, J., Abbott, W.M., et al., *Functional arteries grown in vitro.* Science, 1999. **284**(5413): p. 489-93.

22. Carrier, R.L., Rupnick, M., Langer, R., et al., *Perfusion Improves Tissue Architecture of Engineered Cardiac Muscle.* Tissue Eng, 2002. **8**(2): p. 175-188.

23. Kofidis, T., Lenz, A., Boublik, J., et al., *Pulsatile perfusion and cardiomyocyte viability in a solid three-dimensional matrix.* Biomaterials, 2003. **24**(27): p. 5009-5014.

24. Radisic, M., Park, H., Chen, F., et al., *Biomimetic Approach to Cardiac Tissue Engineering: Oxygen Carriers and Channeled Scaffolds.* Tissue Eng, 2006. **12**(8): p. 2077-2091.

25. Tabata, Y., *Recent progress in tissue engineering.* Drug Discov Today, 2001. **6**(9): p. 483-487.

26. Martin, Y. and Vermette, P., *Bioreactors for tissue mass culture: Design, characterization, and recent advances.* Biomaterials, 2005. **26**(35): p. 7481-7503.

27. Nerem, R.M., *The Challenge of Imitating Nature*, in *Principles of tissue engineering*, Lanza, R.P., Langer, R.S., and Vacanti, J., *eds*. 2000, Academic Press: San Diego. p. 9-16.

28. Vunjak-Novakovic, G., Obradovic, B., Martin, I., et al., *Bioreactor studies of native and tissue engineered cartilage.* Biorheology, 2002. **39**(1-2): p. 259-68.

29. Strehl, R., Schumacher, K., de Vries, U., et al., *Proliferating cells versus differentiated cells in tissue engineering.* Tissue Eng, 2002. **8**(1): p. 37-42.

30. Minuth, W.W., Schumacher, K., Strehl, R., et al., *Physiological and cell biological aspects of perfusion culture technique employed to generate differentiated tissues for long term biomaterial testing and tissue engineering.* J Biomat Sci-Polym E, 2000. **11**(5): p. 495-522.

31. Vunjak-Novakovic, G. and Freed, L.E., *Culture of organized cell communities.* Adv Drug Deliv Rev, 1998. **33**(1-2): p. 15-30.

32. Tabata, I.I., *The importance of drug delivery systems in tissue engineering.* Pharm Sci Techno To, 2000. **3**(3): p. 80-89.

33. Stegemann, J.P. and Nerem, R.M., *Phenotype modulation in vascular tissue engineering using biochemical and mechanical stimulation.* Ann Biomed Eng, 2003. **31**(4): p. 391-402.

34. Lokmic, Z. and Mitchell, G.M., *Engineering the Microcirculation.* Tissue Eng Pt B-Rev, 2008. **14**(1): p. 87-103.

35. Carrier, R.L., Papadaki, M., Rupnick, M., et al., *Cardiac tissue engineering: Cell seeding, cultivation parameters, and tissue construct characterization.* Biotechnol Bioeng, 1999. **64**(5): p. 580-589.

36. Carrier, R.L., Rupnick, M., Langer, R., et al., *Effects of oxygen on engineered cardiac muscle.* Biotechnol Bioeng, 2002. **78**(6): p. 617-625.

37. Freed, L.E. and Vunjak-Novakovic, G., *Tissue Engineering Bioreactors*, in *Principles of tissue engineering*, Lanza, R., Langer, R., and Vacanti, J., *eds*. 2000, Academic Press: San Diego. p. 143-157.

38. Goldstein, A.S., Juarez, T.M., Helmke, C.D., et al., *Effect of convection on osteoblastic cell growth and function in biodegradable polymer foam scaffolds.* Biomaterials, 2001. **22**(11): p. 1279-1288.

39. Eiselt, P., Kim, B.S., Chacko, B., et al., *Development of technologies aiding large-tissue engineering.* Biotechnol Prog, 1998. **14**(1): p. 134-40.

40. Fuchs, J.R., Pomerantseva, I., Ochoa, E.R., et al., *Fetal tissue engineering: in vitro analysis of muscle constructs.* J Pediatr Surg, 2003. **38**(9): p. 1348-53.

41. Obradovic, B., Carrier, R.L., Vunjak-Novakovic, G., et al., *Gas exchange is essential for bioreactor cultivation of tissue engineered cartilage.* Biotechnol Bioeng, 1999. **63**(2): p. 197-205.

42. Galban, C.J. and Locke, B.R., *Analysis of cell growth kinetics and substrate diffusion in a polymer scaffold.* Biotechnol Bioeng, 1999. **65**(2): p. 121-132.

43. Galban, C.J. and Locke, B.R., *Effects of spatial variation of cells and nutrient and product concentrations coupled with product inhibition on cell growth in a polymer scaffold.* Biotechnol Bioeng, 1999. **64**(6): p. 633-643.

44. Chung, C.A., Yang, C.W. and Chen, C.W., *Analysis of cell growth and diffusion in a scaffold for cartilage tissue engineering.* Biotechnol Bioeng, 2006. **94**(6): p. 1138-1146.

45. Dunn, J.C.Y., Chan, W.Y., Cristini, V., et al., *Analysis of cell growth in three-dimensional scaffolds.* Tissue Eng, 2006. **12**(4): p. 705-716.

46. Lewis, M.C., MacArthur, B.D., Malda, J., et al., *Heterogeneous proliferation within engineered cartilaginous tissue: The role of oxygen tension.* Biotechnol Bioeng, 2005. **91**(5): p. 607-615.

47. Obradovic, B., Meldon, J.H., Freed, L.E., et al., *Glycosaminoglycan deposition in engineered cartilage: Experiments and mathematical model.* AIChE J, 2000. **46**(9): p. 1860-1871.

48. Pisu, M., Lai, N., Cincotti, A., et al., *Modeling of engineered cartilage growth in rotating bioreactors.* Chem Eng Sci, 2004. **59**(22-23): p. 5035-5040.

49. Sanz-Herrera, J.A., García-Aznar, J.M. and Doblaré, M., *Micro-macro numerical modelling of bone regeneration in tissue engineering.* Comput Method Appl M, 2008. **197**(33-40): p. 3092-3107.

50. Lappa, M., *The growth and the fluid dynamics of protein crystals and soft organic tissues: models and simulations, similarities and differences.* J Theor Biol, 2003. **224**(2): p. 225-240.

51. Lappa, M., *A CFD level-set method for soft tissue growth: theory and fundamental equations.* J Biomech, 2005. **38**(1): p. 185-190.

52. Coletti, F., Macchietto, S. and Elvassore, N., *Mathematical modeling of three-dimensional cell cultures in perfusion bioreactors.* Ind Eng Chem Res, 2006. **45**(24): p. 8158-8169.

53. Mehta, K. and Linderman, J.J., *Model-based analysis and design of a microchannel reactor for tissue engineering.* Biotechnol Bioeng, 2006. **94**(3): p. 596-609.

54. Ma, C.Y.J., Kumar, R., Xu, X.Y., et al., *A combined fluid dynamics, mass transport and cell growth model for a three-dimensional perfused biorector for tissue engineering of haematopoietic cells.* Biochem Eng J, 2007. **35**(1): p. 1-11.

55. Freshney, R., *Culture of Animal Cells: A Manual of Basic Technique*. 5th ed. 2005, Hoboken: Wiley.

56. Park, H., Cannizzaro, C., Vunjak-Novakovic, G., et al., *Nanofabrication and microfabrication of functional materials for tissue engineering.* Tissue Eng, 2007. **13**(8): p. 1867-77.

57. Hollister, S.J., *Porous scaffold design for tissue engineering.* Nat Mater, 2005. **4**(7): p. 518-524.

58. Sashiwa, H. and Aiba, S.I., *Chemically modified chitin and chitosan as biomaterials.* Prog Polym Sci, 2004. **29**(9): p. 887-908.

59. Sung, H.J., Meredith, C., Johnson, C., et al., *The effect of scaffold degradation rate on three-dimensional cell growth and angiogenesis.* Biomaterials, 2004. **25**(26): p. 5735-42.

60. Kim, K., Yu, M., Zong, X., et al., *Control of degradation rate and hydrophilicity in electrospun non-woven poly(D,L-lactide) nanofiber scaffolds for biomedical applications.* Biomaterials, 2003. **24**(27): p. 4977-85.

61. Mooney, D.J. and Langer, L.S., *Engineering Biomaterials for Tissue Engineering: The 10-100 Micron Size Scale.*, in *The Biomedical Engineering Handbook*, Bronzino, J.D., *eds*. 1995, CRC Press: Boca Raton. p. 1609-1618.

62. Kleinman, H.K., Philp, D. and Hoffman, M.P., *Role of the extracellular matrix in morphogenesis.* Curr Opin Biotechnol, 2003. **14**(5): p. 526-32.

63. Griffith, L.G. and Naughton, G., *Tissue engineering--current challenges and expanding opportunities.* Science, 2002. **295**(5557): p. 1009-14.

64. Cassell, O.C., Morrison, W.A., Messina, A., et al., *The influence of extracellular matrix on the generation of vascularized, engineered, transplantable tissue.* Ann N Y Acad Sci, 2001. **944**: p. 429-42.

65. Vogel, V. and Baneyx, G., *The Tissue Engineering Puzzle: A Molecular Perspective.* Ann Rev Biomed Eng, 2003. **5**(1): p. 441-463.

66. Badylak, S.F., *The extracellular matrix as a biologic scaffold material.* Biomaterials, 2007. **28**(25): p. 3587-93.

67. Badylak, S., Meurling, S., Chen, M., et al., *Resorbable bioscaffold for esophageal repair in a dog model.* J Pediatr Surg, 2000. **35**(7): p. 1097-103.

68. Elkins, R.C., Dawson, P.E., Goldstein, S., et al., *Decellularized human valve allografts.* Ann Thorac Surg, 2001. **71**(5, Supplement 1): p. S428-S432.

69. Schenke-Layland, K., Vasilevski, O., Opitz, F., et al., *Impact of decellularization of xenogeneic tissue on extracellular matrix integrity for tissue engineering of heart valves.* J Struct Biol, 2003. **143**(3): p. 201-8.

70. Schaner, P.J., Martin, N.D., Tulenko, T.N., et al., *Decellularized vein as a potential scaffold for vascular tissue engineering.* J Vasc Surg, 2004. **40**(1): p. 146-153.

71. Simon, P., Kasimir, M.-T., Rieder, E., et al., *Tissue Engineering of heart valves--Immunologic and inflammatory challenges of the allograft scaffold.* Prog Pediatr Cardiol, 2006. **21**(2): p. 161-165.

72. Dalton, P., Woodfield, T. and Hutmacher, D., *SnapShot: Polymer Scaff olds for Tissue Engineering.* Biomaterials, 2009. **30**(4): p. 701-702.

73. Ma, P.X. and Zhang, R., *Synthetic nano-scale fibrous extracellular matrix.* J Biomed Mater Res, 1999. **46**(1): p. 60-72.

74. Yang, S., Leong, K.-F., Du, Z., et al., *The Design of Scaffolds for Use in Tissue Engineering. Part I. Traditional Factors.* Tissue Eng, 2001. **7**(6): p. 679-689.

75. Mikos, A.G., Thorsen, A.J., Czerwonka, L.A., et al., *Preparation and characterization of poly(l-lactic acid) foams.* Polymer, 1994. **35**(5): p. 1068-1077.

76. Mecham, R.P., *Overview of extracellular matrix.* Curr Protoc Cell Biol, 2001. **10**: p. 10-1.

77. Ahmed, M. and Dickinson, E., *Effect of ethanol on the foaming of aqueous protein solutions.* Colloid Surface, 1990. **47**(1): p. 353-365.

78. Kitabatake, N. and Doi, E., *Surface tension and foaming of protein solutions.* J Food Sci, 1982. **47**(4): p. 1218-1221.

79. Vani, B. and Zayas, J.F., *Foaming properties of selected plant and animal proteins.* J Food Sci, 1995. **60**(5): p. 1025-1028.

80. Chang, W.H., Chang, Y., Lai, P.H., et al., *A genipin-crosslinked gelatin membrane as wound-dressing material: In vitro and in vivo studies.* J Biomat Sci-Polym E, 2003. **14**(5): p. 481-495.

81. Jenkins, H.P. and Janda, R., *Studies on the use of gelatin sponge or foam as an hemostatic agent in experimental liver resections and injuries to large veins.* Ann Surg, 1946. **124**(5): p. 952-961.

82. Koide, M., Osaki, K., Konishi, J., et al., *A new type of biomaterial for artificial skin: Dehydrothermally cross- linked composites of fibrillar and denatured collagens.* J Biomed Mater Res, 1993. **27**(1): p. 79-87.

83. Sung, H.W., Huang, D.M., Chang, W.H., et al., *Evaluation of gelatin hydrogel crosslinked with various crosslinking agents as bioadhesives: In vitro study.* J Biomed Mater Res, 1999. **46**(4): p. 520-530.

84. Ulubayram, K., Cakar, A.N., Korkusuz, P., et al., *EGF containing gelatin-based wound dressings.* Biomaterials, 2001. **22**(11): p. 1345-1356.

85. Kozlov, P.V. and Burdygina, G.I., *The structure and properties of solid gelatin and the principles of their modification.* Polymer, 1983. **24**(6): p. 651-666.

86. Liang, H.C., Chang, W.H., Liang, H.F., et al., *Crosslinking structures of gelatin hydrogels crosslinked with genipin or a water-soluble carbodiimide.* J Appl Polym Sci, 2004. **91**(6): p. 4017-4026.

87. Jumblatt, M.M., Maurice, D.M. and Schwartz, B.D., *A gelatin membrane substrate for the transplantation of tissue cultured cells.* Transplantation, 1980. **29**(6): p. 498-499.

88. Li, M., Cui, T., Mills, D.K., et al., *Comparison of selective attachment and growth of smooth muscle cells on gelatin- and fibronectin-coated micropatterns.* J Nanosci Nanotechno, 2005. **5**(11): p. 1809-1815.

89. Dutta, A.K., Panda, A.K. and Mukhopadhyay, A. *Porous gelatin matrix for tissue engineering: micro-structure mimicry of collagen based extra cellular matrix*. 1995.

90. Kang, H.G., Kim, S.Y. and Lee, Y.M., *Novel porous gelatin scaffolds by overrun/particle leaching process for tissue engineering applications.* J Biomed Mater Res B, 2006. **79**(2): p. 388-397.

91. Kang, H.W., Tabata, Y. and Ikada, Y., *Fabrication of porous gelatin scaffolds for tissue engineering.* Biomaterials, 1999. **20**(14): p. 1339-1344.

92. Leddy, H.A., Awad, H.A. and Guilak, F., *Molecular diffusion in tissue-engineered cartilage constructs: Effects of scaffold material, time, and culture conditions.* J Biomed Mater Res B, 2004. **70**(2): p. 397-406.

93. Lee, S.B., Kim, Y.H., Chong, M.S., et al., *Study of gelatin-containing artificial skin V: Fabrication of gelatin scaffolds using a salt-leaching method.* Biomaterials, 2005. **26**(14): p. 1961-1968.

94. Lien, S.-M., Li, W.-T. and Huang, T.-J., *Genipin-crosslinked gelatin scaffolds for articular cartilage tissue engineering with a novel crosslinking method.* Mat Sci Eng C-Solid, 2008. **28**(1): p. 36-43.

95. Liu, J., Xu, G., Yuan, S., et al., *The effect of macromolecules on foam stability in sodium dodecyl sulfate/cetylpyridinium bromide mixtures.* J Disper Sci Technol, 2003. **24**(6): p. 779-787.

96. Van Vlierberghe, S., Cnudde, V., Masschaele, B., et al., *Porous gelatin cryogels as cell delivery tool in tissue engineering.* J Control Release, 2006. **116**(2): p. e95-e98.

97. Zhang, Y.Z., Venugopal, J., Huang, Z.M., et al., *Crosslinking of the electrospun gelatin nanofibers.* Polymer, 2006. **47**(8): p. 2911-2917.

98. Lastowka, A., Maffia, G.J. and Brown, E.M., *A comparison of chemical, physical and enzymatic cross-linking of bovine type I collagen fibrils.* J Am Leather Chem As, 2005. **100**(5): p. 196-202.

99. Yannas, I.V. and Tobolsky, A.V., *Cross-linking of gelatine by dehydration.* Nature, 1967. **215**: p. 509-510.

100. Ulubayram, K., Aksu, E., Gurhan, S.I.D., et al., *Cytotoxicity evaluation of gelatin sponges prepared with different cross-linking agents.* J Biomat Sci-Polym E, 2002. **13**(11): p. 1203-1219.

101. Ozeki, M. and Tabata, Y., *In vivo degradability of hydrogels prepared from different gelatins by various cross-linking methods.* J Biomat Sci-Polym E, 2005. **16**(5): p. 549-561.

102. Berthiaume, F. and Yarmush, M., *Fundamentals of Tissue Engineering*, in *Tissue Engineering*, Parsson, B., *eds*. 2003, CRC Press: Boca Raton.

103. Bell, E., *Tissue Engineering in Perspective*, in *Principles of Tissue Engineering*, Lanza, R., Langer, R., and Vacanti, J., *eds*. 2000, Academic Press: San Diego. p. xxxv-xl.

104. Polak, J.M. and Bishop, A.E., *Stem Cells and Tissue Engineering: Past, Present, and Future.* Ann N Y Acad Sci, 2006. **1068**(1): p. 352-366.

105. InanÃ§, B.l., ElÃ§in, A.E. and ElÃ§in, Y.M., *Human Embryonic Stem Cell Differentiation on Tissue Engineering Scaffolds: Effects of NGF and Retinoic Acid Induction.* Tissue Eng Pt A, 2008. **14**(6): p. 955-964.

106. Vacanti, C.A., *Tissue Engineering: Where Are We Headed?* J Am Coll Surgeons, 2008. **206**(6): p. 1095-1096.

107. Croagh, D., Phillips, W.A., Redvers, R., et al., *Identification of candidate murine esophageal stem cells using a combination of cell kinetic studies and cell surface markers.* Stem Cells, 2007. **25**(2): p. 313-8.

108. Izumi, K., Tobita, T. and Feinberg, S.E., *Isolation of human oral keratinocyte progenitor/stem cells.* J Dent Res, 2007. **86**(4): p. 341-6.

109. Michael, B. and Kate, B. *Biochemistry of Muscle Contraction: Smooth Muscle*. 2002. http://www.uic.edu/classes/phyb/phyb516/smoothmuscleu3.htm.

110. Tew, W.P., Kelsen, D.P. and Ilson, D.H., *Targeted therapies for esophageal cancer.* Oncologist, 2005. **10**(8): p. 590-601.

111. Caroline, M., *The early histogenesis of striated muscle in the œsophagus of the pig and the dogfish.* Anat Rec, 1910. **4**(1): p. 23-47.

112. Chamley-Campbell, J., Campbell, G.R. and Ross, R., *The smooth muscle cell in culture.* Physiol Rev, 1979. **59**(1): p. 1-61.

113. Cassell, O.C., Hofer, S.O., Morrison, W.A., et al., *Vascularisation of tissue-engineered grafts: the regulation of angiogenesis in reconstructive surgery and in disease states.* Br J Plast Surg, 2002. **55**(8): p. 603-10.

114. Ko, H.C.H., Milthorpe, B.K. and McFarland, C.D., *Engineering thick tissues - The vascularisation problem.* Eur Cells Mater, 2007. **14**: p. 1-18.

115. Finkenzeller, G., Torio-Padron, N., Momeni, A., et al., *In Vitro Angiogenesis Properties of Endothelial Progenitor Cells: A Promising Tool for Vasculatization.* Tissue Eng, 2007. **13**(7): p. 1413-1420.

116. Rouwkema, J., Rivron, N.C. and van Blitterswijk, C.A., *Vascularization in tissue engineering.* Trends Biotechnol, 2008. **26**(8): p. 434-441.

117. Hoerstrup, S.P., Zünd, G., Sodian, R., et al., *Tissue engineering of small caliber vascular grafts.* Eur J Cardio-Thorac, 2001. **20**(1): p. 164-169.

118. Isenberg, B.C. and Tranquillo, R.T., *Long-term cyclic distention enhances the mechanical properties of collagen-based media-equivalents.* Ann Biomed Eng, 2003. **31**(8): p. 937-49.

119. Bilodeau, K. and Mantovani, D., *Bioreactors for Tissue Engineering: Focus on Mechanical Constraints. A Comparative Review.* Tissue Eng, 2006. **12**(8): p. 2367-2383.

120. Mol, A., Bouten, C., Zund, G., et al., *The Relevance of Large Strains in Functional Tissue Engineering of Heart Valves.* Thorac Cardiov Surg, 2003. **51**: p. 78-83.

121. Syedain, Z.H., Weinberg, J.S. and Tranquillo, R.T., *Cyclic distension of fibrin-based tissue constructs: Evidence of adaptation during growth of engineered connective tissue.* P Natl Acad Sci, 2008. **105**(18): p. 6537-6542.

122. Hammond, T.G. and Hammond, J.M., *Optimized suspension culture: the rotating-wall vessel.* Am J Physiol Renal Physiol, 2001. **281**(1): p. F12-25.

123. Duke, J., Daane, E., Arizpe, J., et al., *Chondrogenesis in aggregates of embryonic limb cells grown in a rotating wall vessel.* Adv Space Res, 1996. **17**(6-7): p. 289-93.

124. Becker, J.L., Prewett, T.L., Spaulding, G.F., et al., *Three-dimensional growth and differentiation of ovarian tumor cell line in high aspect rotating-wall vessel: morphologic and embryologic considerations.* J Cell Biochem, 1993. **51**(3): p. 283-9.

125. Vunjak-Novakovic, G., Searby, N., Luis, J.D., et al., *Microgravity Studies of Cells and Tissues.* Ann N Y Acad Sci, 2002. **974**: p. 504-517.

126. Botchwey, E.A., Pollack, S.R., Levine, E.M., et al., *Quantitative analysis of three-dimensional fluid flow in rotating bioreactors for tissue engineering.* J Biomed Mater Res A, 2004. **69A**(2): p. 205-215.

127. Chen, H.-C. and Hu, Y.-C., *Bioreactors for tissue engineering.* Biotechnol Lett, 2006. **28**(18): p. 1415-1423.

128. Saini, S. and Wick, T.M., *Concentric Cylinder Bioreactor for Production of Tissue Engineered Cartilage: Effect of Seeding Density and Hydrodynamic Loading on Construct Development.* Biotechnol Prog, 2003. **19**(2): p. 510-521.

129. Schumacher, K., Strehl, R., de Vries, U., et al., *Advanced technique for long term culture of epithelia in a continuous luminal-basal medium gradient.* Biomaterials, 2002. **23**(3): p. 805-815.

130. Cowin, S., *How Does Nature Build a Tissue?*, in *Functional Tissue Engineering*, Guilak, F., *eds*. 2003, Springer-Verlag: New York. p. 3-16.

131. Sodian, R., Hoerstrup, S.P., Sperling, J.S., et al., *Tissue engineering of heart valves: in vitro experiences.* Ann Thorac Surg, 2000. **70**(1): p. 140-144.

132. Guyton, A., *Textbook of Medical Physiology*. 1996, Philadelphia: W.B. Saunders.

133. Solan, A., Mitchell, S., Moses, M., et al., *Effect of pulse rate on collagen deposition in the tissue-engineered blood vessel.* Tissue Eng, 2003. **9**(4): p. 579-86.

134. Haasper, C., Zeichen, J., Meister, R., et al., *Tissue engineering of osteochondral constructs in vitro using bioreactors.* Injury, 2008. **39**(1, Supplement 1): p. 66-76.

135. Gooch, K. and Tennat, C., *Mechanical Forces: Their Effects on Cells and Tissues*. 1997, Berlin: Springer-Verlag.

136. Hunter, C.J., Mouw, J.K. and Levenston, M.E., *Dynamic compression of chondrocyte-seeded fibrin gels: effects on matrix accumulation and mechanical stiffness.* Osteoarthr Cartilage, 2004. **12**(2): p. 117-130.

137. Kelly, T.-A.N., Ng, K.W., Wang, C.C.B., et al., *Spatial and temporal development of chondrocyte-seeded agarose constructs in free-swelling and dynamically loaded cultures.* J Biomech, 2006. **39**(8): p. 1489-1497.

138. Gooch, K., Blunk, T. and Vunjak-Novakovic, G., *Mechanical Forces and Growth Factors*, in *Frontiers in Tissue Engineering*, Patrick, C., Mikos, A., and McIntire, L., *eds*. 1998, Pergamon: Oxford. p. 61-82.

139. Evans, R.C. and Quinn, T.M., *Dynamic Compression Augments Interstitial Transport of a Glucose-Like Solute in Articular Cartilage.* Biophys J, 2006. **91**(4): p. 1541-1547.

140. Vriezen, N., Van Dijken, P. and Haggstrom, L., *Mammalian Cell Culture*, in *Basic Biotechnology*, Ratledge, C. and Kristiansen, B., *eds*. 2001, Cambridge University Press: Cambridge. p. 449-470.

141. Pound, J.C., Green, D.W., Roach, H.I., et al., *An ex vivo model for chondrogenesis and osteogenesis.* Biomaterials, 2007. **28**(18): p. 2839-2849.

142. Marolt, D., Augst, A., Freed, L.E., et al., *Bone and cartilage tissue constructs grown using human bone marrow stromal cells, silk scaffolds and rotating bioreactors.* Biomaterials, 2006. **27**(36): p. 6138-6149.

143. Knothe, T. and Melissa, L., *"Whither flows the fluid in bone?" An osteocyte's perspective.* J Biomech, 2003. **36**(10): p. 1409-1424.

144. Holtorf, H.L., Sheffield, T.L., Ambrose, C.G., et al., *Flow Perfusion Culture of Marrow Stromal Cells Seeded on Porous Biphasic Calcium Phosphate Ceramics.* Ann Biomed Eng, 2005. **33**(9): p. 1238-1248.

145. Fassina, L., Visai, L., Asti, L., et al., *Calcified Matrix Production by SAOS-2 Cells Inside a Polyurethane Porous Scaffold, Using a Perfusion Bioreactor.* Tissue Eng, 2005. **11**(5-6): p. 685-700.

146. Grayson, W.L., Bhumiratana, S., Cannizzaro, C., et al., *Effects of Initial Seeding Density and Fluid Perfusion Rate on Formation of Tissue-Engineered Bone.* Tissue Eng Pt A, 2008. **14**(11): p. 1809.

147. Freyria, A.M., Yang, Y., Chajra, H., et al., *Optimization of Dynamic Culture Conditions: Effects on Biosynthetic Activities of Chondrocytes Grown in Collagen Sponges.* Tissue Eng, 2005. **11**(5-6): p. 674-684.

148. Pazzano, D., Mercier, K.A., Moran, J.M., et al., *Comparison of Chondrogensis in Static and Perfused Bioreactor Culture.* Biotechnol Prog, 2000. **16**(5): p. 893-896.

149. Kilburn, D.G., Lilly, M.D., Self, D.A., et al., *The Effect of Dissolved Oxygen Partial Pressure on the Growth and Carbohydrate Metabolism of Mouse LS Cells.* J Cell Sci, 1969. **4**(1): p. 25-37.

150. Kilburn, D.G., Lilly, M.D. and Webb, F.C., *The Energetics of Mammalian Cell Growth.* J Cell Sci, 1969. **4**(3): p. 645-654.

151. Lightfoot, E., *Transport Phenomena and Living Systems: Biomedical Aspects of Momentum and Mass Transport*. 1974, NY: Wiley.

152. Forster, R.E. and Estabrook, R.W., *Is Oxygen an Essential Nutrient?* Ann Rev Nutr, 1993. **13**(1): p. 383-403.

153. Graham, R.M., Frazier, D.P., Thompson, J.W., et al., *A unique pathway of cardiac myocyte death caused by hypoxia-acidosis.* J Exp Biol, 2004. **207**(18): p. 3189-3200.

154. Bailey, J. and Ollis, D., *Biochemical Engineering Fundamental*. 2nd ed. 1986, NY: McGraw-Hill.

155. Goda, N., Ryan, H.E., Khadivi, B., et al., *Hypoxia-Inducible Factor 1{alpha} Is Essential for Cell Cycle Arrest during Hypoxia.* Mol Cell Biol, 2003. **23**(1): p. 359-369.

156. Kim, J.-Y., Ahn, H.-J., Ryu, J.-H., et al., *BH3-only Protein Noxa Is a Mediator of Hypoxic Cell Death Induced by Hypoxia-inducible Factor 1 {alpha}.* J Exp Med, 2003: p. jem.20030613.

157. Oller, A.R., Buser, C.W., Tyo, M.A., et al., *Growth of mammalian cells at high oxygen concentrations.* J Cell Sci, 1989. **94**(1): p. 43-49.

158. Lightfoot, E. and Duca, K., *The Role of Mass Transfer in Tissue Function*, in *Tissue Engineering*, Palsson, B. and Hubbel, J., *eds*. 2003, CRC Press: Boca Raton.

159. Freed, L., Rupnick, M. and Schaefer, D., *Engineering Functional Cartilage and Cardiac Tissue: In Vitro Culture Parameters*, in *Functional Tissue Engineering*, Guilak, F., *eds*. 2003, Springer-Verlag: NY. p. 360-376.

160. Malda, J., van Blitterswijk, C.A., van Geffen, M., et al., *Low oxygen tension stimulates the redifferentiation of dedifferentiated adult human nasal chondrocytes.* Osteoarthr Cartilage, 2004. **12**(4): p. 306-313.

161. Murphy, C.L. and Sambanis, A., *Effect of oxygen tension and alginate encapsulation on restoration of the differentiated phenotype of passaged chondrocytes.* Tissue Eng, 2001. **7**(6): p. 791-803.

162. Brown, D.A., MacLellan, W.R., Laks, H., et al., *Analysis of oxygen transport in a diffusion-limited model of engineered heart tissue.* Biotechnol Bioeng, 2007. **97**(4): p. 962-75.

163. Heywood, H.K., Bader, D.L. and Lee, D.A., *Rate of oxygen consumption by isolated articular chondrocytes is sensitive to medium glucose concentration.* J Cell Physiol, 2006. **206**(2): p. 402-10.

164. Kim, H.W. and Greenburg, A.G., *Artificial oxygen carriers as red blood cell substitutes: a selected review and current status.* Artif Organs, 2004. **28**(9): p. 813-28.

165. Malda, J., Rouwkema, J., Martens, D.E., et al., *Oxygen gradients in tissue-engineered Pegt/Pbt cartilaginous constructs: Measurement and modeling.* Biotechnol Bioeng, 2004. **86**(1): p. 9-18.

166. Kellner, K., Liebsch, G., Klimant, I., et al., *Determination of oxygen gradients in engineered tissue using a fluorescent sensor.* Biotechnol Bioeng, 2002. **80**(1): p. 73-83.

167. Wilson, C.G., Bonassar, L.J. and Kohles, S.S., *Modeling the dynamic composition of engineered cartilage.* Arch BiochemBiophys, 2002. **408**(2): p. 246-254.

168. Klisch, S.M., DiMicco, M.A., Hoger, A., et al. *Bioengineering the growth of articular cartilage*. in *Functional Tissue Engineering Workshop*. 2000. Tampa, Fl.

169. Freed, L.E., Vunjaknovakovic, G., Marquis, J.C., et al., *Kinetics of Chondrocytes Growth in Cell-Polymer Implants.* Biotechnol Bioeng, 1994. **43**(7): p. 597-604.

170. Williams, K.A., Saini, S. and Wick, T.M., *Computational fluid dynamics modeling of steady-state momentum and mass transport in a bioreactor for cartilage tissue engineering.* Biotechnol Prog, 2002. **18**(5): p. 951-63.

171. Begley, C.M. and Kleis, S.J., *RWPV bioreactor mass transport: earth-based and in microgravity.* Biotechnol Bioeng, 2002. **80**(4): p. 465-76.

172. Ochoa, J.A., Stroeve, P. and Whitaker, S., *Diffusion and reaction in cellular media.* Chem Eng Sci, 1986. **41**(12): p. 2999-3013.

173. Wood, B.D., Quintard, M. and Whitaker, S., *Calculation of effective diffusivities for biofilms and tissues.* Biotechnol Bioeng, 2002. **77**(5): p. 495-516.

174. Wood, B.D. and Whitaker, S., *Diffusion and reaction in biofilms.* Chem Eng Sci, 1998. **53**(3): p. 397-425.

175. Wood, B.D. and Whitaker, S., *Cellular growth in biofilms.* Biotechnol Bioeng, 1999. **64**(6): p. 656-670.

176. Wood, B.D. and Whitaker, S., *Multi-species diffusion and reaction in biofilms and cellular media.* Chem Eng Sci, 2000. **55**(17): p. 3397-3418.

177. Saltzman, W., *Drug Delivery. Engineering Principles for Drug Therapy*. 2001, NY: Oxford University Press.

178. Ochoa-Tapia, A.J., Stroeve, P. and Whitaker, S., *Diffusive transport in two-phase media: spatially periodic models and maxwell's theory for isotropic and anisotropic systems.* Chem Eng Sci, 1994. **49**(5): p. 709-726.

179. Bear, J. and Bachmet, Y., *Introduction to Modeling of Transport Phenomena in Porous Media*. 1991, Boston: Kluwer Academic.

180. Grodzinsky, A., Kamm, R. and Lauffenburger, D., *Quantitaive Aspects of Tissue Engineering: Basic Issues in Kinetics, Transport and Mechanics*, in *Principles of tissue engineering*, Lanza, R.P., Langer, R.S., and Vacanti, J., *eds*. 2000, Academic Press: San Diego. p. 195-206.

181. Murphy, E.M. and Ginn, T.R., *Modeling microbial processes in porous media.* Hydrogeol J, 2000. **8**(1): p. 142-158.

182. Ross, J., *Cell-Extracellular Matrix Interactions*, in *Frontiers in Tissue Engineering*, Patrick, C., Mikos, A., and McIntire, L., *eds*. 1998, Pergamon: Oxford. p. 15-27.

183. Wood, B.D., Radakovich, K. and Golfier, F., *Effective reaction at a fluid-solid interface: Applications to biotransformation in porous media.* Adv Water Resour, 2007. **30**(6-7): p. 1630-1647.

184. Ochoa-Tapia, J.A. and Whitaker, S., *Momentum-transfer at the Boundary between a Porous-medium and a Homogeneous Fluid .1. Theoretical Development.* Int J Heat Mass Tran, 1995. **38**(14): p. 2635-2646.

185. Li, Y., Ma, T., Kniss, D.A., et al., *Effects of filtration seeding on cell density, spatial distribution, and proliferation in nonwoven fibrous matrices.* Biotechnol Prog, 2001. **17**(5): p. 935-944.

186. Bird, B., Stewart, W. and Lightfoot, E., *Transport Phenomena*. 1960, NY: John Wiley and Sons.

187. Slattery, J., *Advanced transport Phenomena*. 1999, NY: Cambridge University Press.

188. Contois, D.E., *Kinetics of Bacterial Growth: Relationship between Population Density and Specific Growth Rate of Continuous Cultures.* J Gen Microbiol, 1959. **21**(1): p. 40-50.

189. Nielsen, J., *Microbial Process Kinetics*, in *Basic Biotechnology*, Ratledge, C. and Kristiansen, B., *eds*. 2001, Cambridge University Press: Cambridge. p. 127-150.

190. Nield, D. and Bejan, A., *Convection in Porous Media*. 1992, NY: Springer-Verlag.

191. Whitaker, S., *The Method of Volume Averaging*. 1999, Dordrecht: Kluwer Academic.

192. Versteeg, H. and Malalasekera, W., *An Introduction to Computational Fluid Dynamics. The Finite Volume Method*. 1995, Essex: Longman Scientific & Technical.

193. Rostami, A., Murthy, J. and Hajaligol, M., *Modeling of smoldering process in a porous biomass fuel rod.* Fuel, 2004. **83**(11-12): p. 1527-1536.

194. Bernard, A., Brocklebank, M.P., Card, C.C.H., et al., *Low Reynolds number developing flows.* AIChE J, 1969. **15**(4): p. 548-553.

195. Kim, Y.-Y., Sah, R.L.Y., Doong, J.Y.H., et al., *Fluorometric assay of DNA in cartilage explants using Hoechst 33258.* Anal Biochem, 1988. **174**(1): p. 168-176.

196. Goudar, C., Matanguihan, R., Long, E., et al., *Decreased pCO_2 Accumulation by Eliminating Bicarbonate Addition to High Cell-Density Cultures.* Biotechnol Bioeng, 2007. **96**(6): p. 1107-1117.

197. Lynn, A.K., Yannas, I.V. and Bonfield, W., *Antigenicity and immunogenicity of collagen.* J Biomed Mater Res B, 2004. **71**(2): p. 343-354.

198. Williams, C.G., Malik, A.N., Kim, T.K., et al., *Variable cytocompatibility of six cell lines with photoinitiators used for polymerizing hydrogels and cell encapsulation.* Biomaterials, 2005. **26**(11): p. 1211-1218.

199. Kitabatake, N. and Doi, E., *Surface tension and foamability of protein ans surfactant solutions.* J Food Sci, 1988. **53**(5): p. 1542-1569.

200. Yao, C.H., Liu, B.S., Chang, C.J., et al., *Preparation of networks of gelatin and genipin as degradable biomaterials.* Mater Chem Phys, 2004. **83**(2-3): p. 204-208.

201. Yannas, I.v., *Stress relaxation of anhydrous gelatin rubbers.* J Appl Polym Sci, 1968. **12**: p. 1-8.

202. Muinuddin, A., Naqvi, K., Sheu, L., et al., *Regional differences in cholinergic regulation of potassium current in feline esophageal circular smooth muscle.* Am J Physiol Gastrointest Liver Physiol, 2005. **288**(6): p. G1233-1240.

203. Salapatek, A.M.F., Ji, J. and Diamant, N.E., *Ion channel diversity in the feline smooth muscle esophagus.* Am J Physiol Gastrointest Liver Physiol, 2002. **282**(2): p. G288-299.

204. Thyberg, J. and Kwang, W.J., *Differentiated Properties and Proliferation of Arterial Smooth Muscle Cells in Culture*, in *Int Rev Cytol*. 1996, Academic Press. p. 183-265.

205. Kuriyama, H., Kitamura, K., Itoh, T., et al., *Physiological Features of Visceral Smooth Muscle Cells, With Special Reference to Receptors and Ion Channels.* Physiol Rev, 1998. **78**(3): p. 811-920.

206. Jorjani, P. and Ozturk, S., *Effect of Cell Density and Temperature on Oxygen Consumption Rate for Different Mammalian Cell Lines.* Biotechnol Bioeng, 1999. **64**: p. 349-356.

207. Instructional Manual of CO_2 Incubator (MCO-17AIC), SANYO.

208. Waldman, S.D., Couto, D.C., Omelon, S.J., et al., *Effect of sodium bicarbonate on extracellular pH, matrix accumulation, and morphology of cultured articular chondrocytes.* Tissue Eng, 2004. **10**(11-12): p. 1633-40.

209. Zieger, M.A., Glofcheski, D.J., Lepock, J.R., et al., *Factors influencing survival of mammalian cells exposed to hypothermia. V. Effects of hepes, free radicals, and H2O2 under light and dark conditions.* Cryobiology, 1991. **28**(1): p. 8-17.

210. Casey, T.M. and Arthur, P.G., *Hibernation in Noncontracting Mammalian Cardiomyocytes.* Circulation, 2000. **102**(25): p. 3124-3129.

211. Bereiter-Hahn, J., Luck, M., Miebach, T., et al., *Spreading of trypsinized cells: cytoskeletal dynamics and energy requirements.* J Cell Sci, 1990. **96 (Pt 1)**: p. 171-88.

212. Foy, B.D., Lee, J., Morgan, J., et al., *Optimization of hepatocyte attachment to microcarriers: Importance of oxygen.* Biotechnol Bioeng, 1993. **42**(5): p. 579-588.

213. Sterpetti, A.V., Cucina, A., Santoro, L., et al., *Modulation of arterial smooth muscle cell growth by haemodynamic forces.* Eur J Vascular Surg, 1992. **6**(1): p. 16-20.

214. Fitzgerald, T.N., Shepherd, B.R., Asada, H., et al., *QS150. Laminar Shear Stress Stimulates Vascular Smooth Muscle Cell Apoptosis Via The Akt Pathway.* J Surg Res, 2008. **144**(2): p. 327-327.

215. Sterpetti, A.V., Cucina, A., Napoli, F., et al., *Growth factor release by smooth muscle cells is dependent on haemodynamic factors.* Eur J Vascular Surg, 1992. **6**(6): p. 636-638.

216. Alshihabi, S.N., Chang, Y.S., Frangos, J.A., et al., *Shear Stress-Induced Release of PGE2and PGI2by Vascular Smooth Muscle Cells.* Biochem Bioph Res Co, 1996. **224**(3): p. 808-814.

217. Wang, H., Yan, S., Chai, H., et al., *Shear stress induces endothelial transdifferentiation from mouse smooth muscle cells.* Biochem Bioph Res Co, 2006. **346**(3): p. 860-865.

218. Dvir, T., Benishti, N., Shachar, M., et al., *A Novel Perfusion Bioreactor Providing a Homogenous Milieu for Tissue Regeneration.* Tissue Eng, 2006. **12**(10): p. 2843-2852.

219. Griffith, C.K., Miller, C., Sainson, R.C.A., et al., *Diffusion Limits of an in Vitro Thick Prevascularized Tissue.* Tissue Eng, 2005. **11**(1-2): p. 257-266.

220. Heijnen, J., *Stoichiometry and Kinetics of Microbial Growth from a Thermodynamic Perspective*, in *Basic Biotechnology*, Ratledge, C. and Kristiansen, B., *eds*. 2001, Cambridge University Press: Cambridge. p. 45-58.

221. Nauman, E., *Chemical Reactor Design, Optimization, and Scaleup*. 2001, New York: McGraw-Hill.

Appendix A: Derivation of Mathematical Model

A.1 VOLUME AVERAGING

Phases can be found within the representative elementary volume (REV), denoted by V, in a multiphase domain. For instance, three phases were defined in the tissue construct. VAM requires dependent variables in the governing equations to be averaged over the REV ("superficial volume-averaged") or volume of phase j ("intrinsic volume-averaged"). By definition, for a physical property of phase j, Ψ_j, such as concentration and temperature can be volume-averaged by:

Superficial volume-averaged: $$< \Psi_j >= \frac{1}{V}\int_{V_j} \Psi_j \, dV \qquad \text{A.1}$$

Intrinsic volume-averaged: $$< \Psi_j >^j = \frac{1}{V_j}\int_{V_j} \Psi_j dV \qquad \text{A.2}$$

Physical quantities inside the bracket $< >$ and $< >^j$ represent superficial volume-averaged and intrinsic volume-averaged quantity, respectively. They can be related through volume fraction of phase j, ε_j:

$$< \Psi_j >= \varepsilon_j < \Psi_j >^j \quad ; \quad \varepsilon_j = \frac{V_j}{V} \qquad \text{A.3}$$

The volume fractions of all phases in the REV must be summed to one:

$$\sum_{j=1}^{n} \varepsilon_j = 1 \qquad \text{A.4}$$

The volume-averaged derivatives are required to formulate governing equations (Bear and Bachment, 1991):

$$\text{Divergence: } < \nabla \cdot \Psi_j >= \nabla \cdot < \Psi_j > + \frac{1}{V} \int_A \Psi_j \cdot \vec{n}\, dA \qquad \text{A.5}$$

$$\text{Gradient: } < \nabla \Psi_j >= \nabla < \Psi_j > + \frac{1}{V} \int_A \Psi_j \vec{n}\, dA \qquad \text{A.6}$$

$$\text{Time derivative: } < \frac{\partial \Psi_j}{\partial t} >= \frac{\partial < \Psi_j >}{\partial t} - \frac{1}{V} \int_A \Psi_j \vec{u} \cdot \vec{n}\, dA \qquad \text{A.7}$$

Both definitions contain area integral terms. In the integral, A is surface area at the interface between two phases, $\vec{n}$ the outward unit normal vector of the interface and $\vec{u}$ the displacement rate of the interface. In this analysis, the displacement of interface was neglected because its contribution is comparatively small.

Referring to multiphase system shown in Figure 4.1B, additional subscripts such as "σβ" was adopted to indicate the particular interface and direction of unit vector. Hence, $A_{\sigma\beta}$ and $n_{\sigma\beta}$ were adopted to indicate interfacial area of σβ-interface and the unit normal vector that points from σ-phase towards β-phase at the σβ-interface, respectively. Positive vector is defined if the surface is convex. Definitions can be made for interfacial area and unit normal vector: $A_{\beta\sigma} = A_{\sigma\beta}$ and $n_{\beta\sigma} = -n_{\sigma\beta}$.

A.2 VOLUME-AVERAGED GOVERNING EQUATIONS IN ω-REGION

Volume averaging the microscopic governing equations 4.1.2 to 4.1.5 using relations given in Appendix A.1 gives volume-averaged governing equations:

Volume-averaged continuity equation (with no-slip condition) in ω-region

$$\nabla \cdot < \vec{v}_\beta >= 0 \qquad \text{A.8}$$

Volume-averaged momentum equation in ω-region

$$0 = -\nabla(\varepsilon_\beta < p_\beta >^\beta) + \mu_\beta \nabla^2 < \vec{v}_\beta > + \frac{1}{V}\int_{A_{\beta\sigma}} \vec{n}_{\beta\sigma} \cdot [-\mathbf{I} p_\beta + \mu_\beta \nabla \vec{v}_\beta]\, dA \qquad \text{A.9}$$

0 = Pressure force + Viscous force + Interfacial exchange

Volume-averaged mass balance for species i for β-phase in ω-region

$$\frac{\partial(\varepsilon_\beta < C_{i,\beta} >^\beta)}{\partial t} + \nabla \cdot < C_{i,\beta} \vec{v}_\beta >= \nabla \cdot [\mathbf{D}_{i,\beta} \nabla(\varepsilon_\beta < C_{i,\beta} >^\beta) + \frac{1}{V}\int_{A_{\beta\sigma}} \vec{n}_{\beta\sigma} C_{i,\beta}\, dA] + \frac{1}{V}\int_{A_{\beta\sigma}} \vec{n}_{\beta\sigma} \cdot D_{i,\beta} \nabla C_{i,\beta} dA \qquad \text{A.10}$$

Accumulation + Convection = Diffusion + Interfacial exchange

Volume-averaged mass balance for species i for σ-phase in ω-region

$$\frac{\partial(\varepsilon_\sigma < C_{i,\sigma} >^\sigma)}{\partial t} = \nabla.[\mathbf{D}_{i,\sigma}\nabla(\varepsilon_\sigma < C_{i,\sigma} >^\sigma) + \frac{1}{V}\int_{A_{\beta\sigma}} \vec{n}_{\sigma\beta} C_{i,\sigma}\, dA] + \frac{1}{V}\int_{A_{\beta\sigma}} \vec{n}_{\sigma\beta} \cdot \mathbf{D}_{i,\sigma}\nabla C_{i,\sigma} dA + \varepsilon_\sigma < R_i >^\sigma \quad \text{A.11}$$

Accumulation = Diffusion + Interfacial exchange + Reaction (Source or sink)

A description of each term is defined under each equation. These equations are the general volume-averaged governing equations in the ω-region. Any reasonable simplifications or modifications can be made from this point. The two area integrals in equation A.10 and A.11 are results of applying equation A.5 and A.6. The first integral can be lumped into the diffusion term to form one single term (see later discussion) whereas the second integral indicates the interfacial exchange of mass between σ- and β-phase, which is directly expressed in a constitutive form in some analyses. Superficial volume-averaged velocity, $< v_\beta >$, is preferred in solving these equations whereas intrinsic volume-averaged forms are used for other dependent variables, that is, pressure and concentrations (i.e. $< p_\beta >^\beta$, $< C_{i,\beta} >^\beta$ and $< C_{i,\sigma} >^\sigma$). The governing equations expressed in these forms containing area integrals are not useful in solving the system. Further derivations and simplifications are required. First, attention is directed to the volume-averaged momentum equation.

A.3 MACROSCOPIC MOMENTUM EQUATION IN ω-REGION

Before making further simplifications, it is necessary to give some definitions that facilitate the process. First, the difference between a point quantity (quantity without bracket) and intrinsic volume-averaged quantity is the spatial deviation, $\tilde{\Psi}_j$, which can be defined as:

$$\Psi_j = \langle \Psi_j \rangle^j + \tilde{\Psi}_j \quad \text{for } j = \beta \text{ and } \sigma \tag{A.12}$$

The process of expressing point quantity in this form is called "decomposition". Another useful relation is introduced in order to simplify the governing equations:

$$\nabla \varepsilon_j = -\frac{1}{V}\int_A \vec{n}\, dA \tag{A.13}$$

This relation is obtained by inserting $\Psi = 1$ into equation A.6. Considering the volume-averaged momentum equation given in equation A.9, the terms containing volume fraction are expanded and point values of pressure p_β and v_β are decomposed using equation A.12.

$$\begin{aligned} 0 = {} & -\varepsilon_\beta \nabla \langle p_\beta \rangle^\beta - \langle p_\beta \rangle^\beta \nabla \varepsilon_\beta + \mu_\beta \nabla^2 \langle \vec{v}_\beta \rangle \\ & + \frac{1}{V}\int_{A_{\beta\sigma}} \vec{n}_{\beta\sigma} \cdot [-\mathbf{I} \langle p_\beta \rangle^\beta + \mu_\beta \nabla \langle \vec{v}_\beta \rangle^\beta]\, dA \\ & + \frac{1}{V}\int_{A_{\beta\sigma}} \vec{n}_{\beta\sigma} \cdot [-\mathbf{I}\tilde{p}_\beta + \mu_\beta \nabla \tilde{v}_\beta]\, dA \end{aligned} \tag{A.14}$$

The dot product of equation A.13 and $\nabla < \vec{v}_\beta >^\beta$, and multiplying equation A.13 by $< p_\beta >^\beta$ give two relations:

$$\nabla \varepsilon_i \cdot \nabla < \vec{v}_\beta >^\beta = -\frac{1}{V} \int_{A_{\beta\sigma}} \vec{n}_{\beta\sigma} \cdot \nabla < \vec{v}_\beta >^\beta dA \qquad \text{A.15}$$

$$\nabla \varepsilon_i < p_\beta >^\beta = -\frac{1}{V} \int_{A_{\beta\sigma}} \vec{n}_{\beta\sigma} < p_\beta >^\beta dA \qquad \text{A.16}$$

After these two relations are substituted into equation A.14, the second term and the first area integral are eliminated and we obtain a more useful form:

$$0 = -\varepsilon_\beta \nabla < p_\beta >^\beta + \mu_\beta \nabla^2 < v_\beta > - \mu_\beta \nabla \varepsilon_\beta \cdot \nabla (\varepsilon_\beta^{-1} < v_\beta >) + \frac{1}{V} \int_{A_{\beta\sigma}} n_{\beta\sigma} \cdot [-I\tilde{p}_\beta + \mu_\beta \nabla \tilde{v}_\beta] dA \qquad \text{A.17}$$

In this equation, the second and third term on right hand side are called the first and the second Brinkman correction, respectively. Here, it was assumed that certain length-scale constraints given in [184] are satisfied:

$$\mu_\beta \nabla^2 < \vec{v}_\beta > >> \mu_\beta \nabla \varepsilon_\beta \cdot \nabla (\varepsilon_\beta^{-1} < \vec{v}_\beta >) \qquad \text{A.18}$$

The area integral in equation A.17 can be expressed by:

$$\mu_\beta \Phi_\beta = -\frac{1}{V} \int_{A_{\beta\sigma}} \vec{n}_{\beta\sigma} \cdot [-\mathbf{I}\tilde{p}_\beta + \mu_\beta \nabla \tilde{v}_\beta] dA \qquad \text{A.19}$$

where

$$\Phi_\beta = \mathbf{K}_\beta^{-1} \cdot \langle \vec{v}_\beta \rangle \qquad \text{A.20}$$

$\mathbf{K}_\beta^{-1}$ represents permeability tensor in Darcy's law that the Kozeny-Carman equation can be used for its estimation [190]:

$$K_\beta = \frac{d_{\sigma\beta} \varepsilon_\beta^{\,3}}{180\,(1-\varepsilon_\beta)^2} \qquad \text{A.21}$$

Substituting equation A.19 and A.21 into A.17 and using the assumption given in equation A.18 gives Darcy's law with the first Brinkman correction:

$$\langle \vec{v}_\beta \rangle = -\frac{K_\beta}{\mu_\beta}(\nabla \langle p_\beta \rangle^\beta + \varepsilon_\beta^{-1} \mu_\beta \nabla^2 \langle \vec{v}_\beta \rangle) \qquad \text{A.22}$$

Or, another useful form for solving:

$$0 = -\nabla \langle p_\beta \rangle^\beta + \varepsilon_\beta^{-1} \mu_\beta \nabla^2 \langle \vec{v}_\beta \rangle - \mu_\beta K_\beta^{-1} \cdot \langle \vec{v}_\beta \rangle \qquad \text{A.23}$$

Here, equation A.23 is ready to solve for velocity and pressure profiles in ω-region.

A.4 MACROSCOPIC MASS BALANCES OF SPECIES i IN ω-REGION

General forms of volume-averaged mass balances of species i for β- and σ-phases are given in equation A.10 and A.11, respectively. First, these equations were treated by expanding the first term on the right hand side from the first derivative and

decomposing the concentration using equation A.12 inside the first area integral. Then, similar techniques (applying equation A.13) used in deriving the macroscopic momentum equation were re-applied to simplify these two equations into:

$$\beta\text{-phase: } \frac{\partial}{\partial t}(\varepsilon_\beta < C_{i,\beta} >^\beta) + \nabla\cdot < C_{i,\beta}\vec{v}_\beta > \qquad \text{A.24}$$

$$= \nabla\cdot \mathbf{D}_{i,\beta}[\varepsilon_\beta \nabla < C_{i,\beta} >^\beta + \frac{1}{V}\int_{A_{\beta\sigma}} \vec{n}_{\beta\sigma}\tilde{C}_{i,\beta}\, dA] + \frac{1}{V}\int_{A_{\beta\sigma}} \vec{n}_{\beta\sigma}\cdot \mathbf{D}_{i,\beta}\nabla C_{i,\beta} dA$$

$$\sigma\text{-phase: } \frac{\partial}{\partial t}(\varepsilon_\sigma < C_{i,\sigma} >^\sigma) \qquad \text{A.25}$$

$$= \nabla\cdot \mathbf{D}_{i,\sigma}[\varepsilon_\sigma \nabla < C_{i,\sigma} >^\sigma + \frac{1}{V}\int_{A_{\beta\sigma}} \vec{n}_{\sigma\beta}\tilde{C}_{i,\sigma}\, dA]$$

$$+ \frac{1}{V}\int_{A_{\beta\sigma}} \vec{n}_{\sigma\beta}\cdot \mathbf{D}_{i,\sigma}\nabla C_{i,\sigma} dA + \varepsilon_\sigma < R_i >^\sigma$$

Now, the second term of this equation can be expanded using the mulplicative rule in VAM [179]:

$$\nabla\cdot < C_{i,\beta}\vec{v}_\beta > = \nabla\cdot(\varepsilon_\beta < C_{i,\beta}\vec{v}_\beta >^\beta) = \nabla\cdot(< C_{i,\beta} >^\beta < \vec{v}_\beta >) + \nabla\cdot < \tilde{C}_{i,\beta}\tilde{v}_\beta >^\beta \qquad \text{A.26}$$

The second term of the right hand side of equation A.26 represents dispersive flux. By using the order of magnitude, it was found that the dispersive flux can be neglected if the velocity is small enough. With this assumption, mass balance for β-phase can be written as:

$$\frac{\partial(\varepsilon_\beta < C_{i,\beta} >^\beta)}{\partial t} + \nabla \cdot (< C_{i,\beta} >^\beta < \vec{v}_\beta >) \qquad \text{A.27}$$

$$= \nabla . \mathbf{D}_{j,\beta} [\varepsilon_\beta \nabla < C_{j,\beta} >^\beta + \frac{1}{V} \int_{A_{\beta\sigma}} \vec{n}_{\beta\sigma} \tilde{C}_{j,\beta} \, dA] + \frac{1}{V} \int_{A_{\beta\sigma}} \vec{n}_{\beta\sigma} \cdot \mathbf{D}_{i,\beta} \nabla C_{i,\beta} dA$$

A.5 LOCAL MASS EQUILIBRIUM AND SINGLE MACROSCOPIC MASS BALANCE OF SPECIES i IN ω-REGION

From a practical view, it might be preferable to impose a local mass equilibrium that simplifies the two-equation model into a one-equation model and uses a single concentration (called "weighted equilibrium concentration") rather than concentrations in β- and σ-phases to represent concentration in the ω-region. The local mass equilibrium was first applied in an analysis on diffusion within cellular materials [172] based on local thermal equilibrium applied in heat transfer problems [191]. This model stated that when the concentrations in both phases are close enough to the equilibrium state, the mass balances of species i for both phases could be combined into a single equation with elimination of the interfacial terms [174]. First, the weight equilibrium concentration, denoted by $\{C_i\}$, is defined:

$$\{C_i\} = < C_{i,\beta} >^\beta + K_{eq,i} < C_{i,\sigma} >^\sigma \qquad \text{A.28}$$

At equilibrium, the weight equilibrium, and the σ-phase and β-phase concentrations can be correlated through the relation below:

$$\{C_i\} = < C_{i,\beta} >^{\beta} = K_{eq,i} < C_{i,\sigma} >^{\sigma} \qquad \text{A.29}$$

Wood *et al.* [173, 174] claimed that even the equilibrium state does not exist; equation A.29 provides a reasonable approximation for many cellular systems (communication with Whitaker). Due to this, it might be possible to apply local mass equilibrium in this system. The difference between intrinsic volume averaged concentration and weighted equilibrium concentration is termed as spatial deviation concentration ($\hat{C}_{i,\beta}$), which is defined through:

$$< C_{i,\beta} >^{\beta} = \{C_i\} + \hat{C}_{i,\beta} \qquad \text{A.30}$$

$$K_{eq,i} < C_{i,\sigma} >^{\sigma} = \{C_i\} + \hat{C}_{i,\sigma} \qquad \text{A.31}$$

Substituting these definitions into the volume-averaged mass balance equations A.25 and A.27 and summing the resulting equations finally gives one mass balance equation:

$$\begin{aligned} &\frac{\partial}{\partial t}[(\varepsilon_\beta + K_{eq,i}^{-1}\varepsilon_\sigma)\{C_i\}] + \nabla\cdot(\{C_i\} < \vec{v}_\beta >) \\ &= \nabla.(\varepsilon_\beta \mathbf{D}_{i,\beta} + K_{eq,i}^{-1}\varepsilon_\sigma \mathbf{D}_{i,\sigma})\nabla\{C_i\} \\ &\quad + \frac{\mathbf{D}_{i,\beta}}{V}\int_{A_{\beta\sigma}} \vec{n}_{\beta\sigma}\tilde{C}_{i,\beta}\, dA + \frac{\mathbf{D}_{i,\sigma}}{V}\int_{A_{\sigma\beta}} \vec{n}_{\sigma\beta}\tilde{C}_{i,\sigma}\, dA + \{R_i\} \\ &\quad - \frac{\partial}{\partial t}(\varepsilon_\beta \hat{C}_{i,\beta} + K_{eq,i}^{-1}\varepsilon_\sigma \hat{C}_{i,\sigma}) - \nabla\cdot(\hat{C}_{i,\sigma} < \vec{v}_\beta >) \\ &\quad + \nabla.(\varepsilon_\beta \mathbf{D}_{i,\beta}\nabla\hat{C}_{i,\beta} + K_{eq,i}^{-1}\varepsilon_\sigma \mathbf{D}_{i,\sigma}\nabla C_{i,\sigma}) + \hat{R}_i \end{aligned} \qquad \text{A.32}$$

Note that when the two mass balances are added together, the interfacial exchange terms cancel each other since they are identical in magnitude but opposite in direction. The spatial deviation concentration applied here ($\hat{C}_{i,\beta}$ or $\hat{C}_{i,\sigma}$) is the measure of how deviated the volume-averaged concentration is from the equilibrium value. If local mass equilibrium is imposed, it must follow that these deviation concentrations are very small. Terms with the deviation concentrations refer to "non-equilibrium" that should be much smaller than the convection and diffusion terms (i.e., second term on the left hand side and first term of the right hand side) if local mass equilibrium is valid. Hence, neglecting the non-equilibrium terms give a simpler form of mass balance:

$$\frac{\partial}{\partial t}[(\varepsilon_\beta + K_{eq,i}{}^{-1}\varepsilon_\sigma)\{C_i\}] + \nabla\cdot(\{C_i\} < \vec{v}_\beta >) = \underline{\nabla.[(\varepsilon_\beta \mathbf{D}_{i,\beta} + K_{eq,i}{}^{-1}\varepsilon_\sigma \mathbf{D}_{i,\sigma})\nabla\{C_i\}} + \frac{\mathbf{D}_{i,\beta}}{V}\int_{A_{\beta\sigma}} \vec{n}_{\beta\sigma}\tilde{C}_{i,\beta}\,dA + \frac{\mathbf{D}_{i,\sigma}}{V}\int_{A_{\sigma\beta}} \vec{n}_{\sigma\beta}\tilde{C}_{i,\sigma}\,dA] + \{R_i\} \quad \text{A.33}$$

This equation can be further expressed in a form without area integrals by lumping first term on the right hand side of equation A.33 (underlined) into a more compact form, which appears in the form of a diffusive term identical to Fick's law.

$$\frac{\partial}{\partial t}[(\varepsilon_\beta + K_{eq,i}{}^{-1}\varepsilon_\sigma)\{C_i\}] + \nabla\cdot(\{C_i\} < \vec{v}_\beta >) = \underline{\nabla\cdot\mathbf{D}_{eff,i}\nabla\{C_i\}} + \{R_i\} \quad \text{A.34}$$

It is reasonable to assume that the time derivative of concentration is much greater than that of volume fractions of the β- and σ-phases (i.e. $(\varepsilon_\beta + K_{eq,i}^{-1}\varepsilon_\sigma)$), so that a more concise form can be obtained [174]:

$$\frac{\partial\{C_i\}}{\partial t} + \varepsilon^{-1}\nabla\cdot(\{C_i\} < \vec{v}_\beta >) = \nabla\cdot\mathbf{D}''_{eff,i}\nabla\{C_i\} + \varepsilon^{-1}\{R_i\} \qquad \text{A.35}$$

where

$$\mathbf{D}''_{eff,i} = \frac{\mathbf{D}_{eff,i}}{\varepsilon_\beta + K_{eq,i}^{-1}\varepsilon_\sigma} \qquad \text{A.36}$$

and

$$\mathbf{D}_{eff,i} = (\varepsilon_\beta \mathbf{D}_{i,\beta} + K_{eq,i}^{-1}\varepsilon_\sigma \mathbf{D}_{i,\sigma}) + \frac{\mathbf{D}_{i,\beta}}{V}\int_{A_{\beta\sigma}} \vec{n}_{\beta\sigma}\vec{f}\,dA + \frac{\mathbf{D}_{i,\sigma}}{V}\int_{A_{\sigma\beta}} \vec{n}_{\sigma\beta} K_{eq,i}^{-1}\vec{g}\,dA \qquad \text{A.37}$$

$\mathbf{D}_{eff,i}$ refers to the effective diffusivity that is related to the closure vectors $\vec{f}$ and $\vec{g}$. These vectors can be solved from the closure problem for a particular geometry, which will be discussed later. The effective diffusivity and equation A.37 are derived on the basis of the solutions suggested by Whitaker [175]:

$$\tilde{C}_{i,\beta} = \vec{f}\cdot\nabla\{C_i\} \qquad \text{A.38}$$

$$K_{eq,i}\tilde{C}_{i,\beta} = \vec{g}\cdot\nabla\{C_i\} \qquad \text{A.39}$$

The length scale criterion in equation 2.4.1 must be satisfied in order that the weighted equilibrium concentrations can be treated as a constant in the area integrals in equation A.37.

A.6 CLOSURE PROBLEM AND EFFECTIVE DIFFUSIVITY

Since the closure vectors, $\vec{f}$ and $\vec{g}$, are introduced, solving for these vectors requires setting up the closure problem from point (or microscopic) to volume-averaged mass balances alongside microscopic boundary conditions. Next, the geometry has to be determined in order to solve the closure problem.

Procedures of setting up the closure problem include:

Reorganize volume-averaged and microscopic mass balances for the β- and σ-phases. Subtract the former from the latter for the respective phase. This results in two equations mainly expressed in the spatial deviation concentration:

$$\beta\text{-phase: } \frac{\partial \tilde{C}_{i,\beta}}{\partial t} + \vec{v}_\beta \cdot \nabla \tilde{C}_{i,\beta} + \tilde{v}_\beta \cdot \nabla < C_{i,\beta} >^\beta \qquad \text{A.40}$$

$$= \nabla \cdot \mathbf{D}_{i,\beta} \nabla \tilde{C}_{i,\beta} - \varepsilon_\beta^{-1} \nabla \cdot \left[\frac{\mathbf{D}_{i,\beta}}{V} \int_{A_{\beta\sigma}} \vec{n}_{\beta\sigma} \tilde{C}_{i,\beta} dA \right] - \frac{\varepsilon_\beta^{-1}}{V} \int_{A_{\beta\sigma}} \vec{n}_{\beta\sigma} \cdot \mathbf{D}_{i,\beta} \nabla \tilde{C}_{i,\beta} dA$$

$$\sigma\text{-phase: } \frac{\partial \tilde{C}_{i,\sigma}}{\partial t} = \nabla \cdot \mathbf{D}_{i,\sigma} \nabla \tilde{C}_{i,\sigma} \qquad \text{A.41}$$

$$-\varepsilon_\sigma^{-1}\nabla\cdot\left[\frac{\mathbf{D}_{i,\sigma}}{V}\int_{A_{\beta\sigma}}\vec{n}_{\sigma\beta}\widetilde{C}_{i,\sigma}dA\right]-\frac{\varepsilon_\sigma^{-1}}{V}\int_{A_{\beta\sigma}}\vec{n}_{\sigma\beta}\cdot\mathbf{D}_{i,\sigma}\nabla\widetilde{C}_{i,\sigma}dA+\widetilde{R}_i$$

All terms have been previously defined. $\widetilde{R}_i$ is the resulting term from the subtraction of macroscopic from the microscopic reaction term.

Assume convection is negligible in the microscopic scale at low medium velocity (from the estimation of magnitude of order) and pseudo steady state is valid in this scale [174]. It is also claimed that non-local diffusive terms (second terms on the right hand side for both equations) and the reaction term in σ-phase could be neglected [174]. Diffusivities of species i was assumed to be constant (i.e. no longer a tensor) over the phase within the REV. These two equations can be simplified to:

$$\beta\text{-phase:}\quad D_{i,\beta}\nabla^2\widetilde{C}_{i,\beta}=\frac{\varepsilon_\beta^{-1}}{V}\int_{A_{\beta\sigma}}\vec{n}_{\beta\sigma}\cdot D_{i,\beta}\nabla\widetilde{C}_{i,\beta}dA \qquad \text{A.42}$$

$$\sigma\text{-phase:}\quad D_{i,\sigma}\nabla^2\widetilde{\chi}_{i,\sigma}=\frac{\varepsilon_\sigma^{-1}}{V}\int_{A_{\beta\sigma}}\vec{n}_{\sigma\beta}\cdot D_{i,\sigma}\nabla\widetilde{\chi}_{i,\sigma}dA \qquad \text{A.43}$$

where

$$\widetilde{\chi}_{i,\sigma}=K_{eq,i}\widetilde{C}_{i,\sigma} \qquad \text{A.44}$$

Decompose the microscopic boundary conditions, equation 2.4.7 to 2.4.9 using equation A.12 and impose local mass equilibrium. The boundary conditions for solving closure problems take the form:

B.C.1: $$\vec{n}_{\beta\sigma}\cdot\nabla\widetilde{C}_{i,\beta}=\vec{n}_{\beta\sigma}\cdot\kappa_i\nabla\widetilde{\chi}_{i,\sigma}+\vec{n}_{\beta\sigma}\cdot(\kappa_i-1)\nabla\{C_i\}\ \text{at}\ A_{\beta\sigma}$$ A.45a

B.C.2: $$\widetilde{C}_{i,\beta}-\widetilde{\chi}_{i,\sigma}=-\vec{n}_{\beta\sigma}\cdot\xi_i\nabla\{C_i\}-\vec{n}_{\beta\sigma}\cdot\xi_i\nabla\widetilde{\chi}_{i,\sigma}\ \text{at}\ A_{\beta\sigma}$$ A.45b

B.C.3: $$\vec{n}_{\sigma\gamma}\cdot\nabla\{C_i\}=-\vec{n}_{\sigma\gamma}\cdot\nabla\widetilde{\chi}_{i,\sigma}\ \text{at}\ A_{\sigma\gamma}$$ A.45c

B.C.4 $$\vec{n}_{\beta\sigma}\cdot\nabla\{C_i\}=-\vec{n}_{\beta\sigma}\cdot\nabla\widetilde{C}_{i,\beta}\ \text{at}\ A_{\beta\gamma}$$ A.45d

where

$$\kappa_i=\frac{D_{i,\sigma}}{K_{eq,i}D_{i,\beta}}$$ A.46a

$$\xi_i=\frac{D_{i,\sigma}}{K_{eq,i}k_m}$$ A.46b

Substitute the spatial deviation concentration with the proposed solutions, equation A.38 and A.39 into the equations obtained from the first 3 steps. Thus, a closure problem is established (below) and closure vectors, $\vec{f}$ and $\vec{g}$ can be solved according to the theoretical model described below.

β-phase: $$\nabla^2\vec{f}=\frac{\varepsilon_\beta^{-1}}{V}\int_{A_{\beta\sigma}}\vec{n}_{\beta\sigma}\cdot\nabla f\,dA$$ A.47

σ-phase: $\nabla^2\vec{g} = \frac{\varepsilon_\sigma^{-1}}{V}\int_{A_{\beta\sigma}} \vec{n}_{\sigma\beta}\cdot\nabla g\, dA$ A.48

B.C.1: $n_{\beta\sigma}\cdot\nabla\vec{f} = \vec{n}_{\beta\sigma}\cdot\kappa_i\nabla\vec{g} + \vec{n}_{\beta\sigma}(\kappa_i - 1)$ at $A_{\beta\sigma}$ A.49a

B.C.2: $\vec{f} - \vec{g} = -\vec{n}_{\beta\sigma}\xi_i - \vec{n}_{\beta\sigma}\cdot\xi_i\nabla\vec{g}$ at $A_{\beta\sigma}$ A.49b

B.C.3: $\vec{n}_{\sigma\gamma} = -\vec{n}_{\sigma\gamma}\cdot\nabla\vec{g}$ at $A_{\sigma\gamma}$ A.49c

B.C.4 $\vec{n}_{\sigma\gamma} = -\vec{n}_{\sigma\gamma}\cdot\nabla\vec{f}$ at $A_{\beta\gamma}$ A.49d

In nature, there are no real isotropic and homogeneous porous media, but isotropic and homogeneous concepts can be used for the diffusion process, even for a random porous structure [191] as shown in Figure 4.1B or A.2B. Theoretically, this real model could be simplified into a theoretical model, according to which the closure problem can be solved with a reasonable approximation of effective diffusivity since the detailed microscopic information of the real structure except porosity is filtered out over the integrals in equation A.37 [191]

In the literature, a spatially periodic porous medium has been widely used to solve the closure problem that gives good agreement with experimental results. Consider a spatially periodic porous medium composed an array of cylinders in Figure A.1A. Unit cell (enclosed with a dotted square) shown in Figure A.1A and B is treated as the

theoretical model of real structure (Figure A.2B). Ochoa-Tapia *et al.* [178] showed the analytical solution for Chang's unit cell (Figure A.2A) that gives a good approximation for numerical solution of the unit cell. The system considered was a two-phase biofilm system comprising a cell phase and an extracellular phase, which has then been applied in a similar manner in the estimation of the effective diffusivity of tissue-engineered cartilage in the mathematical model of Galban and Locke [42, 43].

In the analysis performed in this first-year study, by virtue of its reasonable accuracy and simplicity, effective diffusivity, $D_{eff,i}$ was derived using the similar method of Ochoa-Tapia *et al.* [178] and Whitaker [191]. The difference in this study was that three-phase (scaffold-, cell- and medium-phase) system was defined for a tissue construct and each phase was assumed to be arranged in a hierarchical manner shown in Figure A.2A. Solving the closure problem in conjunction with the theoretical model (Figure A.2A), the analytical solution for effective diffusivity correlated to the volume fraction can be obtained. It has been proven that for a symmetrical unit cells such as Chang's unit cell, the integrals in closure problems (equation A.47 and A.48) are zeroes. On the other hand, the arrangement of Chang's unit cell allowed us to omit B.C. 4 (equation A.49d). The final governing equations of the closure problem are shown below in cylindrical coordinate:

$$\beta\text{-phase:}\quad \frac{\partial^2 \vec{f}}{\partial r^2} = 0 \qquad r_{\sigma\beta} \le r \le R \qquad \text{A.50}$$

σ-phase: $\frac{\partial^2 \vec{g}}{\partial r^2} = 0$ $\quad r_{\sigma\gamma} \le r \le r_{\sigma\beta}$ A.51

B.C.1: $$\vec{n}_{\beta\sigma} \cdot \frac{\partial \vec{f}}{\partial r} = \vec{n}_{\beta\sigma} \cdot \kappa_i \frac{\partial \vec{g}}{\partial r} + \vec{n}_{\beta\sigma}(\kappa_i - 1) \text{ at } r_{\sigma\beta}$$ A.52a

B.C.2: $$\vec{f} - \vec{g} = -\vec{n}_{\beta\sigma}\xi_i - \vec{n}_{\beta\sigma} \cdot \xi_i \frac{\partial \vec{g}}{\partial r} \text{ at } r_{\sigma\beta}$$ A.52b

B.C.3: $$\vec{n}_{\sigma\gamma} = -\vec{n}_{\sigma\gamma} \cdot \frac{\partial \vec{g}}{\partial r} \text{ at } r_{\sigma\gamma}$$ A.52c

R, $r_{\sigma\beta}$ and $r_{\sigma\gamma}$ are the radius of Chang's unit cell, the radial distance from the center to σβ-interface and the radial distance from the center to the σγ-interface, respectively.

After solving the closure problem with some arrangements, the effective diffusivity of species i takes the form:

$$\frac{D_{eff,i}}{D_{i,\beta}} = \frac{G_{1,i}(1-\varepsilon_\gamma \kappa_i) - G_{2,i}(\varepsilon_\beta - \varepsilon_\gamma \kappa_i) - G_{3,i}}{G_{1,i} - G_{2,i}} \qquad \text{A.53}$$

where

$$G_{1,i} = -\varepsilon_\beta r_{\sigma\beta}^{\,2}(\varepsilon_\sigma \kappa_i + \varepsilon_\gamma r_{\sigma\beta}^{\,2}) \qquad \text{A.54a}$$

$$G_{2,i} = r_{\sigma\beta}(2-\varepsilon_\beta)[(1-\varepsilon_\beta)(r_{\sigma\beta}+\xi_i) + (r_{\sigma\beta}-\xi_i) \qquad \text{A.54b}$$

$$G_{3,i} = -r_{\sigma\beta}^{\,2}\kappa_i(2-\varepsilon_\beta)(1-\varepsilon_\beta)(1-\varepsilon_\beta+\varepsilon_\gamma) \qquad \text{A.54c}$$

$$r_{\sigma\beta} = \ell\left(\frac{1-\varepsilon_\beta}{\pi}\right)^{1/2} \qquad \text{A.54d}$$

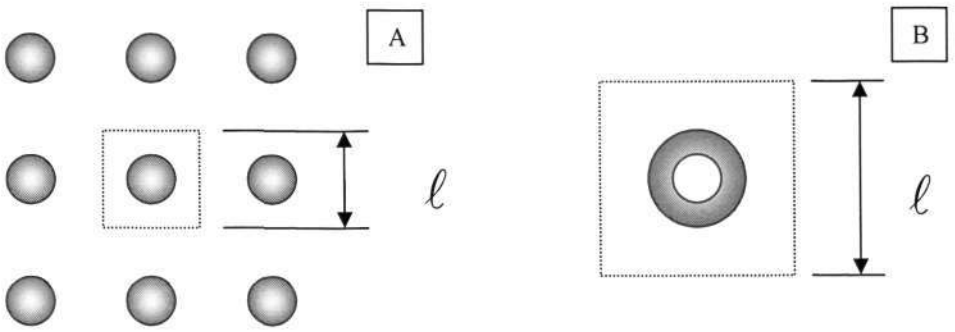

Figure A.1: (A) Spatially periodic porous medium composed of an array of cylinders. Dotted square is the (B) representative unit cell that contains medium phase (white space outside the cylinder), cell phase (grey) and scaffold phase (white space enclosed by cell phase).

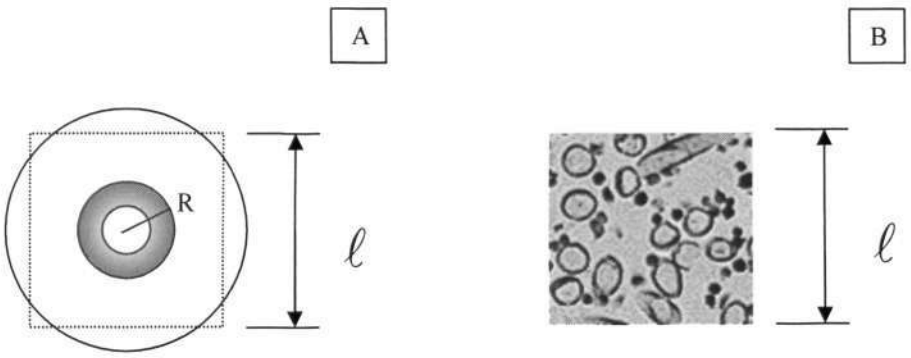

Figure A.2: (A) Theoretical model: Chang's unit cell (with radius R). It was used to approximate the numerical solution of unit cell (square shown in the figure). (B) Experimental model: real structure (Li et al., 2001)

A few parameters require explanations. r is the radial position extended from the center Chang's unit cell (Figure A.2A). ℓ is the length of unit cell (see the dotted square in Figure A.2A). Other parameters are defined in Chapter 4. It should be

noticed that the unit cell does not fully enclose the Chang's cell. Applying Chang's unit cell to approximate the numerical solution of the unit cell requires that Chang's unit cell has identical volume (or area for 2D) as the unit cell and it is not difficult to find ℓ = R, that is, ℓ < R. The value ℓ used is the same order as the characteristic length of the REV, which is approximately 5 x 10^{-5} m. There is no definite method for determination of this value, but it must lie between the characteristic length of the system (thickness of construct) and the characteristic length of cell and scaffold (fiber diameter or pore size).

A.7 GROWTH MODEL

Many "black-box" growth models regardless of the detailed growth information have been proposed in the past literature. The cell growth model, which has been used in this study, was based on one of these growth models that are to be reviewed below. Among them, Monod's kinetics have been widely used and it takes a form similar to Michaelis-Menten kinetics for enzymatic kinetics [189]. Assuming oxygen is the substrate, the cell growth rate (R_σ) of Monod's kinetics can be expressed in the form:

$$R_\sigma = r_\sigma \rho_\sigma = r_{\sigma,max}\, \rho_\sigma \left[\frac{C_{O,\sigma}}{C_{O,\sigma} + K_S} \right] \qquad \text{A.55}$$

It is also conventional to express R_σ in terms of a specific growth rate, r_σ having the unit of inverse of time, s^{-1}. Oxygen concentration, $C_{O,\sigma}$, appears in both numerator and denominator, so the growth rate will reach an asymptotic value as $C_{O,\sigma} >> K_S$. K_S is similar to the half saturation constant in Michaelis-Menten kinetics, having a range of

0.005 to 0.2 kg/m^3 over many types of microbial cells [189]. The rate of cell mass deposition, R_σ, has the unit of kg/m^{3}s, which is proportional to cell mass concentration, ρ_σ (in kg/m^3), and proportionality constant, $r_{\sigma,max}$, or called maximum specific growth rate (with unit similar to r_σ). This value can lies between 1 and 0.001 h^{-1} depending on cell types and cultivation conditions [220]. These nomenclatures are applicable for other growth models discussed below unless stated.

In addition to Monod kinetics, other black-box models are also presented here [189]:

Tessier model: $r_\sigma = r_{\sigma,max}\left(1 - e^{-C_{O,\sigma}/K_S}\right)$ A.56

Moser model: $r_\sigma = r_{\sigma,max}\left[\frac{C_{O,\sigma}{}^n}{C_{O,\sigma}{}^n + K_S}\right]; \quad n \in \Re \text{ and } n > 1$ A.57

Contois model: $r_\sigma = r_{\sigma,max}\left[\frac{C_{O,\sigma}}{C_{O,\sigma} + K_C\rho_\sigma}\right]$ A.58

Blackman model: $r_\sigma = \begin{cases} r_{\sigma,max}\left[\frac{C_{O,\sigma}}{2K_S}\right] & \text{when } C_{O,\sigma} \le 2K_S \\ r_{\sigma,max} & \text{when } C_{O,\sigma} \ge 2K_S \end{cases}$ A.59

Logistic law: $r_\sigma = r_{\sigma,max}\left[1 - \frac{\rho_\sigma}{K_X}\right]$ A.60

Tessier model simply describes cell growth as exponential function of substrate. Based on Monod's kinetics, Moser's model accounts higher order dependence of substrate. Blackman model expresses the specific growth rate in conditional form, that is, the cell

growth reaches its maximum rate when the substrate is $2K_S$, where K_S is the substrate concentration at $r_{\sigma,max}/2$. The community effect is taken account in the Contois and Logistic models in that cell growth decelerates when cell mass concentration increases. It should be noted that these models are purely empirical that have no rigorous physical significance [189] but provide a useful correlation with experimental results. Other models had been proposed to model the inhibitory effects subjected by limiting substrate in excess or metabolic product in excess:

Inhibition by limiting substrate: $$r_\sigma = r_{\sigma,max}\left[\frac{C_{O,\sigma}}{C_{O,\sigma}^{\ 2}/K_I + C_{O,\sigma} + K_S}\right] \qquad \text{A.61}$$

Inhibition by metabolic product:

$$r_\sigma = r_{\sigma,max}\left[\frac{C_{O,\sigma}}{C_{O,\sigma} + K_S}\right]\left[\frac{1}{1 + P_\sigma / K_I}\right] \qquad \text{A.62a}$$

$$r_\sigma = r_{\sigma,max}\left[\frac{C_{O,\sigma}}{C_{O,\sigma} + K_M}\right]\left[1 - \frac{P_\sigma}{P_{\sigma,max}}\right] \qquad \text{A.62b}$$

The toxic effect is present when the substrate is in excess and/or metabolite accumulates to non-physiological level. Under these conditions, cells cease to grow and cell death results. In these two equations, K_I is the inhibition coefficient and P_σ in equation A.62 refers to concentration of metabolite that has an inhibitory effect on growth. $P_{\sigma,max}$ is the threshold metabolite concentration that is the "cut-off point" for cell growth. The models mentioned above only accommodate one limiting substrate. If the number of limiting substrate is more than one (say, the carbon source and nitrogen source are selected as a limiting substrate), a multiplicative form or minimum form

can be used. For two limiting substrates, denoted as 1 and 2 (dual limitation), Monod's model takes the form:

$$\text{Multiplicative form: } r_\sigma = r_{\sigma,max}\left[\frac{C_{1,\sigma}}{C_{1,\sigma}+K_1}\right]\left[\frac{C_{2,\sigma}}{C_{2,\sigma}+K_2}\right] \quad \text{A.63}$$

$$\text{Minimum form: } r_\sigma = r_{\sigma,max}\text{MIN}\left\{\frac{C_{1,\sigma}}{C_{1,\sigma}+K_1}, \frac{C_{2,\sigma}}{C_{2,\sigma}+K_2}\right\} \quad \text{A.64}$$

Both expressions cannot estimate the specific growth rate in a reasonable way in that the multiplicative form usually underestimates the rate whereas the minimum form overestimates its magnitude [221].

For the cell mass deposition model applied in this study, a single limiting substrate, oxygen, was selected and the inhibitory effect due to excessive substrate and metabolite was neglected. Inclusion of a "community effect" could be necessary, which contributes to down-regulation of proliferation. In this regard, Contois model [188] was chosen and the cell growth rate can be expressed by:

$$R_\sigma = \frac{d\rho_\sigma}{dt} = r_{\sigma,max}\left[\frac{C_{O,\sigma}}{C_{O,\sigma}+K_C\rho_\sigma}\right]\rho_\sigma \quad \text{A.65}$$

A.8 MACROSCOPIC CELL GROWTH RATE, SOURCE AND SINK TERMS

It should be noted that growth and consumption only take place in the cell phase; so volume-averaged cell mass deposition, species formation and consumption rates

should be expressed in intrinsic volume-averaged form in σ-phase. First, the cell mass deposition rate, equation A.65 can be volume-averaged and yield:

$$\varepsilon_\sigma <R_\sigma>^\sigma = <\rho_\sigma>^\sigma \frac{d\varepsilon_\sigma}{dt} = \varepsilon_\sigma <r_{\sigma,max}\left[\frac{C_{O,\sigma}}{C_{O,\sigma}+K_C\rho_\sigma}\right]\rho_\sigma>^\sigma \qquad \text{A.66}$$

This result has been simplified by ignoring the displacement rate of the interface, $\vec{w}$, as in equation A.7, when volume-averaging the time derivative. The density of cell phase, $<\rho_\sigma>^\sigma$, was treated as constant that has been used in the analysis of Galban and Locke [42, 43]. They claimed that this density was the average of the new and old cells and since a "black box" assumption was used, this should be plausible to apply here. The non-linearity of equation A.66 should be further treated using decomposition and power series to attain a useful form. The process can be found in paper of Wood and Whitaker [176] and the more useful equation is given here:

$$\varepsilon_\sigma <R_\sigma>^\sigma = <\rho_\sigma>^\sigma \frac{d\varepsilon_\sigma}{dt} = \varepsilon_\sigma\left[\frac{r_{\sigma,max}<C_{O,\sigma}>^\sigma}{<C_{O,\sigma}>^\sigma + K_C <\rho_\sigma>^\sigma \varepsilon_\sigma}\right]<\rho_\sigma>^\sigma \qquad \text{A.67}$$

A similar procedure can be applied to equation 2.4.10 to 2.4.13 to obtain the intrinsic volume-averaged reaction rate of species i, for example, oxygen:

$$\varepsilon_\sigma <R_O>^\sigma = -\varepsilon_\sigma\left[\frac{r_{O,max}<C_{O,\sigma}>^\sigma}{<C_{O,\sigma}>^\sigma + K_{M,O}}\right] \qquad \text{A.68}$$

In the process of deriving the macroscopic cell mass deposition rate and macroscopic one-equation mass balance, local mass equilibrium was applied. It is also necessary to express $\{R_i\}$ in equation A.35 explicitly. Now, decomposing $<C_{O,\sigma}>^{\sigma}$ using equation A.31, equations A.67 and A.68 can be consequently arranged in these forms:

$$<\rho_\sigma>^\sigma \frac{d\varepsilon_\sigma}{dt} = \varepsilon_\sigma\left[\frac{r_{\sigma,max}\{C_O\}}{\{C_O\}+K_C K_{eq,O}\varepsilon_\sigma}\right]<\rho_\sigma>^\sigma + \varepsilon_\sigma\left[\frac{r_{\sigma,max}K_{eq,O}\hat{C}_{O,\sigma}}{(\{C_O\}+K_C K_{eq,O}\varepsilon_\sigma)(\{C_O\}+K_C K_{eq,O}\varepsilon_\sigma+\hat{C}_{O,\sigma})}\right]<\rho_\sigma>^{\sigma^2} \quad \text{A.69}$$

and

$$\varepsilon_\sigma <R_O>^\sigma = -\varepsilon_\sigma\left[\frac{r_{O,max}\{C_O\}}{\{C_O\}+K_{M,O}K_{eq,O}}\right] - \varepsilon_\sigma\left[\frac{r_{\sigma,max}K_{eq,O}\hat{C}_{O,\sigma}}{(\{C_O\}+K_{M,O}K_{eq,O})(\{C_O\}+K_{M,O}K_{eq,O}+\hat{C}_{O,\sigma})}\right] \quad \text{A.70}$$

The first and second terms on the right hand side of equation A.70 are $\{R_O\}$ and $\hat{R}_O$, respectively, which have been appeared in equation A.32. With equation A.70, other $\{R_i\}$ and $\hat{R}_i$ for glucose, carbon dioxide and lactate, for example, can be determined. Local mass equilibrium allowed us to neglect the non-equilibrium term (i.e. second term on the right hand side in equation A.69 and A.70). Hence, the results turn out to be in simpler forms:

$$\frac{d\varepsilon_\sigma}{dt} = \varepsilon_\sigma \left[\frac{r_{\sigma,max}\{C_O\}}{\{C_O\} + K_C K_{eq,O} \varepsilon_\sigma} \right] \quad \text{A.71}$$

and

$$\{R_O\} = -\varepsilon_\sigma \left[\frac{r_{O,max}\{C_O\}}{\{C_O\} + K_{M,O} K_{eq,O}} \right] \quad \text{A.72}$$

The cell growth rate in equation A.71 is expressed as a dynamic change of volume fraction of cell phase ($\frac{d\varepsilon_\sigma}{dt}$) for the convenience of solving other governing equations. Other $\{R_i\}$s can be written with the same procedure and the form should be similar to equation A.72.

Appendix B: User Defined Functions (UDF)

The numerical solution was obtained using commercial CFD software FLUENT®. It is required that user defined functions (UDFs) be written to execute some particular features in FLUENT®. The UDFs must be written in the C language and macros provided by FLUENT®. After the UDF file is written and interpreted through FLUENT®, these functions can be executed during the simulation. In this section, a sample UDF file used in the simulation for a single flow is presented for reference. In this file, the items stated below are specified:

Initial volume fraction of cell phase (ε_o);

Momentum sink terms in x and y directions ($\mu_\beta K_\beta^{-1} \cdot < v_\beta >$);

Reaction terms (sink or source) of species in mass balance ($\{R_i\}$);

Cell mass deposition rate ($\frac{d\varepsilon_\sigma}{dt}$);

Effective diffusivity of species i ($D_{eff,i}$);

Diffusion coefficient of cell mass (= 0);

Density of medium (ρ_β);

Viscosity of medium (μ_β);

Velocity profile at inlet ($<v_\beta>$ at inlet)

```
/****udfs for single flow, 2-region model with O2-limiting
growth****/
```

```
/****Define source terms and mass diffusivities and effective
permeability***/

#include "udf.h"

#define DA1 7.863604E+01 /*Dakholmer no. for oxygen consumption, [-
]*/

#define KM_O 9.673559E-01 /*dimensionless half saturation constant,
[-]*/

#define DA2 2.657454E-02 /*Dakholmer no. for cell growth, [-]*/

#define KC_O 1.419776E+01 /*dimensionless contonis constant, [-]*/

#define VF_SCAFF0 0.040973235 /*initial volume fraction of scaffold
with 95.9% porosity*/

#define DEN_M 1.0 /*dimensionless density of medium, [-]*/

#define UNIT_CELL_LEN 0.000186 /*cell pore size [m]*/

#define LEN_SCALE 0.000186 /*length scale, [m]*/

#define SC 3.398058E+02 /*Schdmit no. [-]*/

#define YMAX 2.75

#define YMIN 0.0

#define VMAX 4.17E+01

DEFINE_INIT (INIT_VF_CELL, domain)

{

  cell_t c;

  Thread *t;

  thread_loop_c(t,domain)

   {

    if (THREAD_ID(t) == 2)

     {
```

```
      begin_c_loop_all(c,t)
       {
        C_UDSI(c,t,0) = 5.241615E-03;
       }
      end_c_loop_all(c,t)
     }
    else if (THREAD_ID(t) == 3)
      {
       begin_c_loop_all(c,t)
              {
               C_UDSI(c,t,0) = 0.0;
              }
       end_c_loop_all(c,t)
      }
   }
}

DEFINE_SOURCE(X_M_SINK,c,t,dS,eqn)
{
 double VF_CELL = C_UDSI(c,t,0);
 double VF_SCAFF = VF_SCAFF0;
 double POR = 1.0 - VF_CELL - VF_SCAFF;
 double DIA_BS = 2.0*sqrt((1.0-POR)/M_PI)*UNIT_CELL_LEN;
 double K = pow((DIA_BS*POR),2)/(180.0*pow((1.0-POR),2))/LEN_SCALE;
```

```
 double SC1 = C_MU_L(c,t);
 double X_SOURCE;
      dS[eqn] = -SC1/K;
      X_SOURCE = -SC1/K*C_U(c,t);
 return X_SOURCE;
}
DEFINE_SOURCE(Y_M_SINK,c,t,dS,eqn)
{
 double VF_CELL = C_UDSI(c,t,0);
 double VF_SCAFF = VF_SCAFF0;
 double POR = 1.0 - VF_CELL - VF_SCAFF;
 double DIA_BS = 2.0*sqrt((1.0-POR)/M_PI)*UNIT_CELL_LEN;
 double K = pow(DIA_BS*POR,2)/(180.0*pow((1.0-POR),2))/LEN_SCALE;
 double SC1 = C_MU_L(c,t);
 double Y_SOURCE;

      dS[eqn] = -SC1/K;
      Y_SOURCE = -SC1/K*C_V(c,t);
 return Y_SOURCE;
}
DEFINE_SOURCE (O2_SINK,c,t,dS,eqn)
{
 double VF_CELL = C_UDSI(c,t,0);
 double MF_O = C_YI(c,t,0);
```

```
 double RATE_O = -DA1*MF_O/(MF_O+KM_O);
 double RATE;
                                dS[eqn] = 0.0;
                                RATE = VF_CELL*RATE_O;
 return RATE;
}
DEFINE_SOURCE (GROWTH_RATE,c,t,dS,eqn)
{
 double VF_CELL = C_UDSI(c,t,0);
 double limit = 1.0 - VF_SCAFF0;
 double MF_O = C_YI(c,t,0);
 double F_O;
 double RATE;
      if (VF_CELL < limit || MF_O > 0.2)
         {
           F_O = DA2*MF_O/(MF_O+KC_O*VF_CELL);
           dS[eqn] = 0.0;
           RATE = VF_CELL*F_O;
         }
      else
        {
           dS[eqn] = 0.0;
           RATE = 0.0;
        }
```

```
 return RATE;
}
/*0=OXYGEN, 1=GLUCOSE, 2=LACTATE, 3=CARBON DIOXIDE*/
DEFINE_DIFFUSIVITY(DIFF,c,t,i)
{
 double VF_CELL = C_UDSI(c,t,0);
 double VF_SCAFF = VF_SCAFF0;
 double POR = 1.0-VF_CELL-VF_SCAFF;
 double D[1];
if (THREAD_ID(t) == 2)
   {
    D[i] = 0.7817*POR + 0.1895;
    }
 else if (THREAD_ID(t) == 3)
    {
     D[i] = 1.0;
    }
 return D[i];
}
DEFINE_DIFFUSIVITY(UDS_DIFF,c,t,i)
{
  double UDS_D;
  UDS_D = 0.0;
  return UDS_D;
```

```
}
DEFINE_PROPERTY(DEN,c,t)
{
  double RHO = DEN_M;
  return RHO;
}
DEFINE_PROPERTY(VISO,c,t)
{
  double VF_CELL = C_UDSI(c,t,0);
  double VF_SCAFF = VF_SCAFF0;
  double POR = 1.0-VF_CELL-VF_SCAFF;
  double SC1;
  if (THREAD_ID(t) == 2) SC1 = SC/POR;
  else if (THREAD_ID(t) == 3) SC1 = SC;
  return SC1;
}
DEFINE_PROFILE(VEL_PROF, t, i)
{
 double RAD = 0.5*(YMAX-YMIN);
 double x[ND_ND],Y;
 face_t f;
 begin_f_loop(f,t)
  {
   F_CENTROID(x,f,t);
```